SCUOLA DI DOTTORATO
UNIVERSITÀ DEGLI STUDI DI MILANO-BICOCCA

Department of Earth and Environmental Sciences

PhD program: Chemical, Geological and Environmental Sciences, Cycle XXXVII

Curriculum: Geological Sciences

THE PAST AS THE KEY TO THE IMMINENT FUTURE: RECONSTRUCTING CLIMATE EVOLUTION FROM THE GEOLOGICAL RECORD

Surname Name: **Ali Mubashir**

Registration number: **886085**

Tutor: **Prof. Eduardo Garzanti** (University of Milano Biococca, Italy)

Supervisor: **Prof. Eduardo Garzanti**

Supervisor: **Prof. Pietro Sternai** (University of Milano Biococca, Italy)

Co-Supervisor: **Dr. Giovanni Coletti** (University of Milano Biococca, Italy)

Mobility Supervisor: **Prof. Sébastien Castelltort** (University of Geneva, Switzerland)

Mobility Supervisor: **Prof. Thierry Adatte** (University of Lausanne, Switzerland)

Coordinator: Prof. Marco Giovanni Malusà

ACADEMIC YEAR 2023/2024

SCUOLA DI DOTTORATO
UNIVERSITÀ DEGLI STUDI DI MILANO-BICOCCA

THE BAROCH NALA, SURGHAR RANGE, NE PAKISTAN

Contents

Thesis Abstract

This doctoral research investigates the effect of Early Paleogene warming events, with a particular focus on the Pre-Onset Excursion (POE) and the Paleocene-Eocene Thermal Maximum (PETM), on shallow marine carbonate systems within the Tethys realm. The study adopts a multi-proxy approach by combining paleontological, sedimentological, mineralogical, and geochemical data to reveal the responses of carbonate producers to extreme climate events. Rising atmospheric CO_2 levels from human activities have disrupted marine environments, particularly shallow coastal ecosystems, emphasizing the need to explore geological analogs for understanding long-term ecosystem responses to warming. This research examines four carbonate successions spanning the Late Cretaceous to the Early Eocene: the Maiella section in Italy (western Tethys) and the Ghumanwan, Baroch Nala, and Nammal Gorge sections in Pakistan (eastern Tethys). Findings highlight the fast recovery of coral-algal systems following the K/Pg extinction in the Maiella section. The corals become less abundant during the early Thanetian at the boundary between shallow benthic zone (SBZ) 3 and 4, while the skeletal assemblages become dominated by large benthic foraminifera (LBF) in the Ghumanwan section. In the Baroch Nala and Nammal Gorge section, two hyperthermal events, the POE and PETM recorded, which show the initial changes in Late Paleocene skeletal assemblages start at the onset of POE while the complete LBF turnover recorded at PETM, During the POE and PETM, the increased global temperature and a more pronounced shift towards humid conditions enhanced weathering intensity and nutrient supply. Stressful environmental conditions favored a major biotic turnover with long-lasting consequences. Among large benthic foraminifera, nummulitids outcompeted the *Lockhartia* assemblages that were dominant earlier in the Paleocene, and they remained as the primary carbonate producers in the eastern Tethys for the following 20 million years.A comprehensive comparison with global records provides insights into the adaptability and long-term changes in carbonate producers under climatic stress, offering a perspective on how modern marine ecosystems might respond to current and future climate change.

Chapter 1 – Introduction

This doctoral research aims at deepening our understanding of Paleogene warming events and focuses particularly on the Pre-Onset Excursion (POE) and the Paleocene-Eocene Thermal Maximum (PETM), and their effects on carbonate producers across the Tethys region. The study employs a multi-proxy approach, integrating quantitative paleontological and sedimentological analyses coupled with mineralogical and geochemical data sets.

Due to anthropogenic activities, the current atmospheric CO_2 level, approximately close to 400 ppm (parts per million), is nearly double the pre-industrial level of around 250 ppm (Ritchie & Roser, 2017). This sharp and rapid rise in carbon dioxide concentrations has significantly contributed to global warming, resulting in a rapid increase in Earth's temperature (Edenhofer, IPCC 5th AR 2014). Consequently, marine ecosystems, particularly shallow coastal seas where most of human activities are concentrated, are facing severe impacts. Rising temperatures are disrupting the delicate balance of marine habitats, altering oceanic currents, and causing acidification, all of which threaten the biodiversity and survival of countless marine species, especially in shallow marine environments.

Today, modern carbonate factories are predominantly located in the shallow sea of tropical and subtropical regions. These carbonate producers are highly sensitive and vulnerable to anthropogenic warming (Cornwall et al., 2021). In recent years, coral reefs and other shallow marine carbonate producers, such as those in the Maldives and the Great Barrier Reef (GBR) in Australia have been suffering from bleaching due to rising ocean temperatures (Berkelmans & Oliver, 1999; Perry & Morgan, 2017). While we have some clues on the short-term (years to decades) response of these environments to climate changes, we have limited knowledge regarding processes that extend across centuries and millennia. To get insights on the long-term answer of marine environments to climate changes we have to look at the geological record as the past is the key to the future. In this regard, Early Paleogene warming events represent good analogues for future carbonate production and the long-term response of marine ecosystems to the ongoing warming.

The Early Paleogene warming events have been extensively studied in deep marine environments from the North to the South Pole. However, shallow marine carbonate

factories during the Early Paleogene interval are less well-studied, and comprehensive datasets of environmental changes (biological, mineralogical, and geochemical) in response to hyperthermal events are very rare. Furthermore, most of the Paleogene carbonates are overall poorly exposed along the Tethyan margin from east to west. The shallow-water carbonates of the western Tethys (currently Spain, France, Slovenia, Italy, etc.) are well studied and provide a complete record of paleoenvironmental changes across the Early Paleogene interval. However, much less is known about the eastern part of the Tethys (currently Iran, Pakistan, and India)

This is partially caused by the complex geodynamics of the eastern Tethys, including the Himalayan collision of the Early Paleogene, which makes it difficult to continuously track Paleocene climate changes.

Given the importance of this topic and the lack of data available for the eastern side of the Tethys, four shallow-water carbonate successions spanning from the Late Cretaceous to the Early Eocene (Figure 1.1) were selected across Tethys to track the responses of carbonate producers to Early Paleogene warming events.

These include:

- Maiella section, Central Italy, western Tethys (Late Cretaceous to Early Paleocene, SBZ1-SBZ2),
- Ghumanwan section, Hazara Basin, Pakistan, eastern Tethys (Middle-Late Paleocene, SBZ3-4),
- Baroch Nala section, Surghar Range, Pakistan, eastern Tethys (Middle Paleocene-Early Eocene, SBZ3-5),
- Nammal Gorge section, Salt Range, Pakistan, eastern Tethys (Middle Paleocene-Early Eocene, SBZ3-5.

The thesis will be organized into five chapters. The first chapter provides a detailed overview of the topic, briefly describing past climatic events from the Cambrian period to the Early Paleogene. It also introduces the fundamental concepts of carbonate production through the carbon cycle and explains how warming events can affect carbonate production and cause biotic turnovers. The chapter concludes with a discussion of the research gaps and the aim of the thesis.

The second chapter highlights the significance of the studied succession from the western Tethys, specifically the "Maiella Mountain (Vallone delle Tre Grotte,

Pennapiedimonte, Central Italy)". This section presents a quantitative analysis of the rapid recovery of coral-dominant carbonate factories following the massive Cretaceous-Tertiary (K/Pg) mass extinction event. It also demonstrates the dominance of coral-algal bioconstruction during the Early Paleocene (Serra-Kiel 1998-Shallow Benthic Zones SBZ1-SBZ2). This chapter has been submitted for publication to the "Rivista Italiana di Paleontologia e Stratigrafia" and it's currently in the revision stage.

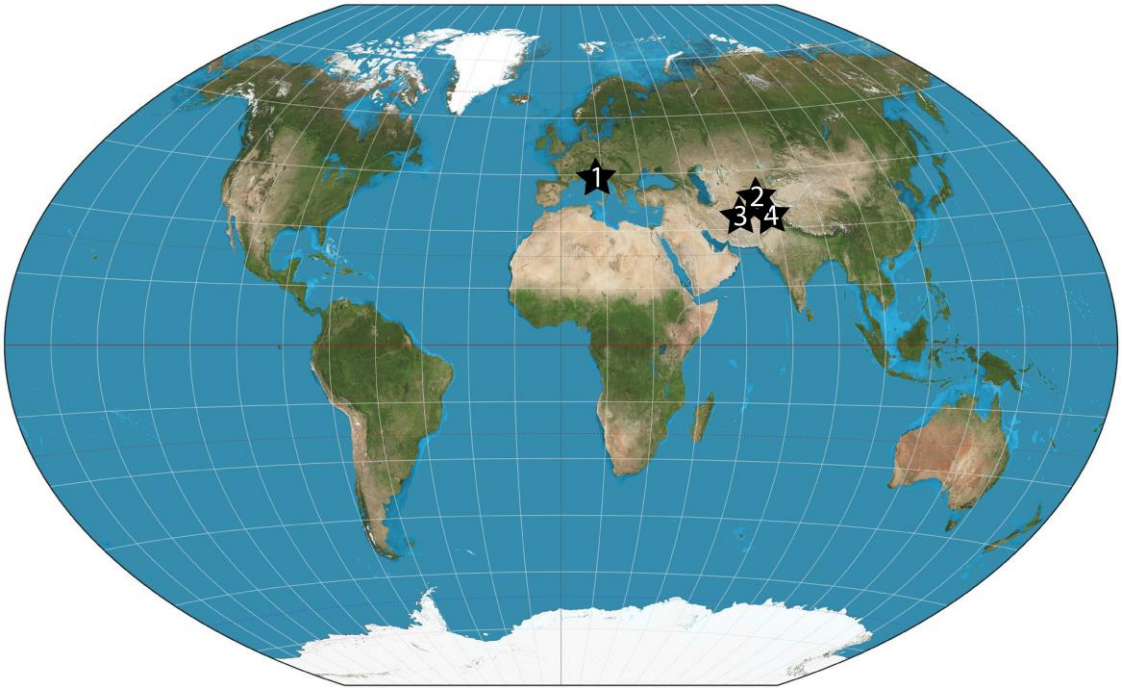

Figure 1.1: This global map shows the geographic position of the studied area. 1) Maiella section, Central Italy 2) Ghumanwan section, Hazara Basin Pakistan 3) Baroch Nala section, Surghar range, Pakistan 4) Nammal Gorge section, Salt range Pakistan

The third chapter focuses on the paleontological and sedimentological studies of the eastern Tethys during the Middle-Late Paleocene (SBZ3-4), specifically the succession of the Lockhart Formation in the Ghumanwan section of the Hazara Basin of Pakistan. This section provides the first insights into changes in skeletal assemblages in response to Paleocene warming events preceding the PETM. It shows a decline in coral reefs and a proliferation of large benthic foraminifera (LBF). This chapter has been published, as a paper in the Journal of Asian Earth Sciences: X, Volume 11, 1 June 2024, 100169

The fourth chapter focuses on the Late Paleocene to Early Eocene shallow-water succession of the Lockhart and Patala Formations (SBZ3-5) in the Baroch Nala section of the Surghar Range of Pakistan. A detailed multiproxy approach has been used,

comprising integrated analyses of organic and inorganic geochemical data, coupled with biostratigraphic data. In this section, two major hyperthermal events have been identified: the first event corresponds to the Pre-Onset Excursion within SBZ4, and the second corresponds to the globally recognized Paleocene-Eocene Thermal Maximum (PETM) at the SBZ4-5 transition. These events are linked to significant environmental and ecological changes. In this chapter, the geochemical dataset is correlated with data from the Paleocene-Eocene Global Stratotype Section and Point (GSSP) in Dababiya (Khozyem et al., 2023), the North Sea (Kemp al., 2016; Kender et al., 2021), and a section from Cameroon (Bitchong et al., 2023). This chapter has been submitted for publication to the "Marine and Petroleum Geology" and it is currently in the revision stage.

The final chapter integrates geochemical and paleontological analyses from the Nammal Gorge section (Salt Range), Baroch Nala section (Surghar Range) and Ghumanwan section (Hazara Basin) of Pakistan. These sections spans from SBZ3 to SBZ5. A detailed correlation is drawn between the Hazara Basin, Baroch Nala, and Nammal Gorge sections. Subsequently, the chapter focuses on the large benthic foraminifera turnover (LBFT) in the Tethys, where a total of 34 shallow marine sections across the Tethys (SBZ3 to SBZ5/6) have been correlated with the studied sections. Finally, these data are compared with those from other general review of carbonate production across Tethys and around the world to further analyze global patterns.

1.1 Past Climatic Events

Since the evolution of marine life during the Early Paleozoic, planet Earth has experienced several warming periods throughout its geological history (Figure 1.2) (Castelltort et al., 2023).

From the Cambrian to the Middle Ordovician (541 to 443 million years ago), high atmospheric CO_2 levels contributed to a hothouse phase (Figure 2), resulting in a warm climate with no glaciation in the polar regions (Kump & Arthur, 1999; Read & Repetski, 2012). The continents were aligned along the equator, and due to the high sea level and consequent flooding of continental shelves, the coastal environment greatly expanded (Kabanov et al., 2023). The sedimentary rock record from this period is dominated by shallow marine carbonates, with carbonate production primarily

driven by cyanobacteria and algal mats (stromatolites). Additionally, trilobites and brachiopods were abundant during the Cambrian. This hot phase was followed by glaciation, beginning in the Late Ordovician (Ghienne, 2003; Sheehan, 2001).

The Late Ordovician glaciation was followed by the Middle Devonian warming phase (393 to 383 million years ago) (Figure 1.2). The latter event was associated with global atmospheric CO_2 levels ranging between 2000 ppm and 4500 ppm, far higher than today's level of 400 ppm (Thompson & Newton, 1988). This increase in CO_2 turned the Middle Devonian into a warm period, with no polar ice caps. The paleo-continents were mainly located in tropical to subtropical regions, and the warm seawater created favorable conditions for reef-building organisms, which were dominated by stromatoporoids (sponges), rugose corals, and tabulate corals (Copper & Scotese, 2003). The Middle Devonian hothouse phase was followed by a long-lasting cooling phase, caused by CO_2 sequestration through silicate weathering in the Late Devonian (Pisarzowska & Racki, 2020).

Following the Middle Devonian hothouse phase, the next major warming event occurred during the Permian-Triassic (P/T) hothouse phase, about 252 million years ago. This was one of the most extreme global warming events in Earth's history and was associated with the Permian-Triassic mass extinction of flora and fauna. During this hothouse phase, active volcanism in the Siberian Traps released vast amounts of greenhouse gases, including CO_2, methane, and sulfur dioxide. Atmospheric CO_2 concentrations raised to nearly 5000 ppm, resulting in a global temperature increase ranging from 6°C to 10°C. The P/T mass extinction event led to the extinction of approximately 90% of marine species and 70% of terrestrial species (Lo et al., 2002; Preto et al., 2010; Sun et al., 2012). This ocean warming caused the collapse of coral reefs and the extinction of long-lived taxa such as trilobites and brachiopods (Taylor, 2004). In the sedimentary record, this warming phase is marked by black shales, indicating ocean anoxia, acidification, and sea-level rise (Sun et al., 2024). The hot and arid conditions at the Permian-Triassic boundary also led to widespread wildfires and enhanced silicate weathering (Winguth et al., 2015).

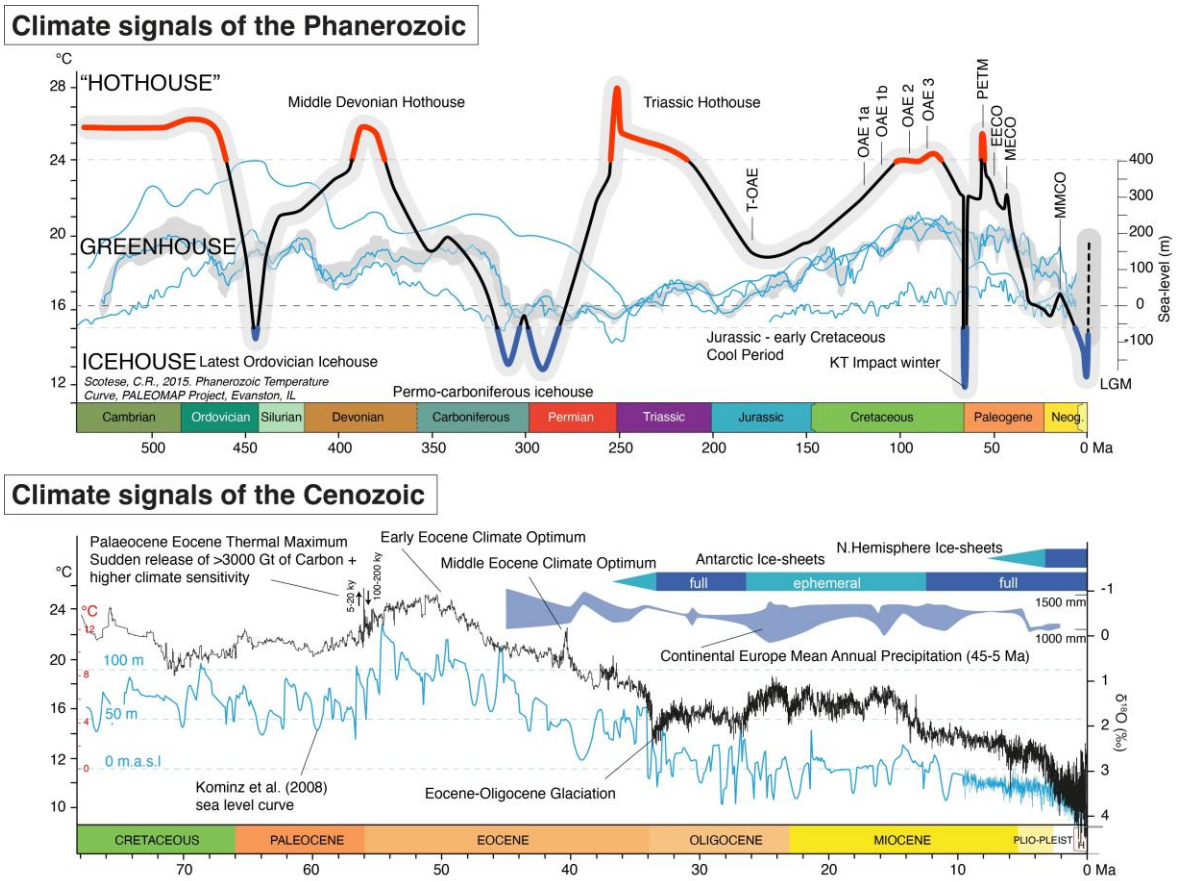

Figure 1.2 : shows the past climatic hyperthermal starting from the Early Cambrian to the Neogene (Castelltort et al., 2023)

The recovery phase after the P/T mass extinction extended into the Early Triassic period (252–247 million years ago), which remained a hot phase for millions of years. This prolonged heat made it unsuitable for the recovery of marine ecosystems and terrestrial biodiversification (Ogg et al., 2020). The high CO_2 levels during the Early Triassic were driven by extensive volcanic activity (Capriolo et al., 2022). The actual cooling and recovery trend began only in the Middle Triassic period (around 247 million years ago) (Kiessling, 2010). Enhanced silicate weathering helped draw down CO_2 levels, cooling the Earth's climate and allowing the recovery of marine and terrestrial ecosystems, including the emergence of the "Dinosaur Era" (Goddéris et al., 2008).

Following the long-lasting P/T hothouse phase, the climate of the Jurassic period (201 to 145 million years ago) also includes warming phases (Harris et al., 2017). This warming peaked during the Toarcian Oceanic Anoxic Event (T-OAE) around 183 million years ago (Them et al., 2017).

During this event, the atmospheric CO_2 levels were ranging between 2,000 and 3,000 ppm, caused by volcanism from the Karoo-Ferrar Large Igneous Province (Percival et al., 2015). This volcanism led to an increase in global temperatures and sea levels. The warming was also associated with ocean anoxia and acidification, which negatively impacted marine productivity and biodiversification (Boulila & Hinnov, 2017).

The warm periods of the Jurassic were followed by the long-lasting Cretaceous hothouse phase (145 to 66 million years ago) which included several intense warming intervals, including Ocean Anoxic Events (OAEs): OAE 1a (Early Aptian), OAE 1b (Early Albian), OAE 1c, OAE 1d (Late Albian), OAE 2 (Cenomanian-Turonian), and OAE 3 (Late Coniacian to Santonian). These warming events were linked to high atmospheric CO_2 levels, hot and dry climates, and greenhouse gases released by volcanic activity and gas-hydrate reactivation. The Cretaceous period was also characterized by high sea levels, glacier-free polar regions, and relatively acidic oceans (Figure 2) (Bomou et al., 2013; Kellar et al., 2008; Li et al., 2016; Mort et al., 2007; Sachse et al., 2012; Sanchez-Hernandez and Maurrasse, 2016; Singh et al., 2022)

The Cretaceous period culminated with the well-known Cretaceous-Paleogene (K-Pg) mass extinction event around 66 million years ago (Meredith et al., 2011). This extinction was triggered by a combination of extensive Deccan volcanism and the Chicxulub impact (Font et al., 2016; Keller et al., 2016). These events severely affected both deep and shallow marine benthic communities and led to the permanent demise of the Cretaceous rudist-dominated reefs and of the non-avian dinosaurs (Umbarger & Snedden, 2016).

1.2 Paleogene climate (66-23mya)

Following the K/Pg mass extinction connected to the Chicxulub impact and Deccan volcanism-connected, Earth's climate recovered around the beginning of the Early Danian (Paleocene), suggesting a relatively fast recovery of marine and terrestrial ecosystems (Figure 1.2) (Smit, 1999). During this time the carbonate platforms across the Tethyan realm were mainly dominated by shallow-water, symbiont-bearing, scleractinian corals associated with green algae (Baceta et al., 2005; Coletti et al., 2024 under review), whereas large benthic foraminifera, that were common during the Late Cretaceous, had become rare.

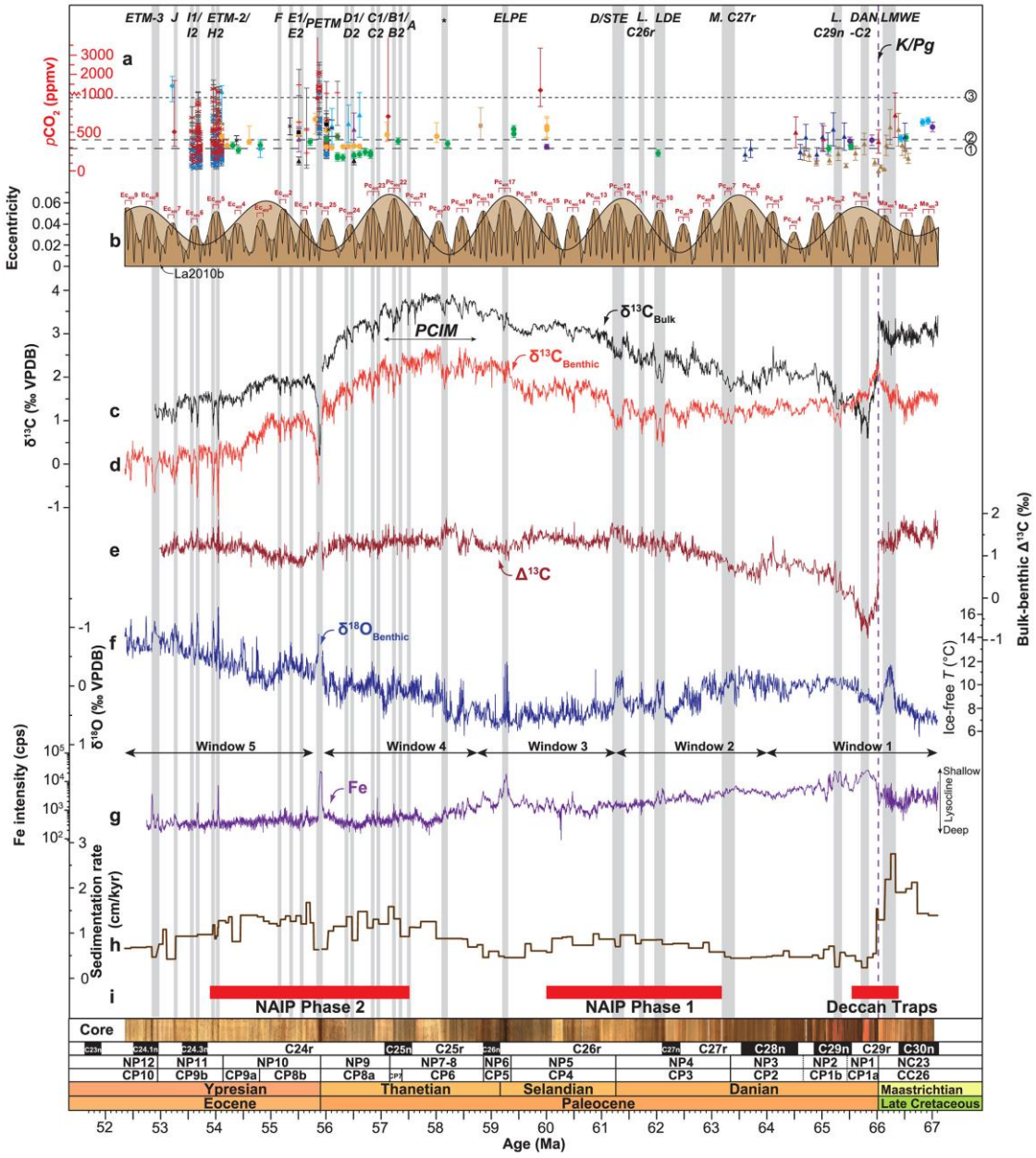

Figure 1.3: This figure shows the complete picture of Early Paleogene warming events. (Barnet et al., 2019)

The early Paleogene (66-23mya) witnessed many warming events often called hyperthermals due to the brief but sharp peak in temperature that characterise them. These include the Early Danian event, the Late Danian Event, the Danian/Selandian Transition Event, the Early Late Paleocene Event (ELPE), the Pre-Onset Excursion (POE), the Paleocene-Eocene Thermal Maximum (PETM), and possibly the Early Eocene Climatic Optimum (EECO) and Middle Eocene Climatic Optimum (MECO) (Figure 1.3)(Bowen et al., 2015: Barnet et al., 2019; Babila et al., 2022; Tremblin et al., 2022). The event was caused by the addition of isotopically light carbon or other

greenhouse gases into the atmosphere. Some of these events like ELPE, POE, PETM, and EECO are associated with mineralogical, biotic, and geochemical changes across the globe.

1.3 Pre-Onset Excursion (POE)

Prior to the PETM, another Late Paleocene warming event Pre-Onset Excursion (POE) occurred, its existence was firstly recognized and reported by (Bowen et al., 2015). This warming event is less studied compared to PETM, because of the lack of continuous and high-resolution data availability. POE is characterized by carbon isotope excursion (CIE) ranging between 1.0 to 1.5‰. (Babila et al., 2022; Doubrawa et al., 2022), and is comparatively much smaller than the negative shift of the PETM. This event is also associated with minor changes in skeletal assemblages in the eastern Tethyan carbonate platforms with the increase in lockhartiids and a decrease in orbitoidiforms large benthic foraminifera (e.g *Lakadongia sp.,* and *Orbitiosiphon* sp.). Base on biostratigraphy, the POE should have happened during the time characterised by SBZ4 (Shallow Benthic Zone, based on large benthic foraminifera) (Ali et al., 2025) and NP9a (Nannoplankton Zone, Doubrawa et al., 2022). POE is also marked by an increase in global temperature by ~2 to 5°C, a relatively small rise in temperature compared to the PETM. The POE is also characterized by changes in geochemical and mineralogical assemblages. An abrupt increase in Kaolinite abundance and a drop in palygorskite during POE indicates the transition towards a humid and wet climate (Ali et al., 2025). Across the Tethys, the POE interval is marked by mercury peaks indicating a possible volcanic cause to the event, most likely related to North Atlantic Igneous Provence (NAIP). (Tremblin et al., 2022; Ali et al., 2025) In low latitudes, shallow marine POE sections in eastern Tethys are characterized by evidence of enhanced weathering, increase in primary productivity driven by increased continental runoff, enhanced reduction processes, bottom water deoxygenation, and enhanced denitrification (Dong et al., 2024). The recovery phase of POE is shorter compared to the one of PETM.

1.4 Paleocene-Eocene Thermal Maximum (PETM)

During the Early Cenozoic, around 56 million years ago, at time of the Paleocene-Eocene transition, the release of 3,000 to 7,000 gigatons of isotopically light carbon into the atmosphere, and hydrosphere (Penman et al., 2018), raised the global temperature by 5-8 °C (Zachos et al., 2005, 2008; Slujis et al., 2011). The major evidence of this event is represented by a prominent negative shift in carbon stable isotope ($\delta^{13}C$) in both marine and terrestrial rock record (McInerney and Wing, 2011). The warming and the negative CIE correspond to the well-studied hyperthermal known as the Paleocene-Eocene Thermal Maximum (PETM) (Figure 1.2.1) (Slujis et al., 2007; Walsh, 2004). PETM was first reported in the Ocean drilling program ODP 690B cores from the coast of Antarctica (Kennett & Stott, 1991). During the PETM, a 10–15°C increase in temperature in polar regions while in deep oceans a 4–5°C increase in temperature was recorded (Zachos et al., 2008). The complete duration of the PETM is considered to be around 170-200 Kya (Röhl et al., 2007). The event can be is subdivided into three phases, 1) PETM onset, 2) PETM body, and 3) PETM recovery phase (Röhl et al., 2007).

The PETM age in shallow marine and deep marine systems, from the north pole to the south pole is very well constrained by the use of multiple biostratigraphic markers. In shallow marine, the PETM onset is marked at the transition between SBZ 4 and SBZ5-6 (Afzal et al., 2011; Li et al., 2020) characterized by the first appearance of *Alveolina sp.*, *Nummulite sp.*, and *Assilina sp*. (Afzal et al., 2011). The boundary between SBZ5-6 is unclear due to the overlapping of species in both biozones. Several LBF species of *Alveolina, Nummulites*, and *Orbitolites* are common in both biozones. However, these genera often display gradual evolutionary changes at the species level rather than distinct shifts, further obscuring the separation between SBZ5 and SBZ6 (Afzal et al., 2011; Serra-Kiel et al., 1998). As the separation between these two biozones is strongly based on species assemblages and the latter can be identified mainly through the use of oriented thin sections (or of CT-scan) in many researches the boundary between these two biozones is often blurred or unreliable (Afzal et al., 2011). Consequently, in the current analysis, they have been considered as one, representing the post-PETM recovery of LBF assemblages.

Based on calcareous nannofossils, the PETM corresponds to the boundary between NP9a and NP9b with the first appearance of *Discoaster sp.,* and *Rhomboasters sp.,* (Agnini et al., 2007). Based on planktonic foraminifera, the PETM is attributed to the P5 zone with the presence *Morozovella* and *Acarinina* (Luciani et al., 2007).

The PETM is associated with major environmental and ecological changes in marine and terrestrial ecosystems, comprising changes in biotic and mineralogical assemblages as well as changes in the organic and inorganic geochemical signals (Khozyem et al., 2013; 2015; 2023; 2024). The PETM is also characterized by deep-sea acidification, carbonate dissolution, perturbation in rainfall regime, high detrital input, intense hydrological cycles, high rates of evaporation, and precipitation, and releatively high eustatic sea-level (Zachos et al., 2005; McInerney and Wing, 2011; Chen et al., 2018; Westerhold et al., 2020). Enhance weathering, high continental runoff, and high kaolinite presence in the tropical region indicate the abrupt shift toward a hot and humid climate from a semi-arid climate (Adatte et al., 2000; 2002). The high CO_2 levels also caused ocean acidification in deeper marine environments, which affected the deep marine calcifiers like small benthic foraminifera, calcareous nannofossils, and planktic foraminifera (Zachos et al., 2005). In response to ocean acidification, deep marine benthic foraminifera indeed experienced mass extinctions during the PETM CIE (Thomas & Shackleton, 1996). The PETM is also associated with the oxidation of carbon-rich sediments. The presence of organic-rich, dark shale layers indicates the dissolution of calcite and the accumulation of organic matter along the PETM interval (Schulte et al., 2011).

The source of isotopically light carbon released during the PETM is still under debate, but some of the theories have been discussed frequently in recent years. PETM is strongly associated with the volcanism North Atlantic Igneous Province (NAIP). In the North Sea, several studies indicate a high ratio of mercury in the organic matter (mercury is mostly released by volcanic activity, thus its presence in organic matter is considered a proxy for volcanic activity) suggesting a proximity to a major volcanic source (Jones et al., 2019; 2023). Another hypothesis connects the PETM to the release of gases from methane hydrates trapped in marine sediments (Thomas et al., 2002). Finally, the analysis of stable isotopes of carbon and oxygen in foraminifera of deep-sea core relates the PETM and the other Paleocene hyperthermals to orbital cycles, possibly connecting the origin of the greenhouse gases to the cycle of twaning of

waining of permafrost at high latitudes (McInerney and Wing, 2011; Barnet et al., 2019; Westerhold et al., 2020).

In shallow marine carbonate platforms, the PETM has a strong impact on carbonate producers. Across the margin of Tethys, a turnover in large benthic foraminifera (LBF) is recorded (Ali et al., 2025; Kamran et al., 2021; Scheibner & Speijer, (2008).

High silicate weathering and burial of organic matter during the PETM resulted in the sequestration of tons of carbon and fostered a cooling of the climate and a recovery of the ecosystems after the PETM (Bains et al., 2017; Zeebe & Caldeira, 2008).

1.5 Carbon cycle and carbonate production

Past warming events like PETM, are associated with the rise in atmospheric CO_2, which is regulated by the carbon cycle. The carbon cycle plays a vital role in carbonate production and is controlled by the exchange of carbon between surficial and geological reservoirs (Figure 1.4) (Berner and Caldeira, 1997). A full understanding of the complex feedback mechanisms of the carbon cycle represents one of the main goals of modern geosciences (Cloetingh et al., 2023). In this cycle, calcium carbonate ($CaCO_3$) is a major component in the biosphere and lithosphere.

Currently, the upper part of the ocean is oversaturated with regards to $CaCO_3$, and this has seemingly been the case since at least 3.5 Ga (Ridgwell and Zeebe, 2005; Westerhold et al., 2020). Moreover, photosynthesis causes a depletion of aqueous CO_2 that induces a shift in the bicarbonate equilibrium, raises pH, and promotes calcification (e.g., Pentecost, 1991; Gattuso et al., 1999; Perito and Mastromei, 2011). During the evolution of life, these favorable chemical gradients eventually pushed living organisms to take advantage of calcium carbonate precipitation leading to the advent of widespread carbonate biomineralization at the Precambrian-Cambrian boundary (Wood et al., 2002). Since Cambrian times, sediment generated by the accumulation of calcareous skeletons represented an important part of the geological cycle that controls CO_2 concentration in the atmosphere. Shallow water carbonate producers, such as foraminifera, and algae, help in CO_2 sequestration through the formation of calcium carbonate ($CaCO_3$) structures. Calcium carbonate production by living organisms represents a source of CO_2 in the short term because it results in a

local increase of the concentration of aqueous CO_2 that, in turn, can drive an increase of CO_2 in the atmosphere (see *Box 1* in Ridgwell and Zeebe, 2005 for a detailed explanation).

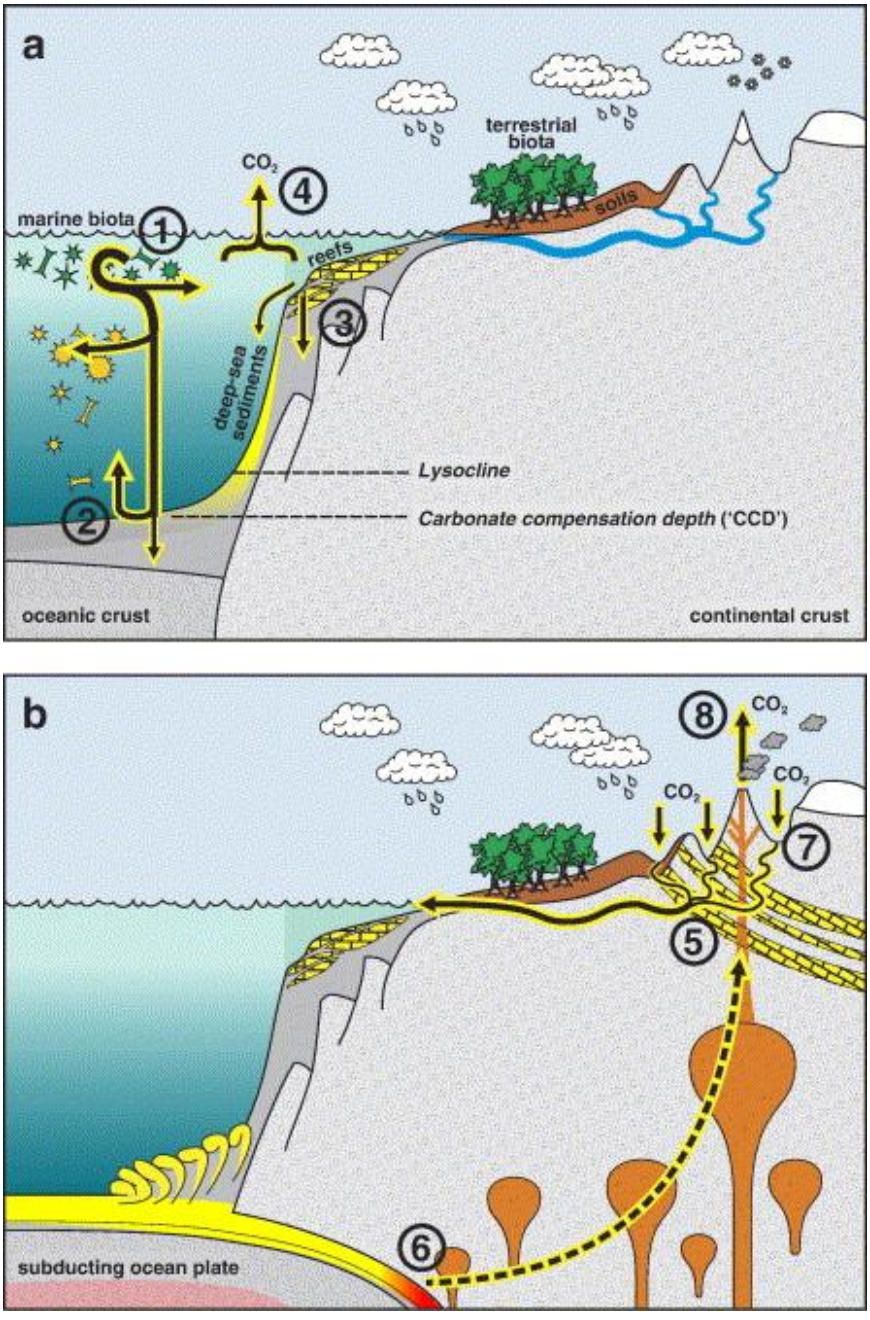

Figure 1.4: shows the global biogeochemical cycling of calcium carbonate between surficial and geological reservoirs (Ridgwell and Zeebe, 2005)

Conversely, $CaCO_3$ dissolution reduces aqueous CO_2 and is consequently a sink of atmospheric CO_2. In the long term, carbonate-rich sediments are either exposed or

subducted. In the former case, carbonate minerals are partly weathered and dissolved, representing a CO_2 sink. In the latter case, $CaCO_3$ is recycled back into the mantle by the formation of calcium silicates with a release of CO_2 that can be subsequently ejected into the atmosphere by volcanic activity (Figure 4) (see *Box 1* in Ridgwell and Zeebe, 2005 for a detailed explanation). Calcium silicate minerals, once exposed to weathering processes become another sink for atmospheric CO_2. Processes and feedbacks of this complex biogeochemical cycle are still incompletely understood, and the amount of carbon involved in each step is thus poorly constrained.

Given the relevance of this subject, several key priorities have been globally recognized to improve the knowledge of the global biogeochemical carbonate cycle, including a better understanding and definition of: (i) the modern global budget, especially as shallow-marine deposits are concerned; (ii) the response of calcifiers to ocean acidification; (iii) the dissolution of carbonate particles in marine environments; and, last but not least, (iv) remarkable climate warming events recorded in the geological record, such as the Paleocene Eocene Thermal Maximum (PETM). The PETM corresponds to a massive release of carbon into the hydrosphere-atmosphere system that occurred over a geologically brief period (less than 200 kyr) and caused an increase of 5 – 8 °C in global temperatures (McInerney and Wing, 2011). Because of the event's short duration and magnitude, it is considered a useful analog for present-day global warming (McInerney and Wing, 2011).

1.6 Effect of hyperthermal events on carbonate producers

As discussed above, carbonate producers play a major role in the carbon cycle. Shallow-water marine producers like large benthic foraminifera (LBF), green calcareous algae (GCA), red calcareous algae (RCA), and scleractinian corals (the major builders of modern tropical reefs) are sensitive and vulnerable to climate evolution mainly in tropical and subtropical regions (Benedetti et al., 2024).

Since the evolution of life on the earth, six stages of reef abundance have been identified (Cooper 1988). Among these stages, coral-dominated one have been terminated by extreme events like the K-Pg event, and PETM (Cooper, 1988).Warming events cause stressful ecological conditions like rising temperature, high detrital input, high nutrient supply, and ocean acidification, can affect the growth

of coral reefs in tropical marine systems, which can also lead to the loss of symbiotic relationship between coral and zooxanthellae (algae) and contributing to coral reef bleaching (Glynn, 1996).

After the scleractinian corals one of the other important group of carbonate producers in modern oceans is constituted by large benthic foraminifera (LBF). Symbiont bearing LBF belong to the Protista group (single-celled organisms), and they are usually considered, among single-celled organisms, as K-strategist (organisms that follow a reproductive strategy and typically thrive in stable environments such as oligotrophic and clean photic condition, low nutrient supply with normal salinity, pH, warm temperature). They display a shell (called test) consisting of either calcium carbonate (either high-magnesium calcite or low-magnesium calcite) or of agglutinated particles stabilized by a calcium carbonate cement (Hottinger, 1999). Given the presence of algal symbiont in the test, the latter display a complex morphology (Hottinger, 1999). Early Paleogene LBF assemblages are dominated by hyaline trocospiral forms like *Lockhartia* and orbitoidiforms, miscellanids, orthophragminids, and nummulitids which are considered K-strategists (among unicellular organism). Smaller porcelaneous species, such as most miliolids, agglutinated and hyaline taxa (Benedetti and Papazzoni, 2022; Sinanoğlu et al., 2022; Benedetti and Sinanoğlu, 2022), are considered as R-strategists (among unicellular organisms.

During the Paleogene, within carbonate platforms starting from the Late Salendian, LBF were among the most important carbonate producers. This group flourished during the Late Paleocene–Early Eocene and dominated for most of the Eocene, thanks to the elevated temperatures of the period. Due to their diversification and their abundance they are a fundamental tool for paleoenvironment.

Other important carbonate producers of the interval are green calcareous algae (GCA) and red calcareous algae (RCA). GCA occur in shallow and low-energy marine environments, typically in the upper euphotic zone (0 to -25 meters) and secrete a calcareous coating, usually made of aragonite, although calcite could have been present in some species. The CGA, such as *Halimeda*, *Penicillus*, *Acetabularia*, and *Cymopolia*, play an important role in modern carbonate production from fine clay-sized particles to larger grain sizes and even meter-sized structures (Granier, 2012).

In modern-day red calcareous algae (RCA), like Corallinales, Sporolithales, Peyssonneliales, and Nemaliales, play a vital role in carbonate production and are particularly present in temperate and cold seas (Basso, 2012). Global challenges, such as ocean warming and acidification, and decreasing pH levels threaten the calcification process, reducing algae growth, reproduction, abundance, and diversity. This results in the dominance of non-calcifying algae and can lead to ecosystem shifts.

1.7 Research gap and aim of the Thesis

Deep marine environments provide a complete and continuous rock record without any geological gap or hiatus and display a complete tracking of Paleoenvironmental changes that occur during climatic events. Conversely, shallow marine environments are associated with several geological problems that include, more lateral variability, frequent break in sedimentation (hiatus), the more extensive effect of diagenesis on geochemical and biological proxies, etc.

For these reasons, across the globe from the Northern Hemisphere to the Southern Hemisphere, based on planktonic foraminifera, dinoflagellates, biomarkers, and calcareous nannofossils assemblages, deep marine environmental changes (biotic, mineralogical, and geochemical) in response to Early Paleogene warming are very well documented (Barnet et al., 2019; Frieling & Sluijs, 2018; Jones et al., 2023, Mutterlose et al., 2007; Petrizzo, 2007; Schoon et al., 2011; Sluijs et al., 2013, Zachos et al. 2005). However, shallow water biotic and paleo-environmental changes (geochemical and mineralogical) are the less thoroughly studied when it comes to large scale paleoenvironmental changes. The available knowledge on the effect of Paleogene warming on shallow water carbonate producers is still limited. Only a few numbers of outcropping shallow marine carbonate successions ranging from the Late Paleocene – Early Eocene interval have been examined and are available. Most of these carbonate successions are exposed along the Tethyan realm. Several studies have been conducted on shallow water carbonate succession in western Tethys (Spain, Egypt, Slovenia, Italy and Turkey) (Aguirre et al., 2022; Baceta et al., 2005, 2011; Martín-Martín et al., 2020; Ozgen-Erdem et al., 2005; Pujalte et al., 2003, 2009; Orue-Etxebarria et al., 2001; Scheibner et al., 2005; Speijer et al., 2012 Scheibner and Speijer, 2008, 2009, Zamagni et al., 2008, 2012), On another side, the eastern Tethys

realm (China, India and Pakistan) is least investigated (Afzal et al., 2011 Zhang et al., 2013, 2019, Li et al., 2020, Kamran et al., 2021, Sakar et al., 2018, 2022).

However, very few quantitative data are available for tracking the response of carbonate producers during the Late Paleocene to Early Eocene interval. More quantitative data and research on ancient habitats are needed to improve our capacity to unveil the past, thereby allowing us to better comprehend the present, and foresee the future (Bialik et al., 2023). The question of how shallow water carbonate producers responded to past thermal event is unclear and needs more interpretation and more detailed high-resolution studies. Therefore, the present study aims at improving our knowledge on the distribution of carbonate-producing organisms during this crucial time interval by providing a quantitative analysis of the skeletal assemblages of a Paleocene to Early Eocene shallow-water carbonate succession exposed in Maiella platform central Italy, Ghumawan section, Hazara Basin, Surghar and Salt range, NE Pakistan. The studied succession deposited during the crucial Paleocene interval and comprise facies dominated by LBF, thus documenting the complete response of this important type of benthic calcifiers to periods of global warming. Here the quantitative paleontological analyses of skeletal and foraminiferal assemblages is combined with high-resolution, multiproxy geochemical data including stable carbon and oxygen isotope , mercury enrichment of organic matter, whole rock mineralogy, clay assemblages and TOC data to record environmental variations. Our results also indicate the Surghar section, as one of the most continuous and complete sections deposited in the eastern Tethyan realm during the Paleocene to Eocene time, tracking the complete biotic and environmental changes record of the PETM interval.

1.8 References

Adatte, T., Bolle, M. P., Kaenel, E. D., Gawenda, P., Winkler, W., & Von Salis, K. (2000). Climatic evolution from Paleocene to earliest Eocene inferred from clay-minerals: A transect from northern Spain (Zumaya) to southern (Spain, Tunisia) and southeastern Tethys margins (Israel, Negev). *GFF*, *122*(1), 7-8.

Adatte, T., Keller, G., & Stinnesbeck, W. (2002). Late Cretaceous to early Paleocene climate and sea-level fluctuations: the Tunisian record. *Palaeogeography, Palaeoclimatology, Palaeoecology*, *178*(3-4), 165-196.

Afzal, J., Williams, M., Leng, M. J., & Aldridge, R. J. (2011). Dynamic response of the shallow marine benthic ecosystem to regional and pan-Tethyan environmental change at the Paleocene–Eocene boundary. Palaeogeography, Palaeoclimatology, Palaeoecology, 309(3-4), 141-160.

Agnini, C., Fornaciari, E., Rio, D., Tateo, F., Backman, J., & Giusberti, L. (2007). Responses of calcareous nannofossil assemblages, mineralogy and geochemistry to the environmental perturbations across the Paleocene/Eocene boundary in the Venetian Pre-Alps. Marine Micropaleontology, 63(1-2), 19-38.

Aguirre, J., Baceta, J. I., & Braga, J. C. (2022). Coralline Algae at the Paleocene/Eocene Thermal Maximum in the Southern Pyrenees (N Spain). Frontiers in Marine Science, 9, 899877.

Babila, T. L., Penman, D. E., Standish, C. D., Doubrawa, M., Bralower, T. J., Robinson, M. M., Self-Trail, J.J., Speijer, R., Stassen, P., Foster, G., & Zachos, J. C. (2022). Surface ocean warming and acidification driven by rapid carbon release precedes Paleocene-Eocene Thermal Maximum. Science Advances, 8(11), eabg1025.

Baceta, J. I., Pujalte, V., & Bernaola, G. (2005). Paleocene coralgal reefs of the western Pyrenean basin, northern Spain: New evidence supporting an earliest Paleogene recovery of reefal ecosystems. Palaeogeography, Palaeoclimatology, Palaeoecology, 224(1-3), 117-143.

Baceta, J. I., Pujalte, V., Wright, V. P., Schmitz, B., Arenas, C., Pomar, L., & Colombo, F. (2011, July). Carbonate platform models, sea-level changes and extreme climatic events during the Paleocene-early Eocene greenhouse interval: a basin-platform-coastal plain transect across the southern Pyrenean basin. In Pre-Meeting Field trips Guidebook. Zaragoza, 28th IAS Meeting, Geo-Guías (Vol. 7, pp. 101-150).

Bains, P., Psarras, P., & Wilcox, J. (2017). CO_2 capture from the industry sector. *Progress in Energy and Combustion Science*, *63*, 146-172.

Basso, D. (2012). Carbonate production by calcareous red algae and global change. Geodiversitas, 34(1),

Barnet, J. S., Littler, K., Westerhold, T., Kroon, D., Leng, M. J., Bailey, I., Rohl, U. & Zachos, J. C. (2019). A high-Fidelity benthic stable isotope record of late Cretaceous–early Eocene climate change and carbon-cycling. *Paleoceanography and Paleoclimatology*, *34*(4), 672-691.

Benedetti, A., Papazzoni, C. A., & Bosellini, F. R. (2024). Unparallel resilience of shallow-water tropical calcifiers (foraminifera and scleractinian reef corals) during the early Paleogene global warming intervals. Palaeogeography, Palaeoclimatology, Palaeoecology, 651, 112393.

Benedetti, A., & Papazzoni, C. A. (2022). Rise and fall of rotaliid foraminifera across the Paleocene and Eocene times. *Micropaleontology*, *68*(2).

Benedetti, A., & Sinanoglu, D. (2022). Ornatorotalia ozgenerdemi n. sp. (Ornatorotaliidae, Foraminiferida) from the late Danian (SBZ2) of Eastern Turkey. Micropaleontology, 68(4), 389-399.

Berkelmans, R., & Oliver, J. K. (1999). Large-scale bleaching of corals on the Great Barrier Reef. *Coral reefs*, *18*, 55-60.

Berner, R.A., Caldeira, K., 1997. The need for mass balance and feedback in the geochemical carbon cycle. Geology 25(10), 955-956.

Bialik, O. M., Coletti, G., Mariani, L., Commissario, L., Desbiolles, F., & Meroni, A. N. (2023). Availability and type of energy regulate the global distribution of neritic carbonates. *Scientific Reports*, *13*(1), 19687.

Bitchong, A. M., Adatte, T., Ngos III, S., Keller, G., Karabeyoğlu, A. U., & Spangenberg, J. E. (2023). The Paleocene-Eocene transition in the Gulf of Guinea: Evidence of the PETM in the Douala basin, Cameroon. Marine and Petroleum Geology, 157, 106504.

Boulila, S., & Hinnov, L. A. (2017). A review of tempo and scale of the early Jurassic Toarcian OAE: implications for carbon cycle and sea level variations. Newsletters on Stratigraphy, 50(4), 363-389.

Bomou, B., Adatte, T., Tantawy, A. A., Mort, H., Fleitmann, D., Huang, Y., & Föllmi, K. B. (2013). The expression of the Cenomanian–Turonian oceanic anoxic event in Tibet. Palaeogeography, Palaeoclimatology, Palaeoecology, 369, 466-481.

Bowen, G. J., Maibauer, B. J., Kraus, M. J., Röhl, U., Westerhold, T., Steimke, A., Gingerich, P.D., Wing, S.L., & Clyde, W. C. (2015). Two massive, rapid releases of carbon during the onset of the Paleocene–Eocene thermal maximum. Nature Geoscience, 8(1), 44-47.

Capriolo, M., Mills, B. J., Newton, R. J., Dal Corso, J., Dunhill, A. M., Wignall, P. B., & Marzoli, A. (2022). Anthropogenic-scale CO_2 degassing from the Central Atlantic Magmatic Province as a driver of the end-Triassic mass extinction. Global and Planetary Change, 209, 103731.

Castelltort, S., Fillon, C., Lasseur, É., Ortiz, A., Robin, C., Guillocheau, F., ... & Calassou, S. (2023). *The Source-to-Sink Vade-mecum: History, Concepts and Tools| Vade-mecum de l'approche Source-To-Sink: Histoire, Concepts et Outils*. SEPM (Society for Sedimentary Geology).

Canadell, J.G., Monteiro, P.M.S., Costa, M.H., da Cunha, L.Cotrim, Cox, P.M., Eliseev, A.V., Henson, S., Ishii, M., Jaccard, S., Koven, C., Lohila, A., Patra, P.K., Piao, S., Rogelj, J., Syampungani, S., Zaehle, S., Zickfeld, K., 2021. Global Carbon and other biogeochemical cycles and feedbacks. In: Masson-Delmotte, V., Zhai, P., Pirani, A., Connors, S.L., Péan, C., Berger, S., Caud, N., Chen, Y., Goldfarb, L., Gomis, M.I., Huang, M., Leitzell, K., Lonnoy, E., Matthews, J.B.R., Maycock, T.K., Waterfield, T., Yelekçi, O., Yu, R., Zhou, B. (Eds.): Climate Change 2021: The Physical Science Basis. Contribution of Working Group I to the Sixth Assessment Report of the Intergovernmental Panel on Climate Change. Cambridge University Press.

Chen, C., Guerit, L., Foreman, B.Z., Hassenruck-Gudipati, H.J., Adatte, T., Honegger, L., Perret, M., Sluijs, A., Castelltort, S., 2018. Estimating regional flood discharge during Paleocene-Eocene global warming. Sci. Rep. 8, 1–8. https://doi.org/10.1038/ s41598-018-31076-3.

Cloetingh, S., Sternai, P., Koptev, A., Ehlers, T. A., Gerya, T., Kovács, I., ... & Limberger, J. (2023). Coupled surface to deep Earth processes: Perspectives from TOPO-EUROPE with

an emphasis on climate-and energy-related societal challenges. Global and Planetary Change, 226, 104140.

Copper, P., & Scotese, C. R. (2003). Megareefs in Middle Devonian supergreenhouse climates.

Copper, P. (1988). Ecological succession in Phanerozoic reef ecosystems: is it real?. *Palaios*, 136-151.

Cornwall, C. E., Comeau, S., Kornder, N. A., Perry, C. T., van Hooidonk, R., DeCarlo, T. M., ... & Lowe, R. J. (2021). Global declines in coral reef calcium carbonate production under ocean acidification and warming. *Proceedings of the National Academy of Sciences*, *118*(21), e2015265118

Dong, Y., Gachetti, A., Wu, Q., De Palma, M., Hu, X., Brachfeld, S., ... & Cui, Y. (2024). Paleoenvironment reconstruction of the eastern Tethys during the pre-onset excursion preceding the PETM. Palaeogeography, Palaeoclimatology, Palaeoecology, 647, 112234.

Doubrawa, M., Stassen, P., Robinson, M. M., Babila, T. L., Zachos, J. C., & Speijer, R. P. (2022). Shelf Ecosystems Along the US Atlantic Coastal Plain Prior to and During the Paleocene-Eocene Thermal Maximum: Insights Into the Stratigraphic Architecture. Paleoceanography and Paleoclimatology, 37(10), e2022PA004475.

Edenhofer, O. (Ed.). (2015). *Climate change 2014: mitigation of climate change* (Vol. 3). Cambridge University Press.

Etheridge, D.M., Steele, L.P., Langenfelds, R.L., Francey, R.J., Barnola, J.M., Morgan, V.I., 1998. Historical CO_2 records from the Law Dome DE08, DE08-2, and DSS ice cores. Trends: a compendium of data on global change, 351-364.

Font, E., Adatte, T., Sial, A. N., de Lacerda, L. D., Keller, G., & Punekar, J. (2016). Mercury anomaly, Deccan volcanism, and the end-Cretaceous mass extinction. Geology, 44(2), 171-174.

Frieling, J., & Sluijs, A. (2018). Towards quantitative environmental reconstructions from ancient non-analogue microfossil assemblages: Ecological preferences of Paleocene–Eocene dinoflagellates. Earth-Science Reviews, 185, 956-973.

Granier, B. (2012). The contribution of calcareous green algae to the production of limestones: a review. Geodiversitas, 34(1), 35-60.

Gattuso, J.P., Allemand, D., Frankignoulle, M., 1999. Photosynthesis and calcification at cellular, organismal and community levels in coral reefs: a review on interactions and control by carbonate chemistry. American Zoologist 39(1), 160-183.

Ghienne, J. F. (2003). Late Ordovician sedimentary environments, glacial cycles, and post-glacial transgression in the Taoudeni Basin, West Africa. Palaeogeography, Palaeoclimatology, Palaeoecology, 189(3-4), 117-145.

Glynn, P. W. (1996). Coral reef bleaching: facts, hypotheses and implications. Global change biology, 2(6), 495-509.

Goddéris, Y., Donnadieu, Y., de Vargas, C., Pierrehumbert, R. T., Dromart, G., & van de Schootbrugge, B. (2008). Causal or casual link between the rise of nannoplankton

calcification and a tectonically-driven massive decrease in Late Triassic atmospheric CO_2?. Earth and Planetary Science Letters, 267(1-2), 247-255.

Harris, R., McCall, R., Randall, O., Bin Tawang, M. H., Williams, R., Fairman, J. G., & Schultz, D. M. (2017). Climate change during the Triassic and Jurassic. Geology Today, 33(6), 210-215.

Hellevang, H., Aagaard, P., 2015. Constraints on natural global atmospheric CO_2 fluxes from 1860 to 2010 using a simplified explicit forward model. Scientific Reports 5(1), 1-12.

Hottinger, L. (1997). Shallow benthic foraminiferal assemblages as signals for depth of their deposition and their limitations. Bulletin de la Société géologique de France, 168(4), 491-505.

Hottinger, L. (1998). Shallow benthic foraminifera at the Paleocene-Eocene boundary. Verlag nicht ermittelbar.

Hottinger, L. (1999). 'Odd partnership", a particular size relation between close species of larger foraminifera, with an emendation of an outstandingly odd partner, Glomalveolina delicatissima (Smout, 1954), Middle Eocene. Eclogae Geologicae Helvetiae, 92(3), 385-393.

Jones, M. T., Percival, L. M., Stokke, E. W., Frieling, J., Mather, T. A., Riber, L., ... & Svensen, H. H. (2019). Mercury anomalies across the Paleocene–Eocene thermal maximum. Climate of the Past, 15(1), 217-236.

Jones, M. T., Stokke, E. W., Rooney, A. D., Frieling, J., Pogge von Strandmann, P. A. E., Wilson, D. J., Selnes, H., Mather, T. A., Schreck, S., Schwark, L., & Schultz, B. P. (2023). Tracing North Atlantic volcanism and seaway connectivity across the Paleocene–Eocene thermal maximum (PETM). Climate of the Past, 19(8), 1623-1652. https://doi.org/10.5194/cp-19-1623-2023

Kabanov, P., Hauck, T. E., Gouwy, S. A., Grasby, S. E., & van der Boon, A. (2023). Oceanic anoxic events, photic-zone euxinia, and controversy of sea-level fluctuations during the Middle-Late Devonian. *Earth-Science Reviews*, *241*, 104415.

Kamran, M., Frontalini, F., Xi, D., Papazzoni, C. A., Jafarian, A., Latif, K., ... & Wan, X. (2021). Larger benthic foraminiferal response to the PETM in the Potwar Basin (Eastern Neotethys, Pakistan). Palaeogeography, Palaeoclimatology, Palaeoecology, 575, 110450.

Kiessling, W. (2010). Reef expansion during the Triassic: Spread of photosymbiosis balancing climatic cooling. Palaeogeography, Palaeoclimatology, Palaeoecology, 290(1-4), 11-19.

Keller G, Adatte T, Berner Z, Chellai EH, Stueben D (2008) Oceanic events and biotic effects of the Cenomanian-Turonian anoxic event, Tarfaya Basin. Morocco Cretaceous Res 29(5-6):976–994

Keller, G., Punekar, J., & Mateo, P. (2016). Upheavals during the late Maastrichtian: Volcanism, climate and faunal events preceding the end-Cretaceous mass extinction. *Palaeogeography, Palaeoclimatology, Palaeoecology*, *441*, 137-151.

Kemp, S. J., Ellis, M. A., Mounteney, I., & Kender, S. (2016). Palaeoclimatic implications of high-resolution clay mineral assemblages preceding and across the onset of the Paleocene–Eocene Thermal Maximum, North Sea Basin. Clay Minerals , 51 (5), 793-813.

Kender, S., Bogus, K., Pedersen, G. K., Dybkjær, K., Mather, T. A., Mariani, E., Ridgwell, A., Riding, J.B., Wagner, T., Hesselbo, S.P. & Leng, M. J. (2021). Paleocene/Eocene carbon feedbacks triggered by volcanic activity. Nature communications, 12(1), 5186.

Kennett, J. P., & Stott, L. D. (1991). Abrupt deep-sea warming, palaeoceanographic changes and benthic extinctions at the end of the Paleocene. *Nature*, *353*(6341), 225-229.

Khozyem, H. A. S., Adatte, T., Spangenberg, J. E., Tantawy, A. A., & Keller, G. (2013). Palaeoenvironmental and climatic changes during the Paleocene–Eocene Thermal Maximum (PETM) at the Wadi Nukhul Section, Sinai, Egypt. *Journal of the Geological Society, 170*(2), 341–352. https://doi.org/10.1144/jgs2012-067

Khozyem, H., Adatte, T., Spangenberg, J. E., Keller, G., Tantawy, A. A., & Ulianov, A. (2015). New geochemical constraints on the Paleocene–Eocene thermal maximum: Dababiya GSSP, Egypt. *Palaeogeography, Palaeoclimatology, Palaeoecology*, *429*, 117-135.

Khozyem, H., Adatte, T., & Keller, G. (2023). Climatic and Environmental Changes During Paleocene-Eocene Thermal Maximum in Egypt: An Overview. The Phanerozoic Geology and Natural Resources of Egypt, 305-338.

Khozyem, H., Adatte, T., Brunet, M. F., Chiaradia, M., Keller, G., Thibault, N., ... & Castelltort, S. (2024). Multidisciplinary study on the stratigraphy of the upper Cretaceous-Paleogene successions in the western Tajik Basin, Uzbekistan. *Journal of Asian Earth Sciences*, *267*, 106137.

Kump, L. R., & Arthur, M. A. (1999). Interpreting carbon-isotope excursions: carbonates and organic matter. *Chemical Geology*, *161*(1-3), 181-198.

Li X, Wei Y, Li Y, Zhang C (2016) Carbon isotope records of the early Albian oceanic anoxic event (OAE) 1b from eastern Tethys (southern Tibet, China). Cretac Res 62:109–121

Li, J., Hu, X., Zachos, J. C., Garzanti, E., & BouDagher-Fadel, M. (2020). Sea level, biotic and carbon-isotope response to the Paleocene–Eocene thermal maximum in Tibetan Himalayan platform carbonates. Global and Planetary Change, 194, 103316.

Lo, C. H., Chung, S. L., Lee, T. Y., & Wu, G. (2002). Age of the Emeishan flood magmatism and relations to Permian–Triassic boundary events. Earth and Planetary Science Letters, 198(3-4), 449-458.

Luciani, V., Giusberti, L., Agnini, C., Backman, J., Fornaciari, E., & Rio, D. (2007). The Paleocene–Eocene Thermal Maximum as recorded by Tethyan planktonic foraminifera in the Forada section (northern Italy). Marine Micropaleontology, 64(3-4), 189-214.

Martín-Martín, M., Guerrera, F., Tosquella, J., & Tramontana, M. (2020). Paleocene-Lower Eocene carbonate platforms of westernmost Tethys. Sedimentary geology, 404, 105674.

McInerney, F. A., & Wing, S. L. (2011). The Paleocene-Eocene Thermal Maximum: A perturbation of carbon cycle, climate, and biosphere with implications for the future. Annual Review of Earth and Planetary Sciences, 39, 489-516.

Meredith, R. W., Janečka, J. E., Gatesy, J., Ryder, O. A., Fisher, C. A., Teeling, E. C., ... & Murphy, W. J. (2011). Impacts of the Cretaceous Terrestrial Revolution and KPg extinction on mammal diversification. science, 334(6055), 521-524.

Mort H, Jacquat O, Adatte T, Steinmann P, Föllmi K, Matera V, Berner Z, Stüben D (2007) The Cenomanian/Turonian anoxic event at the Bonarelli level in Italy and Spain: enhanced productivity and/ or better preservation? Cretac Res 28(4):597–612

Mutterlose, J., Linnert, C., & Norris, R. (2007). Calcareous nannofossils from the Paleocene–Eocene Thermal Maximum of the equatorial Atlantic (ODP Site 1260B): evidence for tropical warming. Marine Micropaleontology, 65(1-2), 13-31.

Ogg, J. G., Chen, Z. Q., Orchard, M. J., & Jiang, H. S. (2020). The triassic period. In *Geologic time scale 2020* (pp. 903-953). Elsevier.

Orue-Etxebarria, X., Pujalte, V., Bernaola, G., Apellaniz, E., Baceta, J. I., Payros, A., ... & Tosquella, J. (2001). Did the Late Paleocene thermal maximum affect the evolution of larger foraminifers? Evidence from calcareous plankton of the Campo Section (Pyrenees, Spain). Marine Micropaleontology, 41(1-2), 45-71.

Özgen-Erdem, N., İnan, N., Akyazı, M., & Tunoğlu, C. (2005). Benthonic foraminiferal assemblages and microfacies analysis of Paleocene–Eocene carbonate rocks in the Kastamonu region, Northern Turkey. Journal of Asian Earth Sciences, 25(3), 403-417.

Penman, D. E., & Zachos, J. C. (2018). New constraints on massive carbon release and recovery processes during the Paleocene-Eocene Thermal Maximum. Environmental Research Letters, 13(10), 105008.

Pentecost, A., 1991. Calcification processes in algae and cyanobacteria. In: Riding, R. (Ed.), Calcareous algae and stromatolites. Springer, Berlin, Heidelberg, pp. 3-20.

Perry, C. T., & Morgan, K. M. (2017). Bleaching drives collapse in reef carbonate budgets and reef growth potential on southern Maldives reefs. *Scientific reports*, *7*(1), 1-9.

Percival, L. M. E., Witt, M. L. I., Mather, T. A., Hermoso, M., Jenkyns, H. C., Hesselbo, S. P., ... & Ruhl, M. (2015). Globally enhanced mercury deposition during the end-Pliensbachian extinction and Toarcian OAE: A link to the Karoo–Ferrar Large Igneous Province. Earth and Planetary Science Letters, 428, 267-280.

Perito, B., Mastromei, G., 2011. Molecular basis of bacterial calcium carbonate precipitation. In: Müller, W. (Ed.) Molecular Biomineralization: Aquatic Organisms Forming Extraordinary Materials. Progress in Molecular and Subcellular Biology 52. Springer, Berlin, Heidelberg, pp. 113-139.

Petrizzo, M. R. (2007). The onset of the Paleocene–Eocene Thermal Maximum (PETM) at Sites 1209 and 1210 (Shatsky Rise, Pacific Ocean) as recorded by planktonic foraminifera. Marine Micropaleontology, 63(3-4), 187-200.

Pisarzowska, A., & Racki, G. (2020). Comparative carbon isotope chemostratigraphy of major Late Devonian biotic crises. In Stratigraphy & Timescales (Vol. 5, pp. 387-466). Academic Press.

Preto, N., Kustatscher, E., & Wignall, P. B. (2010). Triassic climates—state of the art and perspectives. Palaeogeography, Palaeoclimatology, Palaeoecology, 290(1-4), 1-10.

Pujalte, V., Orue-Etxebarria, X., Schmitz, B., Tosquella, J., Baceta, J. I., Payros, A., ... & Apellaniz, E. (2003). Basal Ilerdian (earliest Eocene) turnover of larger foraminifera: Age constraints based on calcareous plankton and 13C isotopic profiles from new southern

Pyrenean sections (Spain). Causes and consequences of globally warm climates in the early Paleogene: Geological Society of America Special Paper, (369), 205-221.

Pujalte, V., Schmitz, B., CABALLERO, J. B., Orue-Echebarría, X., BILBAO, G. B., Dinarès-Turell, J., ... & SANTAMARIA, F. C. (2009). Correlation of the Thanetian-Ilerdian turnover of larger foraminifera and the Paleocene-Eocene thermal maximum: confirming evidence from the Campo area (Pyrenees, Spain). Geologica Acta, 7(1-2), 161-175.

Read, J. F., & Repetski, J. E. (2012). Cambrian–lower Middle Ordovician passive carbonate margin, southern Appalachians.

Ritchie, H., & Roser, M. (2017). CO_2 and other greenhouse gas emissions. *Our world in data*.

Ridgwell, A., Zeebe, R.E., 2005. The role of the global carbonate cycle in the regulation and evolution of the Earth system. Earth and Planetary Science Letters 234(3-4), 299-315.

Röhl, U., Westerhold, T., Bralower, T. J., & Zachos, J. C. (2007). On the duration of the Paleocene-Eocene thermal maximum (PETM). Geochemistry, Geophysics, Geosystems , 8 (12).

Sarkar, S. (2018). The enigmatic Paleocene-Eocene coralline Distichoplax: Approaching the structural complexities, ecological affinities and extinction hypotheses. Marine Micropaleontology, 139, 72-83.

Sarkar, S., Cotton, L. J., Valdes, P. J., & Schmidt, D. N. (2022). Shallow water records of the PETM: Novel insights from NE India (eastern Tethys). Paleoceanography and Paleoclimatology , 37 (7), e2021PA004257.

Sanchez-Hernandez Y, Florentin JMM (2016) The infuence of regional factors in the expression of oceanic anoxic event 1a (OAE1a) in the semi-restricted Organyà Basin, south-Central Pyrenees, Spain. Palaeogeogr Palaeoclimatol Palaeoecol 441:582–598

Sachse VF, Littke R, Jabour H, Schümann T, Kluth O (2012) Late Cretaceous (late Turonian, Coniacian and Santonian) petroleum source rocks as part of an OAE, Tarfaya Basin, Morocco. Mar Pet Geol 29(1):35–49

Schulte, P., Scheibner, C., & Speijer, R. P. (2011). Fluvial discharge and sea-level changes controlling black shale deposition during the Paleocene–Eocene Thermal Maximum in the Dababiya Quarry section, Egypt. Chemical Geology , 285 (1-4), 167-183.

Scheibner, C., & Speijer, R. P. (2008). Late Paleocene–early Eocene Tethyan carbonate platform evolution—a response to long-and short-term paleoclimatic change. Earth-science reviews, 90(3-4), 71-102.

Scheibner, C., Speijer, R. P., & Marzouk, A. M. (2005). Turnover of larger foraminifera during the Paleocene-Eocene Thermal Maximum and paleoclimatic control on the evolution of platform ecosystems. Geology, 33(6), 493-496.

Scheibner, C., & Speijer, R. P. (2009). Recalibration of the Tethyan shallow-benthic zonation across the Paleocene-Eocene boundary: the Egyptian record. Geologica Acta, 195-214.

Schoon, P. L., Sluijs, A., Sinninghe Damsté, J. S., & Schouten, S. (2011). Stable carbon isotope patterns of marine biomarker lipids in the Arctic Ocean during Eocene Thermal Maximum 2. Paleoceanography, 26(3).

Serra-Kiel, J., Hottinger, L., Caus, E., Drobne, K., Ferrandez, C., Jauhri, A. K., ... & Zakrevskaya, E. (1998). Larger foraminiferal biostratigraphy of the Tethyan Paleocene and Eocene. Bulletin de la Société géologique de France, 169(2), 281-299.

Sheehan, P. M. (2001). The late Ordovician mass extinction. Annual Review of Earth and Planetary Sciences, 29(1), 331-364.

Sinanoğlu, D., Benedetti, A., & Özgen-Erdem, N. (2022). Danian (SBZ2) larger foraminifera from the Becirman Formation (southeastern Turkey) as evidence of rotaliids diversity in lower Paleocene shallow-water environments. Rivista Italiana di Paleontologia e Stratigrafia, 128(2). https://doi.org/10.54103/2039-4942/17987

Singh, B., Singh, S., & Bhan, U. (2022). Oceanic anoxic events in the Earth's geological history and signature of such event in the Paleocene-Eocene Himalayan foreland basin sediment records of NW Himalaya, India. *Arabian Journal of Geosciences*, *15*(3), 317.

Sluijs, A., Bowen, G. J., Brinkhuis, H., Lourens, L. J., & Thomas, E. (2007). The Paleocene–Eocene Thermal Maximum super greenhouse: biotic and geochemical signatures, age models and mechanisms of global change.

Sluijs, A., Bijl, P.K., Schouten, S., Rohl, U., Reichart, G.J., Brinkhuis, H., 2011. Southern ocean warming, sea level and hydrological change during the Paleocene-Eocene thermal maximum. Clim. Past 7, 47–61. https://doi.org/10.5194/cp-7-47-2011.

Sluijs, A., van Roij, L., Harrington, G. J., Schouten, S., Sessa, J. A., LeVay, L. J., ... & Slomp, C. P. (2013). Extreme warming, photic zone euxinia and sea level rise during the Paleocene/Eocene Thermal Maximum on the Gulf of Mexico Coastal Plain; connecting marginal marine biotic signals, nutrient cycling and ocean deoxygenation. Climate of the Past Discussions, 9(6).

Smit, J. (1999). The global stratigraphy of the Cretaceous-Tertiary boundary impact ejecta. *Annual Review of Earth and Planetary Sciences*, *27*(1), 75-113.

Speijer, R., Scheibner, C., Stassen, P., & Morsi, A. M. M. (2012). Response of marine ecosystems to deep-time global warming: A synthesis of biotic patterns across the Paleocene-Eocene thermal maximum (PETM). Austrian Journal of Earth Sciences, 105(1), 6-16.

Sun, Y., Joachimski, M. M., Wignall, P. B., Yan, C., Chen, Y., Jiang, H., ... & Lai, X. (2012). Lethally hot temperatures during the Early Triassic greenhouse. Science, 338(6105), 366-370.

Sun, Y. (2024). Dynamics of nutrient cycles in the Permian–Triassic oceans. *Earth-Science Reviews*, 104914.

Taylor, P. D. (Ed.). (2004). *Extinctions in the History of Life*. Cambridge University Press.

Trench, R. (1993). Microalgal-invertebrate Ssmbioses-a review. Endocyt. Cell. Res., 9, 135-175.

Them, T. R., Gill, B. C., Selby, D., Gröcke, D. R., Friedman, R. M., & Owens, J. D. (2017). Evidence for rapid weathering response to climatic warming during the Toarcian Oceanic Anoxic Event. Scientific reports, 7(1), 5003.

Thomas, D. J., Zachos, J. C., Bralower, T. J., Thomas, E., & Bohaty, S. (2002). Warming the fuel for the fire: Evidence for the thermal dissociation of methane hydrate during the Paleocene-Eocene thermal maximum. Geology, 30(12), 1067-1070.

Tremblin, M., Khozyem, H., Adatte, T., Spangenberg, J. E., Fillon, C., Grauls, A., Hunger, T., Nowak, A., Läuchli, C., Lasseur, E., Roig , J. Y., Serrano, O., Calassou, S., Guillocheau, F., & Castelltort, S. (2022). Mercury enrichments of the Pyrenean foreland basins sediments support enhanced volcanism during the Paleocene-Eocene thermal maximum (PETM). Global and Planetary Change, 212, 103794.

Thompson, J. B., & Newton, C. R. (1988). Late Devonian mass extinction: episodic climatic cooling or warming?

Umbarger, K. F., & Snedden, J. W. (2016). Delineation of post-KPg carbonate slope deposits as a sedimentary record of the Paleogene linkage of De Soto Canyon and Suwannee Strait, northern Gulf of Mexico. *Interpretation*, *4*(1), SC51-SC61.

Walsh, S. L. (2004). Solutions in chronostratigraphy: the Paleocene/Eocene boundary debate, and Aubry vs. Hedberg on chronostratigraphic principles. Earth-Science Reviews, 64(1-2), 119-155.

Westerhold, T., Marwan, N., Drury, A. J., Liebrand, D., Agnini, C., Anagnostou, E., Barnet, J. S. K., Bohaty, S. M., De Vleeschouwer, D., Florindo, F., Frederichs, T., Hodell, D. A., Holbourn, A. E., Kroon, D., Lauretano, V., Littler, K., Lourens, L. J., Lyle, M., Pälike, H., Röhl, U., Tian, J., Wilkens, R. H., Wilson, P. A., & Zachos, J. C. (2020). An astronomically dated record of Earth's climate and its predictability over the last 66 million years. Science, 369(6509), 1383-1387.

Winguth, A. M., Shields, C. A., & Winguth, C. (2015). Transition into a hothouse world at the Permian–Triassic boundary—a model study. *Palaeogeography, Palaeoclimatology, Palaeoecology*, *440*, 316-327.

Wood, R.A., Grotzinger, J.P., Dickson, J.A.D., 2002. Proterozoic modular biomineralized metazoan from the Nama Group, Namibia. Science 296(5577), 2383-2386.

Zachos, J. C., Röhl, U., Schellenberg, S. A., Sluijs, A., Hodell, D. A., Kelly, D. C., ... & Kroon, D. (2005). Rapid acidification of the ocean during the Paleocene-Eocene thermal maximum. science, 308(5728), 1611-1615.

Zachos, J. C., Dickens, G. R., & Zeebe, R. E. (2008). An early Cenozoic perspective on greenhouse warming and carbon-cycle dynamics. nature, 451(7176), 279-283.

Zeebe, R. E., & Caldeira, K. (2008). Close mass balance of long-term carbon fluxes from ice-core CO_2 and ocean chemistry records. *Nature Geoscience*, *1*(5), 312-315.

Zamagni, J., Mutti, M., & Košir, A. (2008). Evolution of shallow benthic communities during the Late Paleocene–earliest Eocene transition in the Northern Tethys (SW Slovenia). Facies, 54, 25-43.

Zamagni, J., Mutti, M., Ballato, P., Kosir, A., 2012. The Paleocene-Eocene thermal maximum (PETM) in shallow-marine successions of the Adriatic carbonate platform (SW Slovenia). Geol. Soc. Am. Bull. 124, 1071–1086. https://doi.org/10.1130/ B30553.1.

Zhang, Q., Willems, H., & Ding, L. (2013). Evolution of the Paleocene-Early Eocene larger benthic foraminifera in the Tethyan Himalaya of Tibet, China. International Journal of Earth Sciences, 102, 1427-1445.

Zhang, Q., Willems, H., Ding, L., & Xu, X. (2019). Response of larger benthic foraminifera to the Paleocene-Eocene thermal maximum and the position of the Paleocene/Eocene boundary in the Tethyan shallow benthic zones: Evidence from south Tibet. GSA Bulletin, 131(1-2), 84-98.

Chapter 2 – Pre-PETM conditions [SBZ1 to SBZ2]

This second chapter describes an example of pre- PETM conditions, corresponding to SBZ1 to SBZ2, the Maiella section (Pennapiedimonte, Central Italy) in Italy, in western Tethys.

The chapter displays the evolution of skeletal assemblages during the Early Paleocene after the K-Pg mass extension. It has been arranged as a paper and ***"Accepted"*** in the "Rivista Italiana di Paleontologia e Stratigrafia" for publication with the contribution of other authors.

"CORAL CARBONATE PRODUCTION DURING THE PALEOCENE: INSIGHTS FROM THE MAIELLA MASSIF (PENNAPIEDIMONTE, CENTRAL ITALY

Giovanni Coletti, Lucrezi Commissario, **Mubashir Ali**, Luca Mariani, Bruno Granier, Marco Brandano, Alessandro Mancini, Giovanni Rusciadelli, Cristiano Ricci, Juan Ignacio Baceta, Guillem Mateu-Vicens, Daniela Maria Basso

2.1. Abstract

The succession of the Maiella massif is analyzed, focusing on the colonial-coral bearing deposits occurring just below and immediately above the Cretaceous/Paleogene boundary. The Upper Cretaceous material is dominated by rudists and larger benthic foraminifera with a significant contribution from colonial corals. In the Lower Paleocene, the first two groups are absent and colonial corals dominate the skeletal assemblage. This supports the hypothesis of a good recovery of colonial corals carbonate production following the end Cretaceous extinction and their overall resilience. Similar to modern reefs, Lower Paleocene bioconstructions have a framework dominated by corals and red calcareous algae. However, unlike modern reefs, micrite makes up the vast majority of the internal sediment, suggesting a development into a low-energy environment. Compared to Upper Paleocene coral boundstones, those from the Lower Paleocene of Maiella display a higher abundance of corals, suggesting a reduction in coral carbonate production during the Late Paleocene. This decline is also reflected by a period of scarcity of coral-dominated facies throughout the Tethys, starting from the latest Paleocene and extending till the end of the Middle Eocene. This can be connected to global temperatures, which rise in the Thanetian and remain

relatively high till the end of the Middle Eocene, however, other factors most likely played a role. The quantitative analysis of the skeletal assemblage turns out to be a useful instrument for tracking the effect of environmental changes. Further data, especially from long and extensive successions of neritic carbonates such as those of Maiella, may help in disentangling the effects of the other environmental variables.

2.2. Introduction

Tropical coral reefs account for approximately one-sixth of Earth's coastlines, representing one of the most biologically diverse shallow-marine ecosystems in the ocean and providing invaluable ecosystem services for millions of people (Birkeland 1997; Paulay 1997; Moberg & Folke 1999; Knowlton et al. 2010). Most of these biogenic structures are directly threatened by human activities and by bleaching events driven by rising temperatures (Bryant et al. 1998; Wilkinson 2004; Bellwood et al. 2006; Descombes et al. 2015; Cheung et al. 2021). Scleractinian corals, and the bioconstructions they develop, have existed since the Triassic and managed to survive even during rapid and catastrophic events such as the Cretaceous/Paleogene extinction (Flügel & Flügel-Kahler 1992; Moussavian & Vecsei 1995; Wood 1995; Vecsei & Moussavian 1997; Kiessling et al. 1999; Kiessling & Baron-Szabo 2004; Pomar & Hallock 2008; Pandolfi & Kiessling 2014; Kiessling & Kocsis 2015). Coral bioconstructions are also documented for most of the Cenozoic, including during global warming events (e.g., Zamagni et al. 2012; Pomar et al. 2017; Bosellini et al. 2022; Martin-Martin et al. 2023; Ali et al. 2024). This suggests that coral bioconstructions are an overall resilient ecosystem, able to endure both catastrophic events and prolonged periods of unfavorable conditions over the geological time/space scale. Although they might be quite resilient, the features of these bioconstructions can change over time in response to environmental stressors. In order to gain insights over the potential long-term effects of global warming on these structures, several papers have analyzed the evolution and distribution of corals, bioconstructions, and coral-bioconstructions through time (e.g., Wood 1995; Kiessling et al. 1999, 2003; Bosellini & Perrin 2008; Johnson 2008; Morsilli et al. 2012; Stolarski et al. 2016; Pomar et al. 2017; Cornacchia et al. 2021; Benedetti et al. 2024; Cipriani et al. 2024). This research effort highlighted major trends, but also uncertainties and gaps of knowledge. It has been suggested that coral bioconstructions might have significantly changed their ecological niche during the Cenozoic (Pomar & Hallock 2007,

2008; Pomar et al. 2012, 2017). Some authors noted the complex relationship between the distribution of corals and temperature (Bosellini & Perrin 2008; Coletti et al. 2022). Others discussed the connection between building capacity and biodiversity, highlighting how the latter sometimes is positively coupled with the former (Bosellini et al. 2021) and sometimes is not (Johnson et al. 2008). However, the lack of quantitative data on fossil carbonate deposits, particularly on their skeletal assemblages, severely hinders our ability to compare fossil coral bioconstructions and rigorously test the various hypotheses regarding their evolution trough time (Kiessling et al. 1999; Coletti et al. 2022; Bialik et al. 2023).

Bioclastic sediments and bioconstructions, ranging in age from the Jurassic to the Miocene (Crescenti et al. 1969; Vecsei et al. 1998, Rusciadelli et al. 2003), are exposed along the flanks of the Maiella massif in Central Italy, offering a unique window into the evolution of these carbonate-producing environments. Within the 'Vallone delle Tre Grotte' (VTG, from here onward), in the basal breccia of the Santo Spirito Formation, there are boulders and blocks of coral-boundstone, lying right above Upper Cretaceous, rudist-rich, bioclastic carbonates (Vecsei 1991; Moussavian & Vecsei 1995; Vecsei & Moussavian 1997; Vecsei et al. 1998) (Fig. 2.1). These blocks are remnants of coral bioconstructions that developed shortly after one of the main biotic crises of the Cenozoic (the K/Pg extinction) and before the latest Paleocene – Early Eocene warm interval, a period of global decline in the abundance of coral-dominated bioconstructions (Kiessling et al. 1999; Scheibner & Speijer 2008; Zamagni et al. 2012; Pandolfi & Kiessling 2014; Kiessling & Kocsis, 2015; Aguilera et al. 2020; Pomar et al. 2017; Coletti et al. 2022). The main goal of this paper is thus to provide an updated analysis of the skeletal assemblages of these coral-dominated bioconstructions initially described by Vecsei (1991), Moussavian & Vecsei (1995), and Vecsei & Moussavian (1997). More accurate descriptions of the outcrops and their position within the VTG are provided, including details on the lithostratigraphic units immediately below and above the investigated interval. The microfacies are analyzed in detail, providing a quantitative framework to describe and compare the investigated Paleocene bioconstructions, first with the underlying Upper Cretaceous bioconstructions, and then with other Paleocene bioconstructions of the Tethys. This comparison, based on the quantitative features of the skeletal assemblage, is subsequently used to better understand the effects of Late Paleocene warming on coral-dominated bioconstructions.

2.3. Geological setting

The Maiella massif, situated in Central Apennines (Fig. 2.1A-B), represents the northernmost part of the Apulian Carbonate Platform, a thick carbonate sequence developed from the Jurassic to the Miocene in the interior of Adria (Eberli et al. 1993; Bernoulli et al. 1996; Vecsei & Moussavian 1997; Vecsei et al. 1998; Nicolai & Gambini 2007; Rusciadelli & Di Simone 2007; Sani et al. 2016; Vitale & Ciarcia 2022) (Fig. 2.1C-E). The latter is a northern promontory of the African Plate, that collided with the Eurasian Plate following the closure of the Alpine Tethys during the Alpine orogenesis (Muttoni et al. 2013) (Fig. 2.1D). The successions exposed in the Maiella massif span from the Upper Jurassic to the Miocene and can be divided into various units (Crescenti et al. 1969; Accarie 1988; Moussavian & Vecsei 1995; Vecsei & Moussavian 1997; Vecsei et al. 1998) (Fig. 2.1E, F). The oldest exposed units are the Upper Jurassic to upper Albian carbonates deposited in both shallow (Morrone di Pacentro Formation) and deep-water settings (Fig. 2.1) (Vecsei et al. 1998; Rusciardelli & Di Simone 2007; Eberli et al. 2019). These limestones are capped by a karst surface with bauxitic soils testifying a prolonged period of subaerial exposure (late Albian - early Cenomanian) (Fig. 2.1). The period of platform exposure was followed by the formation of a deep and steep escarpment (paleoescarpment), abruptly separating the platform in the south from the basin in the north (Crescenti et al. 1969; Accarie, 1988; Eberli et al. 1993; Vecsei 1991; Morsilli et al. 2002; Rusciadelli 2005; Rusciadelli & Di Simone 2007 among others).Between the middle and the late Cenomanian, the platform was once again submerged, leading to the recovery of shallow-water carbonate sedimentation (Vecsei et al. 1998; Rusciardelli & Di Simone, 2007; Eberli et al. 2019). This resulted in the deposition of subtidal to supratidal limestones, rudist bioconstructions and bioclastic sand bodies of the Cima delle Murelle Formation (Rusciadelli & Di Simone 2007) (Fig. 2.1). These deposits concentrate in the central portion of the Maiella, along the platform margin. The inner platform is instead characterized by the Fondo di Maiella Formation, whereas pelagic, scaglia-like, facies developed to the south, representing the temporary drowning of the former platform deposits (Morsilli et al. 2002; Rusciardelli & Di Simone 2007). North of the platform escarpment the succession is mainly represented by base-of-slope deposits dominated by megabreccias and turbidites (Valle dell'Inferno and Tre Grotte formations; Fig. 2.1). All these formations collectively represent Supersequence 1 (SS1; sensu Vecsei 1991; Vecsei et al. 1998; Eberli et al. 2019) (Fig. 2.1).

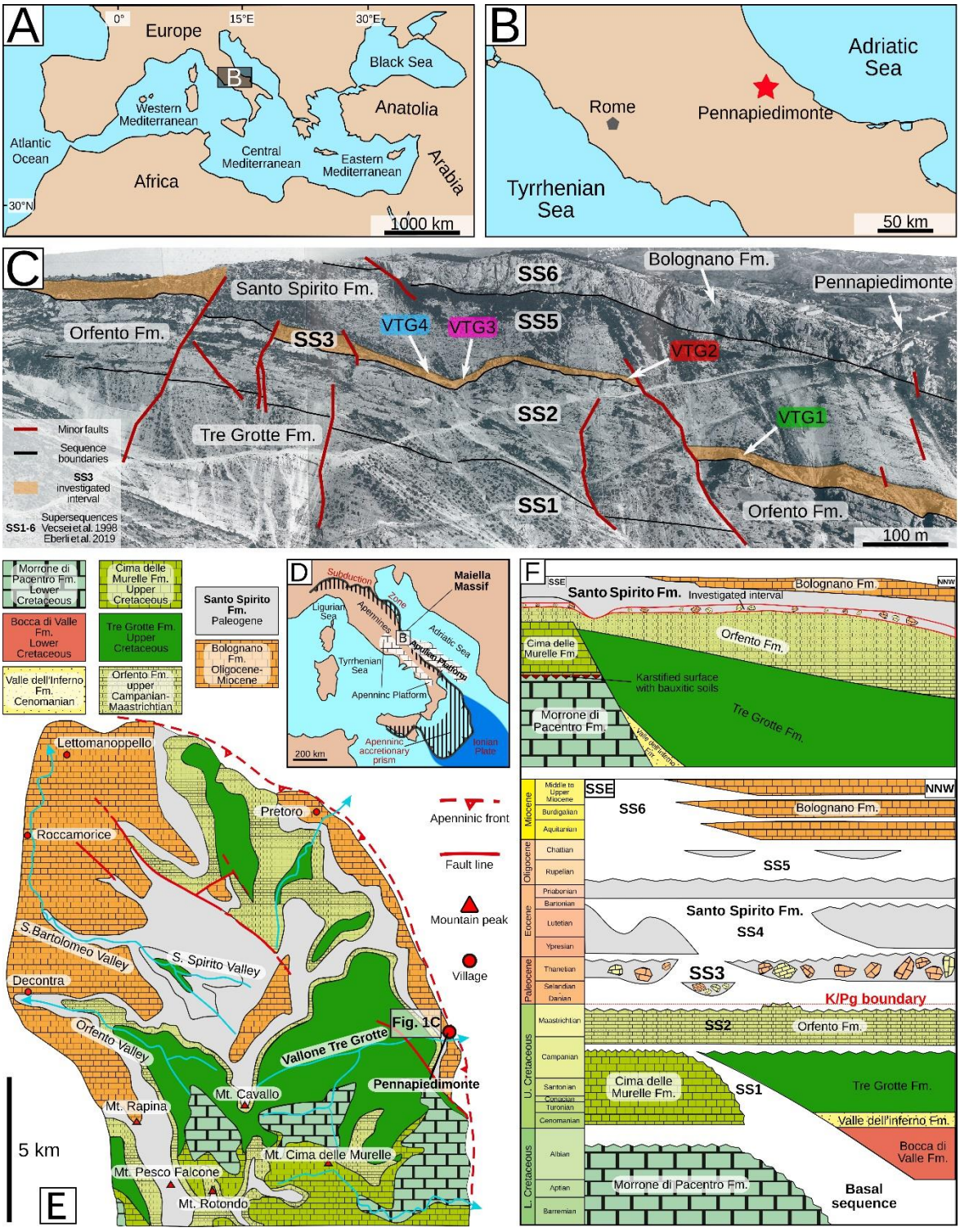

Figure 2.1: Geographic position and geological setting of the study area. A) The Mediterranean Sea. B) Central Italy. C) Sequence stratigraphic framework of the VTG, indicating the main sequences, highlighting the analyzed sequence (SS3) and the investigated outcrops, superimposed to the panoramic of the investigated area; modified from Vecsei (1991). D) Schematic geological map of Italy modified from Pomar et al. (2004) and Brandano et al. (2016b); the area covered by panel B is indicated by a gray box. E) Simplified geological map, with the main formations of the study area within the Maiella massif, modified from Vecsei & Sanders (1999) and Brandano et al. (2016b); the study area represented in Fig. 1C is indicated

by a gray box. F) Schematic stratigraphic relationships, architecture and chronostratigraphic diagram of the Maiella platform margin modified from Eberli et al. (2019); supersequences (SS1-6) are described into the Geological Setting paragraph, for further detail the reader is referred to Vecsei et al. (1998) and Eberli et al. (2019).

The Cima delle Murelle, Fondo di Maiella, Valle dell'Inferno, and Tre Grotte formations are overlain by the Orfento Formation, spanning from the late Campanian to the latest Maastricthian and constituting Supersequence 2 (SS2; sensu Vecsei 1991, Vecsei et al. 1998; Eberli et al. 2019) (Fig. 2.1). The Orfento Formation marks the filling of the basin with the consequent shift in the large-scale stratigraphic architecture of the carbonate platform in the Maiella area from aggradation to progradation (Vecsei et al. 1998; Eberli et al. 2019). It consists of well-sorted bioclastic deposits, mass-transport deposits and limestone breccias. The coarse-grained bioclastic fraction is dominated by rudist debris associated with larger benthic foraminifera (LBF from here onward), sparse colonial corals, and calcareous red algae (Vecsei et al. 1998; Eberli et al. 2019). Small in-situ rudist bioconstructions and breccias with reworked rudists are also reported (Rusciadelli & Di Simone 2007).

The Orfento Formation is separated by the overlying Santo Spirito Formation by an erosive surface (Fig. 2.1). The Santo Spirito Formation itself is a complex unit of Paleogene age, consisting of various lithologies and including Supersequences 3, 4, 5 (SS3-5) (sensu Vecsei 1991, Vecsei et al. 1998; Eberli et al. 2019) (Fig. 2.1). The basal portion (corresponding to SS3) is the main focus of this research (Fig. 2.1C, E) and consists of turbidites, debris-flows, and other mass transport deposits of material that originated in the shallow-water areas of the platform, slumped downslope, and resedimented interbedded with pelagic limestones (Fig. 2.1) (Vecsei et al. 1998; Eberli et al. 2019). At the base large limestone blocks with a dominant boundstone texture have been reported. These large elements probably detached from the top of the platform during the Paleocene and have been originally attributed to two-time intervals: the Danian – early Selandian and the Selandian - early Thanetian (based on the data provided by Moussavian & Vecsei 1995 and recalibrated to the current biostratigraphic schemes of Schmitz et al. 2011; Wade et al. 2011; Serra-Kiel et al. 2020; Papazzoni et al. 2023). The former group includes large-sized blocks (up to 400 m in length and 15 m in thickness), while the latter mainly includes boulder-sized elements (Moussavian & Vecsei 1995; Vecsei & Moussavian 1997). The blocks originally attributed to the Danian to early Selandian interval consist of boundstones with a framework built by a diverse assemblage of colonial corals and bound by calcareous red algae (Moussavian & Vecsei 1995; Vecsei & Moussavian 1997). Encrusting foraminifera and bryozoans also occur

(Moussavian & Vecsei 1995; Vecsei & Moussavian 1997). The internal sediment of the bioconstructions is reported to be dominated by fragments of the bioconstruction itself, as well as by small benthic foraminifera (SBF) and calcareous green algae (Moussavian & Vecsei 1995; Vecsei & Moussavian 1997). No hyaline LBF indicative of late Thanetian age were reported (Shallow Benthic Zone 4 of Serra-Kiel et al. 1998, SBZ4) (Moussavian & Vecsei 1995; Vecsei & Moussavian 1997). The blocks originally attributed to the Selandian to early Thanetian interval include: boundstones dominated by encrusting corals and encrusting red calcareous algae; grainstones dominated by SBF (Moussavian & Vecsei 1995; Vecsei & Moussavian 1997). In both the internal sediment of the boundstones and in the associated grainstones, calcareous green algae, SBF and LBF are common (Moussavian & Vecsei 1995; Vecsei & Moussavian 1997). The latter include *Miscellanea* and *Ranikothalia* and an overall assemblage suggestive of a late Selandian to earliest Ypresian age (SBZ3 to SBZ5; Papazzoni et al. 2023) (Moussavian & Vecsei 1995; Vecsei & Moussavian 1997).

The lower (SS3) and middle (SS4) units of the Santo Spirito Formation (Fig. 2.1) are separated by a discontinuity surface displaying no clear evidence of subaerial exposure (Vecsei et al. 1998). The middle unit (Ypresian to lower Bartonian) consists of slope deposits with shallow-water material transported downslope, interbedded with pelagic limestones (Vecsei et al. 1998). The beds containing shallow-water allochems are often graded and mostly consist of LBF (nummulitids, orthophragmines, and alveolinids) associated with subordinated red calcareous algae and echinoderms (Vecsei et al. 1998). The upper boundary of this unit is represented by an erosive surface, possibly related to the exposure of the platform as suggested by the presence of *Microcodium* and microkarst in the downslope redeposited clasts (Vecsei et al. 1998).

The upper part of the Santo Spirito Formation (SS5) spans from the Bartonian to the late Rupelian (Fig. 2.1) (Vecsei & Moussavian 1997). This interval includes various types of mass transport deposits originating from shallow-water environments and redeposited in a slope setting (Vecsei et al. 1998). Among these, elements originating from the dismantling of coral bioconstructions of Rupelian age have also been reported (Vecsei et al. 1998). The upper boundary of the formation is represented by an erosive surface with evidence of subaerial exposure (Vecsei et al. 1998). Locally, small Rupelian coral bioconstructions have also been reported along this boundary (Vecsei et al. 1998).

The Santo Spirito Formation is overlain by the upper Chattian to lower Messinian Bolognano Formation (which represents SS6) (Fig. 2.1). The latter developed in a carbonate ramp environment, and consists of three shallow-water limestone units separated by deep-water marly limestones (Fig. 2.1) (Brandano et al. 2012, 2016a, b, 2020, 2022; Cornacchia et al. 2017).

2.4.Material and methods

The Maiella carbonate succession was investigated in the field along the northern flank of VTG, approximately 400 meters west of Pennapiedimonte (42.15°N, 14.18°E) (Fig. 2.2). The study area was chosen based on the maps, pictures, and interpretative schemes provided in Vecsei (1991), focusing in particular on the sections identified as "Avella SE", "Tre Grotte", "Avella E", "Avella W", and "Avella NW" (Fig. 2.1C). The limestone exposures located along these sections were initially observed using hand lenses to roughly assess their fossil content and to identify the basal breccia layer of the Santo Spirito Formation and the Paleocene blocks. Major structures and textures were also documented. Representative rock samples were collected right above the boundary between SS2 and SS3 and corresponding to the basal portion of the Santo Spirito Formation. Additional samples were collected also from the units above and below the investigated interval. Thin sections were prepared in the laboratory of the Department of Earth and Environmental Sciences of Milano-Bicocca University by G.C., M.A., and L.M. Rock samples were initially cut into hand-sized pieces and then consolidated through three embedding cycles aimed at reinforcing the rock and filling both macroporosity and microporosity, resulting in high-quality thin sections preserving most of the morphological elements of the microfossils. After being polished with very-fine grained silicon carbide, the samples were glued to standard thin section glasses using UV-sensitive glue. Excess sample was removed using a Brumat thin-section saw and afterward the sections were further reduced to the desired thickness through hand-polishing, initially with a very-fine grained silicon carbide powder and then with aluminum oxide (grain size of 1 μm). Due to the highly lithified nature of the rock, hindering any effort at separating benthic foraminifera, serial thin sections of samples rich in foraminifera were produced for biostratigraphic purposes (the capitalization of the names of chronostratigraphic subdivision of the Cenozoic follows Aubry et al. 2023). In total, 85 thin sections were prepared and examined through a Leica Leitz Laborlux S transmitted light

optical microscope to identify components and rock textures for the subsequent microfacies description. All thin sections are stored in the Department of Earth and Environmental Sciences of the University of Milano-Bicocca. In 31 selected thin sections (the serial thin sections produced for biostratigraphic purposes were not selected for this analysis in order to not overestimate certain groups) microfacies characteristics were quantified using point-counting (Flügel 2010). For this analysis a 200 μm grid was utilized and more than 800 points were identified in each section.

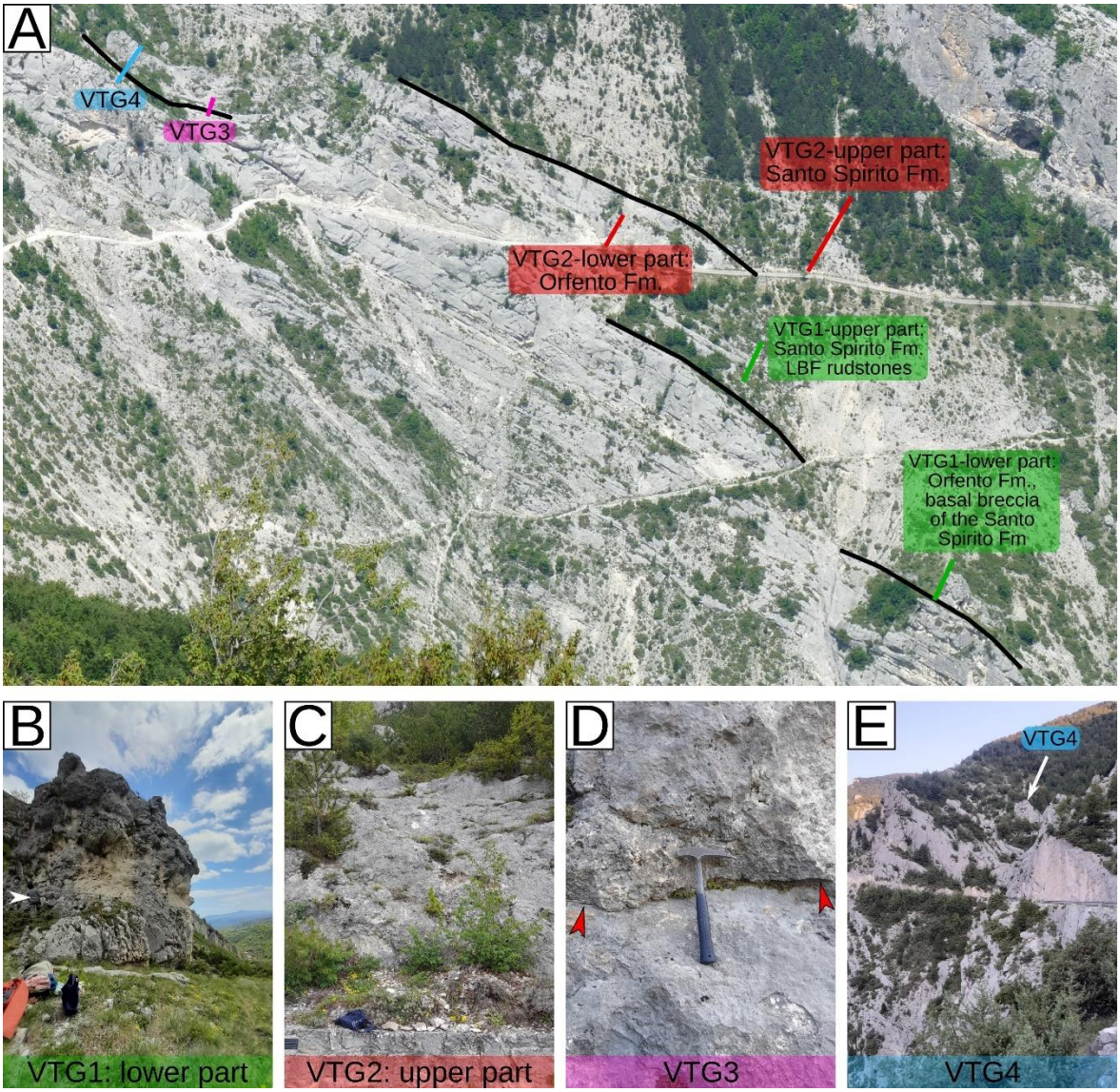

Fig. 2.2 - The investigated VTG sections near Pennapiedimonte. A) Panoramic picture of the investigated area taken from the other side of VTG. B) Basal breccia of the Santo Spirito Formation overlying the Orfento Formation at VTG1; white arrowhead indicates a person for scale. C) Basal breccia of the Santo Spirito Formation overlying the Orfento Formation at VTG2 as seen from the main path of the VTG. D) Boundary between the Orfento Formation (SS2) and Santo Spirito Formation (SS3) at VTG3, red arrowhead indicates the discontinuity surface. E) Panoramic view of the VTG4 outcrop.

2.5.Results

2.5.1. Description of the sections

Moving westward from the uppermost part of Pennapiedimonte village, various sections (VTG1-4), located at the boundary between the Orfento and Santo Spirito formations, have been analyzed (Fig. 2.2).

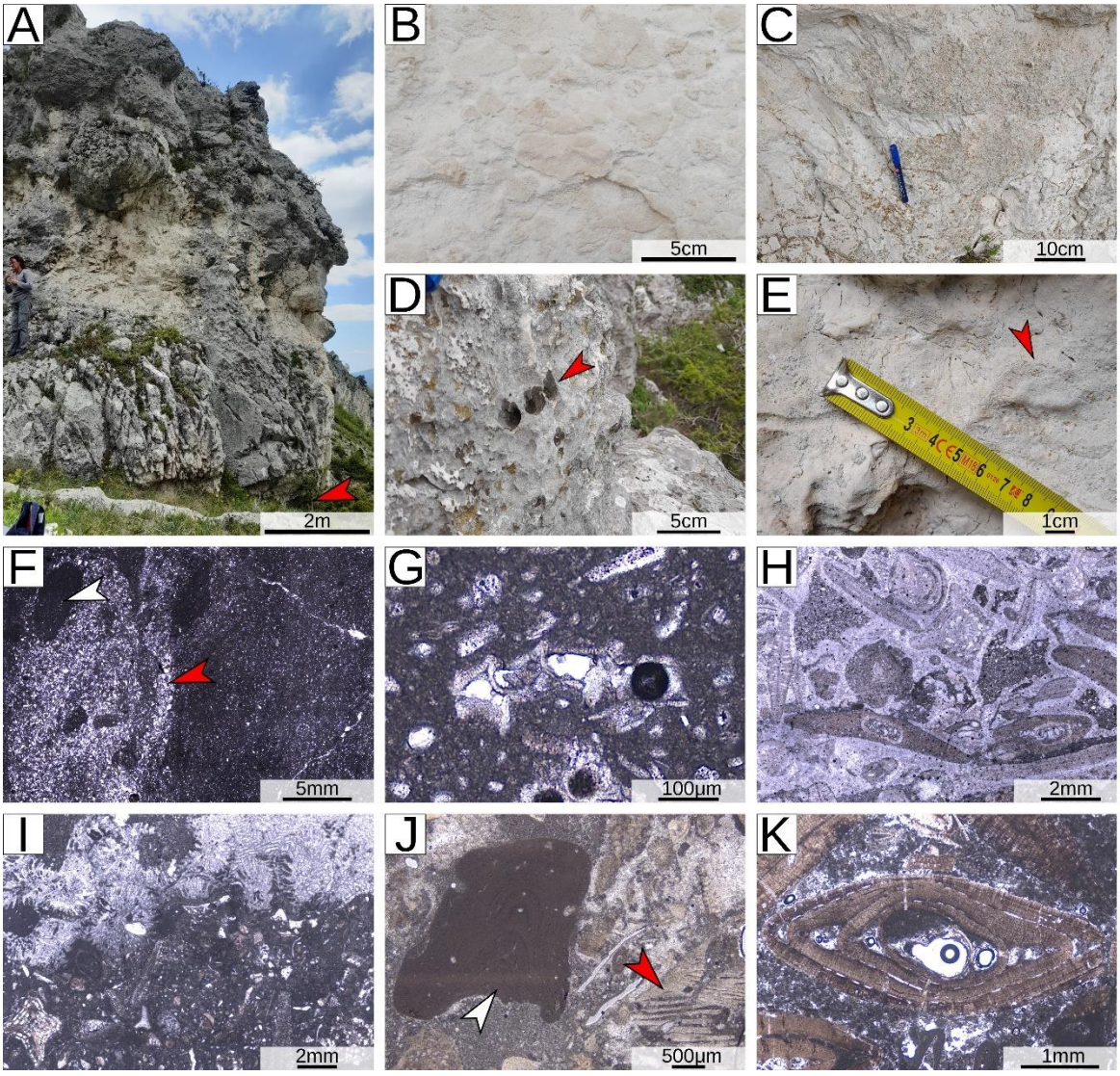

Fig. 2.3 - VTG1. A) Overview of the outcrop; red arrowhead indicates the boundary with the underlying Orfento Formation. B) Clast-supported breccia at the base of the Santo Spirito Formation. C) Cobble sized clast of LBF rudstone in the clast-supported breccia at VTG1. D) Cluster of rudist specimens (red arrowhead). E) Rudist specimen (red arrowhead). F) Mudstone to wackestone with rudist fragments that

constitute the uppermost part of the Orfento Formation, most of the fragments are silt-sized (as in the pictured example), locally larger fragments also occur; red arrowhead indicates a patch packed with silt-sized rudist fragments; white arrowhead= mudstone intraclast within the patch rich of rudist fragments denoting the pervasive mixing of different assemblages in the upper part of the Orfento Formation. G) Globotruncanid from the mudstone to wackestone of the uppermost Orfento Formation. H) Thin section of a LBF rudstone cobble from the clast supported breccia of the Santo Spirito Formation. I) LBF rudstone cobble rich in fragments of colonial corals. J) LBF rudstone with coralline algae (white arrowhead) and rudist fragments (red arrowhead). K) Thin section from the LBF rich rudstone located around 30 m above the basal breccia of the Santo Spirito Formation at VTG1 and displaying the detail of a pseudo-axial sections of *Nummulites*.

VTG1 (42.1517°N, 14.1895°E) is located below the main path and corresponds to section "Avella SE" as described by Vecsei (1991) (Figs. 2.2A, B; 2.3). The lower part of the section consists of a small crag situated near the edge of a cliff composed of Orfento Formation limestones (Fig. 2.3A) (Raffi et al. 2016: fig. 2.2).

The uppermost layer of the Orfento Formation is represented by mudstones to wackestones dominated by silt-sized rudist fragments associated with common planktic foraminifera, such as globotruncanids (Fig. 2.3F-G). Sand-sized rudist fragments are generally concentrated in irregular patches separated by micrite-rich areas (Fig. 2.3F). This upper portion of the Orfento Formation is separated from the Santo Spirito Formation, constituting the small crag, by an erosive surface (Fig. 2.3A-E) (Vecsei 1991). The basal interval of the Santo Spirito Formation comprises clast-supported breccia characterized by pebble- to cobble-sized elements embedded in a fine-grained matrix (Fig. 2.3B-E). The clasts of the breccia consist of rudstones dominated by LBF, mainly *Siderolites* and *Orbitoides,* associated with common coral colonies and rudists (Fig. 2.3D, E, H-J). Towards the top of the crag, these clasts become less abundant. Microfacies analysis of the clasts of the breccia consistently indicates a Late Cretaceous age (see the chapter: Biostratigraphy). Around 30 m upwards (upper part of the section in Fig. 2.2A), the succession comprises fine-grained limestones interbedded with two normally-graded rudstone layers rich in nummulitids, orthophragmines, and coralline algae, suggesting an Eocene age (Fig. 2.3K).

VTG2 (42.1531°N, 14.1892°E) is located directly above the main path (Fig. 2.2A, C) between the upper part of the "Tre Grotte" section and the "Avella E" section as described by Vecsei (1991). Similarly to VTG1, VTG2 is situated at the boundary between the Orfento Formation and the Santo Spirito Formation (Fig. 2.4A). The Orfento Formation is well exposed along the road cut of the main path (lower part of the section VTG2 in Fig. 2.2A), where large blocks (up to 1 m in diameter) of rudist-dominated floatstone to rudstone are

present (Fig. 2.4B, C). These coarse-grained blocks are embedded within a mudstone matrix rich in planktic foraminifera, such as globotruncanids (Fig. 2.4D). Granule- and fine-pebble-sized intraclasts of planktic foraminiferal mudstone can be observed at the boundary between the rudist-dominated floatstone to rudstone and the embedding mudstone (Fig. 2.4E, F). The uppermost part of the Orfento Formation mainly consists of mudstone to wackestone with a sparse bioclastic fraction, including Upper Cretaceous LBF and globotruncanids (Fig. 2.4G).

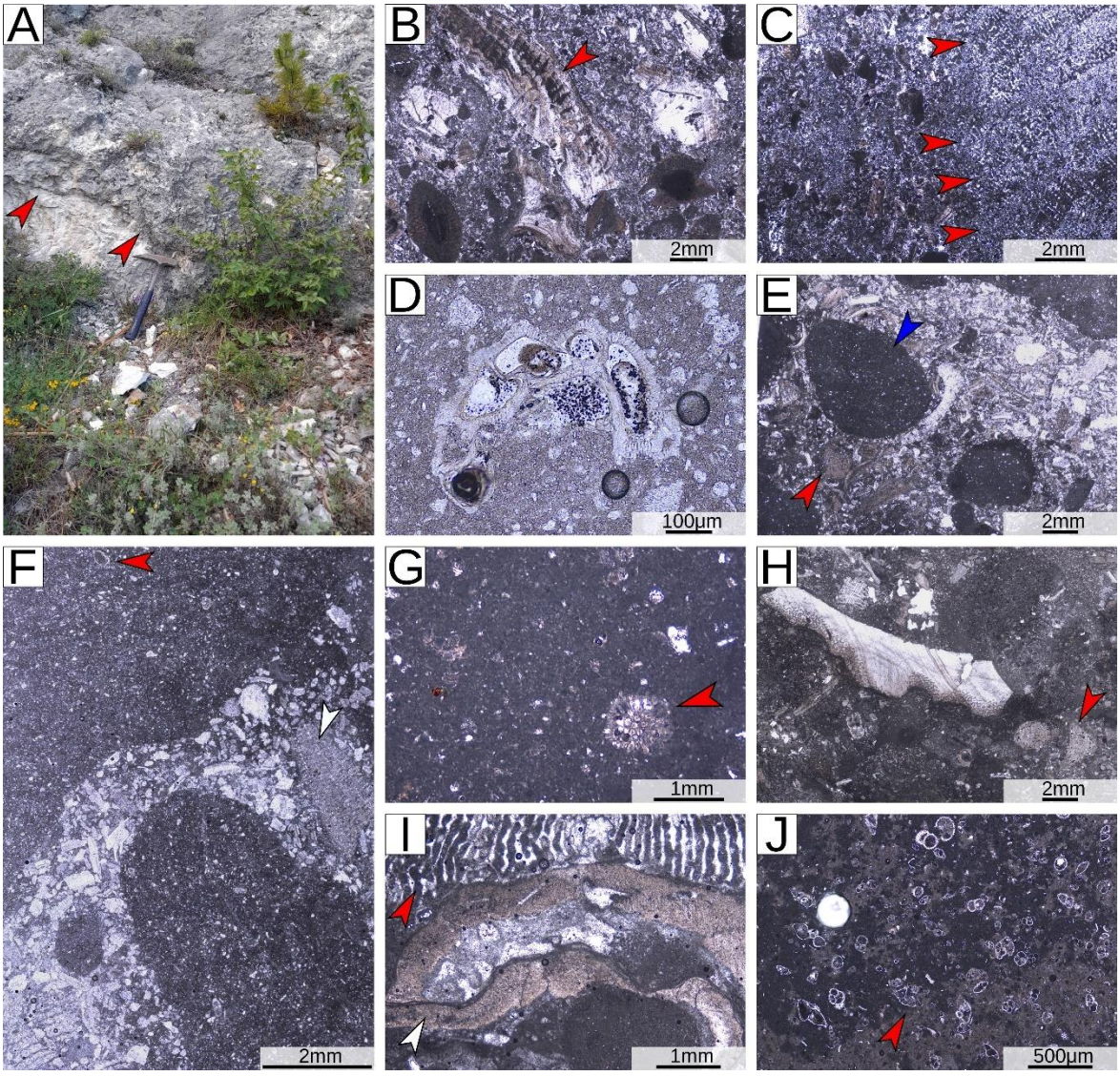

Fig. 2.4 - VTG2. A) Boundary with the underlying Orfento Formation (red arrowheads). B) Thin section from one of the boulder of the rudist-dominated rudstone to floatstone of the upper Orfento Formation, displaying a skeletal assemblage dominated by rudist fragments and LBF. C) Thin section of another boulder of rudist-dominated rudstone to floatstone of the upper Orfento Formation characterized by abundant fragments of colonial corals (red arrowheads) displaying evidence of partial dissolution. D) Globotruncanid within the mudstone embedding the rudist-dominated rudstone to floatstone. E) Upper Orfento formation displaying granule-sized intraclasts of mudstone (blue arrowhead) at the boundary between the rudist-

dominated rudstone to floatstone and the embedding mudstone with planktic foraminifera; red arrowhead indicates a Siderolites specimen within the coarse-grained bioclastic sediment dominated by rudist fragments. F) Detail of planktic foraminifera mudstone intraclasts at the boundary with the rudist-dominated rudstone to floatstone in the upper Orfento Formation at VTG2; red arrowhead indicates a globotruncanid within the mudstone intraclasts; white arrowhead indicates an Orbitoides within the rudist-dominated rudstone to floatstone. G) Mudstone to wackestone with scattered LBF in the uppermost Orfento Formation right below the boundary with the Santo Spirito Formation; red arrowhead indicates a Siderolites specimen. H) Rudist and LBF within the massive floatstone to rudstone at the base of the Santo Spirito Formation; red arrowhead indicates a Siderolites specimen. I) Bindstone clast sampled from the base of the massive floatstone to rudstone at the base of the Santo Spirito Formation, differently from the other analyzed clasts it lacks the typical Late Cretaceous elements; red arrowhead indicates a colonial coral; white arrowhead indicates a red calcareous alga. J) Upper part of VTG2 section, characterized by planktic foraminifera mudstone with possible morozovellids (red arrowhead) and acarinids.

The basal portion of the overlying Santo Spirito Formation consists of 10 m of massive floatstone to rudstone exhibiting pebble- to cobble-sized elements embedded within a wackestone matrix (upper part of VTG2 in Fig. 2.2A). However, the outcrop surface is considerably altered, making it impossible to accurately describe the large-scale texture (Fig. 2.2C). Some clasts include relatively complete rudist specimens whereas other clasts mostly consist of coral colonies. All but one of the pebble- and cobble-sized clasts are characterized by Upper Cretaceous LBF (Fig. 2.4H). The only exception is represented by a bindstone sample dominated by encrusting corals and red calcareous algae (Fig. 2.4I), which does not include any diagnostic elements of either Late Cretaceous or Eocene age. The massive floatstone to rudstone layer is overlain by a layer of mudstone with common planktic foraminifera, possibly acarinids or morozovellids (Fig. 2.4J).

VTG3 is located further westward above the main path (42.1543°N, 14.1868°E) (Fig. 2.2A, D). It roughly corresponds to the section “Avella W” as described by Vecsei and Moussavian (1997). Similar to VTG1 and VTG2, it is situated atop of an erosional surface that separates the underlying Orfento Formation from the overlying Santo Spirito Formation (Figs. 2.2D; 2.5A). Directly above this surface, cobble- to boulder-sized blocks of coral-boundstone can be observed (Fig. 2.5B-H). The corals are moderately well preserved, and it is possible to observe the framework consisting of coral colonies encrusted by secondary binders (Fig. 2.5B-H). Coral colonies display massive, encrusting and branching (mainly phaceloid colonies) growth forms (Fig. 2.5B-D). Secondary binders are mainly represented by calcareous red algae and encrusting foraminifera (Fig. 2.5E-H). Patches of poorly sorted bioclastic material (floatstone to wackestone) can be observed trapped between coral

colonies (Fig. 2.5C). The micropaleontological analysis (see the chapter Biostratigraphy) indicates a Paleocene age. Differently from the description of Vecsei & Moussavian (1997), these boundstone clasts are rather sparse and appear to be embedded within a fine-grained matrix that also includes reworked Upper Cretaceous LBF.

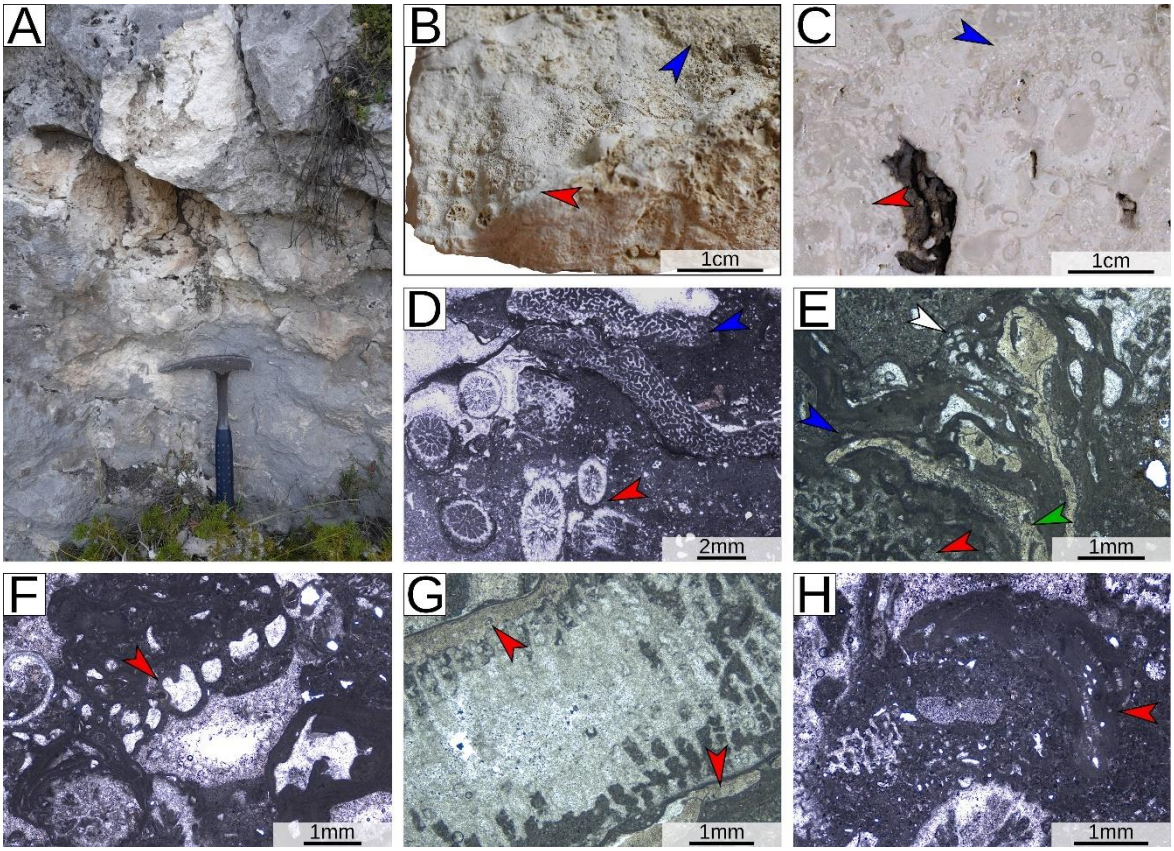

Fig. 2.5 - VTG3. A) Coral-boundstone boulder. B) Detail of a slab cut from the coral-boundstone boulder. C) Polished lower surface of the slab in panel B; red arrowhead indicates the corallites of a coral colony; blue arrowhead indicates a patch of poorly sorted sediment trapped between coral colonies. D) Thin section from the coral-boundstone displaying different coral morphologies; red arrowhead indicates braching, phaceolid, colonial corals; blue arrowhead indicates platy/encrusting colonial corals. E) Colonial coral (red arrowhead) encrusted by Peyssonneliales algae (green arrowhead), coralline algae of the order Corallinales (blue arrowhead), and agglutinated encrusting benthic foraminifera (white arrowhead). F) Agglutinated encrusting benthic foraminifera (red arrowhead). G) Colonial coral encrusted by Peyssonneliales red calcareous algae (red arrowheads). H) Molds of a colonial coral encrusted by a Sporolithales red calcareous alga (red arrowheads).

VTG4 is located further westward (42.1542°N, 14.1862°E), roughly corresponding to the section “Avella NW” as described by Vecsei and Moussavian (1997) (Fig. 2.2A, E). It consists of a roughly 10 m high cliff of coral-boundstone (Figs. 2.2A, E; 2.6A). The outcrop does not display a significant lateral continuity and appears to extent only a few tens of meters over the surface separating the Orfento and Santo Spirito formations. The boundstone

displays a wide variety of coral growth forms, including encrusting colonies and several types of domal and branching forms (Fig 2.6B-E). The micropaleontological analysis of samples from the coral boundstone of VTG4 (see the chapter Biostratigraphy) indicates a Paleocene age.

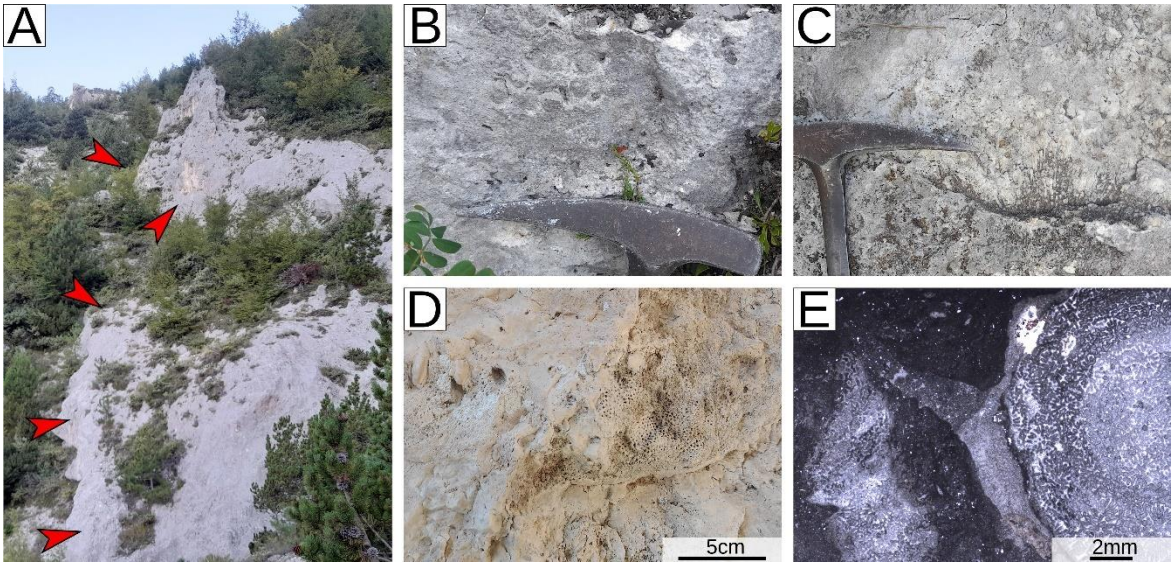

Fig. 2.6 - VTG4. A) Overview of the cliff of Paleocene coral-boundstones with red arrowheads indicating sampling sites. B) Domal colony with large corallites. C) Domal colony. D) Encrusting/domal massive plocoid colony with small corallites, possibly comparable to the genus *Actinacis* (sensu Bosellini & Russo 1995). E) Thin section with colonial corals (possibly comparable to genus *Actinacis*) surrounded by a micritic matrix.

2.5.2. Biostratigraphy

The mudstones and wackstones of the uppermost Orfento Formation at VTG1 and VTG2 are rich in globotruncanids, suggesting a Late Cretaceous age (Sartorio & Venturini 1988) (Figs. 2.3G; 2.4D). This is consistent with magnetostratigraphic and biostratigraphic data that place the uppermost part of the Orfento Formation at Pennapiedimonte in the upper Maastrichtian (Lampert et al. 1997; Eberli et al., 2019).

The floatstone to rudstone blocks embedded within the mudstone of the Orfento Formation at VTG2, include common specimens of *Orbitoides* sp., *Siderolites calcitrapoides* (Lamarck 1801) (Fig. 2.4F, G), supporting a Maastrichtian age (Sartorio & Venturini 1988; Chiocchini & Mancinelli 2001; Robles-Salcedo et al. 2018; Benedetti 2019; Özcan et al. 2021; Vicedo & Robles-Salcedo 2022). Similarly, the clasts of LBF rudstone observed at VTG1, based on the presence of *Orbitoides*, *Simplorbites*, *Hellenocyclina beotica* (Reichel 1949), *Siderolites calcitrapoides*, and *Omphalocyclus macroporus* (Lamarck 1816) (Fig. 2.7A-C), are also of

Maastrichtian age. Upper Cretaceous LBF assemblages were also observed in the clasts of the massive floatstone to rudstone layer constituting the base of the Santo Spirito Formation at VTG2 (Fig. 2.4H).

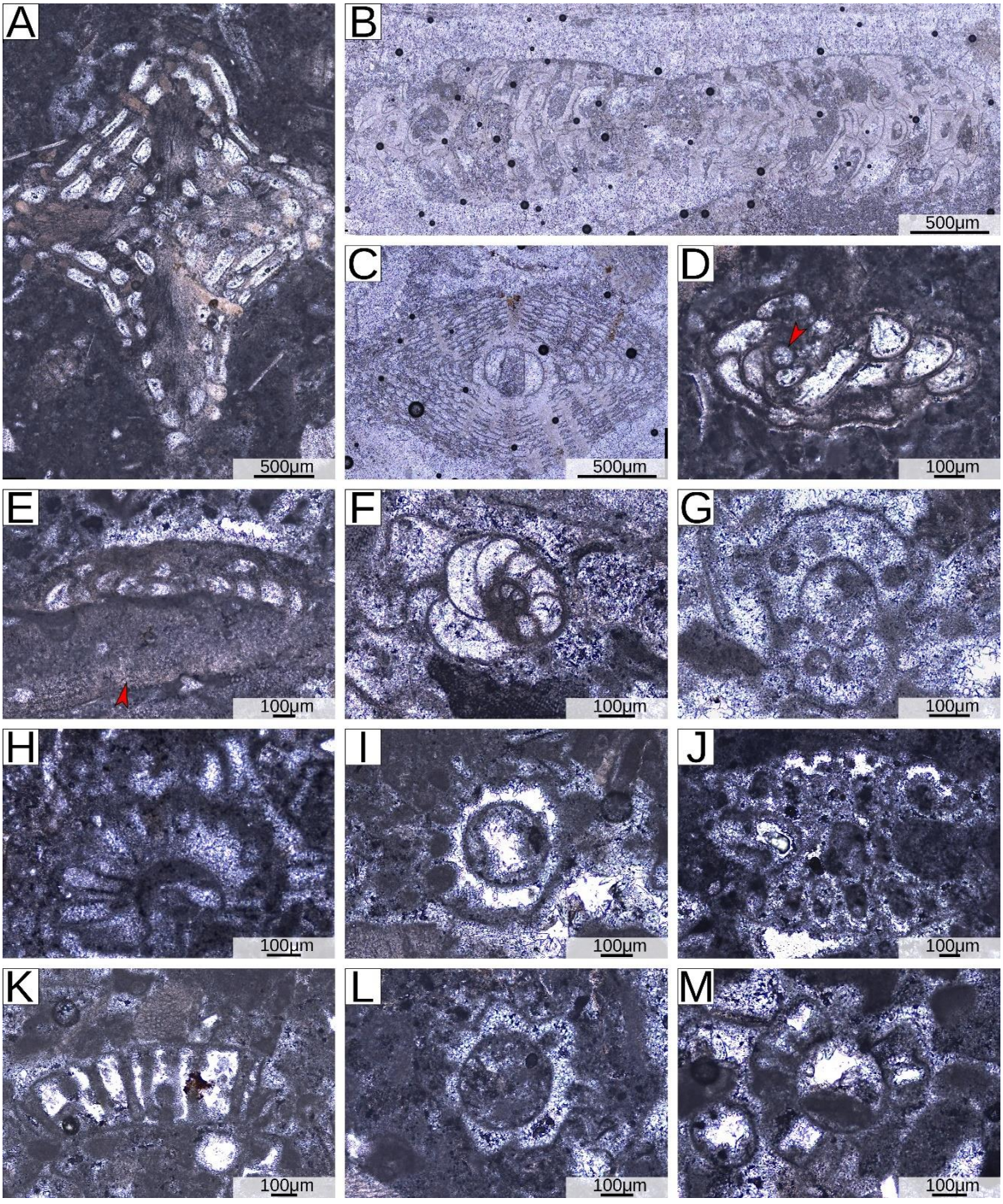

Fig. 2.7 - Age diagnostic microfossils of the investigated outcrops. A) Siderolites calcitrapoides from the LBF rudstone clast of the clast-supported Breccia at the base of the Santo Spirito Formation at VTG1. B) Omphalocyclus macroporus from the LBF rudstone clast of the clast-supported breccia at the base of the Santo Spirito Formation at VTG1. C) Orbitoides sp. from the LBF rudstone clast of the clast-supported breccia at the base of the Santo Spirito Formation at VTG1. D) VTG3, Planorbulina antiqua, red arrowhead indicates the proloculus. E) VTG4, axial section Planorbulina antiqua growing over a specimen of a red

calcareous alga of the order Peyssoneliales (red arrowhead). F) VTG3, poorly oriented section possible belonging to a specimen of Valvulineria patalaensis. G) Microsporangiella cf. buseri from the coral-boundstone of the Santo Spirito Formation at VTG4. H) Clypeina cf. socaensis from the coral-boundstone of the Santo Spirito Formation at VTG4. I) Clypeina sp. from the coral-boundstone of the Santo Spirito Formation at VTG4. J) Orioporella sp. from the coral-boundstone of the Santo Spirito Formation at VTG4. K) Axial cut of an element of a Cymopolia sp., from the coral boundstone of the Santo Spirito Formation at VTG4. L) Coral-boundstone of VTG3, poorly diagnostic sub-transverse cut of an element of a green calcareous alga, vaguely resembling some specimens of Acroporella chiapasis (Deloffre, Fourcade & Michaud 1985) reported by Barattolo (1998) from the Danian of Slovenia. M) Poorly diagnostic sub-transverse cuts of green algal specimens from the coral-boundstone of the Santo Spirito Formation at VTG4.

The coral-boundstones of VTG3 and VTG4 are also located in the basal layer of the Santo Spirito Formation, right above the discontinuity surface that separates the latter from the underlying upper Maastrichtian Orfento Formation. Around 30 meters above the investigated basal breccia of the Santo Spirito Formation, rudstones characterized by Eocene LBF have been recorded in the current analysis (Fig. 2.2A). Using calcareous nannofossils, previous research in the VTG have constrained the lower part of the Santo Spirito Formation above the basal breccia to the Lutetian (Raffi et al. 2016), whereas in the nearby Orfento Valley (Fig. 2.1E) the base of the formation has been constrained to the Selandian - early Thanetian (Cornacchia et al. 2018). The coral-boundstones of VTG3 and VTG4 must have thus formed between the Maastrichtian and the Middle Eocene. The benthic foraminiferal assemblage of the boundstones is quite scarce and consists of small taxa characterized by a simple structure. Some of the observed individuals could be tentatively attributed, given the small size of the test and the diameter of the proloculus, to *Planorbulina antiqua* (Mangin 1960) (Fig. 2.7D, E). This species has a proloculus ranging in diameter between 40 and 60 μm (differently from the larger *Planorbulina cretae* Marsson 1878) and is recorded from the Maastrichtian to SBZ2 (Serra-Kiel et al. 2020). Other specimens bear some resemblance to Lower Paleocene members of the genera *Valvulineria* and *Cocoarota* (Consorti & Köroğlu 2019; Consorti & Schlagintweit 2022; Serra-Kiel et al. 2020; Papazzoni et al. 2023) (Fig. 2.7F). Genera like *Miscellanea* and *Ranikothalia*, reported and depicted by Moussavian & Vecsei (1995), were not observed notwithstanding the large number of thin sections produced from samples rich in benthic foraminifera. Likewise, no other genera clearly diagnostic of a Selandian or Thanetian age were observed. The boundstones of VTG3 and VTG4 include a relatively wide variety of calcareous green algae (Fig. 2.7G-M). Although most of the specimens are poorly preserved, some individuals could be tentatively identified

as *Microsporangiella* cf. *buseri* (Barattolo 1998) (Fig. 7G). *Microsporangiella buseri* has been reported by Barattolo (1998) in Slovenian limestones attributed to SBZ1 and commonly occur in lower Danian lagoonal sediments from the Pyrenees. Other algae could be tentatively attributed to the genera *Orioporella*, *Clypeina*, and *Cymopolia* (Fig. 2.8H-K). Based on the similarities with the green algal assemblages investigated by Barattolo (1998) in Slovenia and northeastern Italy, the investigated coral bioconstructions should have developed during an interval spanning from SBZ1 to SBZ3, thus encompassing the Danian, the Selandian and the early Thanetian (Serra-Kiel et al. 1998, 2020; Papazzoni et al. 2023). Given the presence of *Microsporangiella* cf. *buseri*, and of *Planorbulina antiqua*, the boundstones of VTG3 and VTG4, most likely, developed during the early Danian (Barattolo 1998; Serra-Kiel et al., 2020). This hypothesis is in agreement with all the existing literature on this unit (Moussavian & Vecsei 1995; Vecsei & Moussavian 1997, Vecsei et al. 1998; Eberli et al. 2019). No evidence for a different placement has emerged notwithstanding the large number of produced thin sections that highlighted (within the margin of the reasonable doubt) the lack of Upper Cretaceous LBF (which are instead largely common in the units mere meters below the investigated boundstones), Eocene LBF (which are largely common in the layers above the investigated boundstones), and Thanetian LBF (which have been reported in the overlying shallow-water limestone blocks reported by Moussavian & Vecsei 1995). LBF were particularly affected by the end-Cretaceous mass extinction, few genera passed the K/Pg boundary and, with exception of *Laffitteina,* only taxa with small and simple tests are generally recorded in the lower Danian (Inan et al. 2005; Drobne et al. 2007; Serra-Kiel et al. 2020; Bendetti & Papazzoni 2022). Rotaliids significantly diversified only from the late Danian onward (SBZ2) (Benedetti & Papazzoni 2022; Sinanoğlu et al. 2022). As a result of that, lower Danian communities (SBZ1) are defined by poorly diversified assemblages occurring between the extinction of Upper Cretaceous fauna and the first appearance of the earliest Cenozoic taxa characterized by a complex structure (e.g., *Kayseriella decastroi* Sirel 1999, *Elazigina dienii* Hottinger 2014, miscellaneidae) (Sinanoğlu et al. 2022; Papazzoni et al. 2023). *Bangiana hanseni* (Drobne, Ogorelec & Riccamboni 2007) is one of the few species generally considered suggestive of SBZ1 (Drobne et al. 2007). However, since it is usually associated with very shallow and restricted environments (Drobne et al. 2007), its absence in the investigated assemblages might be related to environmental reasons. *Laffitteina*, one of the few survivors of the end-Cretaceous extinction, has been reported in the lower Danian of Turkey (Inan et al., 2005), but it is

absent in the lower Danian of northern Italy and Spain (Serra-Kiel et al. 2020; Papazzoni et al. 2023), indicating that it was not common throughout Tethys during the early Danian. Consequently, although not diagnostic in and of itself, the low-diversity foraminiferal assemblage of the boundstones of VTG3 and VTG4, which entirely lacks complex forms and includes *Planorbulina antiqua*, would be poorly compatible with a placement other than the early Danian (a placement which is also in agreement with the green calcareous algal assemblage).

2.5.3. Skeletal assemblage and microfacies

As already noted by previous authors based on the chaotic nature of the boundstone blocks, the presence of breccia layers, and the presence of channels and erosive surfaces (Moussavian & Vecsei 1995; Vecsei & Moussavian 1997; Vecsei et al. 1998; Raffi et al. 2016; Eberli et al. 2019), the investigated interval of the VTG succession, spanning the uppermost Orfento Formation and lowermost Santo Spirito Formation, displays clear evidence of reworking of shallow-water material. The latter was transported downslope and mixed with deep-water material (outer-ramp or slope deposits) (e.g., Figs 2.4E, F). However, the LBF rudstone clasts at VTG1 (Fig. 2.3B, C), the boulders of rudist-dominated floatstone to rudstone at VTG2 (Fig. 2.4B, C), and the coral-boundstones at VTG3 and VTG4 (Figs. 2.5; 2.6) represent resedimented elements with their own internal consistency and without clear evidence of mixing of heterogeneous assemblages. Therefore, they can provide information on the environment where they developed (Schlager 1991; Schlager et al. 1996; Coletti et al., 2015, 2016; Buček & Köhler 2017) and, thus, a detailed microfacies analysis was performed on them (Tab. 2.1).

The skeletal assemblage of the upper Maastrichtian pebbles and cobbles of LBF rudstone, reworked in the basal breccia of the Paleogene Santo Spirito Formation at VTG1, is dominated by hyaline LBF (53.5%; mainly *Orbitoides* and *Siderolites*), associated with common rudists (18%; mainly fragments but also whole specimens) (Fig. 2.8A-C), and colonial corals (13%; Tab. 2.1) (Fig. 2.8B, D). Echinoderms (Fig. 2.8C), encrusting benthic foraminifera (mainly hyaline taxa) (Fig. 2.8D), SBF (mainly hyaline), and red calcareous algae also occur. Bryozoans are rare. Skeletal grains are relatively well-sorted and the space between them is filled by significant amounts of micrite and sparite (Fig. 2.8E). Peloids also occur locally, but overall they are rare.

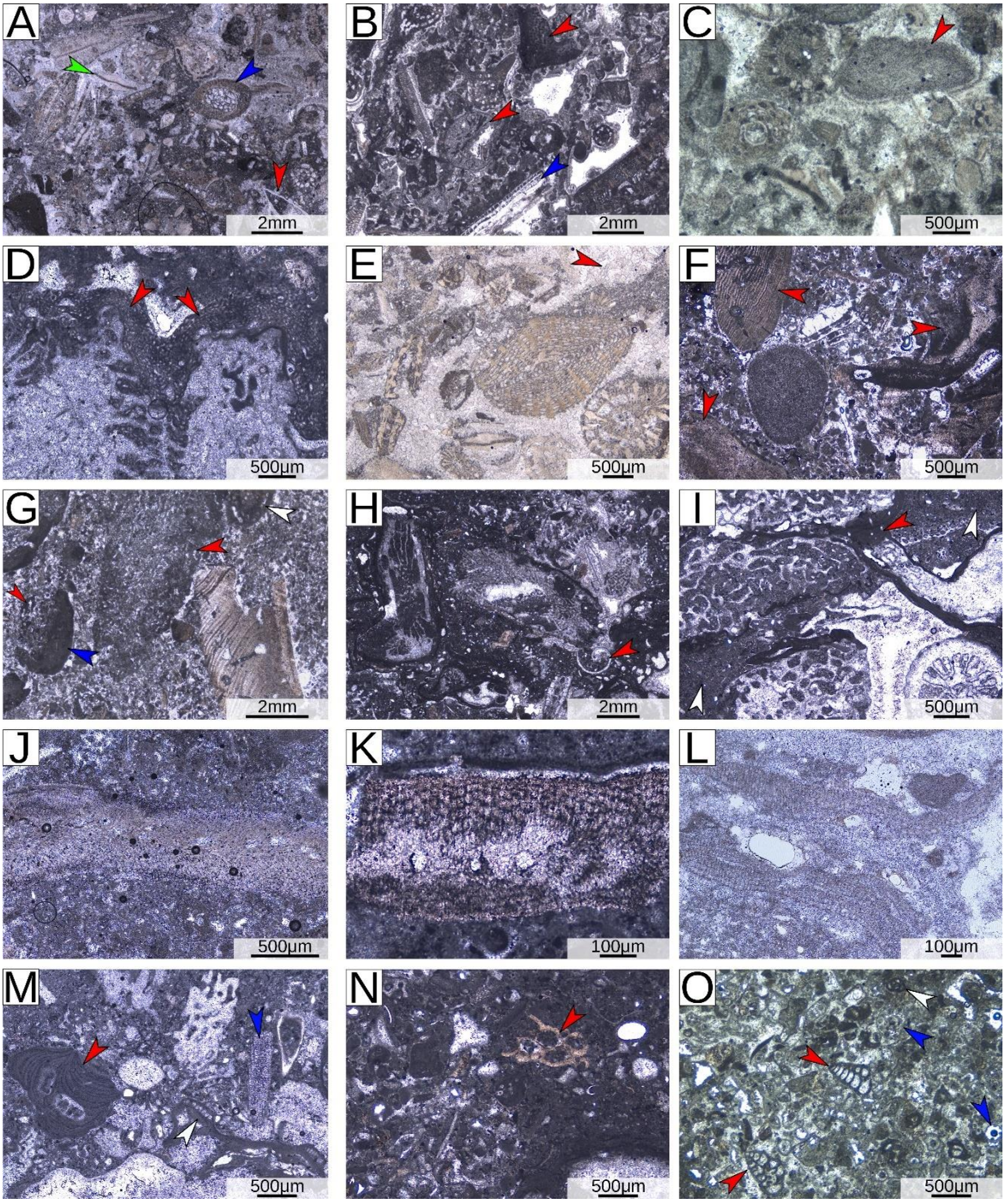

Fig. 2.8 - Microfacies of the analyzed succession. A) LBF rudstone from VTG1; red arrowhead indicates the porosity resulting from the dissolution of a small bivalve; blue arrowhead indicates a specimen of Simplorbites; green arrowhead indicates Hellenocyclina beotica. B) LBF rudstone from VTG1; red arrowheads indicate coral fragments; blue arrowhead indicates a rudist fragment. C) LBF rudstone from VTG1; red arrowhead indicates an echinoderm fragment. D) LBF rudstone from VTG1 displaying a colonial coral encrusted by an acervulinid hyaline encrusting benthic foraminifer= red arrowheads. E) LBF rudstone from VTG; red arrowhead indicates sparry calcitic cement. F) Rudist-dominated rudstone to floatstone from VTG2; red arrowheads indicate rudist fragments. G) Rudist-dominated rudstone to floatstone from VTG2;

red arrowheads indicate partially recrystallized fragments of colonial corals; blue arrowhead indicates an encrusted foraminifera growing over a fragment of a colonial coral; white arrowhead indicates a specimen of Siderolites. H) Coral-boundstone from VTG3; red arrowhead indicates a gastropod. I) Coral-boundstone from VTG3, red arrowhead indicates encrusting coralline algae biding corals together; white arrowheads indicate micrite filling the spaces within the frame. J) Red calcareous alga of the order Peyssonneliales from the coral-boundstone of VTG4. K) Red calcareous alga of the order Peyssonneliales from the coral-boundstone of VTG3. L) Karpathia from the coral-boundstone of VTG4. M) Coralline algae from the coral-boundstone of VTG3; red arrowhead indicates a specimen of coralline alga of the order Hapalidiales; white arrowhead indicates a specimen of coralline alga of the order Sporolithales; blue arrowhead indicates an echinoderm spine. N) Bioclastic sediment occurring within the colonies of the coral-boundstone of VTG3; red arrowhead indicates a bryozoan. O) Bioclastic sediment occurring within the colonies of the coral-boundstone of VTG4; red arrowheads indicate a small agglutinated benthic foraminifer; white arrowhead indicates a small miliolid; blue arrowheads indicate fragments of a green calcareous alga.

The upper Maastrichtian floatstone to rudstone blocks observed in the upper part of the Orfento Formation at VTG2 are dominated by rudists (46%; Tab. 2.1), both complete specimens and small angular fragments (Fig. 2.8F). The rudists are associated with abundant colonial corals (34.5%; Tab. 2.1) displaying extensive evidence of recrystallization (Fig. 2.8G). LBF are also common (9%; mainly *Orbitoides*, but *Siderolites* also occurs) (Fig. 2.8G). Encrusting benthic hyaline foraminifera are often observed on large-sized skeletal grains (Fig. 2.8G). Echinoderms and SBF (mainly hyaline taxa) are rare, whereas red calcareous algae are very rare. Peloids are also rare. The clasts are embedded into a relatively well-sorted fine-sand sized matrix (possibly resulting from the fragmentation of rudist shells and non-skeletal grains) which often displays evidence of recrystallization.

The skeletal assemblages of the lower Danian coral-boundstones of VTG3 and VTG4 are largely dominated by colonial corals (65-66%; Tab. 2.1). The corals are associated with common calcareous red algae (22-24%), which usually bind corals together (Figs. 2.5C-H; 2.8H, I). The calcareous red algal assemblage is dominated by Peyssonneliales and Sporolithales (Figs. 2.5G, E, H; 2.8J-M). Among the former most of the specimens display morphological features very different from those of some of their modern relatives such as *Polystrata* (Kato et al. 2006; Pestana et al. 2021) (Fig. 2.8J, K). Rare *Karpathia* (Fig. 2.8L) and very rare Hapalidiales (Fig. 2.8M) and Corallinales are also present. The frame of the boundstones also includes a significant amount of encrusting benthic foraminifera, mainly agglutinated taxa (e.g., Fig. 2.5F), but also miliolids and rotaliids. The sediment trapped within the small cavities of the frame is poorly sorted and mainly consists of micrite,

associated with small peloids and some skeletal grains (Fig. 2.8H, I, N, O). The latter include SBF (both hyaline and porcelaneous taxa), calcareous green algae, bryozoans, mollusks, echinoderms, and ostracods. The main difference between VTG4 and VTG3 boundstones is that small peloids are more common in VTG4 than in VTG3, and that in VTG4 the micritic matrix that fills most of the space of the bioconstructions can locally display irregular lamination, possibly suggestive of a microbial origin.

	Upper Cretaceous		Lower Danian	
Section	**VTG1**	**VTG2**	**VTG3**	**VTG4**
Lithology	**LBF rudstone**	**Rudist floatstone to rudstone**	**Coral boundstone**	**Coral boundstone**
N° of counted sections	4	7	8	12
Samples	Roal1-4	E1-7	C1a-h	C3-7, R0, R1, R1bis-quater, R2, R2bis
Characteristics of the rock [point counting; %]				
Matrix	42	35	40	40
Prevailing type of matrix	Sparite; micrite	Comminuted bioclastic fragments (sand-sized)	Micrite	Micrite
Skeletal assemblage	58	65	60	60
Builders	22	57	55	56
Colonial corals	7.5	22	40	39
Composition of the skeletal assemblage [point counting; %]				
Colonial corals	13.0	34.5	66.0	65.0
Red calcareous algae	3.0	1.0	22.0	24.0
Green calcareous algae	0	0	1.5	1.5
LBF	53.5	9.0	0.0	0.0
SBF	2.5	1.5	1.5	2.0
Encrusting benthic foraminifera	4.0	6.0	4.5	5.0
Rudists	18.0	46.0	0.0	0.0
Other mollusks	0.5	0.0	1.0	0.5
Echinoderms	5.0	2.0	0.5	1.5
Bryozoans	0.5	0.0	2.5	0.5
Others	0.0	0.0	0.5	0

Tab. 2.1 - Details of the skeletal assemblages of the LBF rudstone of VTG1, rudist-dominated floatstone to rudstone of VTG2, and coral-boundstones of VTG3 and VTG4; counted samples are indicated, their position is indicated in Fig. 2.9; all the thin sections are stored in the Department of Earth and Environmental Sciences of the University of Milano-Bicocca.

2.6.Discussion

The various investigated blocks of shallow-water limestones of Late Cretaceous and Danian age clearly represent reworked elements transported downslope into more fine-grained sediments. This is testified by the stark contrast between the assemblage of these limestone blocks, dominated by carbonate producers typical of the photic zone, and the surrounding fine-grained sediments rich in bioclasts of the pelagic domain (e.g., Fig. 2.4E, F). This

contrast is especially clear in the basal layer of the Santo Spirito Formation. At VTG1 the clasts of Upper Cretaceous shallow water limestone are concentrated right above a major unconformity surface, and they are embedded into fine-grained pelagic sediments that, slightly above the top of VTG1 section, have been dated to the Eocene based on calcareous nannoplankton (Raffi et al., 2016).

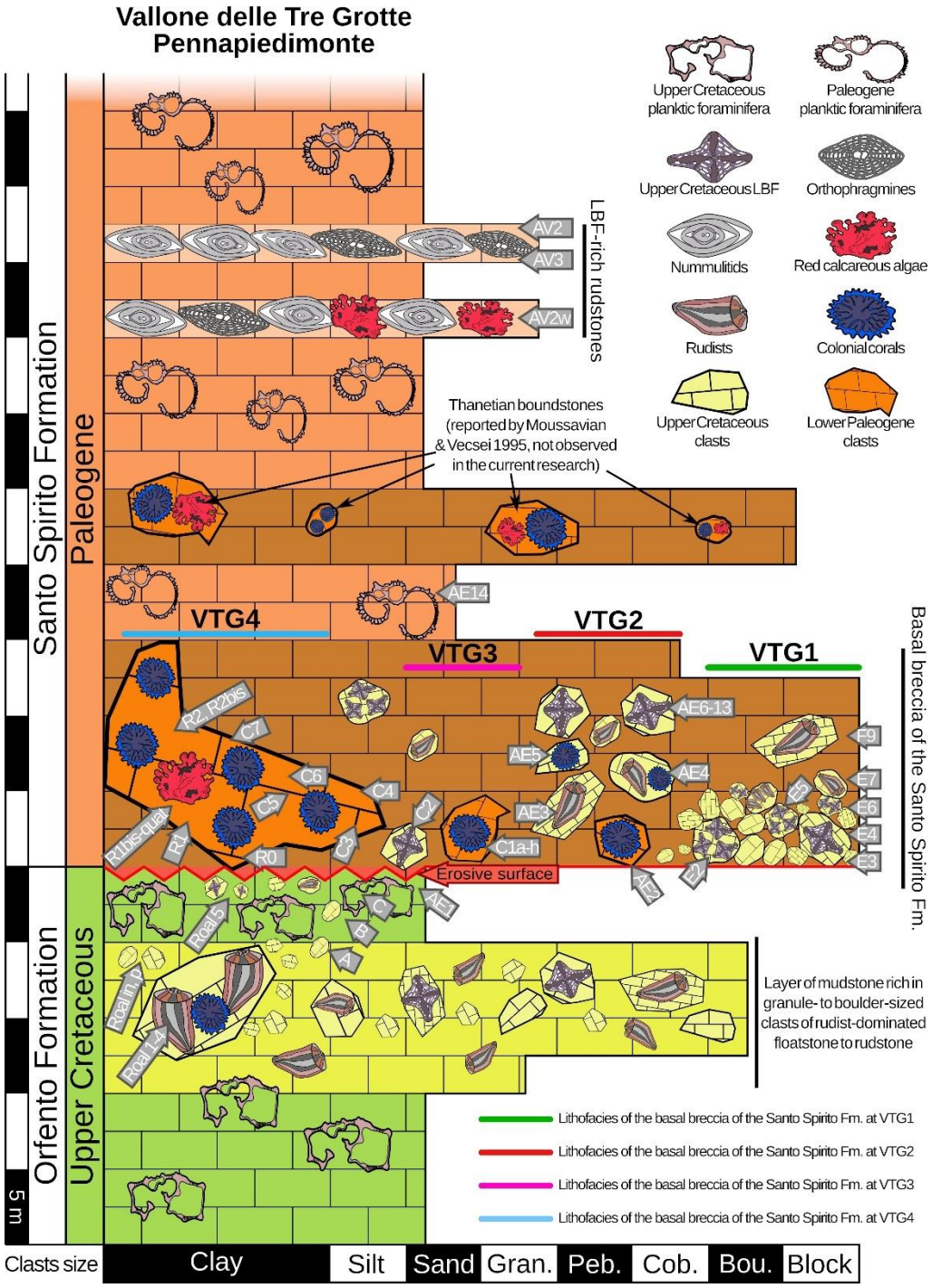

Fig. 2.9 - Idealized interpretative stratigraphic log of the area of the VTG near Pennapiedimonte that incorporates field data from the examination of VTG1-4 with the stratigraphic sections of Vecsei (1991) and

Vecsei & Moussavian (1997); sample positions are indicated by gray arrows; Gran.= granule; Peb.= pebble; Cob.= cobble; Bou.= boulder.

This is in overall agreement with previous researches that, according to sedimentary structures, erosive surfaces, the characteristics of the basal breccia layer, and micropaleontological evidence, interpreted the Santo Spirito Formation as an outer-ramp deposit fed by both pelagic rain and shallow-water material transported downslope (Moussavian & Vecsei 1995; Vecsei & Moussavian 1997; Vecsei et al. 1998; Eberli et al. 2019). Following this assumption and combining the stratigraphic sections of Vecsei (1991) and Vecsei and Moussavian (1997) with the results of the current research, an idealized combined stratigraphic log of the area of the VTG near Pennapiedimonte can be drafted (Figs. 2.2; 2.9). The latter illustrates the great lithological variability of the basal breccia of the Santo Spirito Formation, pointing to a complex genesis resulting from the emersion, erosion, and downslope transport of the different kinds of shallow-water limestones occurring in the breccia (Fig. 2.9) (Moussavian & Vecsei 1995; Vecsei & Moussavian 1997). While some of these shallow-water limestones were clearly significantly reworked and altered during their transport from their original formation environment (i.e., the shallow portions of the platform) to their final depositional setting (i.e., the deeper portions of the platform), others moved downslope as coherent blocks (e.g., the LBF rudstone and the coral boundstones). They have sharp boundaries with the surrounding matrix and do not display evidence of mixing (e.g., presence of pelagic elements scattered within and thoroughly mixed with the shallow-water components). Transported material if not subject to extensive reworking and mixing with the surrounding slope sediments during transport can shed light on the environment where it was initially generated (Schlager 1991; Schlager et al. 1996; Coletti et al. 2015, 2016; Buček & Köhler 2017). Therefore, the Upper Cretaceous clasts and the Lower Paleocene clasts preserved in the Orfento and Santo Spirito formations can give us important information on the evolution of shallow-water, carbonate-producing assemblages of the Maiella platform across the K/Pg boundary and beyond.

The Maiella platform in the aftermath of the end-Cretaceous extinction

Upper Cretaceous shallow-water carbonates are essentially dominated by either rudists or LBF (up to 45% and 53.5% of the skeletal assemblage respectively), associated with a significant contribution from colonial corals (13% in the LBF rudstone and 34.5% in the rudist floatstone to rudstone) (Tab. 2.1). In lower Danian assemblages, the first two groups

are absent, whereas the latter has become significantly more abundant and dominates the skeletal assemblage (65-66%; Tab. 2.1). In the study area, similarly to other parts of the Adriatic and Apulian carbonate platforms (Drobne et al. 2007; Buček & Köhler 2017; Tešović et al. 2020), the K/Pg boundary is represented by a stratigraphic hiatus and the successions are not continuous (Fig. 2.9). However, this remarkable increase in the contribution of colonial corals to the skeletal assemblages is consistent with the findings of other authors: i.e., a relatively rapid recovery of hermatypic corals following the K/Pg mass extinction in comparison to other groups of carbonate producers such as LBF (Kiessling & Baron-Szabo 2004; Pandolfi & Kiessling 2014; Dishon et al. 2020; Tešović et al. 2020; Baron-Szabo et al. 2023; Martinuš et al. 2024).

In terms of the main groups of carbonate producers, lower Danian bioconstructions display a remarkable similarity with modern shallow-water coral reefs, as their framework is essentially built by corals and red calcareous algae (e.g., Hubbard et al. 1990; Harney & Fletcher 2003; Hart & Kench 2007; Perry et al. 2008). In the case of the investigated Danian bioconstructions the framework represents close to 60% of the total rock volume and is overwhelmingly dominated by colonial corals and red calcareous algae (which represent 65-66% and 22-24% of the entire skeletal assemblage, respectively) (Tab. 2.1). With regards to secondary carbonate producers, encrusting benthic foraminifera provide a minor contribution to the framework of both Danian and Upper Cretaceous bioconstructions (Tab. 2.1). While their ecological niche is still poorly understood, encrusting benthic foraminifera have been significantly contributing to shallow-water carbonates at least since the Late Jurassic (Granier 2024), with a peak during the Eocene (Plaziat & Perrin 1992; Coletti et al. 2022). The encrusting benthic foraminifera assemblage of the Danian bioconstructions of VTG is largely dominated by *Haddonia*-like agglutinated taxa. This is different from both younger Cenozoic bioconstructions and modern coral reefs, where encrusting hyaline and porcelaneous taxa prevail (e.g., Plaziat & Perrin 1992; Baceta et al. 2005; Tichenor & Lewis 2018; Coletti et al. 2021). Differently from modern reefs that develop in high-energy setting, the internal sediment of the Danian bioconstructions mainly consists of micrite (Tab. 2.1). This is not an isolated case. In many coral bioconstructions of the Paleocene micrite has been reported as the dominant type of internal sediment (Tab. 2.2) (Zamagni et al. 2008, 2009; Buček & Köhler 2017; Consorti & Köroğlu 2019; Vršič et al. 2021). There are also reports of coral bioconstructions associated with coarse-grained sediments (Accordi et al. 1998; Kiessling et al. 2005), but they are much less common. This suggests that most of the

known coral-dominated bioconstructions of the Paleocene, including those investigated in the current research, likely developed in a more calm and protected (and thus possibly deeper) environment than most of their modern counterparts. With regards to water depth, the overall skeletal assemblage suggests a placement within the photic zone. Given the lack of planktic foraminifera, the low abundance of porcelaneous foraminifera, and the presence of both green and red calcareous algae, it is possible to exclude that the investigated bioconstructions developed in extremely shallow settings or close to the lower limit of the photic zone. Unfortunately, both green algae and foraminifera are too rare (1.5% and 1.5-2% of the skeletal assemblage, respectively) to provide more useful information. Red calcareous algae are far more abundant but the assemblage, is dominated by Sporolithales and Peyssonneliales, whereas Hapalidiales and Corallinales are rare. The depth distributions of the latter two groups are well known in modern oceans and have been used to create reliable paleobathymetric reconstructions (Coletti & Basso, 2020). The scarcity of Hapalidiales and Corallinales prevents more detailed reconstruction based on red calcareous algae. The transported nature and the poor exposure of the investigated boundstones also prevent paleobathymetric interpretations based on the overall geometry of the outcrop. Consequently, while it is clear that these bioconstructions formed within the photic zone in a low-energy environment, the data currently available cannot provide a definitive answer on whether they originated in the upper, middle, or lower part of the photic zone.

The Late Paleocene crisis of coral carbonate production

Comparing VTG coral bioconstructions to other Paleocene coral-dominated structures reveals a general decline in the contribution of corals to carbonate production during the Paleocene (Tab. 2.2). This decline is particularly relevant during the late Thanetian (Tab. 2.2) (Baceta et al. 2005). A similar pattern can be seen in the abundance of shallow-water coral-dominated facies. The latter, from the late Thanetian until the end of the Middle Eocene, are quite rare (Kiessling & Simpson 2011; Zamagni et al. 2012; Coletti et al. 2022). Corals still occur during the whole Early to Middle Eocene interval and they display reef-building capacity (e.g., Baceta et al. 2005; Vescogni et al. 2016; Martin-Martin et al. 2023; Benedetti et al. 2024), but they are much less common than other groups of shallow-water carbonate producers, such as LBF (Pomar et al. 2017; Coletti et al. 2022). The results of the quantitative analysis of the Danian skeletal assemblages from Maiella further support this

overall pattern resulting from the analysis of the abundance of coral bioconstructions, highlighting a late Thanetian crisis in coral carbonate production in shallow-waters.

Site	Central Italy TCG3	Central Italy TCG4	Pyrenean Basin Bz-2	Pyrenean Basin Lizarraga pass	Vel'ky Lipnik-Klippen Belt	Hazara Basin	Pyrenean Basin Leg-2	Hazara Basin
Age	Early Danian	Early Danian	Middle Danian	Late Danian	Selandian – early Thanetian	Selandian – early Thanetian	Thanetian	Late Thanetian
SBZ	SBZ1	SBZ1	SBZ1 - SBZ2	SBZ1 - SBZ2	SBZ3	SBZ3	SBZ3	SBZ3 to SBZ4
Reference	This work	This work	Baceta et al. 2005	Baceta et al. 2005	Köhler & Bucek 2005	Ali et al. 2024	Baceta et al. 2005	Ali et al. 2024
Characteristics of the rock								
Matrix	~ 1/3	~ 1/3	~ 1/2 - 3/4	~ 1/2 - 3/4	~ 1/3	~ 1/2	~ 4/5 - 2/3	~ 2/3
Skeletal assemblage	~ 2/3	~ 2/3	~ 1/4 - 1/2	~ 1/4 - 1/2	~ 2/3	~ 1/2	~ 1/5 - 1/3	~ 1/3
Type of matrix	Micrite	Micrite	Sand-sized bioclastic withn a peloidal micritic matrix	Sand-sized bioclastic	Micrite	Micrite	Micrite and microbioclasts	Micrite
Non skeletal grains	Rare - scarce	Scarce - common	Aggregated grains common at the reef crest; ooids in the back reef and in the lagoon	Aggregated grains common at the reef crest; ooids in the back reef and in the lagoon	Absent	Absent	Absent	Absent – very rare
Main frame builders	CC	CC	CC, RCA, calcareous sponges	CC, RCA, calcareous sponges	CC	CC	RCA , CC	CC
CC %	40	39	//	//	32	38	//	23.5
Secondary frame builders	RCA	RCA	EBF	EBF	RCA	//	EBF	RCA
Composition of the skeletal assemblage								
CC	Dominant (66.0)	Dominant (65.0)	Abundant	Abundant	Abundant (45)	Dominant (80.7)	Common	Dominant (62.2)
RCA	Common (22.0)	Common (24.0)	Abundant	Abundant	Abundant (28)	Absent	Common	Common (20.9)
GCA	Rare (1.5)	Rare (1.5)	Rare	Rare	Present	Rare (1.2)	Rare	Very-rare (0.5)
LBF	Absent	Absent	Absent	Absent	Present	Scarce (4.9)	Common	Scarce (5.4)
SBF	Rare (1.5)	Rare (2.0)	Common	Scarce	Present	Scarce (5.1)	Common	Rare (2.0)
EBF	Rare (4.5)	Scarce (5.0)	Scarce	Scarce	Common (12)	Absent	Scarce	Rare (2.5)
MOL	Very rare (1.0)	Very rare (0.5)	Rare	Scarce	Present	Scarce (5.1)	Scarce	Very-rare (0.7)
ECH	Very rare (0.5)	Rare (1.5)	Rare	Scarce	Present	Rare (2.0)	Rare	Rare (4.4)
BRY	Rare (2.5)	Very rare (0.5)	Scarce	Scarce	Present	Very-rare (0.8)	Common	Very-rare (0.9)
Others	Very rare (0.5)	Absent	Rare	Rare	Present	Very-rare (0.1)	Rare	Very-rare (0.4)
Foraminiferal assemblage	Entirely benthic	Entirely benthic	Entirely benthic	Entirely benthic	Mostly benthic	Entirely benthic	Entirely benthic	Entirely benthic
Dominant benthic taxa	Small hyaline, agglutinated and porcellaneous taxa	Small hyaline, agglutinated and porcellaneous taxa	Small and large hyaline taxa including miscellaneids	Small and large hyaline taxa including miscellaneids	Small and large hyaline taxa including miscellaneids, small and large porcellaneous taxa	Small hyaline taxa, small agglutinated taxa, miscellaneids	Large hyaline taxa including nummulitids, miscellaneids and orthophragmines and small hyaline taxa	Small hyaline taxa, miscellaneids

Tab. 2.2 - Comparison between the Paleocene coral bioconstructions of VTG, the bioconstruction from Vel'ky Lipnik of the Klippen Belt of Slovakia (Köhler & Bucek, 2005), those from the Ghumanwan Section of the Hazara Basin (Ali et al. 2024), and those from the Pyrenees (Baceta et al. 2005). The relative abundance of the various components is given using a modified version of the scale proposed by Carey et al. (1995): 0% = absent; 1% > very rare > 0%; 5% > rare > 1%; 10% > scarce > 5%; 25% > common > 10%; 50% > abundant > 25%; dominant > 50%. CC= colonial corals; RCA= red calcareous algae; GCA= green

calcareous algae; LBF= larger benthic foraminifera; SBF= small benthic foraminifera; EBF= encrusting benthic foraminifera; MOL= mollusks; ECH= echinoderms; BRY= bryozoans.

This crisis seems to have only affected coral's ability to accumulate large quantities of calcium carbonate, not their biodiversity (Bosellini et al. 2022; Benedetti et al. 2024), and it has been linked to various environmental factors, including nutrient availability, ocean chemistry and circulation, biological evolution and, last but not least, temperature (e.g., Baceta et al. 2005; Scheibner & Speijer 2008; Zamagni et al. 2009, 2012; Pomar et al. 2017; Coletti et al. 2022; Ali et al. 2024). The Paleocene was characterized by a general warming trend starting from ca. 61-58 Ma (Selandian – earliest Thanetian), culminating during the latest Thanetian – earliest Eocene, and followed by a prolonged period of elevated temperatures spanning most of the Early and Middle Eocene (Zachos et al. 2001; Barnet et al. 2019). Afterwards global temperatures gradually dropped and continued to do so until the Late Oligocene Warming (Zachos et al. 2001). Within the Tethys, during the same interval, colonial corals carbonate production seems to be negatively correlated with temperature, decreasing from the Danian to the late Thanetian, reaching a minimum during the Early and Middle Eocene and increasing during the Late Eocene and the Oligocene (Coletti et al. 2022). Coral biodiversity does not reflect this and appears to be somewhat unrelated to the overall rate of calcium carbonate production and accumulation (Benedetti et al., 2024), in agreement with the conclusion of Jonson et al. (2008) for the Caribbean. Despite these seeming contradictions and the scarcity of quantitative data, it is possible to propose an overall explanation that combines the evidence based on the composition of skeletal assemblages (this work), with the distribution and frequency of coral dominated facies (Kiessling et al. 1999; Zamagni et al. 2012; Coletti et al. 2022), and data on coral biodiversity (Benedetti et al. 2024). Large, coral-dominated bioconstructions appear less likely to develop during warm periods, particularly during those marked by a rapid and remarkable rise in temperature over a geologically short time span, such as during the late Thanetian (Kiessling et al. 1999; Zamagni et al. 2012; Coletti et al. 2022). While large bioconstructions during these intervals might be rare, colonial corals are usually able to survive, and (possibly pushed to diversification by the adverse conditions) to even gain biodiversity, especially if temperatures are rising gradually (Vescogni et al. 2016; Bendetti et al. 2024). This in turn may open new niches for corals and possibly allows them to better colonize "refuge areas" like the mesophotic zone, where they can more easily endure warm periods (e.g., Morsilli et al. 2012; Pomar & Hallock 2007; Pomar et al. 2017). This wider

perspective suggests that colonial corals, as a group, are indeed resilient to a wide variety of adverse events, including climate change. However, reefs (considered as complex, bioconstructed, shallow-water ecosystems where corals play a major role) are severely affected by processes like global warming and may take a geologically long time to recover.

2.7.Conclusion

The limestones of the Maiella massif hold a wealth of information about the evolution and distribution of shallow-water carbonate producers over critical time intervals such as the Late Cretaceous and Early Paleogene. The current research indicates that colonial corals were a significant part of the skeletal assemblage of the Upper Cretaceous shallow-water carbonates and that their abundance notably increased in the Lower Paleocene. This suggests a faster recovery of corals from the Cretaceous–Paleogene extinction compared to other groups of neritic carbonate producers such as larger benthic foraminifera. The comparison between the Lower Paleocene coral bioconstructions of the Maiella massif and others formed later during the remainder of the Paleocene reveals an overall decline in coral carbonate production with a minimum in the uppermost Paleocene. Quantitative microfacies analysis clearly allows for the recognition of this trend, enabling the refinement of data on carbonate production resulting from the study of the frequency of coral-dominated facies. The latter studies show that, at least in the Tethys, coral carbonate production did not recover until the Late Eocene. This overall pattern appears to be linked to average global temperatures, which progressively increased during the Late Paleocene, peaked during the latest Paleocene - Early Eocene interval, remained elevated for most of the Middle Eocene, and decreased thereafter. Water chemistry, biological evolution, nutrient availability, and ocean circulation most likely also had an impact.

The current analysis based on the composition of skeletal assemblages provides evidence for both the recovery of shallow-water corals carbonate production after the end-Cretaceous extinction and its Late Paleocene decline. This supports the existing data on coral-dominated facies and integrates with the data on coral biodiversity, providing an overall picture of coral carbonate production during the Cenozoic. Warm periods, especially those characterized by rapidly rising temperatures, seem to be unfavorable for the development of large, coral-dominated, bioconstructions. Colonial corals continue to exist during these times, and their biodiversity may even rise, allowing them to better spread in

ecological niches more shielded from the high temperatures (e.g., the mesophotic zone). This indicates that colonial corals are able to endure severe crises by adapting to the changing environmental conditions. However, coral bioconstructions are susceptible to warming events (especially rapid ones) and, although corals as a group can survive these events, their contribution to shallow-water reefs may significantly decline.

2.8.References

Accarie H. (1988) - Dynamique sédimentaire et structurale au passage plateforme/bassin. Les faciès carbonatés crétacés et tertiaires: Massif de la Maiella (Abruzzes, Italie). *Ecole des Mines de Paris, Mémoires Science de la Terre*, 5.

Accordi G., Carbone F. & Pignatti J. (1998) - Depositional history of a Paleogene carbonate ramp (western Cephalonia, Ionian Islands, Greece). Geologica Romana, 34: 131-205.

Aguilera O., Bencomo K., de Araújo O.M.O., Dias B.B., Coletti G., Lima D., Silane A.F., Polk M., Alves-Martin M.V., Jaramillo C., Kutter V.T. & Lopes, R.T. (2020) - Miocene heterozoan carbonate systems from the western Atlantic equatorial margin in South America: The Pirabas Formation. Sedimentary Geology, 407: 1-28. https://doi.org/10.1016/j.sedgeo.2020.105739.

Ali M., Coletti G., Mariani L., Benedetti A., Munawar M.J., Rehman S.U., Sternai P. Basso D., Malinverno E., Shahzad K., Khan S., Awais M., Usman M., Castelltort S., Adatte T. & Garzanti E. (2024) - Shallow-water carbonate facies herald the onset of the Palaeocene-Eocene Thermal Maximum (Hazara basin, Northern Pakistan). Journal of Asian Earth Sciences: X, 11: 100169.

Aubry M.P., Piller W.E., Van Couvering J.A., Berggren W.A., Flynn J.J., Head M.J., Hilgen F., Tian J., Kent D.V. & Miller K.G. (2023) - Unifying Cenozoic chronostratigraphy and geochronology: applying the rules. Newsletters on Stratigraphy, 57: 25-36. DOI: 10.1127/nos/2023/0767.

Baceta J.I., Victoriano P. & Bernaola G. (2005) - Paleocene coralgal reefs of the western Pyrenean basin, northern Spain: New evidence supporting an earliest Paleogene recovery of reefal ecosystems. Palaeogeography, Palaeoclimatology, Palaeoecology, 224(1-3): 117-143.

Barattolo F. (1998) - Dasycladacean green algae and microproblematica of the uppermost Cretaceous–Paleocene in the Karst area (NE Italy and Slovenia). In: Hottinger L. & Drobne K. (Eds.) - Paleogene shallow benthos of the Tethys: 65-127. Opera Dela Slovenske akademije znanosti in umetnosti (SAZU), Ljubljana.

Barnet J. S., Littler K., Westerhold T., Kroon D., Leng M. J., Bailey I., Rohl U. & Zachos J. C. (2019) - A high-Fidelity benthic stable isotope record of late Cretaceous–early Eocene climate change and carbon-cycling. Paleoceanography and Paleoclimatology, 34(4): 672-691.

Baron-Szabo R. C., Schlagintweit F. & Rashidi K. (2023) - Coral fauna across the Cretaceous–Paleogene boundary at Zagros and Sistan Suture zones and Yazd Block of Iran. Swiss Journal of Palaeontology, 142(1): 1-49.

Benedetti A. (2019) - Benthic foraminiferal assemblages from the late Eocene to the early Oligocene of the Caltavuturo Formation in the Madonie Mountains (Sicily): a tool for correlation. Italian Journal of Geosciences, 138(1): 43-55.

Benedetti A. & Papazzoni C.A. (2022) - Rise and fall of rotaliid foraminifera across the Paleocene and Eocene times. Micropaleontology, 68(2): 185-196.

Benedetti A., Papazzoni C.A. & Bosellini F.R. (2024) - Unparallel resilience of shallow-water tropical calcifiers (foraminifera and scleractinian reef corals) during the early Paleogene global warming intervals. Palaeogeography, Palaeoclimatology, Palaeoecology, 651: 112393.

Bellwood D.R., Hoey A.S., Ackerman J.L. & Depczynski M. (2006) - Coral bleaching, reef fish community phase shifts and the resilience of coral reefs. Global Change Biology, 12(9): 1587-1594.

Bernoulli D., Anselmetti F., Eberli G., Mutti M., Pignatti J., Sanders D. & Vecsei A. (1996) - Montagna della Maiella: the sedimentary and sequential evolution of a Bahamian-type carbonate platform of the South-Tethyan continental margin. Memorie della Società Geologica Italiana, 51: 7-12.

Bialik O.M., Coletti G., Mariani L., Commissario L., Desbiolles F. & Meroni A.N. (2023) - Availability and type of energy regulate the global distribution of neritic carbonates. Scientific Reports, 13(1): 19687.

Birkeland C. (1997) - Life and death of coral reefs. Springer Science & Business Media, New York, NY, USA, 536 pp.

Bosellini F. & Russo A. (1995) - The Scleractinian genus Actinacis. Systematic revision and stratigraphic record of the Tertiary species with special regard to Italian occurrences. Rivista italiana di Paleontologia e Stratigrafia, 101: 215-230.

Bosellini F.R. & Perrin C. (2008) - Estimating Mediterranean Oligocene–Miocene sea-surface temperatures: an approach based on coral taxonomic richness. Palaeogeography, Palaeoclimatology, Palaeoecology, 258(1-2): 71-88.

Bosellini F.R., Vescogni A., Budd A.F. & Papazzoni C.A. (2021) - High coral diversity is coupled with reef-building capacity during the Late Oligocene Warming Event (Castro Limestone, Salento Peninsula, S Italy). Rivista Italiana di Paleontologia e Stratigrafia, 127(3): 515-538.

Bosellini F.R., Benedetti A., Budd A.F. & Papazzoni C.A. (2022) - A coral hotspot from a hot past: The EECO and post-EECO rich reef coral fauna from Friuli (Eocene, NE Italy). Palaeogeography, Palaeoclimatology, Palaeoecology, 607: 111284.

Brandano M., Lipparini L., Campagnoni V. & Tomassetti L. (2012) - Downslope-migrating large dunes in the Chattian carbonate ramp of the Majella Mountains (Central Apennines, Italy). Sedimentary Geology, 255: 29-41.

Brandano M., Cornacchia I., Raffi I. & Tomassetti L. (2016)a - The Oligocene–Miocene stratigraphic evolution of the Majella carbonate platform (Central Apennines, Italy). Sedimentary Geology, 333: 1-14.

Brandano M., Tomassetti L., Sardella R. & Tinelli C. (2016)b - Progressive deterioration of trophic conditions in a carbonate ramp environment: the Lithothamnion Limestone, Majella Mountain (Tortonian–early Messinian, central Apennines, Italy). Palaios, 31(4): 125-140.

Brandano M., Tomassetti L., Cornacchia I., Trippetta F., Pomar L. & Petracchini L. (2020) - The submarine dune field of the Bolognano Fm. Depositional processes and the carbonate reservoir potential (Chattian to Burdigalian, Majella Carbonate Platform). Geological Field Trips & Maps, 12(2.3): 1-42.

Brandano M., Tomassetti L., Di Bella L., Barberio D. M., Barbieri M. & Ferrini A. (2022) - Late Burdigalian to early Messinian environmental and climatic evolution of the central paleo Adriatic domain from the shallow water sedimentary record (Bolognano Fm, Eastern Majella, Central Apennines). Sedimentary Geology, 440: 106235.

Bryant D., Burke L., McManus J. & Spalding M. (1998) - Reefs at risk: a map-based indicator of threats to the world's coral reefs. World Resources Institute, New York, USA, 57 pp.

Buček S. & Köhler E. (2017) - Palaeocene Reef Complex of the Western Carpathians. Slovak Geological Magazine, 17(1): 3-163.

Carey J.S., Moslow T.F. & Barrie J.V. (1995) - Origin and distribution of Holocene temperate carbonates, Hecate Strait, western Canada continental shelf. Journal of Sedimentary Research, 65(1a): 185-194.

Cheung M.W., Hock K., Skirving W. & Mumby P. J. (2021) - Cumulative bleaching undermines systemic resilience of the Great Barrier Reef. Current biology, 31(23): 5385-5392.

Chiocchini M. & Mancinelli A. (2001) - Sivasella monolateralis Sirel and Gunduz, 1978 (Foraminiferida) in the Maastrichtian of Latium (Italy). Revue de Micropaléontologie, 44(4): 267-277.

Cipriani M., Apollaro C., Basso D., Bazzicalupo P., Bertolino M., Bracchi V.A., Bruno F., Costa G., Dominici R., Gallo A., Muzzupappa M., Rosso A., Sanfilippo R., Sciuto F., Vespasiano G. & Guido A. (2024) - Origin and role of non-skeletal carbonate in coralligenous build-ups: new geobiological perspectives in biomineralization processes. Biogeosciences, 21: 49–72.

Coletti G., Basso D., Frixa A. & Corselli C. (2015) - Transported rhodoliths witness the lost carbonate factory: a case history from the Miocene Pietra da Cantoni limestone (NW Italy). Rivista Italiana di Paleontologia e Stratigrafia, 121(3): 345-368.

Coletti G., Vezzoli G., Di Capua A. & Basso D. (2016) - Reconstruction of a lost carbonate factory based on its biogenic detritus (Ternate-Travedona Formation and Gonfolite Lombarda Group-Northern Italy). Rivista Italiana di Paleontologia e Stratigrafia, 122: 1-22.

Coletti G. & Basso D. (2020) - Coralline algae as depth indicators in the Miocene carbonates of the Eratosthenes Seamount (ODP Leg 160, Hole 966F). Geobios, 60: 29-46.

Coletti G., Balmer E.M., Bialik O.M., Cannings T., Kroon D., Robertson A.H. & Basso D. (2021) - Microfacies evidence for the evolution of Miocene coral-reef environments in Cyprus. Palaeogeography, Palaeoclimatology, Palaeoecology, 584: 110670.

Coletti G., Commissario L., Mariani L., Bosio G., Desbiolles F., Soldi M. & Bialik O. M. (2022) - Palaeocene to Miocene southern Tethyan carbonate factories: A meta-analysis of the successions of South-western and Western Central Asia. The Depositional Record, 8(3): 1031-1054.

Consorti L. & Köroğlu F. (2019) - Maastrichtian-Paleocene larger Foraminifera biostratigraphy and facies of the Şahinkaya Member (NE Sakarya Zone, Turkey): Insights into the Eastern Pontides arc sedimentary cover. Journal of Asian Earth Sciences, 183: 103965.

Consorti L. & Schlagintweit F. (2022) - Taxonomy and paleoecology of the Maastrichtian-Paleogene benthic foraminifer Valvulineria orali (Inan, 2003) comb. nov. Journal of Mediterranean Earth Sciences, 14: 1-9.

Cornacchia I., Andersson P., Agostini S., Brandano M. & Di Bella L. (2017) - Strontium stratigraphy of the upper Miocene Lithothamnion Limestone in the Majella Mountain, central Italy, and its palaeoenvironmental implications. Lethaia, 50(4): 561-575.

Cornacchia I., Brandano M., Raffi I., Tomassetti L. & Flores I. (2018) - The Eocene–Oligocene transition in the C-isotope record of the carbonate successions in the Central Mediterranean. Global and Planetary Change, 167: 110-122.

Cornacchia I., Brandano M. & Agostini S. (2021) - Miocene paleoceanographic evolution of the Mediterranean area and carbonate production changes: A review. Earth-Science Reviews, 221: 103785.

Crescenti U., Crostella A., Donzelli G. & Raffi G. (1969) - Stratigrafia della serie calcarea dal Lias al Miocene nella regione marchigiano-abruzzese (Parte II. Litostratigrafia, Biostratigrafia, Paleogeografia). Memorie Società Geologica Italiana, 8(2): 343-420.

Descombes P., Wisz M.S., Leprieur F., Parravicini V., Heine C., Olsen S.M., Swingedouw D., Kulbiki M., Moutillout D. & Pellissier L. (2015) - Forecasted coral reef decline in marine biodiversity hotspots under climate change. Global Change Biology, 21(7): 2479-2487.

Dishon G., Grossowicz M., Krom M., Guy G., Gruber D.F. & Tchernov D. (2020) - Evolutionary traits that enable scleractinian corals to survive mass extinction events. Scientific Reports, 10: 3903.

Drobne K., Ogorelec B. & Riccamboni R. (2007) - Bangiana hanseni n. gen. n. sp. Foraminifera, and index species of Danian age (Lower Paleocene) from the Adriatic Carbonate Platform (SW Slovenia, NE Italy, Herzegovina). Razprave 4.Razreda, Slovenska Akademija Znanosti in Umetnosti (SAZU), 45: 5-71.

Eberli G.P., Bernoulli D., Sanders D. & Vecsei A. (1993) - From Aggradation to Progradation: The Maiella Platform, Abruzzi, Italy. In: Simo T., Scott R.W., Masse J.P. (Eds.), Cretaceous Carbonate Platforms. American Association of Petroleoum Geologist Memories, 56: 213-232.

Eberli G.P., Bernoulli D., Vecsei A., Sekti R., Grasmueck M., Lüdmann T., Anselmetti F.S., Mutti M. & Della Porta G. (2019) - A Cretaceous carbonate delta drift in the Montagna della Maiella, Italy. Sedimentology, 66(4): 1266-1301.

Flügel E. & Flügel-Kahler E. (1992) - Phanerozoic reef evolution: basic questions and data base. Facies, 26: 167-277.

Flügel E. (2010) - Microfacies of Carbonate Rocks: Analysis Interpretation and Application. Springer, New York, 984 pp.

Granier B.R. (2024) - Reassessment of Iberopora bodeuri, a primitive plurilocular calcareous encrusting foraminifer from the "Upper Jurassic" (including Berriasian) carbonate platforms of the northern and central Tethys. Cretaceous Research, 155: 105782.

Harney J.N. & Fletcher III C.H. (2003) - A budget of carbonate framework and sediment production, Kailua Bay, Oahu, Hawaii. Journal of Sedimentary Research, 73(6): 856-868.

Hart D.E. & Kench P.S. (2007) - Carbonate production of an emergent reef platform, Warraber Island, Torres Strait, Australia. Coral Reefs, 26: 53-68.

Hubbard D.K., Miller A.I. & Scaturo D. (1990) - Production and cycling of calcium carbonate in a shelf-edge reef system (St. Croix, US Virgin Islands); applications to the nature of reef systems in the fossil record. Journal of Sedimentary Research, 60(3): 335-360.

Inan N., Tasli K. & Inan S. (2005) - Laffitteina from the Maastrichtian-Paleocene shallow marine carbonate successions of the Eastern Pontides (NE Turkey): biozonation and microfacies. Journal of Asian Earth Sciences, 25(2): 367-378.

Johnson K.G., Jackson J.B. & Budd A.F. (2008) - Caribbean reef development was independent of coral diversity over 28 million years. Science, 319(5869): 1521-1523.

Kato A., Baba M., Kawai H. & Masuda M. (2006) - Reassessment of the little-known crustose red algal genus Polystrata (Gigartinales), based on morphology and SSU rDNA sequences. Journal of Phycology, 42(4): 922–933.

Kiessling W., Flügel E. & Golonka J. (1999) - Paleoreef maps: evaluation of a comprehensive database on Phanerozoic reefs. American Association of Petroleoum Geologist Bulletin, 83(10): 1552-1587.

Kiessling W., Flügel E. & Golonka J. (2003) - Patterns of Phanerozoic carbonate platform sedimentation. Lethaia, 36(3): 195-225.

Kiessling W. & Baron-Szabo R.C. (2004) - Extinction and recovery patterns of scleractinian corals at the Cretaceous-Tertiary boundary. Palaeogeography, Palaeoclimatology, Palaeoecology, 214(3): 195-223.

Kiessling W., Aragón E., Scasso R., Aberhan M., Kriwet J., Medina F. & Fracchia D. (2005) - Massive corals in Paleocene siliciclastic sediments of Chubut (Argentina). Facies, 51: 233-241.

Kiessling W. & Simpson C. (2011) - On the potential for ocean acidification to be a general cause of ancient reef crises. Global Change Biology, 17(1): 56-67.

Kiessling W. & Kocsis Á. T. (2015) - Biodiversity dynamics and environmental occupancy of fossil azooxanthellate and zooxanthellate scleractinian corals. Paleobiology, 41(3): 402-414.

Knowlton N., Brainard R.E., Fischer R., Moews M., Plaisance L. & Caley M.J. (2010) - Coral reef biodiversity. In: McIntyre A.D. (Ed.) - Life in the World's Oceans: Diversity Distribution: 65-74. Wiley-Blackwell, Oxford, UK.

Köhler E. & Bucek S. (2005) - Paleocene reef limestones near Velký Lipnık (Pieniny Mts, NE Slovakia): facial environment and biogenic components. Slovak Geological Magazine, 11: 249-267.

Lampert S.A., Lowrie W., Hirt A.M., Bernoulli D. & Mutti M. (1997) - Magnetic and sequence stratigraphy of redeposited Upper Cretaceous limestones in the Montagna della Maiella, Abruzzi, Italy. Earth and Planetary Science Letters, 150(1-2): 79-93.

Martín-Martín M., Tosquella J., Guerrera F., Maaté A., Hlila R., Maaté S., Tramontana M. & Le Breton E. (2023) - The Eocene carbonate platforms of the Ghomaride Domain (Internal Rif Zone, N Morocco): A segment of the westernmost Tethys. Sedimentary Geology, 106423.

Martinuš M., Tešović B. C., Jurić S. & Vlahović I. (2024) - Patch reefs with scleractinian corals and layered domical and bulbous growth forms (calcified sponges?) in the upper Maastrichtian and lowermost Palaeocene platform carbonates, Adriatic islands of Brač and Hvar (Croatia). Palaeogeography, Palaeoclimatology, Palaeoecology, 112056.

Moberg F. & Folke C. (1999) - Ecological goods and services of coral reef ecosystems. Ecological economics, 29(2): 215-233.

Morsilli M., Rusciadelli G. & Bosellini A. (2002) - Large-scale gravity-driven structures: control on margin architecture and related deposits of a Cretaceous Carbonate Platform (Montagna della Maiella, Central Apennines, Italy). Bollettino Società Geolica Italiana, Special Vol. 1: 619-628.

Morsilli M., Bosellini F.R., Pomar L., Hallock P., Aurell M. & Papazzoni C.A. (2012) - Mesophotic coral buildups in a prodelta setting (late Eocene, southern Pyrenees, Spain): a mixed carbonate–siliciclastic system. Sedimentology, 59(3): 766-794.

Moussavian E. & Vecsei A. (1995) - Paleocene reef sediments from the Maiella carbonate platform, Italy. Facies, 32(1): 213-221.

Muttoni G., Dallanave E., & Channell J.E.T. (2013) - The drift history of Adria and Africa from 280 Ma to Present, Jurassic true polar wander, and zonal climate control on Tethyan sedimentary facies. Palaeogeography, Palaeoclimatology, Palaeoecology, 386: 415-435.

Nicolai C. & Gambini R. (2007) - Structural architecture of the Adria platform-and-basin system. Bollettino della Società Geologica Italiana, 7: 21-37.

Özcan E., Yücel A.O., Catanzariti R., Kayğılı S., Okay A.I., Simmons M.D., Pignatti J., Abbasi İ.A. & Erbil Ü. (2021) - Multiple Orbitoides d'Orbigny lineages in the Maastrichtian? Data from the Central Sakarya Basin (Turkey) and Arabian Platform successions (Southeastern Turkey and Oman). Swiss Journal of Palaeontology, 140: 1-30.

Pandolfi J.M. & Kiessling W. (2014) - Gaining insights from past reefs to inform understanding of coral reef response to global climate change. Current Opinion in Environmental Sustainability, 7: 52-58.

Papazzoni C.A., Fornaciari B., Giusberti L., Simonato M. & Fornaciari E. (2023) - A new definition of the Paleocene Shallow Benthic Zones (SBP) by means of larger foraminiferal biohorizons, and their calibration with calcareous nannofossil biostratigrapy. Micropaleontology, 69(4): 363-399.

Paulay G. (1997) - Diversity and distribution of reef organisms. In: Birkeland C. (Ed.) - Life and death of coral reefs: 298-353. Chapman Hall, London.

Pestana E.M.D.S., Nunes J.M.D.C., Cassano V. & Lyra G.D.M. (2021) - Taxonomic revision of the Peyssonneliales (Rhodophyta): Circumscribing the authentic Peyssonnelia clade and proposing four new genera and seven new species. Journal of Phycology, 57(6): 1749-1767.

Perrin C. (1992) - Signification écologique des foraminifères acervulinidés et leur rôle dans la formation de faciès récifaux et organogènes depuis le Paléocène. Geobios, 25(6): 725-751.

Perry C.T., Spencer T. & Kench P.S. (2008) - Carbonate budgets and reef production states: a geomorphic perspective on the ecological phase-shift concept. Coral Reefs, 27: 853-866.

Plaziat J.C. & Perrin C. (1992) - Multikilometer-sized reefs built by foraminifera (Solenomeris) from the early Eocene of the Pyrenean domain (S. France, N. Spain): Palaeoecologic relations with coral reefs. Palaeogeography, Palaeoclimatology, Palaeoecology, 96(3-4): 195-231.

Pomar L., Brandano M. & Westphal H. (2004) - Environmental factors influencing skeletal grain sediment associations: a critical review of Miocene examples from the western Mediterranean. Sedimentology, 51(3): 627-651.

Pomar L. & Hallock P. (2007) - Changes in coral-reef structure through the Miocene in the

Mediterranean province: Adaptive versus environmental influence. Geology, 35: 899-902.

Pomar L. & Hallock P. (2008) - Carbonate factories: a conundrum in sedimentary geology. Earth-Science Reviews, 87(3-4): 134-169.

Pomar L., Bassant P., Brandano M., Ruchonnet C. & Janson X. (2012) - Impact of carbonate producing biota on platform architecture: insights from Miocene examples of the Mediterranean region. Earth-Science Reviews, 113: 186-211.

Pomar L., Baceta J.I., Hallock P., Mateu-Vicens G. & Basso D. (2017) - Reef building and carbonate production modes in the west-central Tethys during the Cenozoic. Marine and Petroleum Geology, 83: 261-304.

Raffi I., Ricci C., Garzarella A., Brandano M., Cornacchia I. & Tomassetti L. (2016) - Calcareous nannofossils as a dating tool in shallow marine environment: an example from an upper Paleogene carbonate platform succession in the Mediterranean. Newsletters on Stratigraphy, 49(3): 481-495.

Robles-Salcedo R., Vicedo V. & Caus E. (2018) - Latest Campanian and Maastrichtian Siderolitidae (larger benthic foraminifera) from the Pyrenees (S France and NE Spain). Cretaceous Research: 81, 64-85.

Rusciadelli G. (2005) - The Maiella Escarpment (Apulia platform, Italy): geology and modelling of an Upper Cretaceous scalloped erosional platform margin. Bollettino della Società geologica Italiana, 124: 661-673.

Rusciadelli G., Sciarra N. & Mangifesta M. (2003) - 2D modelling of large-scale platform margin collapses along an ancient carbonate platform edge (Maiella Mt., Central Apennines, Italy): geological model and conceptual framework. Palaeogeography, Palaeoclimatology, Palaeoecology, 200(1-4): 245-262.

Rusciadelli G. & Di Simone S. (2007) - Differential compaction as a control on depositional architectures across the Maiella carbonate platform margin (central Apennines, Italy). Sedimentary Geology, 196(1-4): 133-155.

Sani F., Vannucci G., Boccaletti M., Bonini M., Corti G. & Serpelloni E. (2016) - Insights into the fragmentation of the Adria Plate. Journal of Geodynamics, 102: 121-138.

Sartorio D. & Venturini S. (1988) - Southern Tethys Biofacies. Agip, Amilcare Pizzi, Italy, pp. 236.

Scheibner C. & Speijer R.P. (2008) - Late Paleocene–early Eocene Tethyan carbonate platform evolution - A response to long-and short-term paleoclimatic change. Earth-Science Reviews, 90(3-4): 71-102.

Schlager W. (1991) - Depositional bias and environmental change—important factors in sequence stratigraphy. Sedimentary Geology, 70(2-4): 109-130.

Schlager W., Reijmer J.J. & Droxler A. (1994) - Highstand shedding of carbonate platforms. Journal of Sedimentary Research: 64(3b), 270-281.

Schmitz B., Pujalte V., Molina E., Monechi S., Orue-Etxebarria X., Speijer R.P., Alegret L., Apellaniz E., Arenillas I., Aubry M.P., Baceta J.I., Berggren W.A., Bernaola G., Caballero F., Clemmensen A., Dinarès-Turell J., Dupuis C., Heilmann-Clausen C., Orús A.H., Knox R., Martín-Rubio M., Ortiz S., Payros A., Petrizzo M.R., von Salis K., Sprong J., Steurbaut E. & Thomsen E. (2011) - The global stratotype sections and points for the bases of the Selandian (Middle Paleocene) and Thanetian (Upper Paleocene) stages at Zumaia, Spain. Episodes, 34: 220–243

Serra-Kiel J., Hottinger L., Caus E., Drobne K., Ferrandez C., Jauhri A.K., Less G., Pavlovec R., Pignatti J., Samso J.M., Schaub H., Sirel E., Strougo A., Tambareau Y., Tosquella J. & Zakrevskaya E. (1998) - Larger foraminiferal biostratigraphy of the Tethyan Paleocene and Eocene. Bulletin de la Société Géologique de France, 169: 281-299.

Serra-Kiel J., Vicedo V., Baceta J.I., Bernaola G. & Robador A. (2020) - Paleocene larger foraminifera from the Pyrenean Basin with a recalibration of the Paleocene shallow benthic zones. Geologica Acta, 18: 1-III.

Sinanoğlu D., Benedetti A. & Özgen-Erdem N. (2022) - Danian (SBZ2) larger foraminifera from the Becirman Formation (southeastern Turkey) as evidence of rotaliids diversity in lower Paleocene shallow-water environments. Rivista Italiana di Paleontologia e Stratigrafia, 128(2): 431-452.

Stolarski, J., Bosellini, F. R., Wallace, C. C., Gothmann, A. M., Mazur, M., Domart-Coulon, I., Gutner-Hoch E., Neuser R.D., Levy O., Shemesh A. & Meibom, A. (2016) - A unique coral biomineralization pattern has resisted 40 million years of major ocean chemistry change. Scientific Reports, 6(1): 27579.

Tešović B. C., Martinuš M., Golec I. & Vlahović I. (2020) - Lithostratigraphy and biostratigraphy of the uppermost Cretaceous to lowermost Palaeogene shallow-marine succession: top of the Adriatic Carbonate Platform at the Likva Cove section (island of Brač, Croatia). Cretaceous Research, 114: 104507.

Tichenor H.R. & Lewis R.D. (2018) - Distribution of Encrusting Foraminifera At San Salvador, Bahamas: a Comparison By Reef Types and Onshore− offshore Zonation. Journal of Foraminiferal Research, 48(4): 373-387.

Vecsei A. (1991) - Aggradation und Progradation eines Karbonatplattform-Randes: Kreide bis mittleres Tertiar der Montagna della Maiella, Abruzzen. - Mitteilungen aus dem Geologischen Institut der Eidgenössischen Technischen Hochschule und der Universität Zürich, Neue Folge, 294: 1-169.

Vecsei A. & Moussavian E. (1997) - Paleocene reefs on the Maiella platform margin, Italy: an example of the effects of the Cretaceous/Tertiary boundary events on reefs and carbonate platforms. Facies, 36: 123-139.

Vecsei A., Sanders D.G., Bernoulli D., Eberli G.P. & Pignatti J.S. (1998) - Cretaceous to Miocene sequence stratigraphy and evolution of the Maiella carbonate platform margin, Italy. In: de Graciansky P.C., Hardenbol J., Jacquin T. & Vail P.R. (Eds.) - Mesozoic and Cenozoic Sequence Stratigraphy of European Basins: 53-74. SEPM Society for Sedimentary Geology, Special Publication, 60.

Vecsei A. & Sanders D.G. (1999) - Facies analysis and sequence stratigraphy of a Miocene warm-temperate carbonate ramp, Montagna della Maiella, Italy. Sedimentary Geology, 123(1-2): 103-127.

Vescogni A., Bosellini F.R., Papazzoni C.A., Giusberti L., Roghi G., Fornaciari E., Dominici S. & Zorzin R. (2016) - Coralgal buildups associated with the Bolca Fossil-Lagerstätten: new evidence from the Ypresian of Monte Postale (NE Italy). Facies, 62: 1-20.

Vicedo V. & Robles-Salcedo R. (2022) - Late Cretaceous larger rotaliid foraminifera from the westernmost Tethys. Cretaceous Research, 133: 105137.

Vitale S. & Ciarcia S. (2022) - The dismembering of the Adria platforms following the Late Cretaceous-Eocene abortive rift: a review of the tectono-stratigraphic record in the southern Apennines. International Geology Review, 64(20): 2866-2889.

Vršič A., Gawlick H. J., Schlagintweit F., Machaniec E. & Gharsalla M. (2021) - Age, microfacies and depositional environment of the Middle to Late Paleocene shallow-marine carbonates in the Sirt Basin of Libya (Upper Sabil Formation): “Are Intisar domal structures pinnacle reefs?”. Facies, 67(4): 27.

Wade B.S., Pearson P.N., Berggren, W.A. & Pälike H. (2011) - Review and revision of Cenozoic tropical planktonic foraminiferal biostratigraphy and calibration to the geomagnetic polarity and astronomical time scale. Earth-Science Reviews, 104(1-3): 111-142.

Wilkinson C. (2004) - Status of Coral Reefs of the World: 2004. Global Coral Reef Monitoring Network and Australian Institute of Marine Science, Townsville, Australia, 557 pp.

Wood R. (1995) - The changing biology of reef-building. Palaios, 10: 517-529.

Zachos J., Pagani M., Sloan L., Thomas E. & Billups K. (2001) - Trends, rhythms, and aberrations in global climate 65 Ma to present. Science, 292(5517): 686-693.

Zamagni J., Mutti M. & Košir A. (2008) - Evolution of shallow benthic communities during the Late Paleocene–earliest Eocene transition in the Northern Tethys (SW Slovenia). Facies, 5: 25-43.

Zamagni J., Košir A. & Mutti M. (2009) - The first microbialite-coral mounds in the Cenozoic (Uppermost Paleocene) from the Northern Tethys (Slovenia): Environmentally-

triggered phase shifts preceding the PETM?. Palaeogeography, Palaeoclimatology, Palaeoecology, 274(1-2): 1-17.

Zamagni J., Mutti M. & Košir A. (2012) - The evolution of mid Paleocene-early Eocene coral communities: How to survive during rapid global warming. Palaeogeography, Palaeoclimatology, Palaeoecology, 317: 48-65.

Chapter 3 – POE and other excursions preceding the PETM [SBZ3 to SBZ4]

This third chapter represents the pre-PETM to early Pre-Onset Excursion (POE) conditions and describes the Late Paleocene warming events corresponding to SBZ3 to SBZ4 and its effect on the shallow water carbonate factory in Ghumanwan section (Hazara Basin: a sub-basin of Indus Basin) in Northern Pakistan, in eastern Tethys.

This chapter is taken from the published scientific paper by Ali et al., 2024, published in the Journal of Asian Earth Science: X, Volume 11, 1 June 2024, 100169.

"Shallow-water carbonate facies herald the onset of the Paleocene-Eocene Thermal Maximum (Hazara Basin, Northern Pakistan)"

Mubashir Ali, Giovanni Coletti, Luca Mariani, Andrea Benedetti, Muhammad-Jawad Munawar, Saif Ur Rehman, Pietro Sternai, Daniela Basso, Elisa Malinverno, Khurram Shahzad, Suleman Khan, Muhammad Awais, Muhammad Usman, Sebastien Castelltort, Thierry Adatte, Eduardo Garzanti

3.1. Abstract

We investigate the Paleocene succession of the Hazara Basin (Northern Pakistan) to better understand the impact of climate change on marine carbonate-producing organisms. These shallow-water carbonates, deposited during the Late Paleocene, before the onset of the Paleocene-Eocene Thermal Maximum, were studied using a quantitative approach to highlight changes in the skeletal assemblage. We recognise a decrease in the abundance of colonial corals and green calcareous algae and an increase in larger benthic foraminifera and red calcareous algae from the early Thanetian to the late Thanetian. Increasing temperatures may represent a plausible cause for the decline of the more sensitive colonial corals in favor of the more tolerant larger benthic foraminifera. A similar pattern is observed in most successions deposited along the margins of the Neotethys Ocean, suggesting a connection with the Late Paleocene environmental changes that heralded the PETM hyperthermal event.

Our stratigraphic analysis of the Hazara Basin strata suggests that the biotic turnovers occurred during the Paleocene – Eocene transition started already before the onset of the Paleocene Eocene Thermal Maximum as recorded by the geochemical proxies.

3.2. Introduction

During the Late Paleocene, large inputs of greenhouse gases into the atmosphere caused perturbations of the carbon-cycle and led to a significant warming of the global climate (Zachos et al., 2008; McInerney and Wing, 2011; Westerhold et al., 2020). Several hyperthemal events are recognised during the Late Paleocene - Early Eocene interval (Barnet et al., 2019). Among these episodes, the Paleocene-Eocene Thermal Maximum (PETM) stands out for its intensity (Zachos et al., 2008; Banerjee et al., 2020). The record of these hyperthermal events, and of the overall Late Paleocene warming, is strongly reflected by the distribution of shallow-water marine carbonate-producing organisms due to their sensitivity to changing climate and the key-role played by biogenic carbonates in the carbon cycle (Stanley and Hardie, 1998; Ridgwell and Zeebe, 2005).

Numerous studies have been conducted to assess shelfal carbonate production across the Cenozoic geological record (e.g., Esteban, 1996; Kiessling et al., 1999, 2002; Halfar and Mutti, 2005; Nebelsick et al., 2005; Bosellini and Perrin, 2008; Johnson et al., 2008; Wilson, 2008; Perrin and Bosellini, 2012; Perrin and Kiessling, 2012; Pomar et al., 2017; Michel et al., 2018; Aguilera et al., 2020; Pomar, 2020; Cornacchia et al., 2021). Several papers highlighted notable changes in the distribution of marine benthic carbonate producers during the Late Paleocene – Early Eocene interval, the most significant of which is the decline in both abundance and size of symbiont-bearing colonial-coral bioconstructions (Scheibner and Speijer, 2008; Zamagni et al., 2012; Pomar et al., 2017; Coletti et al., 2022). However, only a limited amount of well exposed shallow marine carbonates successions covering the Late Paleocene – Early Eocene interval have been thoroughly investigated (e.g., Zamagni et al., 2012). Therefore, very few quantitative data are available for tracking the response of marine carbonate producers during Late Paleocene environmental changes. More quantitative data and research on ancient habitats are needed to improve our capacity to unveil the past, thereby allowing us to better comprehend the present, and foresee the future (Bialik et al., 2023), and this is especially relevant for the Late Paleocene. Therefore, the

aim of the present study is to improve our knowledge on the distribution of carbonate-producing organisms during this crucial time interval by providing a quantitative analysis of the skeletal assemblages of a Thanetian shallow-water carbonate succession exposed in the Hazara Basin of Northern Pakistan. The studied succession accumulated just before the onset of the PETM and comprises facies dominated by both corals and larger benthic foraminifera, thus documenting the initial response of important types of benthic calcifiers to periods of global warming. A close comparison with correlative carbonate successions from the Himalaya studied with a similar approach (Nicora et al., 1987; Li et al., 2015, 2017, 2020, 2022; Jiang et al., 2021), and with other successions of the eastern and western Neotethys domains, allowed us to document, on the large scale, the sedimentary response of carbonate systems to climate change just before the final demise of eastern Neotethys seaway.

3.3.Geological Setting

The Himalayan foreland basin developed since the onset of subduction of the Indian passive continental margin underneath the Asian active margin at middle Paleocene time (~60 Ma; Hu et al., 2016),and witnessed the final demise of eastern Neotethys seaways during the Early to Middle Eocene (~50 Ma; Garzanti et al., 1987; Najman et al., 2017). The Hazara Basin (Northern Pakistan) is one of the many depocenters formed as a consequence of the convergence and collision between the Indian and Asian plates (Fig. 3.1). The studied succession is exposed on the western limb of the Hazara-Kashmir syntaxis (Bossart et al., 1988; Critelli and Garzanti, 1994; Najman et al., 2001) and is bounded by two major thrust faults, the Panjal Thrust in the north and the Main Boundary Thrust in the south (Di Pietro and Pogue, 2004; Ahsan and Chaudhry, 2008) (Fig. 3.1).

The Neoproterozoic-Cambrian basement of the basin consists of the Hazara Formation slates and phyllites (Butt, 1972), non-conformably overlain by the Jurassic (Hettangian) fluvio-deltaic coal-bearing sandstones and limestones of the Datta Formation (Abbasi et al., 2012). The overlying inner- to outer-ramp carbonates of the Toarcian to Callovian Samana-Suk Formation (Ahsan and Chaudhry, 2008; Shah et al., 2020) are unconformably followed by the Upper Jurassic to Lower Cretaceous glauconitic shales of the Chichali Formation (Ahsan and Chaudhry, 2008; Shah, 2009), overlain in turn by the Lower to Upper Cretaceous glauconitic sandstones, limestones and dolostones of the Lumshiwal Formation. The latter

is followed by the Upper Cretaceous deep-water carbonates of the Kawagarh Formation (Ahsan, 2008).

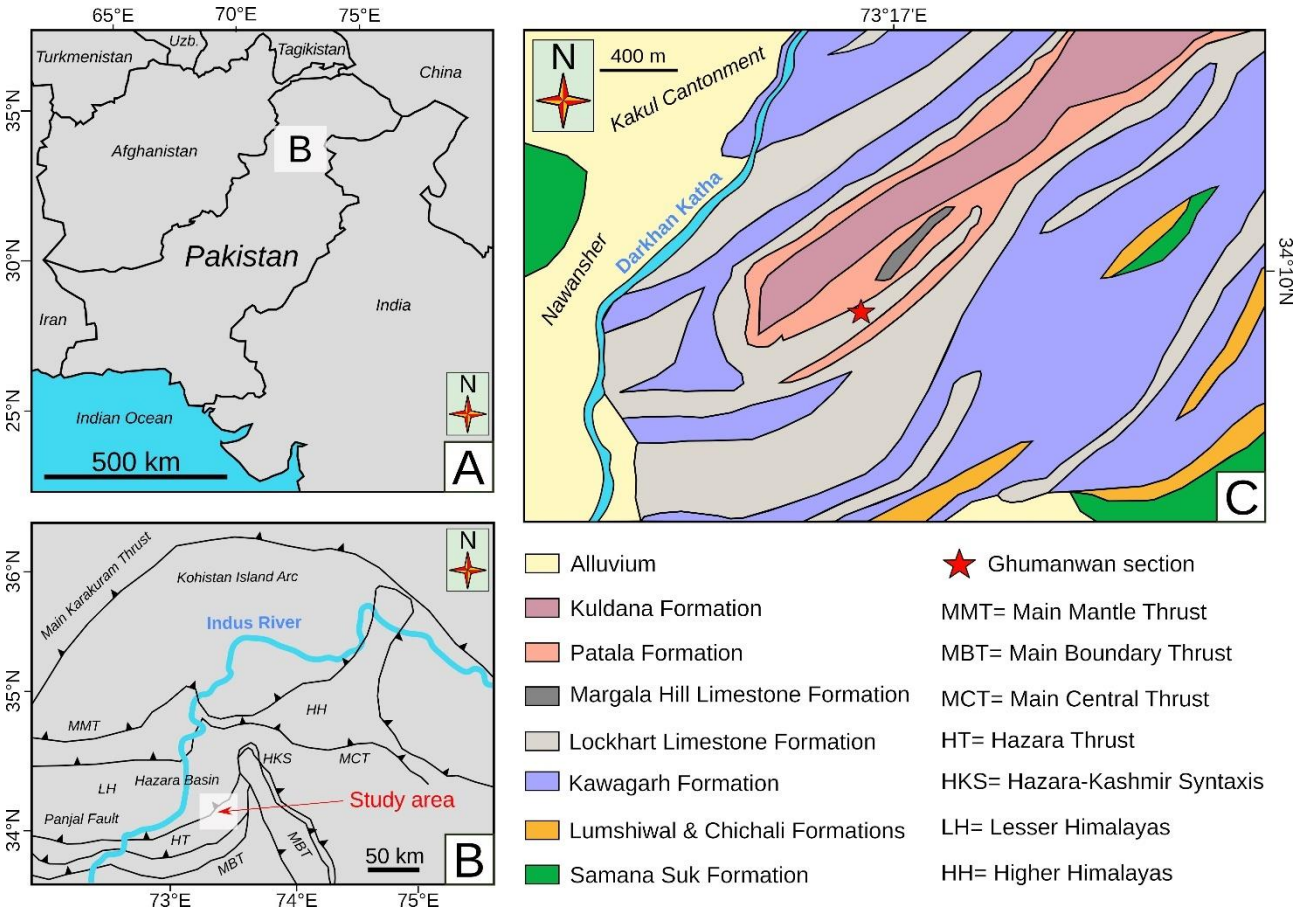

Figure 3.1: Study area. A) Location of the study area in Pakistan. B) Schematic tectonic map of the study area showing the main tectonic features (modified from Kamzi and Rana, 1982). C) Simplified geological map of the study area indicating the main formations and the studied section (modified from Afridi, 2010, and Latif, 1970).

The Cretaceous/Cenozoic boundary is marked by bauxite and lateritic palaeosols overlain by the Lower Paleocene (Danian) Hangu Formation consisting sandstones and coal-rich layers (Ahsan and Chaudhry, 2008; Umar et al., 2015; Saboor et al., 2021). The Hangu Formation is conformably overlain by the shallow-water limestones of the Thanetian Lockhart Formation (Sameeni et al., 2009), which are followed in turn by the upper Thanetian to lower Ypresian shales of the Patala Formation (Umar et al., 2015). A clear turnover in LBF assemblages is recorded around the Paleocene-Eocene boundary, when typical Palaeogene LBF's such as Miscellanea and Ranikothalia were replaced by Nummulites and Alveolina (Scheibner et al., 2005; Afzal et al., 2011a). The stratigraphic

succession of the Hazara Basin continues with the lower Ypresian Margalla Hill Limestone and upper Ypresian nodular limestones of the Chorgali Formation.

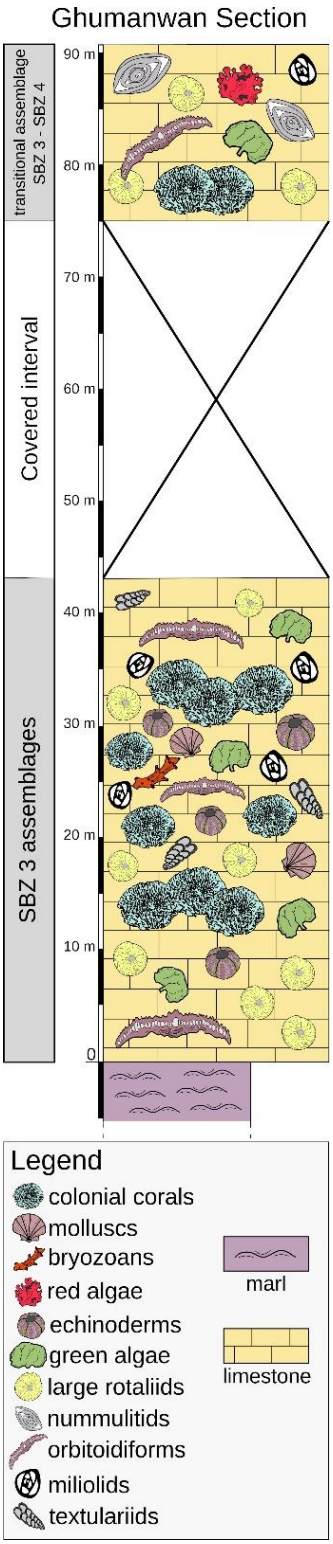

Figure 3.2: The lower part of the section, from 0 to 8 m *abs*, consists of fine-grained, fossiliferous, grayish, partially recrystallized nodular limestone with a Large Benthic Foraminifera (LBF) packstone texture. This interval also exhibits secondary vuggy and stylolite porosity. From 8 to 10 m *abs*, the section transitions to

grayish, fine-grained, less recrystallized limestone ($CaCO_3$ content 70–90%) with an LBF packstone to coral framestone texture. The interval from 10 to 25 m *abs* consists of grayish limestone with a coral framestone texture, where LBFs are less abundant. This interval also features vuggy porosity and raindrop imprints. Between 25 and 43 m *abs*, the section comprises LBF-rich nodular limestone with a packstone texture. This interval is capped by a 32 m covered interval, from 43 to 75 m abs, consisting of fine-grained, unconsolidated, and weathered soil. The topmost interval, from 75 to 90 m *abs*, consists of grayish, nodular limestone with a packstone to coral framestone texture. LBF content increases upward in this section, while coral colonies become less abundant. This interval also exhibits vuggy and stylolite porosity

The investigated Ghumanwan stratigraphic section (34°10'09.16" N; 73°16'39.73" E) is situated in the proximity of the city of Abbottabad (Northern Pakistan). Due to the lack of a detailed geological survey in this part of the Hazara Basin, this section had been previously tentatively correlated with the upper part of the Lockhart Formation (Fig. 2.1).

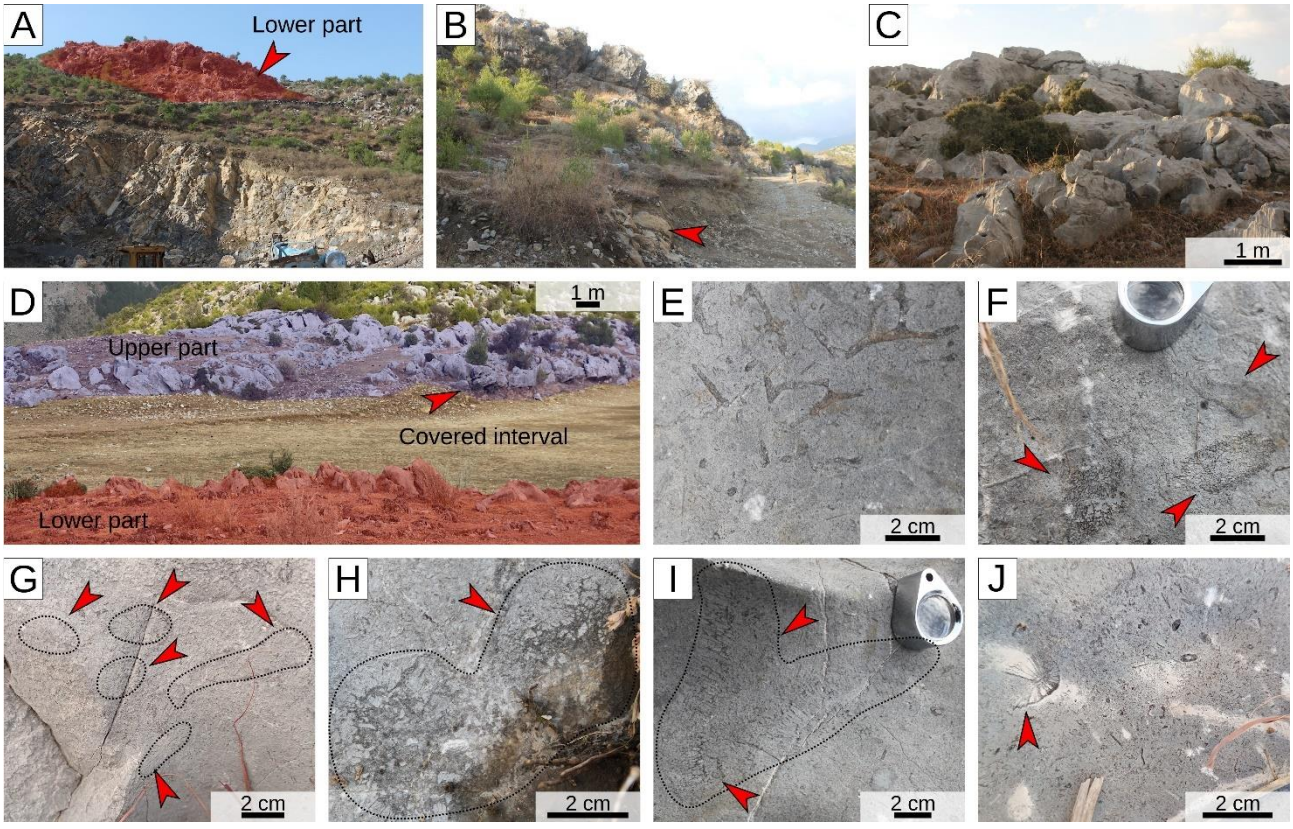

Figure 3.3: Ghumanwan Section. Lower part: A) panoramic view of the (red arrow) the red arrow also indicates the base of studied section composed of coral-dominated Limestone unit; B) close-up view (red arrowhead= limestone base, the limestone dark grayish in color, with vuggy and dissolution features); C) topmost strata. Upper part: D) panoramic view (red arrow= basal strata). E) Thin-branched ramose coral colonies. F) Thick-branched ramose coral colonies (red arrowheads= branches). G) Branching corals (red arrowhead= branches). H) Coral colony with a massive morphology (red arrowheads). I) Coral colony with

meandroid morphology (red arrowheads). J) Bioclastic material of the limestone debris (red arrowhead= coral).

3.4.Materials and methods

The Ghumanwan section was carefully measured, sampled and studied focusing on the distribution of the most relevant fossils (i.e., LBF, corals, and calcareous algae). Palaeontological and petrographic analyses were carried out on 80 thin sections at the Department of Earth and Environmental Sciences (Milano-Bicocca University; Italy). Sixty representative samples of the different lithologies were analysed by powder X-ray diffraction (XRD) at the Geopolis (University of Lausanne; Switzerland). In each of the 29 thin sections prepared from the least recrystallized samples of bioclastic limestones, more than 500 points were counted using a regular spacing of 200 μm (point counting method). Carbonate classification follows Dunham (1962), extended by Embry and Klovan (1971), and refined by Lokier and Al Junaibi (2016). All sufficiently complete and well preserved LBF were identified at the lowest possible taxonomic level and counted together with small porcelaneous, agglutinated, and hyaline benthic and planktic foraminifera (area counting method; Coletti et al., 2021b). LBF identification was performed following mainly Hottinger (2014) for rotaliids, and mainly Leppig (1988), Hottinger (2009), Leppig and Langer (2015), and subordinately other studies (e.g., Di Carlo et al., 2010; Sirel, 2018) for miscellaneids. The taxonomic analysis of LBF was based on a typological approach, whereas miscellaneids were identified at species level by biometric measurements (e.g., Benedetti et al., 2018). The LBF assemblages allowed us to provide biostratigraphic constraints following the biozonal scheme (Shallow Benthic Zones, SBZ) of Serra-Kiel et al. (1998), recently recalibrated for the Paleocene by Serra-Kiel et al. (2020) and currently adopted also in the eastern Neotethys realm (e.g., Zhang et al., 2013; Özcan et al., 2015; Kamran et al., 2021; Kakar et al., 2022).

3.5.Lithology and Biofacies

The Ghumanwan section consists of dark-greyish marls (with carbonate content ranging from 20% to 80%) overlain by partially recrystallized and slightly deformed limestone beds (carbonate content between 85% and 95%) (Figs. 3.2, 3.3). The latter are the focus of this study and can be subdivided into a lower and an upper part. The 43 m-thick lower part mainly consists of very thick beds of massive LBF packstone with patches of colonial-coral framestone (Table 3.1; Figs 3.2, 3.3). The 16-m thick upper part, exposed above a 30-m-

thick covered interval, also consists of LBF packstone beds and patches of colonial-coral framestone, but it is slightly richer in micritic matrix (Table 3.1; Figs 3.2, 3.3). The overall scarce macrofossil content of limestones is dominated by colonial corals clustered in meters-wide small patches; rare molluscs were also observed. Coral colonies are poorly preserved and mainly display ramose morphology and, more rarely, massive and meandroid morphologies (Fig. 3.3E-J).

Lower limestones

Based on point counting, these packstones are matrix-rich (mostly micrite) and their skeletal assemblage is dominated by LBF with subordinate small benthic foraminifera, green calcareous algae, echinoderms, molluscs, colonial corals, and red calcareous algae (Table 2.1; Fig. 3.4).

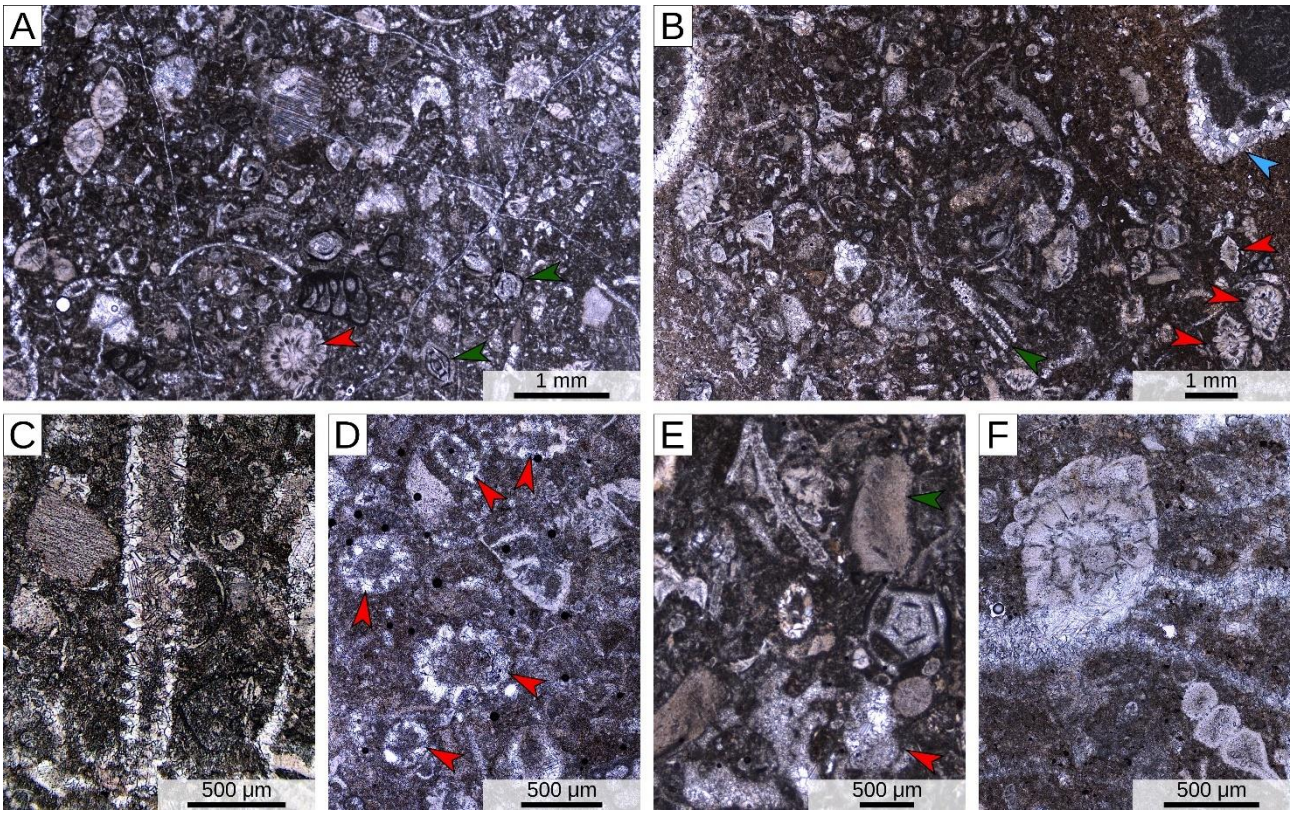

Figure 3.4: The lower LBF packstone facies. A, B) Overview (red arrows= small miscellaneid; green arrows= partially recrystallized miliolids in A and dasycladacean green calcareous alga in B; blue arrow= coral. C) Detail of a dasycladacean alga in axial section. D) Dasycladacean algae in equatorial sections (red arrows). E) Facies detail (red arrow= coral fragment; green arrow= Peyssonneliales red calcareous alga. F) Small miscellaneid.

Area counting indicates that, although volumetrically subordinated, small hyaline benthic foraminifera numerically dominate the foraminiferal assemblage together with small miscellaneids (i.e. *Miscellanea yvettae* and *M. juliettae*), and small agglutinated foraminifera. *Lockhartia* and small porcelaneous taxa are also common. *Coskinon* and orbitoidiform taxa are rare. The calcareous algal assemblage is dominated by poorly preserved and heavily recrystallized dasycladacean algae. Small fragments of Peyssonneliales and rare fragments of *Distichoplax biserialis* are also present.

Based on the abundance of micritic matrix, the meter-wide patches of coral framestone can be considered as intermediate between close-cluster and filled-frame reefs (Table 1; Riding, 2002: fig. 7). Their skeletal assemblage is dominated by ramose coral colonies associated with benthic foraminifera (mainly small hyaline and small miscellaneids, less diverse and less numerous than in the interbedded packstones), molluscs, echinoderms, rare green calcareous algae, and bryozoans (Table 1; Fig. 5). Although imperfect preservation hindered the identification of coral taxa, some of the best preserved specimens resemble the genus Bacarella. The calcareous algal assemblage consists of heavily recrystallized dasycladacean algae, associated with fragments of Peyssonelliales and rare sterile fragments of coralline algae.

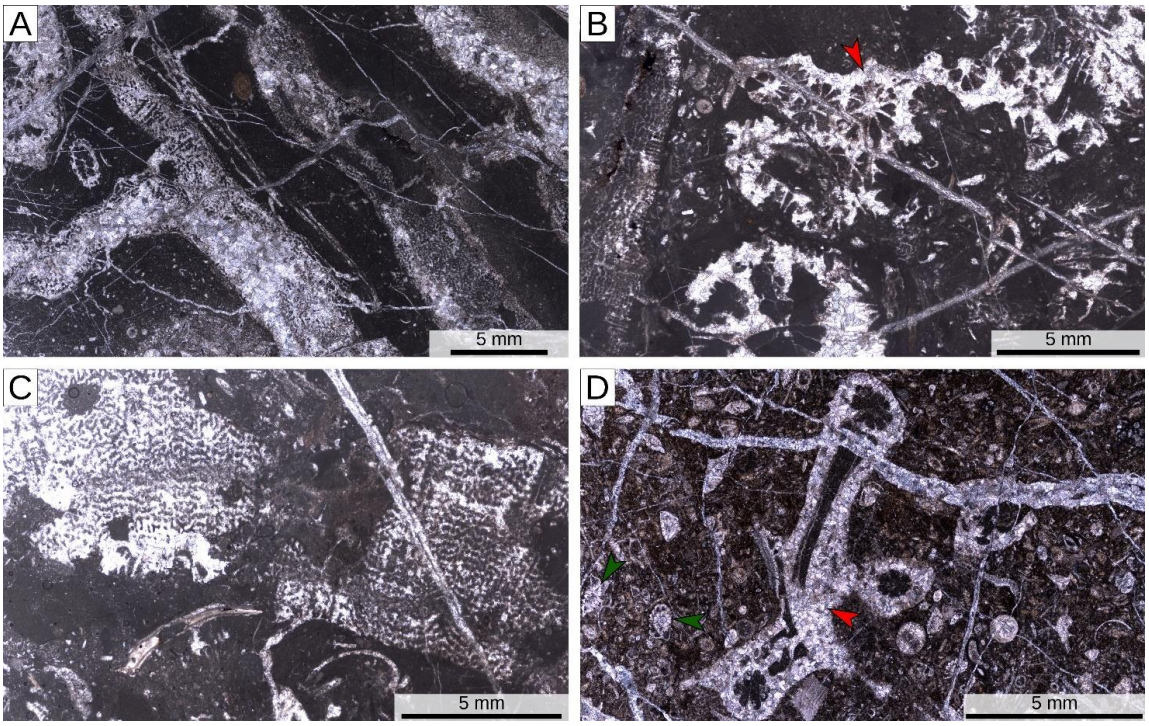

Figure 3.5: The lower coral framestone facies. A) Coral colonies. B) Various morphologies of coral colonies

(red arrow= possible Bacarella). C) Encrusting coral colony.D) Thin-branched coral colony (red arrow) and small miscellaneids (green arrows).

The overall foraminiferal assemblage of the lower limestones includes *Coskinon rajkae, Elazigina lenticula, Lakadongia primitiva, Lockhartia haimei, L. roeae, Miscellanea yvettae, M. juliettae*, and *Ranikothalia sp*. (Fig. 3.7), suggesting a Late Paleocene age (Serra Kiel et al., 1998, 2020; Afzal et al., 2011a; Kahsnitz et al., 2016; Papazzoni et al., 2017). The two small species of Miscellanea (Fig. 3.7I-K) suggest the SBZ3 zone (Selandian - early Thanetian), as for similar coeval assemblages from India (Pereira et al., 2022).

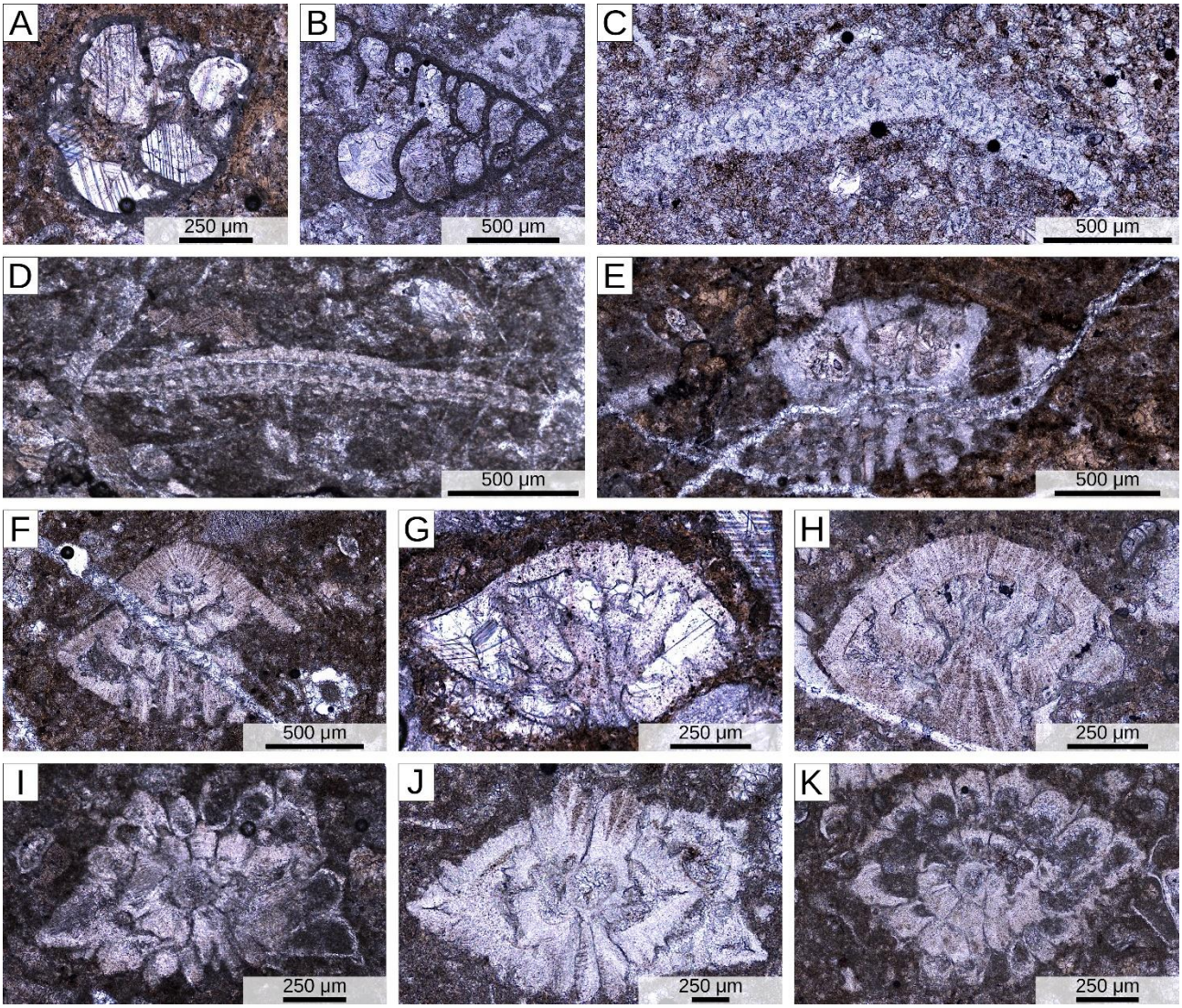

Figure 3.6: LBF assemblage of the lower part of Ghumanwan Section. A) Coskinon raijkae. B) Coskinon raijkae axial section. C) Lakadongia primitiva. D) Lakadongia sp. E) Lockhartia haimei. F) L. roeae. G) Elazigina lenticula. H) Kathina sp. I) Miscellanea yvettae, axial section. J) M. juliettae, axial section. K) M. juliettae, approximately equatorial section.

Upper limestones

Based on point counting, these packstones are dominated by LBF, associated with small benthic foraminifera and rare echinoderms, molluscs, green calcareous algae, and very rare ostracods. Based on area counting, the foraminiferal assemblage is dominated by small hyaline foraminifera, nummulitids (mainly *Operculina*), miscellaneids (mainly large morphotypes such as *Miscellanea cf. miscella*), *Lockhartia*, and other large hyaline taxa. Small miliolids, agglutinated foraminifera, and orbitoidiforms also present (Table 3.1; Fig. 3.7). The scarce calcareous algal assemblage mainly consists of poorly preserved fragments of dasycladacean algae associated with rare sterile coralline algae.

The patches of coral framestone are richer in micrite than those interbedded in the underlying limestone interval, thus displaying a closer affinity with close-cluster reefs (Riding, 2002) (Table 3.1). Although most coral specimens are poorly preserved, some thin branching colonies resemble the genus Bacarella.

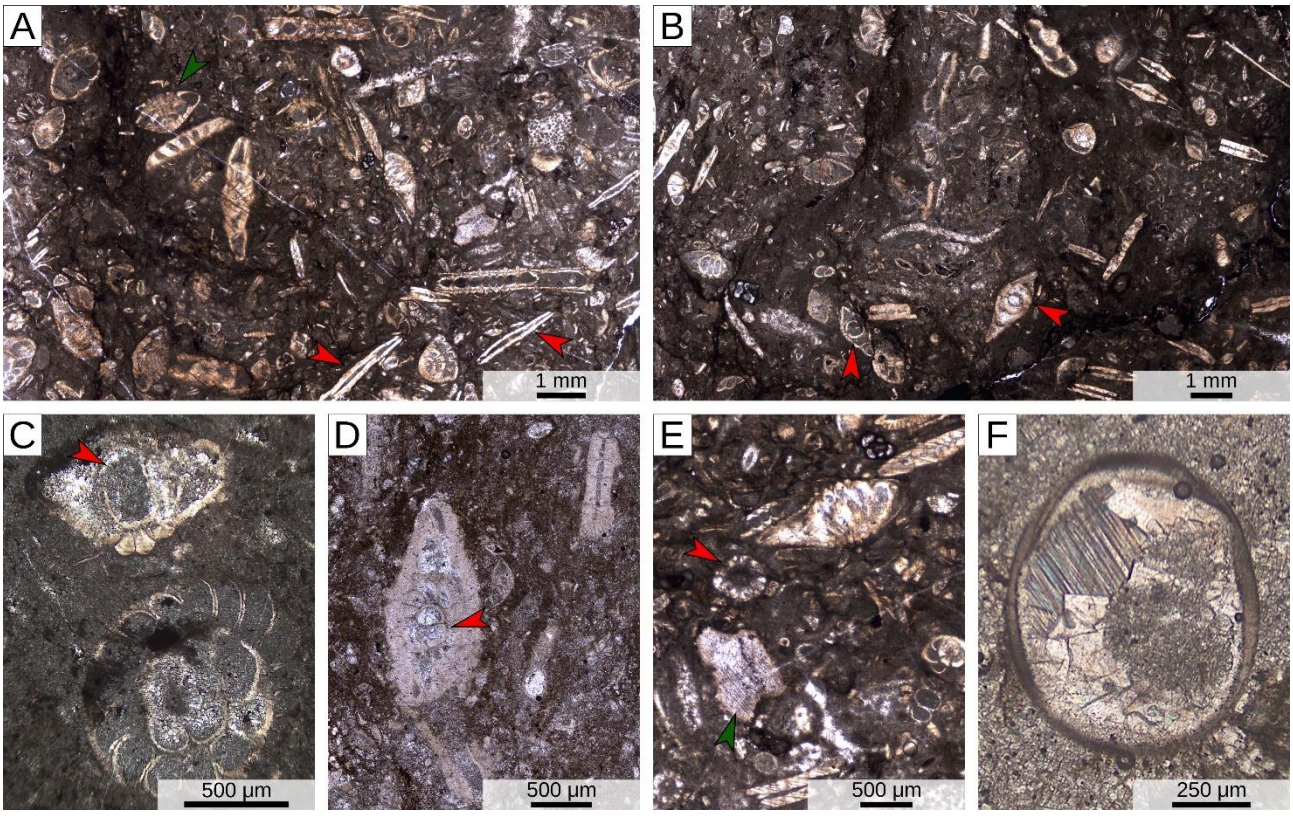

Figure 3.7: The upper LBF packstone facies. A, B) Overview (red arrows= *Operculina* in A, *Miscellanea cf. miscella* in B; green arrow= *Lockhartia*. C) *M. cf. miscella*, axial and equatorial sections of two different specimens (red arrow= large-sized protoconch). D) Section of *M. cf. miscella* crossing the embryo (red arrow). E) Fragment of dasycladacean green alga (red arrow) and echinoderm fragment (green arrow). F) Ostracod.

Colonial corals are associated with common red calcareous algae, lesser amounts of larger and small benthic foraminifera (mainly small hyaline taxa and miscellaneids), echinoderms, encrusting foraminifera, and rare bryozoans and molluscs (Table 3.1; Fig. 3.8). The calcareous algal assemblage is dominated by Peyssonelliales, associated with common coralline algae (including rare fragments characterized by uniporate conceptacles and thus affine to the order Corallinales), and common *Distichoplax biserialis*.

The overall LBF assemblage of the upper limestones includes *Coskinon sp., Daviesina sp., Idalina sp., Lakadongia sp., Lockhartia conditi, L. haimei, L. roeae, L. tipperi, Miscellanea yvettae, M. juliettae, M. cf. miscella, Orbitosiphon sp., Operculina sp., Ranikothalia sahnii,* and possibly *Assilina* (Fig. 3.9), indicating a Thanetian age (Serra Kiel et al., 1998, 2020; Afzal et al., 2011a; Kahsnitz et al., 2016; Papazzoni et al., 2017). *M. yvettae* and *M. juliettae* are generally considered as markers of SBZ3, but the occurrence of *M. miscella* identifies zone SBZ4 (Hottinger, 2009; Serra-Kiel et al., 2020; Pereira et al., 2022).

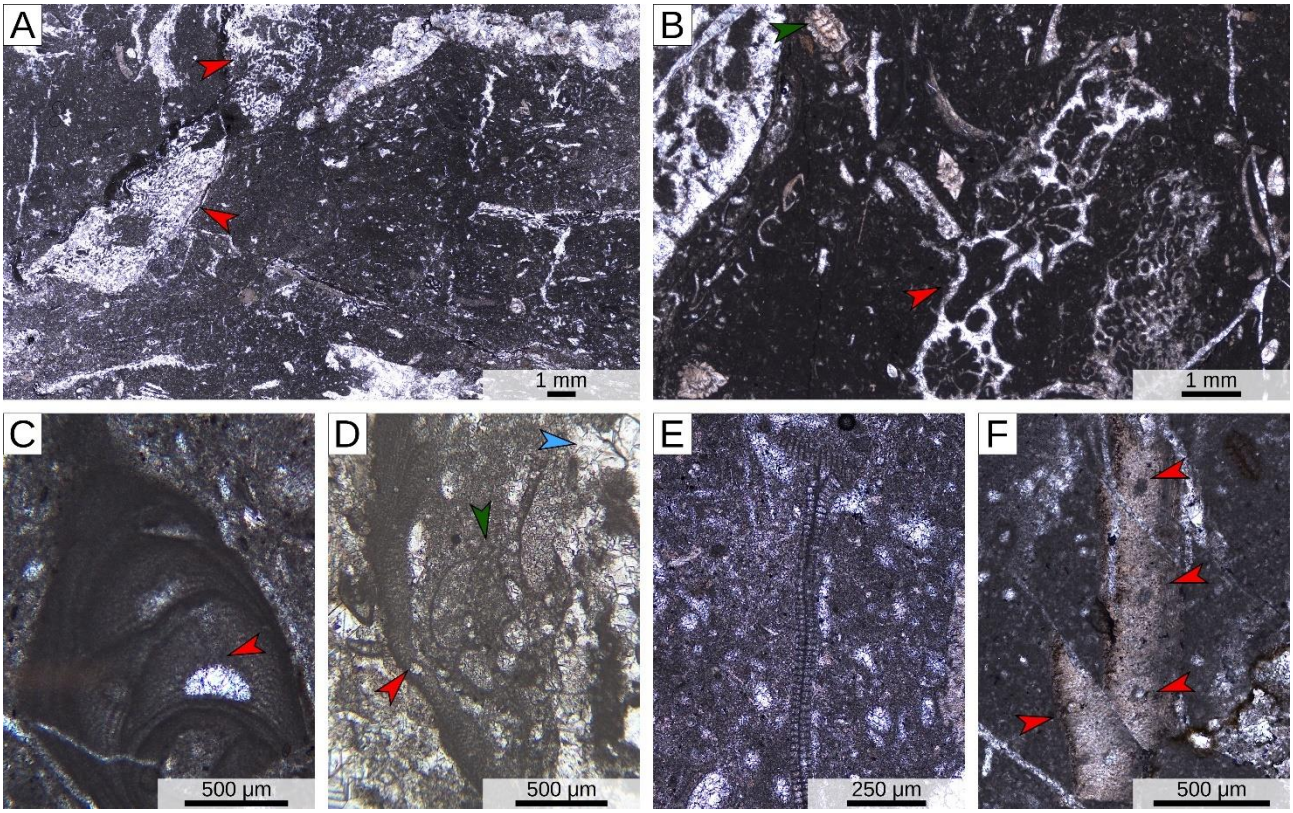

Figure 3.8: The upper coral framestone facies. A) Overview (red arrows= colonial corals in A, thin-branched coral colony (possibly *Bacarella*) in B; green arrow= miscellaneid. C) Coralline alga of the order Corallinales (red arrow= poorly preserved pore of the uniporate conceptacle). D) Encrusting coralline algae

(red arrow), encrusting foraminifera (green arrow), and coral (blue arrow). E*) Distichoplax biserialis*. F) Peyssonneliales red calcareous alga (red arrows indicate possible remnants of reproductive structures).

Although Hottinger (2009) questioned the possibility of distinguishing among the different morphotypes of M. miscella at different evolutionary stages, it must be noted that SBZs are mainly Oppelzones based on the concomitant occurrence of phylogenetically unrelated taxa (Pignatti and Papazzoni, 2017) and thus they are not linked to biohorizons or first/last occurrences of single taxa. Because our specimens differ from typical *M. miscella* by having a slightly smaller proloculus and test, they could be considered as basal representatives of the taxon. Gogoi et al. (2009) also documented the co-occurrence of both large and small miscellaneids within a short interval of the Lakadong Limestone (Meghalaya, India). The presence of *M. cf. miscella, M. yvettae* and *M. juliettae*, therefore, allows us to consider the upper limestones as transitional between SBZ3 and SBZ4 zones.

Lithology	SBZ3		Transition SBZ3 to SBZ4	
	LBF-packstone	coral framestone	LBF-packstone	coral framestone
Skeletal assemblage [point counting; %]				
Matrix	57	51.5	64.0	61.5
Clasts	43	48.5	36.0	38.5
Composition of the bioclastic fraction [point counting; %]				
CC	0.6	80.7	0.0	62.2
RCA	0.5	0.0	0.0	20.9
GCA	15.9	1.2	0.8	0.5
LBF	51.9	4.9	75.7	5.4
SBF	27.2	5.1	17.5	2.0
EBF	0.0	0.0	0.0	2.5
MOL	1.6	5.1	1.2	0.7
ECH	2.1	2.0	2.5	4.4
BRY	0.0	0.8	0.0	0.9
Others	0.2	0.1	2.2	0.4
Foraminifera assemblage [area counting; individuals cm^2]				
planktic/benthic ratio	0.014	0.019	0.007	0.025
porcellanaceous/hyaline ratio	0.055	0.060	0.034	0.049
Miscellanea	5.538	0.805	3.520	0.782
Lockhartia	1.987	0.192	2.794	0.105
Nummulitids	0.037	0.072	3.483	0.061
SBF	15.131	4.470	13.841	4.873
Total free-living benthic foraminifera	24.937	6.137	27.183	6.574

Table 3.1: Skeletal and foraminiferal assemblages in the Ghumanwan Section. CC= colonial corals; RCA= red calcareous algae; GCA= green calcareous algae; LBF= larger benthic foraminifera; SBF= small benthic foraminifera; EBF= encrusting benthic foraminifera; MOL= molluscs; ECH= echinoderms; BRY= bryozoans.

Figure 3.9: LBF assemblage of the upper part of Ghumanwan section. A) *Coskinon sp*. B) *Idalina sp*. C) *Lakadongia sp*. D) *Orbitosiphon sp*. E) *Lockhartia haimei*. F) *L. roeae*. G) *L. conditi*. H) *L. tipperi*. I) *Operculina sp*. J) *Ranikothalia sahnii* (red arrow= marginal cord). K) *Miscellanea yvettae*, axial section. L) *M. juliettae*, equatorial section. M) Fragment of *M. cf. miscella* in axial section. N) *M. cf. miscella*, axial section. O) *M. cf. miscella*, equatorial section.

3.6.Discussion

Palaeoenvironmental evolution

In the studied Ghumanwan succession, LBF packstones are intercalated with patches of coral framestone, pointing to a relatively flat shallow seafloor with flourishing foraminiferal carbonate production interspersed with coral-dominated patch reefs. This type of setting has been envisaged for similar reefs of the Neotethys at different times (e.g., Paleocene of Lybia, Vršič et al., 2021; Early Miocene of SE Cyprus; Follows et al., 1996; Coletti et al., 2021a: fig. 16). The presence of red and green calcareous algae, colonial corals, and LBF (Table 3.1; Figs. 4-9) indicates a placement within the photic zone. Small miscellaneids, which are widespread in all the facies of the Ghumanwan section, have been related to reef environments and suggested to be typical of shallow to intermediate water depth (Zamagni et al., 2008; Pereira et al., 2022). A shallow setting is also independently indicated by the scarcity of planktonic foraminifera (Van Der Zwaan et al., 1990). The overall abundance of micrite reflects instead the limited hydrodynamic energy of the environment.

In the coral framestones belonging to the lower limestone interval, calcareous algae are scarce (< 2% of the skeletal assemblage) and do not provide much information. The presence of common dasycladacean green calcareous algae in the LBF packstones of the lower interval suggests a placement close or within the upper part of photic zone (euphotic zone sensu Pomar, 2001).

In the coral framestones belonging to the upper limestone interval, the more abundant calcareous algal assemblage (20% of the total skeletal assemblage) (Table 3.1) is dominated by Peyssonnelliales and *Distichoplax biserialis* and includes some minor fragments of red algae of the order Corallinales. The latter would suggest a relatively shallow water setting (Aguirre et al., 2000; Coletti et al., 2018; Coletti & Basso, 2020). However, the assemblage is dominated by Peyssonnelliales and *Distichoplax biserialis*. Peyssonelliales are a still-living order of red calcareous algae, but the observed taxa of the Ghumanwan section display morphological features wildly different from their modern relatives (Kato et al., 2006; Pestana et al., 2021), which thus cannot provide us with useful ecological information. Distichoplax biserialis has no direct living relatives, but it resembles Corallinales (Sarkar, 2018; Aguirre et al., 2022), thus pointing towards a relatively shallow-water setting. The

upper LBF packstones are instead characterized by a scarce calcareous algal assemblage mostly consisting of dasycladacean algae.

The comparison of the assemblages of the lower and upper limestones does not suggest significant changes in water depth throughout the succession (Table 3.1). More abundant micrite, more nummulitids (e.g., *Operculina*), and less colonial corals and dasycladacean algae may hint a slightly deeper environment for the upper part of the Ghumanwan section. However, these minor changes are not coupled with other relevant palaeo-bathymetric indicators such as a significant increase in planktic foraminifera or a decrease in miliolids.

Upper Paleocene shallow-water carbonates of eastern Neotethys

Coral-framestones display significant differences between the lower (SBZ3) and upper part (SBZ3/SBZ4) of the studied Ghumanwan section (Table 3.1; Figs. 3.4-5, 3.7-8). Micrite and red calcareous algae (in particular Distichoplax biserialis) are more abundant in the upper part, where colonial corals become less abundant. LBF-packstones also display differences: micrite and LBF are more abundant in the upper part whereas dasycladacean algae are less abundant.

Similar variations are observed in Upper Paleocene to Lower Eocene successions of both eastern and western Neotethys. Upper Paleocene shallow-water carbonates are well represented in northwestern India (Meghalaya area; Jauhri et al., 2006; Sarma and Gosh, 2006; Özcan et al., 2018; Sarkar, 2018, 2020; Sarkar and Rao, 2018; Pereira et al., 2022), where they are rich in calcareous algae and LBF; colonial corals also occur, but significantly less abundant than in the Hazara Basin (Sarma and Gosh, 2006; Jauhri et al., 2006; Sarkar and Rao, 2018). Such a scarcity of corals may be related to the excessively high temperatures envisaged by palaeoceanographic models for the eastern Indian part of eastern Neotethys during the late Thanetian (Sarkar et al., 2022). Similarly to the Ghumanwan section, a remarkable abundance of *Distichoplax biserialis* is reported in the upper Thanetian (Özcan et al., 2018; Sarkar, 2018; Pereira et al., 2022). In the northeastern Indian area the abundance of this species decreases significantly in the overlying Lower Eocene carbonates (Sarkar, 2018). Common to both Indian area and the Hazara Basin is also the upwards decrease of dasycladacean algae.

In the Tibetan Himalayas, upper Paleocene shallow-water carbonates are generally dominated by LBF with minor dasycladacean and red calcareous algae; colonial corals rarely occur and no coral-dominated facies is reported (Zhang et al., 2013, 2019; Li et al., 2015, 2017, 2022; Jiang et al., 2021). In the overlying Lower Eocene carbonates, corals, red and green calcareous algae decrease, whereas LBF increase (Li et al., 2015, 2017, 2020, 2022). Similarly to the Ghumanwan Section, a peak in the abundance of Distichoplax biserialis is reported in the uppermost Paleocene (Jiang et al., 2021).

In Upper Paleocene shallow-water carbonates of Pakistan and Iran, colonial corals are more abundant than in the Himalayas (Afzal et al., 2011b; Bagherpour and Vaziri,2012; Kamran et al,,2021; Shalalvand et al., 2021). Close similarities are observed between the Ghumanwan section and the Taleh Zang Formation in western Iran (Bagherpour and Vaziri, 2012; Shalalvand et al., 2021). Here, the lower Thanetian part of the Taleh Zang Formation is dominated by colonial corals and dasycladacean algae (Bagherpour and Vaziri, 2012 Shalalvand et al., 2021) whereas the upper Thanetian part of the Taleh Zang Formation records a decrease in colonial corals and an increase in LBF (Bagherpour and Vaziri, 2012 Shalalvand et al., 2021). The overlying Lower Eocene shallow-water carbonates are eventually dominated by LBF (Bagherpour and Vaziri, 2012; Shalalvand et al., 2021).

Throughout the eastern Neotethys realm, quantitative analysis of carbonate facies distribution indicates that colonial corals, red calcareous algae, and green calcareous algae are more common in Paleocene carbonates than in Eocene carbonates (Coletti et al., 2022).

Upper Paleocene shallow-water carbonates of western Neotethys

The Late Paleocene – Early Eocene decline in colonial corals and the concurrent rise of LBF is documented also in the western Neotethys (Baceta et al., 2005; Scheibner and Speijer, 2008; Zamagni et al., 2008, 2012; Pomar et al., 2017). This is well detailed in the Pyrenees (Table 3.2). Colonial corals are dominant in Danian strata, decrease progressively through the early and middle Thanetian and sharply in the late Thanetian (Baceta et al., 2005). Similarly to the Ghumanwan Section, an increase of the micrite content in coral-dominated bioconstructions can be observed moving from the Early to the Late Paleocene (Table 3.2). Finally, the peak in the abundance of *Distichoplax biserialis* is once again observed in the uppermost Paleocene (Li et al., 2022; Aguirre et al., 2022). An increase in the micrite content

of coral-bearing carbonate systems was reported also by Zamagni et al. (2008), while comparing lower and upper Thanetian carbonate systems of Slovenia.

Site	Pyrenean Basin Bz-2	Pyrenean Basin Lizarraga pass	Pyrenean Basin Leg-2	Hazara Basin	Hazara Basin
Age	Early-middle Danian	Late Danian	Thanetian	Thanetian	Late Thanetian
	~ 63 Ma	~ 63 - 61 Ma	~ 59 - 57 Ma	~ 59 – 57.5 Ma	~ 57.5 – 57 Ma
SBZ	SBZ1 - SBZ2	SBZ1 - SBZ2	SBZ3 - SBZ4	SBZ3	SBZ3 to SBZ4
Reference	Baceta et al., 2005	Baceta et al., 2005	Baceta et al., 2005	This work	This work
Characteristics and frame builders					
Matrix	~ 1/2 - 3/4	~ 1/2 - 3/4	~ 4/5 - 2/3	~1/2	~2/3
Grains	~ 1/4 - 1/2	~ 1/4 - 1/2	~ 1/5 - 1/3	~1/2	~1/3
Type of matrix	Sand-sized bioclastic	Sand-sized bioclastic	Micrite	Micrite	Micrite
Non skeletal grains	Absent – very rare	Absent – very rare	Absent	Absent	Absent – very rare
Main frame builders	CC & RCA	CC & RCA	CC & RCA	CC	CC
Secondary frame builders	EBF	EBF	//	//	RCA
Skeletal assemblage					
CC	Abundant	Abundant	Common	Dominant (80.7)	Dominant (62.2)
RCA	Abundant	Abundant	Common	Absent (0.0)	Common (20.9)
GCA	Rare	Rare	Rare	Rare (1.2)	Very-rare (0.5)
LBF	Absent	Absent	Common	Scarce (4.9)	Scarce (5.4)
SBF	Common	Scarce	Common	Scarce (5.1)	Rare (2.0)
EBF	Scarce	Scarce	Scarce	Absent (0.0)	Rare (2.5)
MOL	Rare	Scarce	Scarce	Scarce (5.1)	Very-rare (0.7)
ECH	Rare	Scarce	Rare	Rare (2.0)	Rare (4.4)
BRY	Scarce	Scarce	Common	Very-rare (0.8)	Very-rare (0.9)
Others	Rare	Rare	Rare	Very-rare (0.1)	Very-rare (0.4)
Planktic vs benthic	Entirely benthic	Entirely benthic	Entirely benthic	Entirely benthic	Entirely benthic
Dominant benthic taxa	Small and large hyaline taxa including miscellanids	Small and large hyaline taxa including miscellanids	Large hyaline taxa including nummulitids, mescellanids and orthophragminids and small hyaline taxa	Small hyaline taxa, small agglutinated taxa, miscellanids	Small hyaline taxa, miscellanids

Table 3.2: Comparison of coral framestones in the Ghumanwan section and coeval coral reefs of the Pyrenees (Baceta et al., 2005). The relative abundance of diverse components is given using a modified version of the scale proposed by Carey et al. (1995): 0% = absent; 1% > very rare > 0%; 5% > rare > 1%; 10% > scarce > 5%; 25% > common > 10%; 50% > abundant > 25%; dominant > 50%.

Response of carbonate producers to Late Paleocene environmental perturbations

Based on the comparison of carbonate successions from the eastern and western Neotethys, facies changes observed through the Upper Paleocene in the Ghumanwan section are inferred to herald the more prominent shifts that took place during the Paleocene–Eocene transition. Although the PETM is considered one of the most relevant environmental events

of the Cenozoic, the Late Paleocene warming trend and the Late Paleocene hyperthermals are also bound to have caused significant changes in marine ecosystems (long-term Late Paleocene perturbation; Bowen et al., 2015; Barnet et al., 2019; Banerjee et al., 2020; Jiang et al., 2022; Tremblin et al., 2022; Vimpere et al., 2023).

The decline of colonial corals as carbonate producers during the Late Paleocene – Early Eocene interval has been pointed out by several authors (Baceta et al., 2005; Scheibner and Speijer, 2008; Zamagni et al., 2008, 2012; Pomar et al., 2017), and ascribed by Scheibner and Speijer (2008) and Coletti et al. (2022) to the coeval increase in global temperatures (Bowen et al., 2015; Barnet et al., 2019; Tremblin et al., 2022; Vimpere et al., 2023). Modern colonial corals achieve the highest calcification rates within a narrower temperature range than modern LBF (Crabbe, 2008; Marshall and Clode, 2004; Titelboim et al., 2019). Therefore, the highly adaptable LBF could take competitive advantage from the detrimental effect that high temperatures had on other carbonate producers such as hermatypic corals. Major variations in ocean chemistry were also associated with the PETM (McInerney and Wing, 2011; Jiang et al., 2021; Li et al., 2021), stemming from temperature-induced acceleration of the hydrological cycle, enhanced weathering of continental landmasses, and acidification of oceanic waters caused by the higher CO2 concentration in the atmosphere (McInerney and Wing, 2011; Sternai et al., 2020; Jiang et al., 2021; Li et al., 2021). These changes in ocean chemistry represent another plausible cause of the decline of corals during the Late Paleocene – Early Eocene (Zamagni et al., 2012). LBF could have been favored by their greater tolerance to variations in ocean chemistry, and in particular to changes in the supply rate of nutrients (Pomar et al., 2017), and consequently became dominant in the Eocene. Our work shows that the decline of colonial corals as carbonate producers pre-dated the PETM in northern Pakistan, in western Iran, and in the Pyrenees, and thus could be chiefly related to the increase of global temperatures. This is also supported by the distribution of colonial corals along Neotethys margins during the Late Paleocene, when they were rare in the warmer eastern Indian region and increasingly common moving westward and northward towards cooler temperatures (Sarkar et al., 2022). Further researches are however needed to disentangle the complex relationships between diversity, morphology, colony-size and reef-building potential of corals and global warming events (e.g., Johnson et al., 2008; Bosellini et al., 2022), especially in the case of rapid events like the Paleogene hyperthermals.

The observed increase in the abundance of red calcareous algae, largely accounted for by the notable increase of *Distichoplax biserialis* from zone SBZ3 to zone SBZ4 followed by a rapid decline (Sarkar, 2018; Li et al., 2021), is harder to explain. Red algae are more tolerant than colonial corals and are known to be able to outcompete colonial corals at tropical latitudes in non-oligotrophic settings (Halfar et al., 2004; Halfar and Mutti, 2005; Coletti et al., 2017; Pomar et al., 2017). The increase in red calcareous algae may thus be ascribed to an increase in nutrient availability caused by Late Paleocene environmental changes culminating with the PETM. Other explanations are also possible. For instance, coralline algae and other encrusting carbonate producers (e.g., encrusting benthic foraminifera, bryozoans) have been observed to increase in abundance following the deterioration of an environment initially favorable to colonial corals (e.g., upper Oligocene/lower Miocene reefs largely dominated by corals and developed in stable and warm conditions vs. upper Miocene reefs developed in cooler and more stressful conditions and characterized by a variety of encrusting organisms; Bosellini, 2006; Coletti et al., 2019, 2021a). An increase in water depth can also cause a shift from colonial corals to red calcareous algae dominated facies (Benisek et al., 2009). These elements suggest that there could be various mechanisms behind an increase in red calcareous algae abundance. Further studies focused on the quantitative distribution of red calcareous algae and *D. biserialis* in particular, might shed light on the effects of Late Paleocene environmental perturbations on this group of carbonate producers.

Similarly to colonial corals, dasycladacean green calcareous algae also decreased during the Late Paleocene. Present-day dasycladaceans thrive in restricted and warm lagoonal environments (e.g., Ohba et al., 2017). Therefore, Late Paleocene warming may not have been the cause of their decline. The coeval decline and extinction of most taxa supposedly able to produce a calcitic skeleton suggest that the decline of Dasycladales may be partly related to a preservation bias during the transition towards modern assemblages entirely constituted of fragile aragonitic taxa (Granier, 2012; Coletti et al., 2022). Once again, quantitative data on the abundance of carbonate-producing organisms (e.g., Bosellini, 1998; Vescogni et al., 2008, 2016; Bosellini et al., 2021; Benedetti and Papazzoni, 2022), generated with a standardized approach, appears to be essential for making more cogent comparisons and improve our knowledge about the response of shallow-water biota to rising temperatures.

3.7.Conclusions

The so far poorly investigated succession of the Hazara Basin (Pakistan) provides an excellent setting in which to document the initial response of benthic calcifiers to global warming during the Thanetian (Late Paleocene). The quantitative sedimentological and micropaleontological analysis of the Ghumanwan section reveals that this carbonate system underwent significant changes in the Late Paleocene, just before the onset of the Paleocene-Eocene Thermal Maximum event (PETM). Colonial corals and green calcareous algae progressively declined, whereas larger benthic foraminifera, red calcareous algae (in particular *Distichoplax biserialis*) became more abundant. The decline of colonial corals and green calcareous algae continued after the PETM, when the more adaptable larger benthic foraminifera emerged as the most significant shelfal carbonate producers. Coral bioconstructions did not become a widespread feature of carbonate systems until the Oligocene. Similar patterns are recognized in both eastern and western parts of the Neotethys realm, hinting that the Late Paleocene changes might be chiefly associated with global warming that culminated in the PETM. While the concurrent decline of symbiont-bearing colonial corals and rise in larger benthic foraminifera can be associated with a reasonably clear and plausible explanation, the distribution pattern of calcareous algae is harder to explain, stressing the need for more quantitative data, generated with a standardized approach, for better constraining the response of shallow-water biota to large scale environmental changes.

3.8.References

Abbasi, I.A., Haneef, M., Obaid, S., Daud, F., Qureshi, A.W., 2012. The Mesozoic deltaic system along the western margin of the Indian plate: lithofacies and depositional setting of Datta Formation, North Pakistan. Arabian Journal of Geosciences 5(3), 471-480.

Afridi, A.G.K., 2010. Revalidation of Geological Map of Nathiagali Quadrangle, Abbottabad and Mansehra District, Khyber Pakhtunkhwa and Parts of Rawalpindi and Muzafarabad Districts, Pakistan Geological Survey of Pakistan; Ministry of Petroleum and Natural Research: Islamabad, Pakistan. Lahore Geol Map Ser 3, 9.

Afzal, J., Williams, M., Leng, M. J., Aldridge, R. J., & Stephenson, M. H. (2011)a. Evolution of Paleocene to Early Eocene larger benthic foraminifer assemblages of the Indus Basin, Pakistan. Lethaia, 44(3), 299-320.

Afzal, J., Williams, M., Leng, M. J., Aldridge, R.J., 2011b. Dynamic response of the shallow marine benthic ecosystem to regional and pan-Tethyan environmental change at the

Paleocene–Eocene boundary. Palaeogeography, Palaeoclimatology, Palaeoecology, 309(3-4), 141-160.

Aguilera, O., Bencomo, K., de Araújo, O.M.O., Dias, B.B., Coletti, G., Lima, D., Silane, A.F., Polk, M., Alves-Martin, M.V., Jaramillo, C., Kutter, V.T., Lopes, R.T., 2020. Miocene heterozoan carbonate systems from the western Atlantic equatorial margin in South America: the Pirabas formation. Sedimentary Geology 407, 1-28.

Aguirre, J., Riding, R., & Braga, J. C. (2000). Late Cretaceous incident light reduction: evidence from benthic algae. Lethaia, 33(3), 205-213.

Aguirre, J., Baceta, J. I., & Braga, J. C. (2022). Coralline Algae at the Paleocene/Eocene Thermal Maximum in the Southern Pyrenees (N Spain). Frontiers in Marine Science, 9, 899877.

Ahsan, N., Chaudhry, M.N., 2008. Geology of Hettangian to middle Eocene rocks of Hazara and Kashmir basins, Northwest lesser Himalayas, Pakistan. Geological Bulletin of the Punjab University 43, 131-152.

Ahsan, N., 2008. Facies modeling, depositional and diagenetic environments of Kawagarh Formation, Hazara Basin, Pakistan. Unpublished Ph.D. thesis, University of the Punjab, Lahore, Pakistan.

Baceta, J.I., Victoriano, P., Bernaola, G., 2005. Paleocene coralgal reefs of the western Pyrenean basin, northern Spain: New evidence supporting an earliest Paleogene recovery of reefal ecosystems. Palaeogeography, Palaeoclimatology, Palaeoecology 224(1-3), 117-143.

Bagherpour, B., & Vaziri, M. R. (2012). Facies, paleoenvironment, carbonate platform and facies changes across Paleocene Eocene of the Taleh Zang Formation in the Zagros Basin, SW-Iran. Historical Biology, 24(2), 121-142.

Banerjee, S., Choudhury, T. R., Saraswati, P. K., & Khanolkar, S. (2020). The formation of authigenic deposits during Paleogene warm climatic intervals: a review. Journal of Palaeogeography, 9(1), 1-27.

Barnet, J.S.K., Littler, K., Westerhold, T., Kroon, D., Leng, M.J., Bailey, I., Röhl, U., Zachos, J.C., 2019. A high-Fidelity benthic stable isotope record of late Cretaceous–early Eocene climate change and carbon-cycling. Paleoceanography and Paleoclimatology 34(4), 672-691.

Benedetti, A., Marino, M., Pichezzi, R.M., 2018. Paleocene to Lower Eocene larger foraminiferal assemblages from Central Italy: new remarks on biostratigraphy. Rivista Italiana di Paleontologia e Stratigrafia 124, 73–90.

Benedetti, A., Papazzoni, C.A., 2022. Rise and fall of rotaliid foraminifera across the Paleocene and Eocene times. Micropaleontology 68(2), 185-196.

Benisek, M. F., Betzler, C., Marcano, G., & Mutti, M. (2009). Coralline-algal assemblages of a Burdigalian platform slope: implications for carbonate platform reconstruction (northern Sardinia, western Mediterranean Sea). Facies, 55, 375-386.

Bialik, O.M., Coletti, G., Mariani, L. et al. Availability and type of energy regulate the global distribution of neritic carbonates. Sci Rep 13, 19687 (2023). https://doi.org/10.1038/s41598-023-47029-4

Bosellini, F.R., 1998. Diversity, composition and structure of Late Eocene shelf-edge coral associations (Nago Limestone, Northern Italy). Facies 39(1), 203-225.

Bosellini, F.R., 2006. Biotic changes and their control on Oligocene-Miocene reefs: A case study from the Apulia Platform margin (southern Italy). Palaeogeography, Palaeoclimatology, Palaeoecology 241(3-4), 393-409.

Bosellini, F.R., Perrin, C., 2008. Estimating Mediterranean Oligocene–Miocene sea-surface temperatures: an approach based on coral taxonomic richness. Palaeogeography, Palaeoclimatology, Palaeoecology 258(1-2), 71-88.

Bosellini, F.R., Vescogni, A., Budd, A.F., Papazzoni, C.A., 2021. High coral diversity is coupled with reef-building capacity during the Late Oligocene Warming Event (Castro Limestone, Salento Peninsula, S Italy). Rivista Italiana di Paleontologia e Stratigrafia 127(3), 515-538.

Bosellini, F.R., Benedetti, A., Budd, A.F., Papazzoni, C.A., 2022. A Coral Hotspot from a Hot past: The EECO and Post-EECO rich reef coral fauna from Friuli (Eocene, NE Italy), Palaeogeography, Palaeoclimatolology, Palaeoecology 607, 111284.

Bossart, P., Dietrich, D., Greco, A., Ottiger, R., Ramsay, J.G., 1988. The tectonic structure of the Hazara-Kashmir syntaxis, southern Himalayas, Pakistan. Tectonics 7(2), 273-297.

Bowen, G.J., Maibauer, B.J., Kraus, M., Röhl, U., Westerhold, T., Steimke, A., Gingerich, P.D., Wing, S.L., Clyde, W.C., 2015. Two massive, rapid releases of carbon during the onset of the Paleocene-Eocene thermal maximum. Nature Geoscience 8(1), 44–47.

Butt, A.A., 1972. Problems of stratigraphic nomenclature in the Hazara District, NWFP, Pakistan. Geological Bulletin of the Punjab University 9, 65-69.

Carey, J.S., Moslow, T.F., Barrie, J.V., 1995. Origin and distribution of Holocene temperate carbonates, Hecate Strait, western Canada continental shelf. Journal of Sedimentary Research, 65(1a), 185-194.

Coletti, G., & Basso, D. (2020). Coralline algae as depth indicators in the Miocene carbonates of the Eratosthenes Seamount (ODP Leg 160, Hole 966F). Geobios, 60, 29-46.

Coletti, G., El Kateb, A., Basso, D., Cavallo, A., Spezzaferri, S., 2017. Nutrient influence on fossil carbonate factories: Evidence from SEDEX extractions on Burdigalian limestones (Miocene, NW Italy and S France). Palaeogeography, Palaeoclimatology, Palaeoecology, 475, 80-92.

Coletti, G., Basso, D., Betzler, C., Robertson, A.H., Bosio, G., El Kateb, A., Foubert, A., Meilijson A., Spezzaferri, S., 2019. Environmental evolution and geological significance of the Miocene carbonates of the Eratosthenes Seamount (ODP Leg 160). Palaeogeography, Palaeoclimatology, Palaeoecology, 530, 217-235.

Coletti, G., Basso, D., & Corselli, C. (2018). Coralline algae as depth indicators in the Sommières Basin (early Miocene, Southern France). Geobios, 51(1), 15-30.

Coletti, G., Balmer, E.M., Bialik, O.M., Cannings, T., Kroon, D., Robertson, A.H., Basso, D., 2021a. Microfacies evidence for the evolution of Miocene coral-reef environments in Cyprus. Palaeogeography, Palaeoclimatology, Palaeoecology 584, 110670.

Coletti, G., Mariani, L., Garzanti, E., Consani, S., Bosio, G., Vezzoli, G., Hu, X., Basso, D., 2021b. Skeletal assemblages and terrigenous input in the Eocene carbonate systems of the Nummulitic Limestone (NW Europe). Sedimentary Geology 425, 106005.

Coletti, G., Commissario, L., Mariani, L., Bosio, G., Desbiolles, F., Soldi, M., Bialik, O.M., 2022. Paleocene to Miocene southern Tethyan carbonate factories: A meta-analysis of the successions of South-western and Western Central Asia. The Depositional Record 8(3), 1031-1054.

Cornacchia, I., Brandano, M., Agostini, S., 2021. Miocene paleoceanographic evolution of the Mediterranean area and carbonate production changes: A review. Earth-Science Reviews 221, 103785.

Crabbe, M.J.C., 2008. Climate change, global warming and coral reefs: modelling the effects of temperature. Computational Biology and Chemistry 32(5), 311–¬314.

Critelli, S., Garzanti, E., 1994. Provenance of the lower Tertiary Murree redbeds (Hazara-Kashmir Syntaxis, Pakistan) and initial rising of the Himalayas. Sedimentary Geology 89(3-4), 265-284.

Di Carlo, M., Accordi, G., Carbone, F., Pignatti, J., 2010. Biostratigraphic analysis of Paleogene lowstand wedge conglomerates of a tectonically active platform margin (Zakynthos Islands, Greece). Journal of Mediterranean Earth Sciences 2, 31-92.

DiPietro, J.A., Pogue, K.R., 2004. Tectonostratigraphic subdivisions of the Himalaya: A view from the west. Tectonics, 23(5), 1-20.

Dunham, R.J., 1962. Classification of carbonate rocks according to depositional textures. In: Ham, W.E., (Ed.) Classification of carbonate rocks. Memoir of American Association of Petroleum Geologists 1, 108-121.

Embry, A.F., Klovan, J.E., 1971. A late Devonian reef tract on northeastern Banks Island, NWT. Bulletin of Canadian Petroleum Geology 19(4), 730-781.

Esteban, M., 1996. An overview of Miocene reefs from Mediterranean areas: general trends and facies models. In: Franseen, E.K., Esteban, M., Ward, W.C., Rouchy, J.M. (Eds.), Models for carbonate stratigraphy, from Miocene reef complex of the Mediterranean area. Concepts in Sedimentology and Paleontology 5. Tulsa, Oklahoma: Society for Sedimentary Geology, pp. 3-53.

Follows, E.J., Robertson, A.H.F., Scoffin, T.P., 1996. Tectonic control on Miocene reefs and related carbonate facies in Cyprus. In: Franseen, E.K., Esteban, M., Ward, W.C., Rouchy, J.M. (Eds.), Models for Carbonate Stratigraphy, from Miocene Reef Complex of the Mediterranean Area. Concepts in Sedimentology and Paleontology, 5. Society for Sedimentary Geology, Tulsa, Oklahoma, U.S.A, 295–315.

Garzanti, E., Baud, A., Mascle, G., 1987. Sedimentary record of the northward flight of India and its collision with Eurasia (Ladakh Himalaya, India). Geodinamica Acta 1(4-5), 297-312.

Gogoi, B., Deka Kalita, K., Garg, R., Borgohain, R., 2009. Foraminiferal biostratigraphy and palaeoenvironment of the Lakadong Limestone of the Mawsynram area, South Shillong Plateau, Meghalaya. Journal of the Palaeontological Society of India 54(2), 209.

Granier, B., 2012. The contribution of calcareous green algae to the production of limestones: a review. Geodiversitas 34(1), 35-60.

Halfar, J., Godinez-Orta, L., Mutti, M., Valdez-Holguìn, J.E., Borges, J.M., 2004. Nutrient and temperature controls on modern carbonate production: an example from the Gulf of California, Mexico. Geology 32, 213–216.

Halfar, J., Mutti, M., 2005. Global dominance of coralline red-algal facies: a response to Miocene oceanographic events. Geology 33(6), 481-484.

Hottinger, L., 2009. The Paleocene and earliest Eocene foraminiferal Family Miscellaneidae: neither nummulitids nor rotaliids. Carnets de Géologie/Notebooks on Geology, Article 2009/6 (CG2009_A06).

Hottinger, L., 2014. Paleogene larger Rotaliid Foraminifera from the Western and Central Neotethys. Springer Cham, 191.

Hu, X., Garzanti, E., Wang, J., Huang, W., An, W., Webb, A., 2016. The timing of India-Asia collision onset–Facts, theories, controversies. Earth-Science Reviews 160, 264-299.

Jauhri, A. K., Misra, P. K., Kishore, S., & Singh, S. K. (2006). Larger foraminiferal and calcareous algal facies in the Lakadong Formation of the South Shillong Plateau, NE India. Journal of the Palaeontological Society of India, 51(2), 51-61.

Jiang, J., Hu, X., Li, J., BouDagher-Fadel, M., Garzanti, E., 2021. Discovery of the Paleocene-Eocene Thermal Maximum in shallow-marine sediments of the Xigaze forearc basin, Tibet: A record of enhanced extreme precipitation and siliciclastic sediment flux. Palaeogeography, Palaeoclimatology, Palaeoecology 562, 110095.

Jiang, J., Hu, X., Garzanti, E., Li, J., BouDagher-Fadel, M. K., Sun, G., Xu, Y., 2022. Enhanced storm-induced turbiditic events during early Paleogene hyperthermals (Arabian continental margin, SW Iran). Global and Planetary Change 214, 103832.

Johnson, K.G., Jackson, J.B., Budd, A.F., 2008. Caribbean reef development was independent of coral diversity over 28 million years. Science 319(5869), 1521-1523.

Kahsnitz, M.M., Zhang, Q., Willems, H.,2016. Stratigraphic distribution of the larger benthic foraminifera Lockhartia in south Tibet (China). The Journal of Foraminiferal Research 46(1), 34-47.

Kakar A., Kasi A.M., Benedetti A., Kasi A.K., 2022. Stratigraphy and depositional environment of a mixed siliciclastic-carbonate platform and slope succession of the Paleogene Nisai Group, Pakistan. Stratigraphy 19(2), 95-117.

Kamran, M., Frontalini, F., Xi, D., Papazzoni, C.A., Jafarian, A., Latif, K., Jiang, T., Mirza, K., Song, H., Wan, X., 2021. Larger benthic foraminiferal response to the PETM in the Potwar Basin (Eastern NeoNeotethys, Pakistan). Palaeogeography, Palaeoclimatology, Palaeoecology 575, 110450.

Kato, A., Baba, M., Kawai, H., & Masuda, M. (2006). Reassessment of the little-known crustose red algal genus Polystrata (Gigartinales), based on morphology and SSU rDNA sequences. Journal of Phycology, 42(4), 922-933.

Kazmi, A. H., Rana, R. A. (1982). Tectonic map of Pakistan at a scale of 1:200,000. Geological Survey of Pakistan, Quetta.

Kiessling, W., Flügel, E., Golonka, J., 1999. Paleo reef maps: evaluation of a comprehensive database on phanerozoic reefs. American Association of Petroleum Geologists Bulletin 83, 1552-1587.

Kiessling, W., Flügel, E., Golonka, J. 2002. Phanerozoic reef patterns. SEPM Special Publication, Tulsa, Oklahoma, USA. Society for Sedimentary Geology (SEPM), 775 pp.

Latif, M.A., 1970. Explanatory notes on the Geology of South Eastern Hazara, to accompany the revised Geological Map. Wien Jb. Geol. BA, Sonderb, 15.

Leppig, U., 1988. Structural analysis and taxonomic revision of Miscellanea, Paleocene larger Foraminifera.- Eclogae Geologicae Helvetiae, Basel 81(3), 689-721.

Leppig, U., Langer M.R., 2015. Emendation and taxonomic revision of Miscellanea juliettae pfenderae and M. juliettae villattea with designation of the respective holotype. Micropaleontology 61, 227-230.

Li, J., Hu, X., Garzanti, E., An, W., Wang, J., 2015. Paleogene carbonate microfacies and sandstone provenance (Gamba area, South Tibet): Stratigraphic response to initial India–Asia continental collision. Journal of Asian Earth Sciences 104, 39-54.

Li, J., Hu, X., Garzanti, E., BouDagher-Fadel, M., 2017. Shallow-water carbonate responses to the Paleocene–Eocene thermal maximum in the Tethyan Himalaya (southern Tibet): Tectonic and climatic implications. Palaeogeography, Palaeoclimatology, Palaeoecology 466, 153-165.

Li, J., Hu, X., Zachos, J.C., Garzanti, E., BouDagher-Fadel, M., 2020. Sea level, biotic and carbon-isotope response to the Paleocene–Eocene thermal maximum in Tibetan Himalayan platform carbonates. Global and Planetary Change 194, 103316.

Li, J., Hu, X., Garzanti, E., BouDagher-Fadel, M., 2022. Spatial heterogeneity in carbonate-platform environments and carbon isotope values across the Paleocene–Eocene thermal maximum (Neotethys Himalaya, South Tibet). Global and Planetary Change, 103853.

Lokier, S.W., Al Junaibi, M., 2016. The petrographic description of carbonate facies: are we all speaking the same language?. Sedimentology 63(7), 1843-1885.

Marshall, A.T., Clode, P., 2004. Calcification rate and the effect of temperature in a zooxanthellate and an azooxanthellate scleractinian reef coral. Coral Reefs 23(2), 218¬224.

McInerney, F.A., Wing, S.L., 2011. The Paleocene-Eocene Thermal Maximum: A perturbation of carbon cycle, climate, and biosphere with implications for the future. Annual Review of Earth and Planetary Sciences 39, 489-516.

Michel, J., Borgomano, J., Reijmer, J.J., 2018. Heterozoan carbonates: When, where and why? A synthesis on parameters controlling carbonate production and occurrences. Earth-Science Reviews 182, 50-67.

Najman, Y., Jenks, D., Godin, L., Boudagher-Fadel, M., Millar, I., Garzanti, E., Horstwood, M., Bracciali, L., 2017. The Tethyan Himalayan detrital record shows that India–Asia terminal collision occurred by 54 Ma in the Western Himalaya. Earth and Planetary Science Letters 459, 301-10.

Najman, Y., Pringle, M., Godin, L., Oliver, G., 2001. Dating of the oldest continental sediments from the Himalayan foreland basin. Nature 410(6825), 194-197.

Nebelsick, J.H., Rasser, M.W., Bassi, D., 2005. Facies dynamics in Eocene to Oligocene circumalpine carbonates. Facies 51(1), 197-217.

Nicora A., Garzanti E., Fois E., 1987. Evolution of the Neotethys Himalaya continental shelf during Maastrichtian to Paleocene (Zanskar, India). Rivista Italiana Paleontologia E Stratigrafia 92(4), 439-496.

Ohba, H., Matsuda, S., Asami, R., Iryu, Y., 2017. Recent Dasycladales (Chlorophyta) in Okinawa Jima in the Central Ryukyus, southwestern Japan: Paleontological implications. Island Arc 26 (3), e12185.

Özcan, E., Hanif, M., Ali, N., Yücel, A.O., 2015. Early Eocene orthophragminids (Foraminifera) from the type-locality of Discocyclina ranikotensis Davies, 1927, Thal, NW Himalayas, Pakistan: insights into the orthophragminid paleobiogeography. Geodinamica Acta, 27, 267–299.

Özcan, E., Pignatti, J., Pereira, C., Yücel, A.O., Drobne, K., Barattolo, F., Saraswati, P.K., 2018, Paleocene orthophragminids from the Lakadong Limestone, Mawmluh Quarry Section, Meghalaya (Shillong, NE India): Implications for the regional geology and paleobiogeography: Journal of Micropalaeontology, 37, 357–381.

Papazzoni, C.A., Ćosović, V., Briguglio, A., Drobne, K., 2017. Towards a calibrated larger foraminifera biostratigraphic zonation: celebratin 18 years of the application of Shallow Benthic Zones towards calibrated benthic zones. Palaios 32(1), 1-4.

Pereira, C.D., Khanolkar, S., Banerjee, S., Özcan, E., Saraswati, P.K., 2022. Larger benthic foraminifera and microfacies of late Paleocene-early Eocene sections in Meghalaya, Northeast India. Journal of Foraminiferal Research 52, 40–56.

Perrin, C., Bosellini, F.R., 2012. Paleobiogeography of scleractinian reef corals: changing patterns during the Oligocene–Miocene climatic transition in the Mediterranean. Earth-Science Reviews 111(1-2), 1-24.

Perrin, C., Kiessling, W., 2012. Latitudinal trends in Cenozoic reef patterns and their relationship to climate. In: Mutti, M., Piller, W., Betzler, C. (Eds.), Carbonate systems during the Oligocene-Miocene climatic transition 42. Oxford, UK: Wiley-Blackwell. International Association of Sedimentologists Special Publications, pp. 17-34.

Pestana, E.M.D.S., Nunes, J.M.D.C., Cassano, V., Lyra, G.D.M. (2021). Taxonomic revision of the Peyssonneliales (Rhodophyta): Circumscribing the authentic Peyssonnelia clade and proposing four new genera and seven new species. Journal of Phycology, 57(6), 1749-1767.

Pignatti, J., Papazzoni, C.A., 2017. Oppel zones and their heritage in current larger foraminiferal biostratigraphy. Lethaia 50, 369–380.

Pomar, L., 2001. Types of carbonate platforms: a genetic approach. Basin research 13(3), 313-334.

Pomar, L., Baceta, J.I., Hallock, P., Mateu-Vicens, G., Basso, D., 2017. Reef building and carbonate production modes in the west-central Neotethys during the Cenozoic. Marine and Petroleum Geology 83, 261-304.

Pomar, L., 2020. Chapter 12 - Carbonate systems. In: Scarselli, N., Chiarella, D., Bally, A.W., Adam, J., Roberts, D.G. (Eds.), Regional Geology and Tectonics. Elsevier, pp. 235-311.

Ridgwell, A., Zeebe, R.E., 2005. The role of the global carbonate cycle in the regulation and evolution of the Earth system. Earth and Planetary Science Letters 234(3-4), 299-315.

Riding, R., 2002. Structure and composition of organic reefs and carbonate mud mounds: concepts and categories. Earth-Science Reviews 58(1-2), 163-231.

Saboor, A., Ahmad, J., Khan, S., Latif, K., Khan, A., Haider, A.T., 2021. Foraminiferal biostratigraphy, facies, and sequence stratigraphy analysis across the K-Pg Boundary in Hazara, Lesser Himalayas (Dhudial Section). Geodiversitas 43(18), 663-682.

Sarma, A., & Ghosh, A. K. (2006). A new record of calcareous algae from shella Formation (Jaintia Group) of South Jaintia Hills, Meghalaya, India. Current science, 1276-1281.

Sarkar, S., 2018. The enigmatic Paleocene-Eocene coralline Distichoplax: Approaching the structural complexities, ecological affinities and extinction hypotheses. Marine Micropaleontology 139, 72-83.

Sarkar, S. (2020). Ecostratigraphic implications of a Late Paleocene shallow-marine benthic community from the Jaintia Hills, Meghalaya, NE India. Journal of Earth System Science, 129(1), 10.

Sarkar, S., & Narasimha Rao, G. M. (2018). Coralline red algae from late Paleocene–earliest Eocene carbonates of Meghalaya, N–E India: palaeocommunity and trophic-level implications. Carbonates and Evaporites, 33, 767-781.

Sarkar, S., Cotton, L. J., Valdes, P. J., & Schmidt, D. N. (2022). Shallow Water Records of the PETM: Novel Insights From NE India (Eastern Neotethys). Paleoceanography and Paleoclimatology, 37(7), e2021PA004257

Sameeni, S.J., Nazir, N., Abdul-Karim, A., Naz, H., 2009. Foraminiferal biostratigraphy and reconnaissance microfacies of Paleocene Lockhart Limestone of Jabri area, Hazara, northern Pakistan. Geological Bulletin of the Punjab University 44, 85-96.

Scheibner, C., Speijer, R.P., Marzouk, A.M., 2005. Turnover of larger foraminifera during the Paleocene-Eocene Thermal Maximum and paleoclimatic control on the evolution of platform ecosystems. Geology 33(6), 493-496.

Scheibner, C., Speijer, R.P., 2008. Late Paleocene–early Eocene Tethyan carbonate platform evolution - A response to long-and short-term paleoclimatic change. Earth-Science Reviews 90(3-4), 71-102.

Serra-Kiel, J., Hottinger, L., Caus, E., Drobne, K., Ferrandez, C., Jauhri, A.K., Less, G., Pavlovec, R., Pignatti, J., Samso, J.M., Schaub, H., Sirel, E., Strougo, A., Tambareau, Y., Tosquella, J., Zakrevskaya, E., 1998. Larger foraminiferal biostratigraphy of the Tethyan. Bulletin de la Société géologique de France 169, 281-299.

Serra-Kiel, J., Vicedo, V., Baceta, J.I., Bernaola, G., Robador, A., 2020. Paleocene Larger Foraminifera from the Pyrenean Basin with a recalibration of the Paleocene Shallow Benthic Zones. Geologica acta 18, 1-69, I-III.

Shah, S.M.I., 2009. Stratigraphy of Pakistan. Memoirs of the Geological Survey of Pakistan 22.

Shah, M.M., Rahim, H.U., Hassan, A., Mustafa, M.R., Ahmad, I., 2020. Facies control on selective dolomitization and its impact on reservoir heterogeneities in the Samana Suk Formation (Middle Jurassic), Southern Hazara Basin (NW Himalaya, Pakistan): an outcrop analogue. Geosciences Journal 24(3), 295-314.

Shalalvand, M., Adabi, M., & Zohdi, A. (2021). Biological evolution of the carbonate platform of the Taleh Zang Formation in Kermanshah region. Journal of Stratigraphy and Sedimentology Researches, 37(1), 45-66.

Sirel, E., 2018. Revision of the Paleocene and partly early Eocene larger benthic foraminifera of Turkey. Department of Geological Engineering, Ankara University: Ankara Üniversitesi Yayýnevi Yayin 27, 260 pp.

Stanley, S. M., & Hardie, L. A. (1998). Secular oscillations in the carbonate mineralogy of reef-building and sediment-producing organisms driven by tectonically forced shifts in seawater chemistry. Palaeogeography, Palaeoclimatology, Palaeoecology, 144(1-2), 3-19.

Sternai, P., Caricchi, L., Pasquero, C., Garzanti, E., van Hinsbergen, D. J., & Castelltort, S. (2020). Magmatic forcing of Cenozoic climate?. Journal of Geophysical Research: Solid Earth, 125(1), e2018JB016460.

Titelboim, D., Almogi-Labin, A., Herut, B., Kucera, M., Asckenazi-¬ Polivoda, S., Abramovich, S., 2019. Thermal tolerance and range expansion of invasive foraminifera under climate changes. Scientific Reports 9(1), 1-5.

Tremblin, M., Khozyem, H., Adatte, T., Spangenberg, J.E., Fillon, C., Grauls, A., Hunger, T., Nowak, A., Läuchli, C., Lasseur, E., Roig, J.Y., Serrano, O., Calassou, S., Guillocheau, F., Castelltort, S., 2022. Mercury enrichments of the Pyrenean foreland basins sediments support enhanced volcanism during the Paleocene-Eocene thermal maximum (PETM). Global and Planetary Change 212, 103794.

Umar, M., Sabir, M.A., Farooq, M., Khan, M.M.S.S., Faridullah, F., Jadoon, U.K., Khan, A.S., 2015. Stratigraphic and sedimentological attributes in Hazara Basin Lesser Himalaya, North Pakistan: their role in deciphering minerals potential. Arabian Journal of Geosciences 8(3), 1653-1667.

Van der Zwaan, G.J., Jorissen, F.J., De Stigter, H.C., 1990. The depth dependency of planktic/benthic foraminiferal ratios: constraints and applications. Marine Geology 95(1), 1–16.

Vescogni, A., Bosellini, F.R., Reuter, M., Brachert, T.C., 2008. Vermetid reefs and their use as palaeobathymetric markers: New insights from the Late Miocene of the Mediterranean (Southern Italy, Crete). Palaeogeography, Palaeoclimatology, Palaeoecology 267(1-2), 89-101.

Vescogni, A., Bosellini, F.R., Papazzoni, C.A., Giusberti, L., Roghi, G., Fornaciari, E., Dominici, S., Zorzin, R., 2016. Coralgal buildups associated with the Bolca Fossil-Lagerstätten: new evidence from the Ypresian of Monte Postale (NE Italy). Facies 62(3), 1-20.

Vimpere L., Spangenberg J., Roige M., Adatte T., De Kaenel E., Fildani A., Clark J., Sahoo S, Bowman A., Sternai P., Castelltort S. (2023), Carbon isotope and biostratigraphic evidence for an expanded PETM sedimentary record in the deep Gulf of Mexico. Geology, https://doi.org/10.1130/G50641.1

Vršič, A., Gawlick, H.J., Schlagintweit, F., Machaniec, E., Gharsalla, M., 2021. Age, microfacies and depositional environment of the Middle to Late Paleocene shallow-marine carbonates in the Sirt Basin of Libya (Upper Sabil Formation): “Are Intisar domal structures pinnacle reefs?”. Facies 67, 27.

Westerhold, T., Marwan, N., Drury, A.J., Liebrand, D., Agnini, C., Anagnostou, E., Barnet, J.S.K., Bohaty, S.M., De Vleeschouwer, D., Florindo, F., Frederichs, T., Hodell, D.A., Holbourn, A.E., Kroon, D., Lauretano, V., Littler, K., Lourens, L.J., Lyle, M., Pälike, H., Röhl, U., Tian, J., Wilkens, R.H., Wilson, P.A., Zachos, J.C., 2020. An astronomically dated record of Earth's climate and its predictability over the last 66 million years. Science (New York, N.Y.) 369(6509), 1383-1387.

Wilson, M.E., 2008. Global and regional influences on equatorial shallow-marine carbonates during the Cenozoic. Palaeogeography, Palaeoclimatology, Palaeoecology 265(3-4), 262-274.

Zachos, J. C., Dickens, G. R., & Zeebe, R. E. (2008). An early Cenozoic perspective on greenhouse warming and carbon-cycle dynamics. nature, 451(7176), 279-283.

Zamagni, J., Mutti, M., Košir, A., 2008. Evolution of shallow benthic communities during the Late Paleocene–earliest Eocene transition in the Northern Neotethys (SW Slovenia). Facies 54(1), 25-43.

Zamagni, J., Mutti, M., Košir, A., 2012. The evolution of mid Paleocene-early Eocene coral communities: How to survive during rapid global warming. Palaeogeography, alaeoclimatology, Palaeoecology, 317, 48-65.

Zhang, Q., Willems, H., Ding, L., 2013. Evolution of the Paleocene-Early Eocene larger benthic foraminifera in the Tethyan Himalaya of Tibet, China. International Journal of Earth Sciences 102, 1427–1445.

Zhang, Q., Willems, H., Ding, L., & Xu, X. (2019). Response of larger benthic foraminifera to the Paleocene-Eocene thermal maximum and the position of the Paleocene/Eocene boundary in the Tethyan shallow benthic zones: Evidence from south Tibet. GSA Bulletin, 131(1-2), 84-98.

Chapter 4 – Pre PETM, POE & PETM conditions [SBZ3 to SBZ5]

The fourth chapter showcases the five successive stages of Late Paleocene to Early Eocene (SBZ3 to SBZ5) from the Baroch Nala section, (Surghar Range, Pakistan). These stages include 1) pre-PETM, 2) POE, 3) PETM onset 4) PETM body and recovery, and 5) post-PETM phase.

The chapter shows the changes in biotic, geochemical, and mineralogical assemblages in response to POE and PETM. This chapter is taken from the published scientific paper by Ali et al., 2025, published in the Journal of *"Marine and Petroleum Geology"*, Volume 171, January 2025, 107183

"The Baroch Nala Section (NE Pakistan): A new PETM standard for the eastern Tethys"

Mubashir Ali; Giovanni Coletti; Eduardo Garzanti; Thierry Adatte; Sébastien Castelltort; Pietro Sternai; Andrea Benedetti; Elisa Malinverno; Luca Mariani; Jorge E. Spangenberg; Suleman Khan; Daniela Basso; Elias Samankassou; László Kocsis; Muhammad Usman

4.1. Abstract

We present an integrated, high-resolution, biostratigraphical, mineralogical, and geochemical characterization of the well-exposed Upper Paleocene - Lower Eocene stratigraphic succession of the Surghar Range (Baroch Nala section, NE Pakistan). The faunal assemblages from the Baroch Nala section, dominated by hyaline benthic foraminifera and green calcareous algae, along with the significant terrigenous fraction and the presence of terrestrially derived organic matter, testify to deposition in a low-energy shallow-marine environment. Such environmental conditions, coupled with weak diagenetic effects, allow us to integrate a continuous record of carbon stable isotopes with a detailed account of the biotic response by carbonate-producing assemblages, paleoclimatic information based on clay-minerals, and information on volcanic activity-based on mercury concentrations. The environmental evolution from the Late Paleocene up to the Paleocene

Eocene Thermal Maximum (PETM) is clearly documented, including the weaker warm excursion that precedes the PETM (I.e. the Pre-Onset Excursion "POE") and the evolution of large benthic foraminiferal assemblages. The overall record perfectly shows how the turnover in benthic carbonate producers started with the onset of the PETM and was completed by the time the excursion ended, highlighting how brief environmental oscillations can have long lasting effects on the biosphere.

.

4.2. Introduction

The early Paleogene witnessed several warming events, including the Early Danian event, the Late Danian Event, the Danian/Selandian Transition Event, the Early Late Paleocene Event (ELPE), the Pre-Onset Excursion (POE), the Paleocene-Eocene Thermal Maximum (PETM), and the Early Eocene Climatic Optimum (EECO) (Bowen et al., 2015: Barnet et al., 2019; Babila et al., 2022; Tremblin et al., 2022). Among these well-pronounced and short-lived hyperthemals, the PETM stands out (Slujis et al., 2007). The PETM coincides with the Paleocene-Eocene transition (56 Ma; Walsh, 2004) and lasted for 170 – 200 ka. Three sub-stages are identified: PETM onset, body, and recovery (Röhl et al., 2007). The PETM onset is characterized by an abrupt negative carbon isotope excursion (CIE, ~3‰ to 6‰), related to a massive input of ^{13}C-depleted carbon into the atmosphere and hydrosphere (McInerney and Wing, 2011). This caused a global increase in temperatures (4 to 8°C; Zachos et al., 2005; Slujis et al., 2011), deep-sea acidification and carbonate dissolution, perturbation in rainfall regime, and high continental runoff (Zachos et al., 2005; McInerney and Wing, 2011; Chen et al., 2018; Westerhold et al., 2020). The main causes of the remarkable addition of isotopically light CO_2 in the atmospheric system during the PETM remain controversial, with volcanic activity, permafrost melting, and release of methane clathrates indicated as possible sources (McInerney and Wing, 2011). This large, rapid, impactful increase in CO_2 concentration makes the PETM an excellent useful analog for modern climate change.

From high to low-latitude areas, deep-marine PETM successions have been investigated using biotic and abiotic proxy data, including assemblages of planktic foraminifera, dinoflagellates and calcareous nannofossils, together with biomarkers, clay mineralogy, and various geochemical proxies (e.g., Bralower et al., 2018; Charles et al., 2011; Kennett &

Stott, 1991; Thomas & Shackleton, 1996; Zachos et al., 2003, 2005; Khozyem et al., 2023). These studies underscored the magnitude of the environmental variations occurred during the PETM. The few relatively complete shallow-marine successions deposited at that time indicate extensive biotic changes in the shallow-water realm in both western (Pujalte et al., 2003; Ozgen-Erdem et al., 2005; Scheibner and Speijer, 2008; Zamagni et al., 2012a; Yans et al., 2014) and eastern Tethys, (Afzal et al., 2011a, 2011b; Li et al., 2020 and references therein; Kamran et al., 2021; Sakar et al., 2022; Jiang et al., 2023 and references therein). In the eastern Tethys, however no complete section has so far provided a full record of geochemical and mineralogical proxies directly correlated with the biotic changes of the shallow-water realm.

In this research we present the thorough analysis of a well-preserved Himalayan section that covers the complete Late Paleocene to Early Eocene time interval complemented by a full stratigraphic record both of changes in geochemical proxies and shallow benthic assemblages. Our goal is to improve our understanding of past environmental changes during Paleogene hyperthermals by providing a complete dataset from a key reference section for the PETM in the eastern Tethys. Our multiproxy data include carbon and oxygen stable isotopes, bulk and clay mineralogy, mercury and TOC concentrations, coupled with a quantitative study of the microfossil assemblage. These data allowed us to define a pre-PETM stage and to recognize the Pre-Onset Excursion (POE), the PETM onset, and the PETM body and recovery phases while providing a detailed picture of the biotic and environmental changes that occurred during this time in the eastern Tethys realm.

4.3.Geological Setting

The studied Baroch Nala section (32º56'25.74"N, 71º08'57.88"E) is located in the Trans Indus-Surghar fold-thrust belt of northeastern Pakistan, along the western prolongation of the Himalayan orogen grown since the middle Paleocene collision onset between the Indian and Asian continental margins (~60 Ma; Hu et al., 2016; Garzanti, 2019).

The forelandward progression of the frontal thrust resulted in the Pliocene rise of the Salt Range to the east of the Indus River (Yeats and Lawrence, 1982; Abbasi and McElroy, 1991) and of the Trans Indus-Surghar Range to the west (McDougall et al., 1991; Ali et al., 2014).

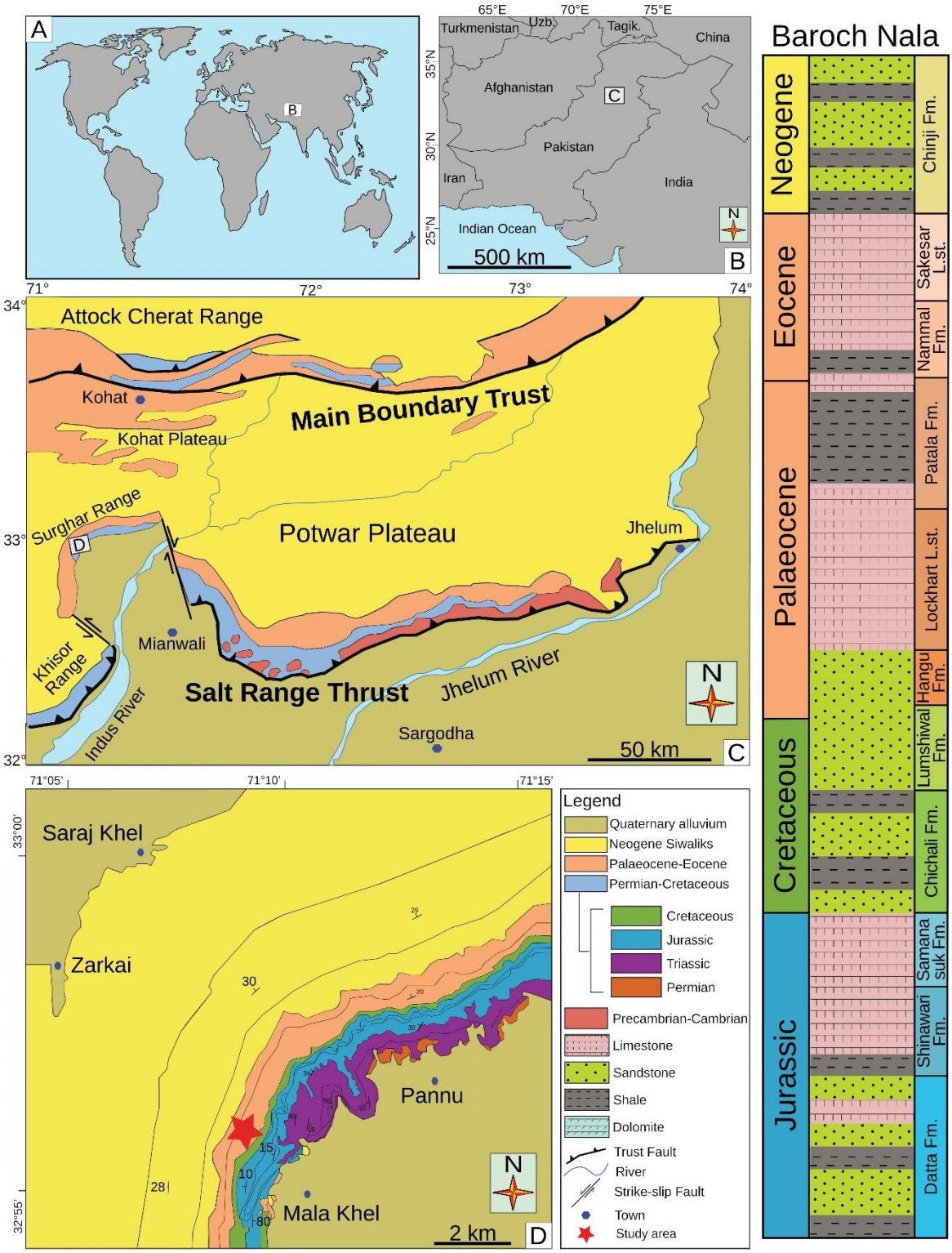

Figure 4.1: Study area and stratigraphic succession at Baroch Nala. A,B) Location of study area in northern Pakistan. C) Schematic tectonic map of study area showing main tectonic features (mod. from Kazmi and Rana, 1982). D) Simplified geological map of the study area (mod. from Ali et al., 2014; red star indicates the location of Baroch Nala section).

The Salt Range is delimited by the Jhelum sinistral fault in the east and by the Kalabagh dextral fault in the west, whereas the Trans Indus-Surghar Range is bounded by the Kalabagh and Kurram faults in the east and west, respectively (Fig. 4.1).

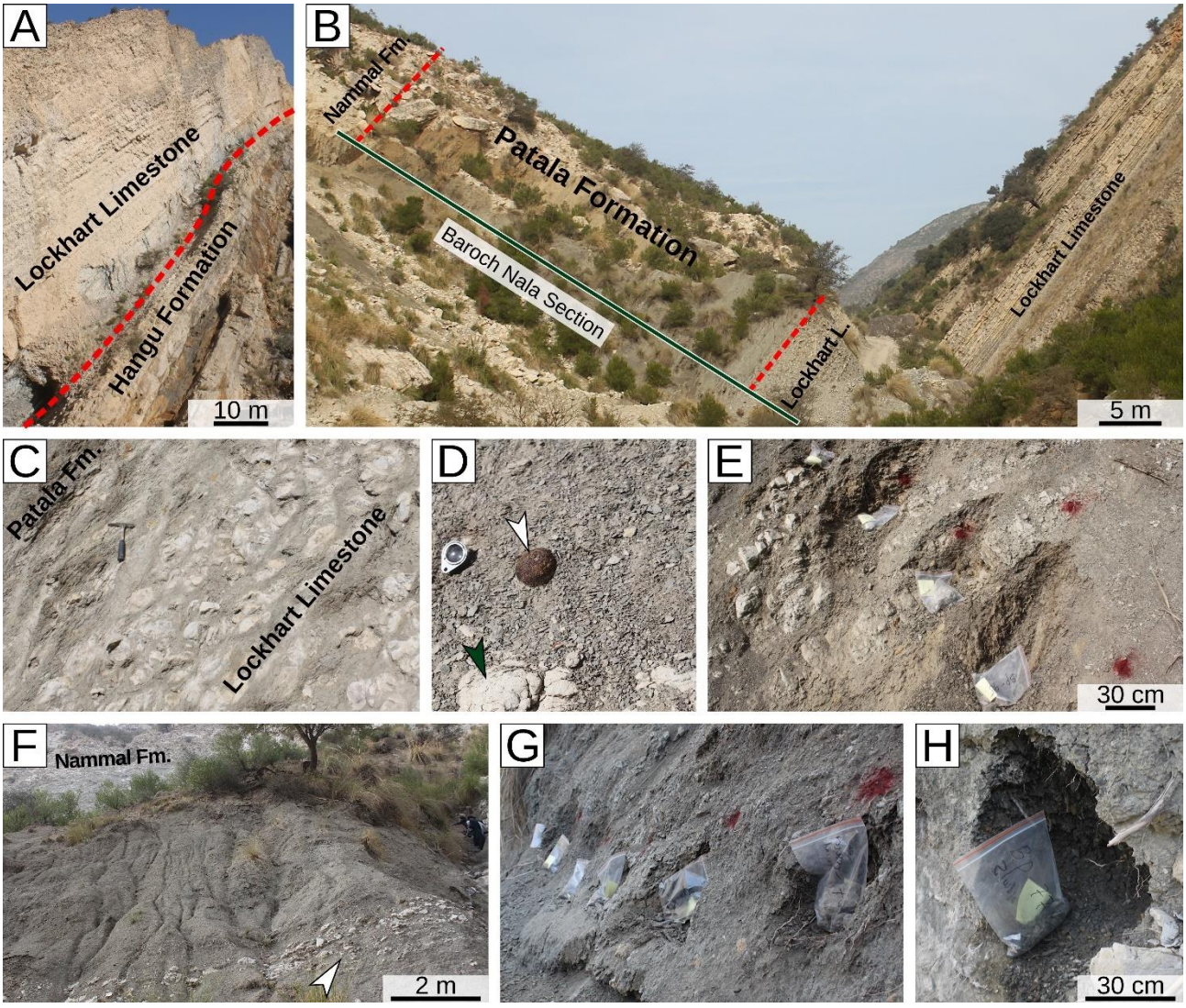

Figure 4.2: Baroch Nala section. A) Unconformable contact between Lower Paleocene Hangu Formation and Middle Paleocene Lockhart Limestone. B) Panoramic view of studied Upper Paleocene to Lower Eocene Patala Fm., showing conformable lower contact with Lockhart Limestone and upper contact with Lower Eocene Nammal Fm. C) Close-up view of gradual contact between Lockhart Limestone and Patala Fm. D) Pyrite nodule in Patala marls. E,F) Nodular limestone layers in Patala Fm. G) High resolution sampling digging ~1 m was required to collect unweathered samples. H) Black shale at 27.5 m *abs* sample recording the PETM onset.

The stratigraphic succession exposed in the Baroch Nala area starts with the Lower Jurassic fluvio-deltaic Datta Formation (Fm), overlain the Lower to Middle Jurassic Shinawari Fm consisting of shallow-water carbonates passing distantly to deeper-marine mudrocks (Figs.

4.1-2). The overlying Upper Jurassic Samana Suk Fm consists of shallow-marine limestones, followed by, green belemnite-bearing glauconitic shales and sandstones of the Lower Cretaceous Chichali Fm, followed in turn by shallow-marine sandy carbonates and deltaic sandstones of the Lower Cretaceous Lumshiwal Fm (Shah, 2009). The unconformably overlying sandstones with interbedded limestones of the Lower Paleocene Hangu Fm are paraconformably followed by the shallow-water nodular limestones of the Upper Paleocene Lockhart Limestone, followed by the hemipelagic shales and limestones of the Upper Paleocene to Lower Eocene Patala Fm (Figs. 4.1-2). The Lower Eocene succession continues with chert-bearing carbonates and shales of the Nammal Fm and nodular limestones of the Sakessar Fm, unconformably capped by Neogene molasses of Siwaliks Supergroup (Figs. 4.1-2).

4.4.Materials and Methods

In the Baroch Nala section, the Paleocene-Eocene interval was measured bed by bed and all macroscopic aspects were described in the field. Ninety-two samples were collected, systematically below and above any significant lithological change, focusing specifically on intervals displaying variations in petrographic and paleontological content. Based on the observed lithological variations and the presence of exposed dark marly layers in the lower part of the section, we were able to implement a high-resolution sampling methodology. Globally, dark marly lithologies are widely regarded as the most suitable candidates for identifying the onset of the Paleocene-Eocene Thermal Maximum (PETM) but later after running multiple sets of biological, geochemical, and mineralogical analyses these dark layers in the lower part of the section proved itself a pre-PETM and Pre onset Excursion (POE) associated lithologies. However, as we progressed upwards through the section, the sampling resolution decreased due to reduced lithological variation. Despite this, a notable dark shale layer was identified at 27.5 meters, which later confirmed itself as the PETM onset layer. The low sampling resolution within the PETM interval can primarily be attributed to the limited lithological variation encountered in this part of the section. In addition, 1 m of digging was required to collect unweathered samples in the poorly lithified mudrock intervals (Fig 4.2G-H).

Thin sections of poorly lithified and porous samples were obtained after consolidation in epoxy resin. Textures, microfacies, and skeletal assemblages were quantitatively determined at the University of Milano-Bicocca by counting more than 800 points in each thin section using a 200 μm grid (Flügel, 2010). Large Benthic Foraminifera (LBF) biostratigraphy followed the shallow benthic zones (SBZ of Serra-Kiel et al., 1998) recalibrated for the Paleocene (Serra-Kiel et al., 2020; Papazzoni et al., 2023). The taxonomic analysis of LBF was based on the typological approach of Hottinger (2009, 2014); selected *Lockhartia* individuals, miscellaneids, and nummulitids were identified at the species level by biometric measurements (e.g., Benedetti et al., 2018).

Calcareous nannofossil analyses were carried out on 76 smear slides prepared using a 22 × 40 mm coverslip and Norland mounting medium. Each sample was scanned through an Olympus BX50 polarized light microscope at 1000x with immersion oil. For most slides, between 4 and 6 transects were observed to find useful markers. The relative abundance of calcareous nannofossils per field of view (FOV) was assessed for each sample and tabulated as follows: A = abundant: >10/FOV; C = common: 1–10 /FOV; F = few: 1/10 FOV; R = rare: ≥ 3/transect; VR = very rare: 1/transect. Taxonomic identification followed Young et al. (2023) using the biostratigraphic schemes of Martini (1971), Agnini et al. (2014), and Menini et al. (2021).

Mineralogical and geochemical analyses were carried out on 92 samples at the Institute of Earth Science (ISTE) and Institute of Earth Surface Dynamics (IDYST), University of Lausanne (UNIL), Switzerland. Samples were oven-dried at 45°C and next gently crushed or − when required − milled using an agate mill. Organic matter characterization was performed at ISTE using a Rock-Eval 6, calibrated with the IFP16000 standard and following the procedures described in Behar et al., 2001. Samples were pyrolyzed first at 300°C, then heated at 650°C in the presence of nitrogen, followed by combustion at up to 850°C in the oxidation chamber. Rock-Eval 6 data sets include total organic carbon (TOC; wt.%), oxygen index (OI; mg CO_2/g TOC), hydrogen index, (HI; mg HC/g TOC), and Tmax (°C; an indicator of thermal maturity). The HI *vs.* OI and HI *vs.* T_{max} plots for samples with TOC ≥ 0.2 wt.% were considered for the interpretation of organic matter type, source, and thermal-maturity level (Fantasia et al., 2019).

The organic matter $\delta^{13}C$ ($\delta^{13}C_{org}$) was determined at IDYST by treating samples with HCl (10% concentration) and combusting them with a Carlo Erba 1108 Elemental Analyzer coupled with a Thermo Fisher Scientific Delta V Plus Isotope Mass Spectrometer. Four

reference materials, including international and UNIL-based standards (Spangenberg et al., 2006), were used for calibration and normalization of measured isotopic values. All results were reported in the δ notation relative to the Vienna Pee Dee Belemnite_(VPDB) international standard. The accuracy and precision of $\delta^{13}C$ org was better than 0.1‰.

Bulk carbonate $\delta^{13}C_{carb}$ and $\delta^{18}O_{carb}$ were determined for 40 samples with $CaCO_3$ >10% following Revesz and Landwehr (2002) and Spötl and Vennemann (2003). Sample aliquots were weighed and analyzed using a Thermo Fisher Scientific Gas Bench Plus coupled with a Delta V Plus Isotope Ratio Mass Spectrometer. The raw data were normalized to a Carrara marble in-house standard, calibrated to NBS-18 and NBS-19 international standards, which was analyzed several times together with the samples. The external reproducibility (1σ) of the in-house standard did not exceed ± 0.1‰ for both isotopes. The internal reproducibility yielded similarly low values and was calculated based on ten CO_2 peaks analyzed for each sample. Since most diagenetic processes do not shift $\delta^{13}C_{carb}$ and $\delta^{13}C_{org}$ in the same direction and with the same rate, consistent major changes in both indexes throughout the geological record are considered to reveal global changes in the carbon cycle (Knoll et al., 1986; Swart, 2015). Consequently, both $\delta^{13}C_{carb}$ and $\delta^{13}C_{org}$ have been determined through the section. Many well-known sections across the PETM display extensive carbonate dissolution (e.g., McInerney and Wing, 2011; Khozyem et al., 2015) or layers with low to extremely low carbonate concentrations leading to discontinuities in the $\delta^{13}C_{carb}$ record. On the other hand, typically increased primary productivity during the PETM resulted in increased accumulation rates of organic carbon burial (Komar and Zeebe, 2017), making organic matter highly available. Focusing more specifically on organic carbon allowed us to obtain data even on carbonate-free layers and thus to illustrate a most continuous record of environmental fluctuations throughout the PETM interval.

Mercury concentration was measured at ISTE using a high-frequency Zeeman R-915F Atomic Absorption Spectrometer tuned at Mode 1, by the direct thermal evaporation of Hg from the bulk sample at 700°C. Data accuracy was determined by treating the certified GSD-11 external standard (Chinese alluvium: 72.0 ± 3.6 ppb; Zintwana et al., 2012). Every sample was processed twice to increase accuracy.

X-ray diffraction analyses were carried out at ISTE using a Thermo Scientific ARL X-TRA diffractometer, following Klug and Alexander (1974). Mineralogy composition was determined from the peak intensity of the identified minerals. Uncertainties are between 5 and 10% for phyllosilicates and < 5% for other minerals. The percentage of the terrigenous fraction was estimated by the detrital index
DI = [(phyllosilicates+quartz+feldspars)/calcite].

Clay-mineral analyses were carried out on the < 2 μm fraction separated with the clay centrifuge method after decarbonatization with 10 % HCl, ultrasonic disaggregation (3 minutes), and treatment with ethylene glycol. The relative amount of kaolinite, chlorite, smectite, palygorskite, illite, and illite-smectite mixed layers was determined based on peak intensities.The *kaolinite/smectite*, *kaolinite/(smectite+palygorskite),* and *kaolinite/(illite+chlortite)* ratios were used for paleoenvironmental interpretation.

4.5.Results

4.5.1. Stratigraphy

Five stratigraphic intervals were identified in the Baroch Nala section based on sedimentological, micropaleontological, and geochemical evidence, each corresponding to a different stage of the Late Paleocene-Early Eocene environmental and ecological transition (Fig. 4.3) : 1) Pre-PETM, up to 15.6 m above the base of the section (*abs*, from here on); 2) pre-onset excursion (POE; 15.6-23.4 m *abs*); 3) PETM onset (23.4-27.5 m *abs*); 4) PETM body and early recovery (27.5-47.5 m *abs*); 5) Post-PETM 47.5–59.5 m *abs*). Because diverse secondary processes can alter the geochemical record preserved in carbonate strata exposed subaerially (Swart, 2015 and references therein), the boundaries of the intervals were defined by combining several proxies and including clear microfacies changes. Detailed data sheets available in Appendix Supplementary Tables BS1, BS2, and BS3

Pre-PETM stage (up to 15.6 m *abs*)

The lowermost 6 m of the interval consists of light-grey nodular mudstones to wackestones belonging to the Lockhart Limestone. The terrigenous fraction (10% of the whole rock) consists, in decreasing order of abundance, of phyllosilicates, quartz, and feldspars; clay minerals include smectite, palygorskite, kaolinite, chlorite, and illite (Figs. 4.4 and 4.5). The upper part of the interval (6.0-15.6 m *abs*) consists of poorly lithified dark-grey marly wackestones to packstones belonging to the Patala Fm.

The terrigenous fraction (30% of the whole rock) consists of phyllosilicates associated with lesser amounts of fine-sand-sized quartz, K-feldspar, and plagioclase; smectite is associated with kaolinite and palygorskite, and minor illite, illite-smectite mixed layers, and chlorite (Figs. 4.4, 4.5). Nodular phosphates, glauconite, and pyrite occur (Fig. 4.2).

The skeletal assemblage is dominated by hyaline LBF (mainly trocospiral forms like *Lockhartia* and orbitoidiforms like *Lakdongia* and *Orbitosiphon*) and small benthic foraminifera (SBF), associated with scarce ostracods, rare Dasycladales, colonial corals, echinoderms and mollusks, and very rare Charophytes (Fig. 4.6).

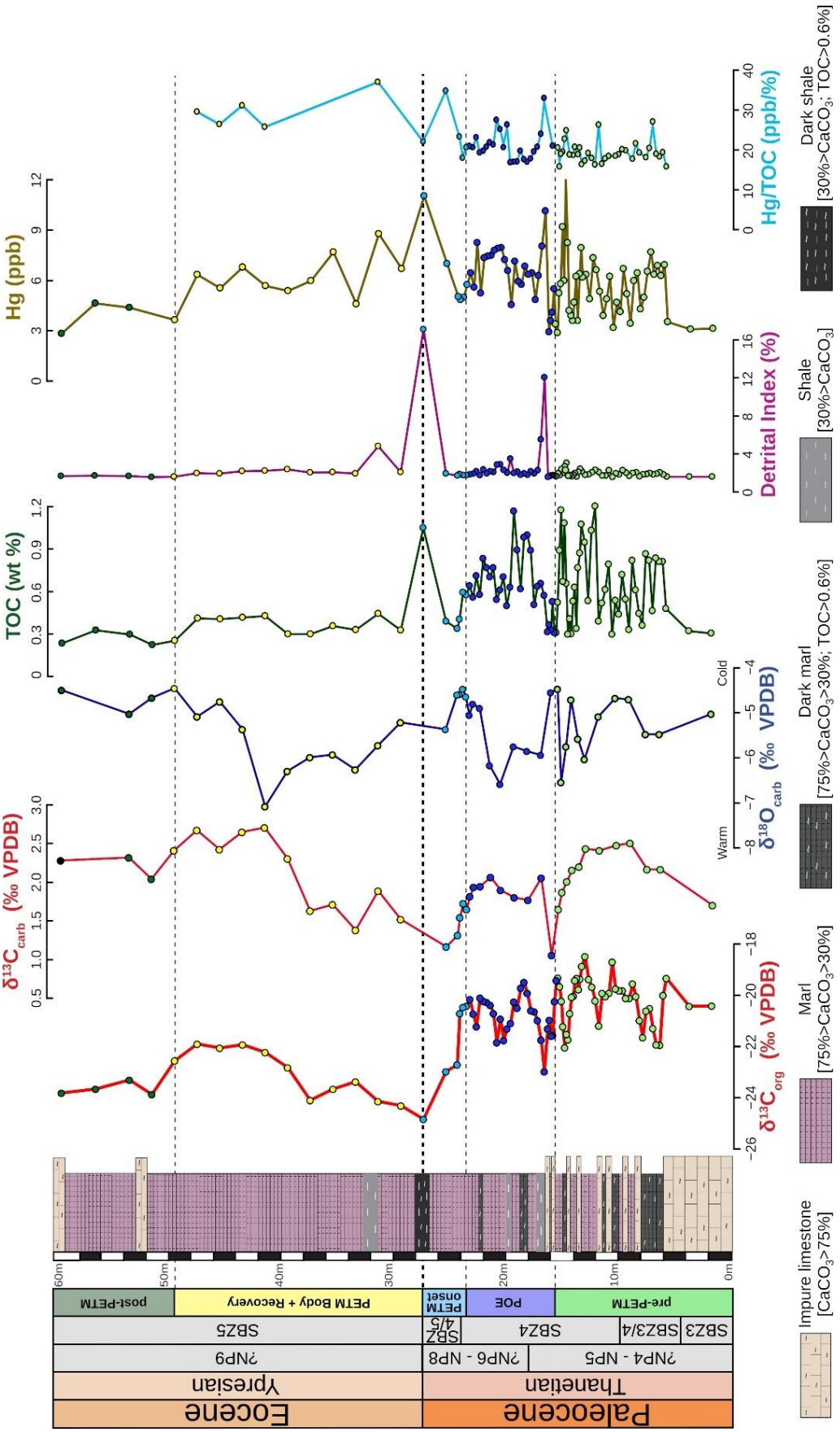

Figure 4.3: Complete carbon and oxygen stable-isotope record [$\delta^{13}C_{org}$, $\delta^{13}C_{carb}$, $\delta^{18}O_{carb}$] through Baroch Nala section, coupled with TOC, detrital index, Hg concentration and Hg/TOC ratio, testify to major environmental perturbations at Late Paleocene to Early Eocene times.

The occurrence of *Miscellanea juliettae* associated with *M.* cf. *duckhani, Miscellanites* sp., *Kathina selveri, Elazigina lenticula, Lockhartia prehaimei, L. haimei*, and *Orbitosiphon* indicate the late Selandian to early Thanetian zone SBZ3 for the lowermost 6 m, whereas *Lakadongia tibetica* mainly associated to several rotaliid species belonging to *Lockhartia, Elazigina,* and *Rotospirella* indicate the SBZ4 for the upper part of the interval (10.0-15.6 m *abs*) (Figs. 4.3, 4.6). Transitional assemblages are observed in between (6.0-10 m *abs*). The rare calcareous nannofossils reflect a time interval comprised between the late Danian and the Selandian (zones NP4 to NP5) (Figs. 4.3, 4.6)

Consistently with biostratigraphy, the $\delta^{13}C$ curve for both carbonate and organic matter displays limited oscillations (Fig. 4.3). In the lowermost 6 m, $\delta^{13}C_{org}$ values range from -19.3‰ to -20.4‰ and TOC ranges from 0.1 to 0.2 wt % (HI 209-288; OI 49-107; T_{max} 420–444°C) (Figure 4). Hg concentrations range from 0.6 to 1.0 ppb and Hg/TOC from 3.6 to 5.8 ppb/wt%. In the upper part, $\delta^{13}C_{org}$ ranges from -18.5‰ to -22.0‰, and $\delta^{13}C_{carb}$ from 1.7‰ to 2.5‰, displaying a similar trend as $\delta^{13}C_{org}$. The $\delta^{18}O_{carb}$ ranged from -4.7‰ to -6.0‰, TOC from 0.1 to 1.0 wt% (HI 76-240; OI 56-235; T-max 424–438°C). Hg ranges from 0.7 to 9.5 ppb, peaking at the top of the interval; Hg/TOC ranges from 4.2 to 14.4 ppb/wt%.

Pre-Onset Excursion (POE) (15.6-23.4 m *abs*)

Grey nodular wackestones to packstones are interbedded with poorly lithified, dark-grey marly wackestones to packstones; dark shale and dolomite-rich layers occur at 16.8 m and 19.8 m *abs* (Fig. 4.3). Phyllosilicates are associated with quartz and feldspars; smectite is occurs with kaolinite and minor palygorskite, illite, and chlorite (Figs. 4.4, 4.5). Kaolinite dominates in the dark-shale layer at 16.8 m *abs*.

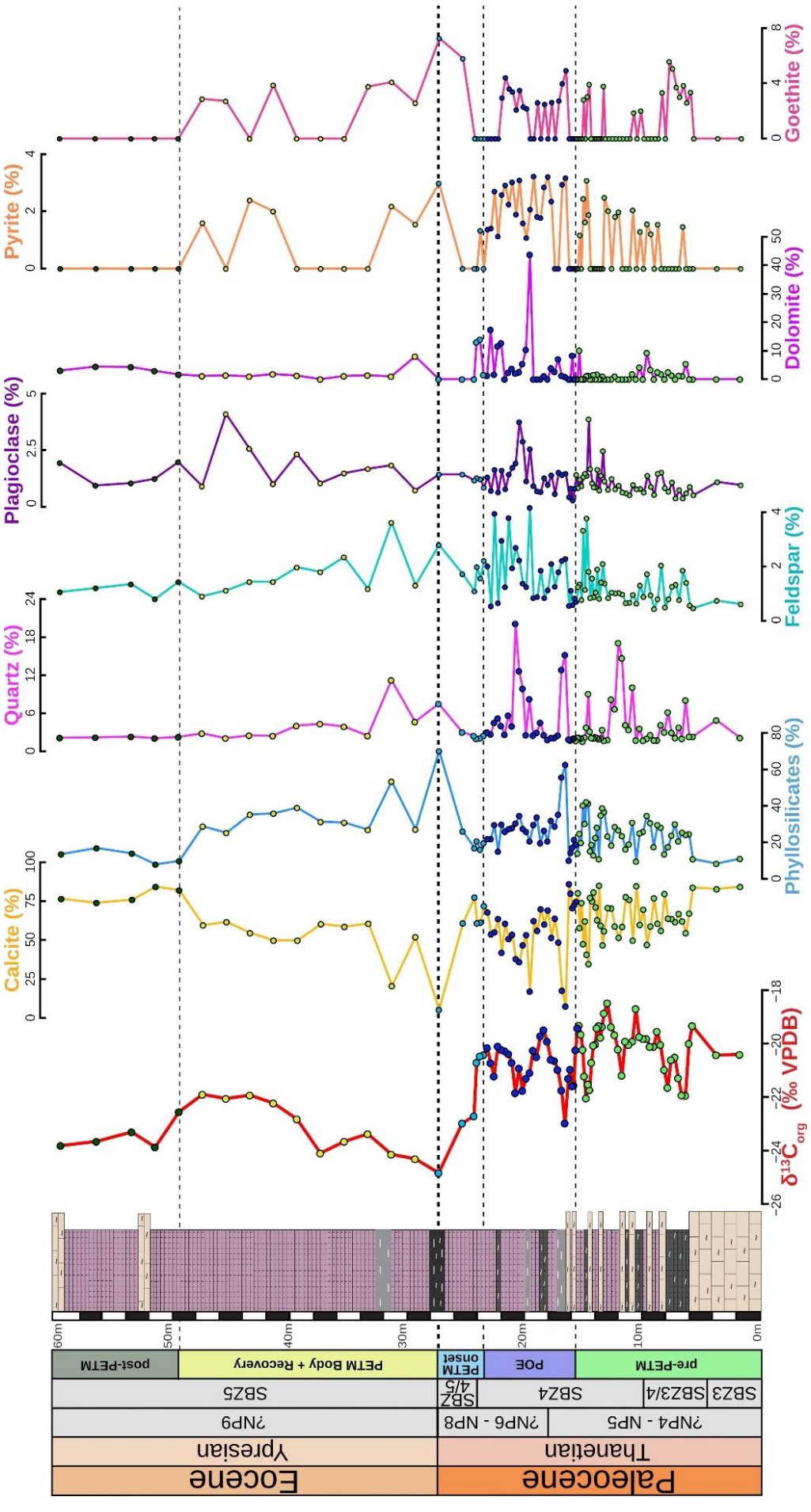

Figure 4.4: Complete record of bulk-rock mineralogical composition through Upper Paleocene to Lower Eocene strata at Baroch Nala section. Note sharp calcite drop and phyllosilicate increase in POE and PETM intervals

Hyaline LBF (mainly trochospiral forms like *Lockhartia* but also large flattened miscellaneids and orbitoidiforms) dominate the assemblage and are associated with SBF, Dasycladales, ostracods, echinoderms, rare corals, and mollusks (Fig. 4.6). The abundance of large miscellaneids and daviesinids such as *Miscellanea miscella, M. dukhani,* and *Daviesina langhami*, associated to *Lockhartia haimei*, *L. roeae, L. tipperi, L. conditi* and *Rotalia* cf. *newboldi*, suggests the late Thanetian SBZ4, in agreement with rare calcareous nannofossils ascribed to zones NP6 to NP8 (Figs. 4.3, 4.6)

Between 15.6 and 16.8 m *abs*, $\delta^{13}C_{org}$ shifts from -19.4‰ to -23.0‰, $\delta^{13}C_{bulk}$ is around 1.0‰, and $\delta^{18}O_{bulk}$ around - 4.5‰. Above, $\delta^{13}C_{org}$ and $\delta^{13}C_{bulk}$ recover back to less negative and more positive values respectively; $\delta^{18}O_{bulk}$ moves towards less negative values. TOC values of the interval fluctuate irregularly between 0.1 and 1.0 wt% (HI 43-182; OI 64-212; T_{max} 417–438°C). Hg content ranges from 0.4 to 7.6 ppb, Hg/TOC from 4.7 to 20 ppb/wt%, in both cases with a sharp peak (7.6 ppb) at 16.8 m *abs*. The dark-shale layer thus records a first relevant negative $\delta^{13}C$ shift that may correspond to the Pre-Onset Excursion (Tremblin et al., 2022). The observed $\delta^{13}C_{org}$ pattern identifies the onset of the POE between 15.6 and 16.8 m *abs* and the recovery phase between 16.8 and 23.4 m *abs* (Fig. 4.3).

PETM onset (23.4-27.5 m *abs*)

Dark grey unconsolidated marly mudstones to packstones are capped by an organic-rich black shale layer at 27.5 m *abs* (Fig. 4.3). Phyllosilicates dominate the terrigenous fraction and are associated with rare quartz and feldspars (Fig. 4.4). Phyllosilicates sharply increase in the dark shale at 27.5 m *abs.* Smectite is generally associated with kaolinite and rare chlorite, illite and palygorskite, but in the dark shale at 27.5 m *abs* kaolinite dominates over smectite and illite and chlorite are rare (Fig. 4.5). Dolomite, glauconite, and pyrite occur.
The faunal assemblage is dominated by miscellaneids (mainly *Miscellanea* cf. *dukhani*) associated with nummulitids (*Ranikothalia* and subordinately *Assilina*), SBF, rare colonial corals, Dasycladales, and echinoderms (Fig. 4.6). Age diagnostic LBF such as *Ranikothalia* sp., *Assilina* cf. *dandotica*, and rotaliids (*Lockharta tipperi*, *L. haimei*, *L. retiata*, *Daviesina langhami*) indicate the topmost Thanetian, i.e. the SBZ4 - SBZ5 transition, in agreement with the calcareous nannofossils representative of zone NP9 that are common in the dark shale at 27.5 m *abs* (Figs. 4.3, 4.6)

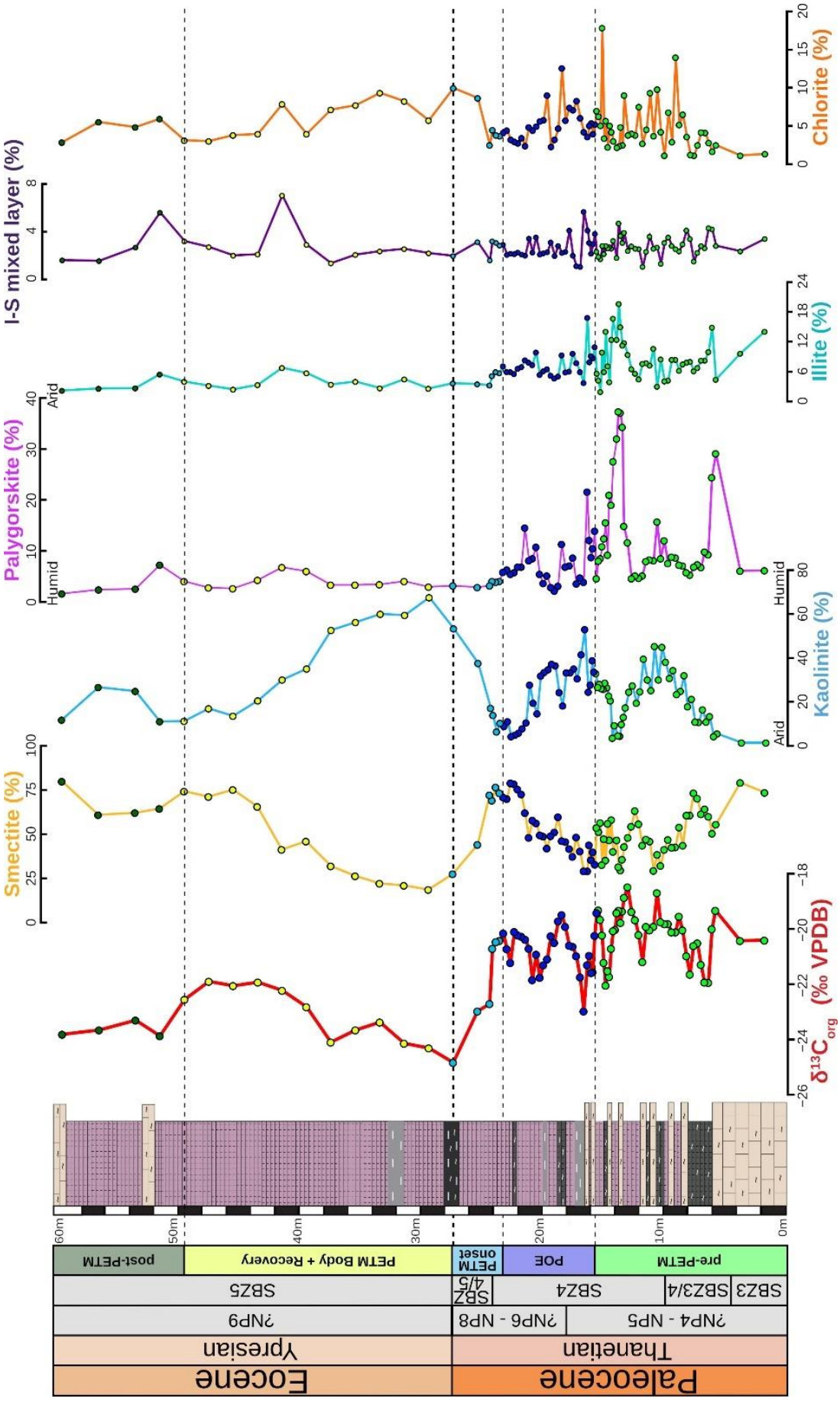

Figure 4.5: Clay mineralogy through Upper Paleocene to Lower Eocene strata at Baroch Nala section. Note the increase in kaolinite at the expense of smectite and palygorskite during POE and PETM intervals.

Consistently with the age assignment $\delta^{13}C_{org}$ and $\delta^{13}C_{carb}$ values range from -20.4‰ to -24.8‰ and from 1.7‰ to 1.1‰, respectively, and display a coherent trend characterized by a sharp negative shift (-4.4 ‰ $\delta^{13}C_{org}$) peaking in the black shale at 27.5 m *abs* (Fig. 3). Both biostratigraphy and the magnitude of the shift identify this CIE with the PETM. The $\delta^{18}O_{carb}$ values range from -4.4‰ to -5.3‰ and TOC from 0.1 to 0.8 wt%, peaking in the dark shale at 27.5 m *abs* (HI 38-163; OI 70-209; T_{max} 415–435°C). Hg ranges from 2.3 to 8.5 ppb, with a spike (8.5 ppb) in the dark shale at 27.5 m *abs*; Hg/TOC ranges between 8.5 and 23 ppb/wt%.

PETM body and recovery (27.5-47.5 m *abs*)

This interval consists of poorly lithified, dark grey, highly fossiliferous marly rudstone (Fig. 4.3). Phyllosilicates are associated with minor quartz and feldspars (Fig. 4.4). Kaolinite dominates the clay-mineral assemblage between 27.5 and 37.5 m *abs* and smectite between 37.5 and 47.5 m *abs* (Fig. 4.5).

The assemblage is dominated by hyaline LBF (*Assilina* and *Operculina, Discocyclina,* rare *Nummulites*, and a few specimens of *Ranikothalia* and *Lockhartia)* associated with common green calcareous algae (Dasycladales and subordinate Bryopsidales), and less common alveolinids, SBF, mollusks, corals, echinoderms, red calcareous algae, and ostracods (Fig. 4.6).

Assilina ranikoti, A. cf. *ornata, A.* cf. *dandotica, Ranikothalia nuttalli,* together with the first common occurrence of *Nummulites* and *Alveolina* − in association with few rotaliids that keep on from the Paleocene such as *Lockhartia conditi, L. haimei, Rotalia cf. newboldi* and *Daviesina langhami* − indicates the earliest Ypresian SBZ5 (Figs., 4.3, 4.6). Calcareous nannofossil assemblages are representative of zone NP9 (Figs. 4.3, 4.6)

Between 27.5 and 37.5 m *abs*, $\delta^{13}C_{org}$ fluctuates from -23.4‰ to -24.3‰, $\delta^{13}C_{carb}$ from 1.3‰ to 1.9‰, and $\delta^{18}O_{(carb)}$ from – 5.2‰ to -6.2‰. TOC ranges from 0.1 to 0.2 wt% (HI 25-68; OI 203-226; T_{max} 402–428°C), Hg from 2.1 to 6.3 ppb, and Hg/TOC from 15.5 to 31.6 ppb/wt%. This lower part of the interval corresponds to the PETM body. In the upper part of the interval (37.5-47.5 m *abs*), corresponding to the recovery phase, $\delta^{13}C_{org}$ ranges from 21.9‰ to -22.8‰, $\delta^{13}C_{carb}$ from 2.3‰ to 2.7‰, and $\delta^{18}O_{carb}$ from - 4.7‰ to -7.0‰. TOC ranges from 0.1 to 0.2 wt% (HI 48-86; OI 178-332; T_{max} 408–434°C), Hg from 2.9 to 3.8 ppb, and Hg/TOC from 14.4 to 27 ppb/wt%.

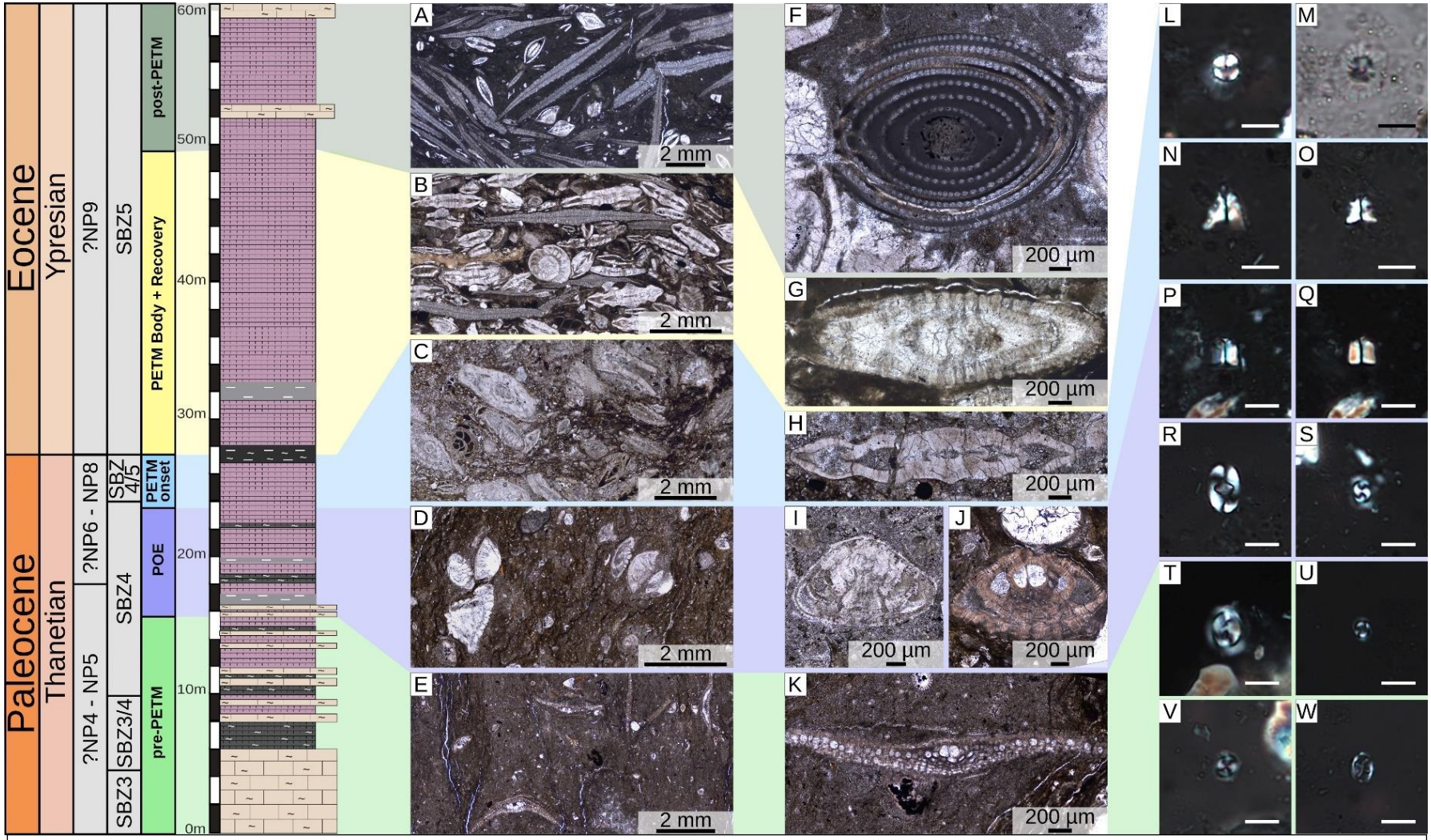

Figure 4.6: Coupled biostratigraphic and microfacies analysis highlights major environmental perturbation at Late Paleocene to Early Eocene times. Most significant LBF (E to K) and calcareous nannofossil biomarkers are shown (L to W); scale bare for calcareous nannofossils is 5 µm A) Nummulitids and orthophragminids biofacies (post-PETM stage). B) Nummulitids and orthophragminids biofacies with green calcareous algae (PETM body and early recovery). C) *Lockhartia, Daviesina, Miscellanea* and hyaline SBF with *Ranikothalia* (PETM onset). D) *Lockhartia, Daviesina, Miscellanea* and hyaline SBF (Pre-Onset Excursion). E) *Lockhartia* and hyaline SBF with orbitoidiform hyaline LBF (pre-PETM stage). F) *Alveolina*; G) *Daviesina langhami*; H) *Assilina* cf. *dandotica*; I) *Lockhartia conditii*; J) *Lockhartia prehaimei*; K) *Lackadongia tibetica*; L) *Bomolithus megastypus* (crossed polars); M) *Bomolithus megastypus* (parallel polars); N) *Fasciculithus alanii*; O) *Fasciculithus lillianiae*; P, Q) *Fasciculithus tympaniformis*; R) *Zygodiscus sheldoniae*; S) *Prinsius martinii*; T) *Prinsius bisulcus*; U) small *Toweius*; V) *Toweius pertusus*; W) *Neochiastozygus modestus*.

Post-PETM stage (47.5-59.5 m *abs*)

Calcareous marls and brown, bioclastic grainstones pass up-section to dark grey marls and impure rudstones (Fig. 4.3). The terrigenous fraction (~15% of bulk rock) consists of phyllosilicates with rare quartz and feldspars; smectite dominates over kaolinite, illite, palygorskite, and chlorite (Figs. 4.4, 4.5).

The fossil assemblage consists almost entirely of hyaline LBF (*Nummulites*, *Assilina, Operculina*, and *Discocyclina*), associated with alveolinids and subordinate SBF, green calcareous algae (mainly Dasycladales), colonial corals, mollusks, and ostracods (Fig. 4.6). The Ypresian zone SBZ5 is indicated by the occurrence of *Assilina dandotica*, *A. ornata*, *Nummulites minervensis* and *Ranikothalia nuttalli* (Figs. 4.3, 4.6). The increasing frequency of *Alveolina* is also distinctive of the Eocene. Calcareous nannofossils in this interval are very rare and not age-diagnostic.

The $\delta^{13}C_{org}$ value ranges from -22.6‰ to -23.9‰, $\delta^{13}C_{carb}$ from 2.0‰ to 2.4‰, $\delta^{18}O_{carb}$ from -4.5‰ and -5.0‰, and TOC from 0.03 to 0.1 wt% (HI 59-105; OI 236-376; T_{max} 405–435°C). Hg ranges from 0.3 to 2.1 ppb, Hg/TOC from 8.6 to 19.3 ppb/wt%. The return of $\delta^{13}C$ to pre-excursion values with a lack of major shifts indicates the beginning of the post-PETM phase.

4.6.Diagenetic overprint

Because the $\delta^{13}C$ record is crucial in constraining the PETM (Walsh, 2004), diagenetic effects need to be carefully evaluated. Bulk $\delta^{13}C$ values of carbonates ($\delta^{13}C_{carb}$) can be affected by meteoric diagenesis during subaerial exposure and by the presence of dolomite (Swart, 2015). Bulk $\delta^{13}C$ values of organic matter ($\delta^{13}C_{org}$) can be resistant to chemical processes (e.g., Midwood and Boutton, 1998) but are potentially affected by mixing of different types of organic matter when poorly consolidated marine sediments are exposed subaerially (Swart, 2015).

The lack of correlation between $\delta^{13}C_{carb}$ and $\delta^{18}O_{carb}$ in the Baroch Nala Section testifies against a significant diagenetic alteration of the carbon stable isotope record (Knauth and Kennedy 2009) (Fig. 4.7). The values $\delta^{13}C_{carb}$ fall within the range of normal marine carbonates (Lohmann 1988). Only the low $\delta^{18}O_{carb}$ is ascribed to minor meteoric alteration at low water/rock ratio, but without major modification of carbon stable-isotope

composition. The Rock-Eval analysis of organic matter indicates the dominance of type III kerogen, suggesting that significant mixing of different types of organic matter did not occur.

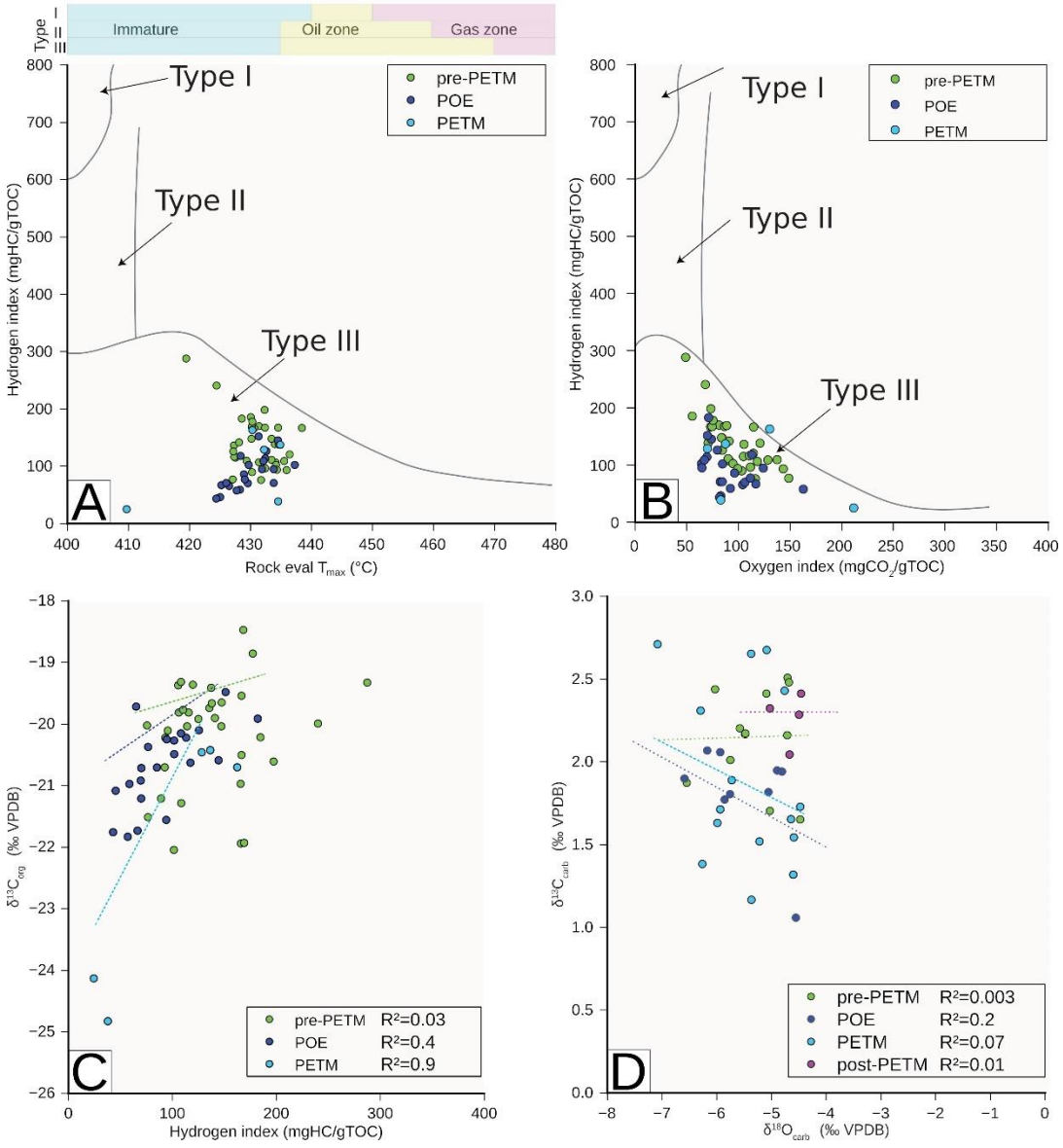

Figure 4.7: Investigating diagenetic overprint. A, B) Scatterplots of HI *vs*. Tmax and OI reveal the type III origin of kerogen in Baroch Nala section. C,D) Scatter plots $\delta^{13}C_{org}$ *vs.* HI and $\delta^{13}C_{carb}$ *vs.* $\delta^{18}O_{carb}$ indicate a lack of significant meteoric diagenesis.

The facies analysis of the Baroch Nala section rules out subaerial exposure: no exposure surfaces were observed, and the skeletal and foraminiferal assemblages point toward deposition at a water depth of ~60 m (Geel, 2000; Coletti et al., 2021). The persistent presence of smectite and palygorksite throughout the section, with very low content of illite-smectite mixed layers, indicates only minor diagenesis at shallow burial depths (Thiry, 2000; Schulte et al., 2011) (Fig. 4.5). Rock-Eval T_{max} values ranging from 410 to 444 °C, together

with all other parameters, classify the organic matter as immature to slightly mature, confirming the minimal effects of burial diagenesis (Fantasia et al., 2019) (Fig. 4.7). Limited diagenetic alteration is independently testified by skeletal assemblages: evidence of significant selective dissolution of skeletal grains is lacking and even delicate fossils like green calcareous algae are preserved (albeit as calcite molds).

4.7.Discussion

The stable isotope records, combined with data on bulk mineralogical composition, clays, organic matter, mercury, and large benthic foraminifera, currently makes the Baroch Nala section unique for studying the PETM in eastern Tethys, as, currently, no other section provides these combined datasets. The overall agreement between $\delta^{13}C_{org}$ and $\delta^{13}C_{carb}$ patterns testifies for the reliability of the recorded signal (Fig. 4.3), which is consistent with the observed variations in the whole rock mineralogical and clay compositions (Figs. 4.3-5). Both geochemical and mineralogical data align with the anticipated events of the Paleocene-Eocene transition (McInerney and Wing, 2011; Komar and Zeebe, 2017; Barnet et al., 2019) and are well constrained in time by both LBF and calcareous nannofossil assemblages (Fig. 4.6). Although the nannofossil assemblages are relatively scarce and poor in age-diagnostic forms, combined with LBF, they make a strong case for placing the PETM interval in agreement with $\delta^{13}C$ pattern.

Due to these characteristics, the Baroch Nala section provides one of the most continuous records of the PETM hyperthermal event in shallow-water settings, considering that the Dababiya GSSP section in Egypt (Khozyem et al., 2023), mostly consists of outer-shelf sediments. On the other hand, the rich faunal assemblage of the Baroch Nala section dominated by LBF and green calcareous algae indicates a deposition within the photic zone in a coastal environment (Bialik et al., 2023). This is consistent with the significant terrigenous fraction and the characteristics of organic matter (type III kerogen derived mainly from terrestrial sources) (Fig. 4.7). The dominance of hyaline benthic foraminifera over porcelaneous ones, as well as the abundance of micrite, suggest a water depth below fair-weather wave-base (possibly around 60 m; Geel, 2000; Coletti et al., 2021). Such conditions are ideal as they provide us with a quite continuous $\delta^{13}C$ record for both organic matter and carbonate with a detailed account of the biotic response by carbonate-producing assemblages, information from clay-mineral assemblages, type of organic matter, and Hg concentrations. The multi-proxy nature of the Baroch Nala section, combined with the

limited diagenetic alteration of the sediment and the lack of erosional and sub-aerial exposure surfaces, provides a strong framework to analyze in detail the Late Paleocene warming and the Paleocene – Eocene transition. As all these elements are aligned and preserved along the Baroch Nala section, the latter can be used to better interpret the overall record of the PETM in the region, even along incomplete sections.

4.7.1. Palaeoenvironmental changes across the PETM

The pre-PETM phase in the Baroch Nala section is characterized by the dominance of late Selandian to early Thanetian LBF taxa, with limited variations in the mineralogy of the terrigenous fraction and in the oxygen and carbon stable isotopes record, indicating relatively stable environmental settings. The abundance of *Lakadongia* and *Orbitosiphon*, with their thin and flat test suited for a life in dim-light conditions (Hallock and Glenn 1984), the lack of bioclastic orientation and sorting, the abundance of micrite, and the presence of green calcareous algae, indicate deposition below fair-weather wave base. The abundance of smectite and presence of palygorskite suggest an arid climate with alternating humid and dry seasons in the source region (Adatte et al., 2000, 2002; Bolle et al., 2000; Khozyem et al., 2023) (Fig. 4.8).

The overlying strata document, a remarkable negative shift in $\delta^{13}C$ (Pre-Onset Excursion "POE") associated with an increase in the terrigenous fraction and in kaolinite abundance, indicating a first marked change from the previously stable pre-PETM conditions. High global temperatures during this late Thanetian hyperthermal (Tremblin et al., 2022) strengthened the hydrological cycle, leading to increasing terrigenous supply (Zachos et al., 2005; McInerney and Wing, 2011; Schulte et al., 2011; Handley et al., 2012) and to the development of more intensely weathered, kaolinite-rich soil profiles indicating a transition towards warm-humid climate (Adatte et al., 2002). This event did not affect significantly the biotic assemblages, and the decreased abundance of thin and flat orbitoidiform LBF may be ascribed to a minor shallowing.

The major biotic turnover is documented in the overlying strata that record the PETM onset. Nummulitids -including taxa like *Assilina* that become more relevant during the Eocene- markedly increase at the expense of Paleocene taxa (in particular *Lakadongia* and *Orbitosiphon*), a change recorded just before the PETM onset all across the Himalayan region (Jiang et al., 2021; Kamran et al., 2021; Ali et al., 2024) as elsewhere in the Tethys (e.g., Zamagni et al., 2012a; Speijer et al., 2012).

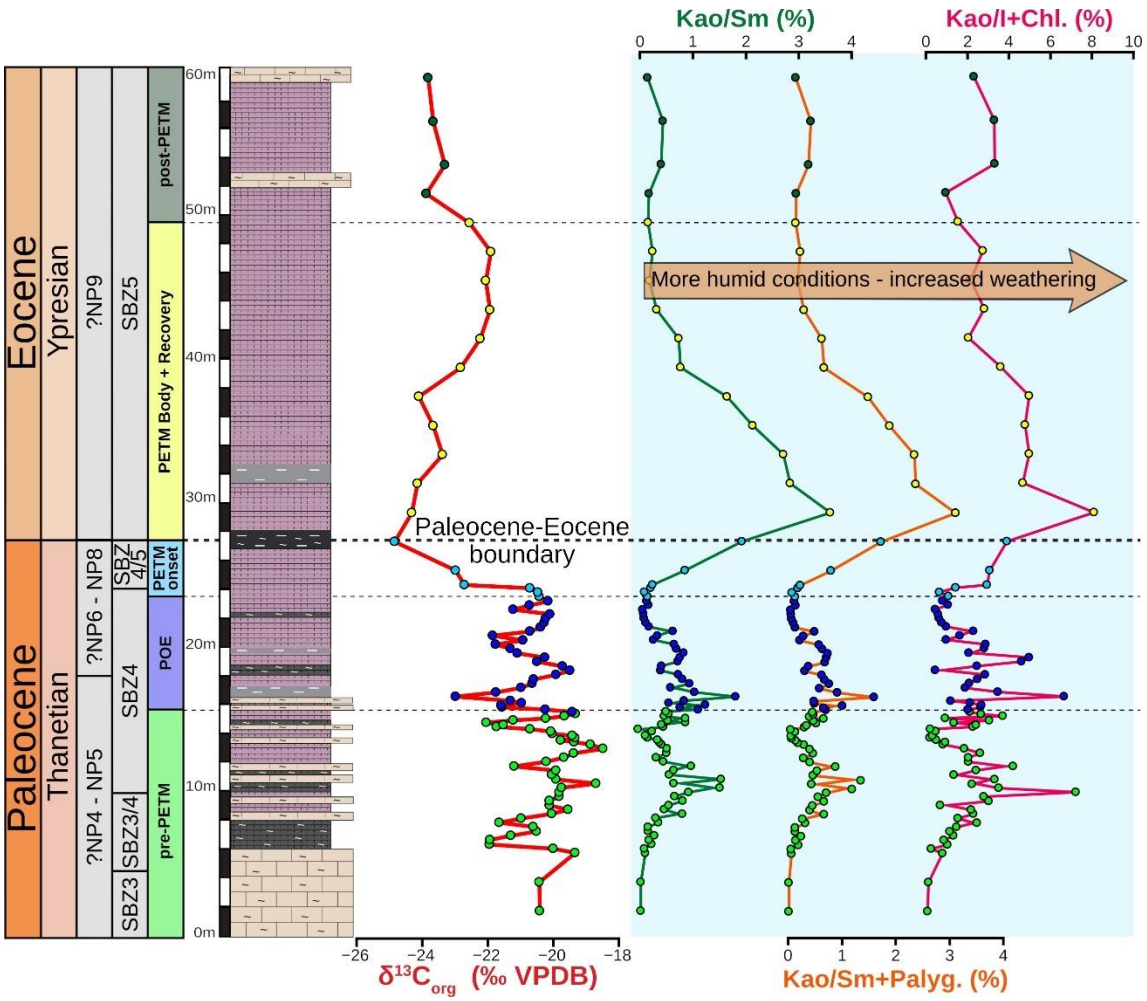

Figure 4.8: Increasing kaolinite indicates transition to more humid and warm conditions at the base of POE and PETM body.

The terrigenous fraction and kaolinite percentages increase up-section suggesting a pronounced shift towards a warmer and more humid climate associated with an increase in weathering intensity. The increase in temperature, coupled with an elevated nutrient supply caused by enhanced weathering rates, may have resulted in stressful conditions for carbonate producers, leading to the biotic turnover that favored nummulitids over Paleocene LBF taxa. *Kaolinite/smectite*, *kaolinite/(smectite+palygorskite),* and *kaolinite/(illite+chlorite)* ratios peak in strata representing the PETM body and progressively decline afterwards (Fig. 4.8). Similar trends are documented across the Tethys (Adatte, 2000; Gibson et al., 2000; Kumar et al., 2023), suggesting that the most hot-humid condition was reached just after the peak of the carbonate-isotope excursion, followed by a progressive return to semi-arid climate during the recovery phase. *Nummulites*, *Assilina*, *Discocyclina,* and *Alveolina* increased

progressively to eventually dominate the LBF assemblage, a biotic evolution paced with the shift in environmental conditions.

A return to relatively stable conditions and a semi-arid climate as in the pre-PETM phase is inferred for the post-PETM interval, where the isotopic and mineralogical records do not show major changes. The PETM event, however, left a profound and irreversible mark on LBF assemblages, dominated by nummulitids, orthophragminids, and alveolinids in the post-PETM phase. The demise of Paleocene taxa and the rise of their competitors unfolded within a relatively brief timespan, well-paced with the variations in the global carbon cycle and climatic conditions (Fig. 4.8). The changes were long-lasting, as the associations successful during the Late Paleocene environmental perturbation will dominate the shallow-water domain during the following 20 Ma, as outlined by the meta-analysis of shallow-water carbonates of eastern Tethys (Coletti et al., 2022).

4.7.2. The global picture

To better evaluate the record of biotic changes recorded in the Baroch Nala section, the latter is here compared with various sections of neritic limestones exposed across the Tethyan realm (Fig. 4.9). All stratigraphic sections studied so far show relevant changes in floral and faunal assemblages. Moving from SBZ3 representing pre-PETM conditions to SBZ4 including the POE, the diversity of typical Late Paleocene taxa (e.g., *Lockhartia*) and of LBF in general increased, with a more marked diversification of rotaliids than of nummulitids (Kahsnitz et al., 2016; Benedetti and Papazzoni, 2022). (Supplementary Table S3). Moving from the Paleocene to the Early Eocene, LBF diversity increased further, with a bloom of genera such as *Nummulites* and *Alveolina*; on the other hand, the diversity of typical Paleocene genera and of rotaliids in general decreased (Supplementary Table S3; Benedetti and Papazzoni, 2022; Benedetti et al., 2024). This change affected global carbonate production. During the Early Eocene, the output from LBF remarkably increased relative to the contribution from reef corals and red and green calcareous algae (Kiessling et al., 1999; Zamagni et al., 2012b; Pomar et al., 2017; Aguilera et al., 2020; Coletti et al., 2022; Benedetti and Papazzoni, 2022; Benedetti et al., 2024). This pattern has been documented worldwide and related to increased global temperature and fluctuations of the nutrient cycle (Zamagni et al., 2012b; Coletti et al., 2022), based on the correlation between the biotic record of certain areas and the geochemical record of others. However, in the case

of the Baroch Nala section, the progressive increase in the abundance of LBF and the turnover between Late Paleocene and Early Eocene assemblage can be directly connected with the geochemical proxy of environmental changes, further supporting the relationship between changing climate and changing ecosystems.

To shed light on the triggers of this climate change isotopic curves, clay assemblages and mercury concentrations measured in the Baroch Nala section are here compared to well-studied sections worldwide that preserve a similarly detailed record of $\delta^{13}C_{org}$, mineralogy, and Hg enrichment normalized over organic matter (Fig. 4.10). These include the Dababiya Section in Egypt (i.e., the GSSP of the Paleocene-Eocene boundary; Khozyem et al., 2023), the deep-sea record of the North Sea (Kemp al., 2016; Kender et al., 2021), and the Dibamba section in Cameroon (Bitchong et al., 2023).

The magnitude of the negative $\delta^{13}C_{org}$ shift recorded in the Baroch Nala section during the PETM is slightly larger than in the Dibamba section and very close to that observed in Egypt and in the North Sea, as well as in many other marine sections globally (McInerney and Wing, 2011). Differently from the Dababiya, Dibamba, and North Sea sections, also the earlier hyperthermal event, the pre-onset excursion (POE), is clearly identified in the Baroch Nala section. Diverse isotopic excursions predating the PETM onset were recognized both in shallow-marine stratigraphic sections (e.g., Dababiya, Khozyem et al., 2023; Lussagnet, Serraduy, and especially Esplugafreda in the Pyrenees; Tremblin et al., 2022; Čebulovica and Kozina in Slovenia, Zamagni et al., 2012a) and in the deep-marine record (e.g., Barnet et al., 2019). These events increased in frequency and became progressively more pronounced during the late Thanetian (four events between 57.5 and 56 Ma). Among the events recorded in deep-sea cores, the D1/D2, pre-dating the PETM by ~400 ka (Barnet et al., 2019), is here considered the most plausible match for the POE recorded in the Baroch Nala section.

In all sections considered in this comparison, the PETM event was associated with an increase in kaolinite abundance, testifying to an increase in weathering rates in warmer and more humid climatic conditions (e.g., Robert and Kennet, 1992; Adatte et al., 2000).

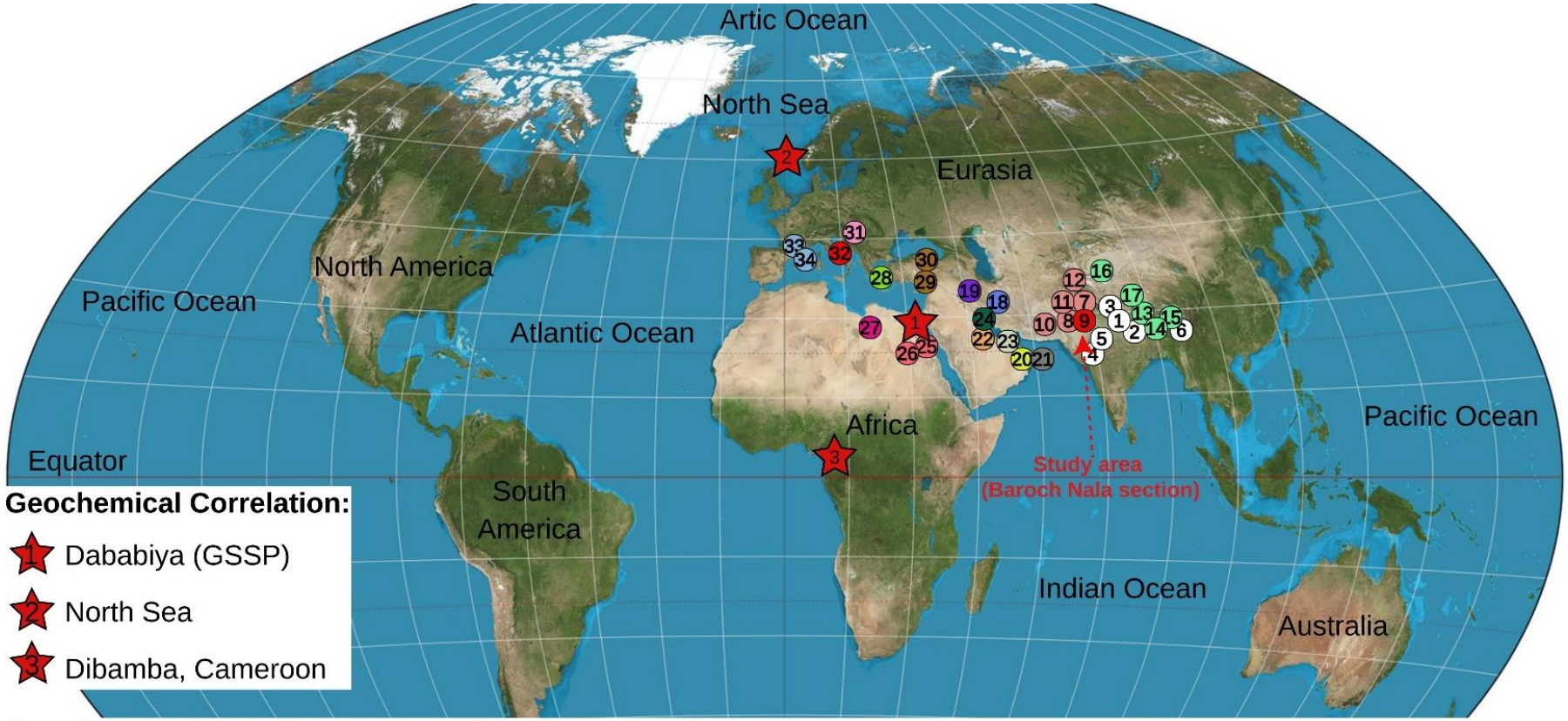

Correlation with shallow-water carbonate successions:

India 1: Ladakh (North Zanskar Tethyan), 2: Ladakh (South Zanskar Tethyan), 3:Ladakh (Indus-Tsangpo Suture Zones), 4: Katuch Basin, 5: Jaisalmer Basin, 6: Meghalaya Region. Pakistan 7: Hazara Basin, 8: Salt Range, 9: Study area (Baroch Nala - Surghar Range), 10: Lower Indus Basin, 11: Potwar Basin, 12: Hazara Kashmir Syntaxies. China 13: Tibet (Tingri area), 14: Tibet (Gamba area),15: Tibet (Düela section),16: Tarim basin,17: Xigaze forearc basin. Iran 18: Lurestan Region. Iraq 19: Kurdistan Region. UAE 20: Western UAE offshore. Oman 21: Sunab Basin. Saudi Arabia 22: Arabian Gulf. Qatar 23: Arabian Gulf. Kuwait 24: Wafra Field. Egypt 25: Farafra Oasis,Western Desert, 26: Galala Plateaus, Eastern Desert, Libya 27: Sirte Basin. Greece 28: Ionian Islands (Cephalonia and Zakynthos). Turkey 29: Tuz Gölü Basin, 30: Kastamonu region. Slovenia 31: Adriatic Platform (Cebulovica and Kozina section). Italy 32: Northern and Central Italy. Spain 33: Pyrenees (Urbasa-Andia plateau), 34: Pyrenees (Serraduy and Campo Section)

Figure 4.9: General comparison of biotic turnover in shallow-water limestone succession across Tethys. They include **India:** Ladakh (North Zanskar Tethyan; Mathur et al., 2009; Nicora et al., 1987), Ladakh (South Zanskar Tethyan; Mathur et al., 2009; Kahsnitz et al., 2018), Ladakh (Indus–Tsangpo suture zones; Mathur et al., 2009), Katuch Basin (Khanolkar & Saraswati, 2019), Jaisalmer Basin (Khanolkar et al., 2021), Meghalaya (Pereira et al., 2022 ; Ozcan et al., 2018 ; Sarkar, 2015, 2018, 2022 ; Sreenivasan et al., 2022), **Pakistan**: Hazara Basin (Ali et al., 2024), Salt Range (Nammal study (in prep); Ahmad et al., 2017; Afzal et al., 2023), Surghar range (This study), Lower Indus basin (Hussian et al., 2024 (pre print); Afzal et al., 2011a, 2011b), Potwar Basin (Ahmad et al., 2017; Afzal et al., 2023; Kamran et al., 2021), Hazara Kashmir Syntaxies (Bilal et al., 2024), **China**: Tibet (Tingri area; Zhang et al., 2013, 2019, 2020, 2023; Li et al., 2020 ; Kahsnitz et al., 2019), Tibet (Gamba and Düela section: Zhang et al., 2013, 2019; Li et al., 2022), Tarim basin (Inland China: Jiang et al., 2023; Dong et al., 2024; Cao et al., 2018), Xigaze forearc basin (Jiang e t al., 2021; Kahsnitz et al., 2018), **Iran**: Lurestan (Bagherpour & Vaziri, 2012; Kakemem et al., 2023; Adabi et al.,2008), **Iraq**: Kurdistan region (Al-Taee et al.,2024a, 2024b; Salih, 2012; Hama Salih et al., 2022, Tamar-agha et al., 2015), **UAE**: Western UAE (offshore) (Beasley et al., 2021), **Oman**: Sunab Basin (Mattern et al., 2019), **Saudi Arabia** Arabian Gulf (Hasson, 1985; Mousa et al., 2023), **Qatar**: Arabian Gulf (Hewaidy, 1994; Hewaidy & Hatimi 1993), **Kuwait:** Wafra Field (Bou-rabee & Burke, 1987). **Egypt**: Farafra Oasis-Western Desert (Farouk et al., 2019), Galala Plateaus-Eastern Desert (Abd-Elhameed et al., 2023; Hontzsch et al., 2011a, 2011b; Ozcan et al., 2014), Libya: Sirte Basin (Vršič et al., 2021a, 2021b, El Hassi, 1995), **Greece:** Ionian Islands (Cephalonia and Zakynthos) (Accordi et al., 1998, 2014), **Turkey**: Tuz Gölü Basin (GÖRMÜŞ et al., 2024), Kastamonu region (Ozgen-Erdem et al., 2005), **Slovenia:** Adriatic Platform (Cebulovica and Kozina section) (Zamangi et al., 2008, 2012) **Italy**: Northern Italy, Belluno Basin and Lombardian Basin (Papazzoni et al., 2023), Central Italy, Abruzzi Platform (Benedetti et al., 2018; Tomassetti & Benedetti, 2020), **Spain**: Pyrenees (Urbasa-Andia plateau) (Baceta et al., 2005), Pyrenees (Serraduy and Campo Section) (Serra-Kiel et al., 2020, Aguirre et al.,2022, Li et al., 2021).

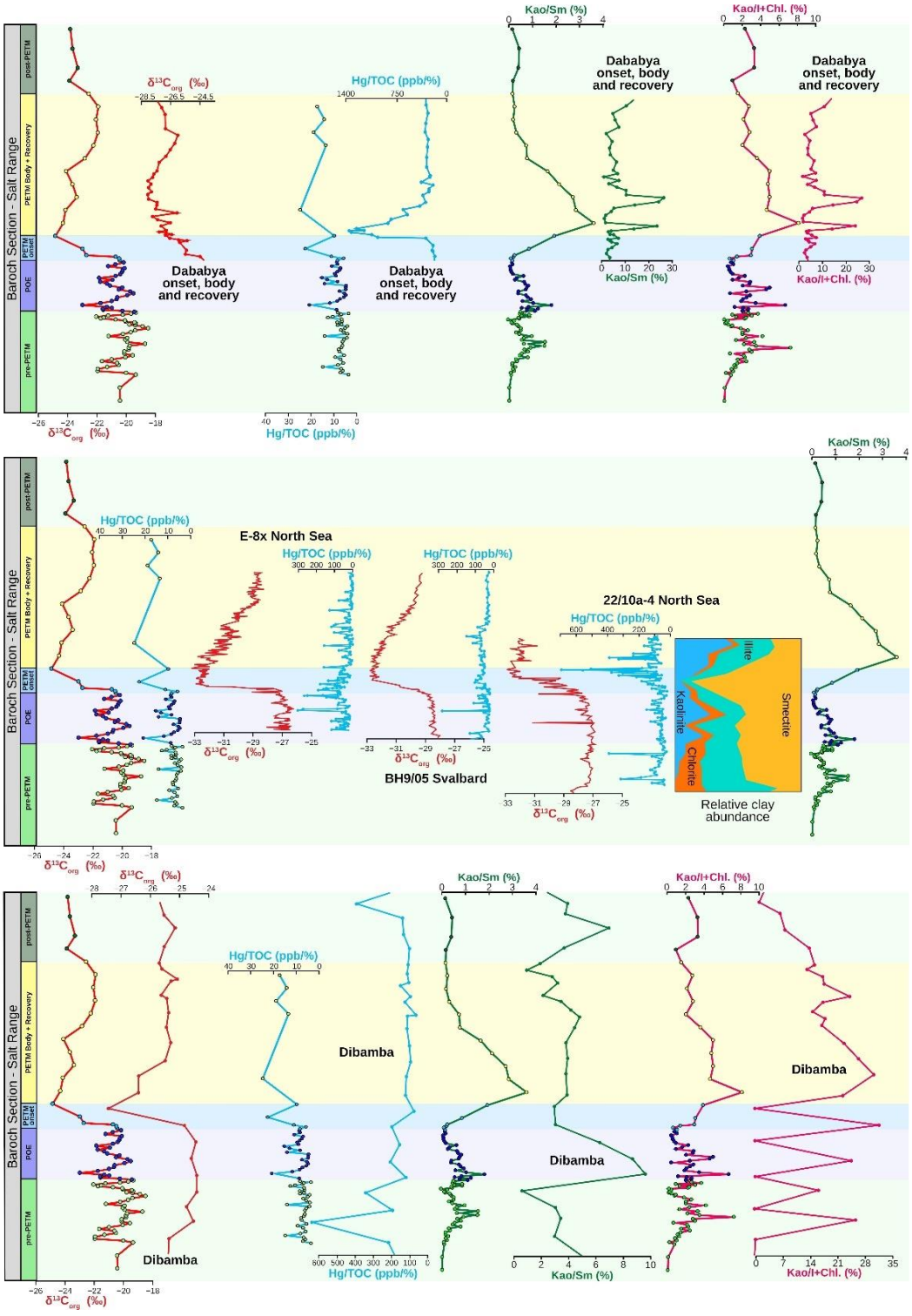

Figure 4.10: Comparison of stratigraphic, mineralogical, and geochemical (carbon isotopes, Hg/TOC) records among Baroch Nala section, Dababya section in Egypt (global stratotype of Paleocene–Eocene transition; Khozyem et al., 2023), Dibamba Section in Cameroon (Bitchong et al., 2023), and deep-water sedimentary succession of the North Sea (Kender et al., 2021; Kemp et al., 2016) (See Figure 9 for the location of all the sections)

The rise in global temperatures most likely led to an enhanced hydrological cycle, increased terrigenous supply to the oceans, and ocean acidification (Zachos et al., 2005), which may explain the sharp decrease in calcite widely recorded during the PETM in both shallow-water and deep-water settings.

The increase in temperature and the biotic turnovers associated with the PETM were significantly larger than during the other Paleocene hyperthermals (Zachos et al., 2005; Barnet et al., 2019). The high-resolution analysis of the deep-sea record of the South Atlantic and equatorial Pacific oceans testifies to the global and periodic nature of Paleocene hyperthermals, suggesting eccentricity as the dominant control: an initial orbitally related warming could have been amplified by the release of isotopically light carbon from temperature-sensitive reservoirs (e.g., biogenic CH_4, high-latitude permafrost; Barnet et al., 2019). The PETM, however, represents a notable exception. Although the peak of the PETM is broadly in phase with a 100-ka eccentricity maximum, this event did not begin during the 405-ka eccentricity maximum like other hyperthermals, suggesting that it may not have been triggered solely by orbital forcing. Volcanism in the North Atlantic Igneous Province may have represented a fundamental additional factor (Barnet et al., 2019). The same conclusion was reached by Kender et al. (2021), based on the study of North-Sea cores using the Hg/TOC ratio as a proxy for volcanic activity (e.g., Tremblin et al, 2022, Jones, et al., 2023), and is consistent with the observed peaks in the Hg/TOC ratio that generally precede the PETM (Fig. 4.10). The massive release of greenhouse volcanic gases is likely to have pushed global conditions beyond a tipping point, resulting in the environmental perturbations that led to the observed massive changes among carbonate-producing LBF communities during the PETM.

4.8.Conclusions

Early Paleogene hyperthermals represent very useful analogues to understand current climate change and foresee its consequences, as they were also triggered by a relatively fast increase in global temperature coupled with massive release of greenhouse gases in the atmosphere. The PETM hyperthermal is well recorded in deep-sea sedimentary successions,

whereas shallow-marine successions are generally incomplete and fail to document environmental and biotic changes with the same level of detail. The stratigraphic continuity across the investigated Upper Paleocene to Lower Eocene strata in the Baroch Nala section (Surghar Range, NE Pakistan) allows us to integrate a perfectly continuous $\delta^{13}C$ record for both organic matter and carbonate with a detailed account of the biotic response by carbonate-producing assemblages, information from clay-mineral assemblages, type of organic matter, and Hg concentration. Because of such an extensive multi-technique dataset, the Baroch Nala section is here proposed as a key reference section for tracking paleoenvironmental variations during the PETM in shallow-marine environments of the eastern Tethys. The Baroch Nala section was deposited on a shallow carbonate shelf below wave base, i.e., in waters deep enough to the preserve pristine geochemical signals and shallow enough to fully document biotic turnovers on the platform. Five stratigraphic intervals were identified in the Baroch Nala section based on sedimentological, micropaleontological, and geochemical evidence, each corresponding to a different stage of the Late Paleocene-Early Eocene environmental and ecological transition: 1) pre-PETM stage; 2) pre-onset excursion (POE); 3) PETM onset; 4) PETM body and recovery; 5) post-PETM stage. Relatively stable conditions during the pre-PETM stage were initially disrupted by a first shift towards a more humid climate and increased terrigenous supply corresponding to the POE, when a first change in skeletal assemblages but no major biotic turnover is observed. During the PETM onset and body, the increased global temperature and a more pronounced shift towards humid conditions enhanced weathering intensity and nutrient supply. Stressful environmental conditions favored a major biotic turnover with long-lasting consequences. Among large benthic foraminifera, nummulitids outcompeted the *Lockhartia* assemblages that were dominant earlier in the Paleocene, and they remained as the primary carbonate producers in the eastern Tethys for the following 20 million years.

4.9.References

Abbasi, I. A., & McElroy, R. (1991). Thrust kinematics in the Kohat plateau, trans Indus range, Pakistan. *Journal of structural geology*, *13*(3), 319-327.

Abd-Elhameed, S., Mahmoud, A. A., & Salama, Y. (2023). Late Paleocene–Early Eocene larger foraminifera from the Galala Plateaus, North Eastern Desert, Egypt: biostratigraphic,

paleoenvironmental and paleoecological implications. Carbonates and Evaporites, 38(4), 84.

Accordi, G., Carbone, F., Di Carlo, M., & Pignatti, J. (2014). Microfacies analysis of deep-water breccia clasts: a tool for interpreting shallow-vs. deep-ramp Paleogene sedimentation in Cephalonia and Zakynthos (Ionian Islands, Greece). Facies, 60, 445-466.

Accordi, G., Carbone, F., & Pignatti, J. (1998). Depositional history of a Paleogene carbonate ramp (western Cephalonia, Ionian Islands, Greece). Geologica Romana, 34, 131–205

Adatte, T., Bolle, M. P., Kaenel, E. D., Gawenda, P., Winkler, W., & Von Salis, K. (2000). Climatic evolution from Paleocene to earliest Eocene inferred from clay-minerals: A transect from northern Spain (Zumaya) to southern (Spain, Tunisia) and southeastern Tethys margins (Israel, Negev). *GFF*, *122*(1), 7-8.

Adatte, T., Keller, G., & Stinnesbeck, W. (2002). Late Cretaceous to early Paleocene climate and sea-level fluctuations: the Tunisian record. *Palaeogeography, Palaeoclimatology, Palaeoecology*, *178*(3-4), 165-196.

Adabi, M. H., Zohdi, A., Ghabeishavi, A., & Amiri-Bakhtiyar, H. (2008). Applications of nummulitids and other larger benthic foraminifera in depositional environment and sequence stratigraphy: an example from the Eocene deposits in Zagros Basin, SW Iran. Facies, 54(4), 499-512.

Afzal, J., Williams, M., Leng, M. J., Aldridge, R. J., & Stephenson, M. H. (2011a). Evolution of Paleocene to Early Eocene larger benthic foraminifer assemblages of the Indus Basin, Pakistan. Lethaia, 44(3), 299-320.

Afzal, J., Williams, M., Leng, M. J., & Aldridge, R. J. (2011b). Dynamic response of the shallow marine benthic ecosystem to regional and pan-Tethyan environmental change at the Paleocene–Eocene boundary. Palaeogeography, Palaeoclimatology, Palaeoecology, 309(3-4), 141-160.

Afzal, J., & Butt, A. A. (2023). Late Paleocene to Early Eocene integrated biostratigraphic framework, chronostratigraphy and Paleocene/Eocene boundary in the Salt Range, Pakistan. In Stratigraphy & Timescales (Vol. 8, pp. 265-330). Academic Press.

Agnini, C., Fornaciari, E., Raffi, I., Catanzariti, R., Palike, H., Backman, J., Rio, D., 2014. Biozonation and biochronology of Paleogene calcareous nannofossils from low and middle latitudes. Newsl. Stratigr. 47, 131–181.

Aguilera, O., Bencomo, K., de Araújo, O.M.O., Dias, B.B., Coletti, G., Lima, D., Silane, A.F., Polk, M., Alves-Martin, M.V., Jaramillo, C., Kutter, V.T. & Lopes, R.T. (2020) Miocene

heterozoan carbonate systems from the western Atlantic equatorial margin in South America: the Pirabas formation. Sedimentary Geology, 407, 1–28.

Aguirre, J., Baceta, J. I., & Braga, J. C. (2022). Coralline Algae at the Paleocene/Eocene Thermal Maximum in the Southern Pyrenees (N Spain). Frontiers in Marine Science, 9, 899877.

Ahmad, S., Kroon, D., Rigby, S., & Khan, S. (2017). Paleogene Nummulitid biostratigraphy of the Kohat and Potwar Basins in north-western Pakistan with implications for the timing

of the closure of eastern Tethys and uplift of the western Himalayas. Stratigraphy, 13(4), 277-301.

Ali, F., Khan, M. I., Ahmad, S., Rehman, G., Rehman, I., & Ali, T. H. (2014). Range front structural style: an example from Surghar Range, North Pakistan. *Journal of Himalayan Earth Sciences*, *47*(2), 193.

Ali, M., Coletti, G., Mariani, L., Benedetti, A., Munawar, M.J., Rehman, S.U., Sternai, P., Basso, D., Malinverno, E., Shahzad, K., Khan, S., Awais, M., Usman. M., Castelltort, S., Adatte, T.,& Garzanti, E. (2024). Shallow-water carbonate facies herald the onset of the Paleocene-Eocene Thermal Maximum (Hazara basin, Northern Pakistan). *Journal of Asian Earth Sciences: X* , *11* , 100169.

Al-Taee, N. T., Ghafor, I. M., Al-Juboury, A. I., & Dettman, D. L. (2024). Biostratigraphy and Paleoecology of the Sinjar Formation (Late Paleocene-Early Eocene) in the Dokan and Sinjar Areas, Iraq. The Iraqi Geological Journal, 221-249.

Al-Taee, N. T., Al-Juboury, A. I., Ghafor, I. M., Zanoni, G., & Rowe, H. (2024). Depositional environment of the late Paleocene-early Eocene Sinjar Formation, Iraq: Implications from facies analysis, mineralogical and geochemical proxies. Heliyon, 10(4).

Babila, T. L., Penman, D. E., Standish, C. D., Doubrawa, M., Bralower, T. J., Robinson, M. M.,

Self-Trail, J.J., Speijer, R., Stassen, P., Foster, G., & Zachos, J. C. (2022). Surface ocean warming and acidification driven by rapid carbon release precedes Paleocene-Eocene Thermal Maximum. Science Advances, 8(11), eabg1025.

Baceta, J. I., Pujalte, V., & Bernaola, G. (2005). Paleocene coralgal reefs of the western Pyrenean basin, northern Spain: New evidence supporting an earliest Paleogene recovery of reefal ecosystems. Palaeogeography, Palaeoclimatology, Palaeoecology, 224(1-3), 117-143.

Barnet, J. S., Littler, K., Westerhold, T., Kroon, D., Leng, M. J., Bailey, I., Rohl, U. & Zachos, J. C. (2019). A high-Fidelity benthic stable isotope record of late Cretaceous–early Eocene climate change and carbon-cycling. *Paleoceanography and Paleoclimatology*, *34*(4), 672-691.

Bagherpour, B., & Vaziri, M. R. (2012). Facies, paleoenvironment, carbonate platform and facies changes across Paleocene Eocene of the Taleh Zang Formation in the Zagros Basin, SW-Iran. Historical Biology, 24(2), 121-142.

Beasley, C., Cotton, L., Al Suwaidi, A., LeVay, L., Sluijs, A., Ullman, C., ... & Littler, K. (2020). Triumph and tribulation for shallow water fauna during the Paleocene–Eocene transition; insights from the United Arab Emirates. Newsletters on Stratigraphy.

Behar, F., Beaumont, V. D. E. B., & Penteado, H. D. B. (2001). Rock-Eval 6 technology: performances and developments. *Oil & Gas Science and Technology*, *56*(2), 111-134.

Benedetti, A., Marino, M., & Pichezzi, R. M. (2018). Paleocene to lower Eocene larger foraminiferal assemblages from Central Italy: new remarks on biostratigraphy. *Rivista italiana di Paleontologia e Stratigrafia*, *124*(1).

Benedetti, A., & Papazzoni, C. A. (2022). Rise and fall of rotaliid foraminifera across the Paleocene and Eocene times. Micropaleontology, 68(2).

Benedetti, A., Papazzoni, C. A., & Bosellini, F. R. (2024). Unparallel resilience of shallow-water tropical calcifiers (foraminifera and scleractinian reef corals) during the early Paleogene global warming intervals. Palaeogeography, Palaeoclimatology, Palaeoecology, 651, 112393.

Bialik, O. M., Coletti, G., Mariani, L., Commissario, L., Desbiolles, F., & Meroni, A. N. (2023). Availability and type of energy regulate the global distribution of neritic carbonates. Scientific Reports, 13(1), 19687.

Bilal, A., Yang, R., Li, Y., Zhang, J., & Janjuhah, H. T. (2024). Microfacies shift in the Late Paleocene–Early Eocene Patala Formation in the Upper Indus Basin (Pakistan): Implications for development of the Ceno-Tethys Ocean. Marine and Petroleum Geology, 161, 106693.

Bitchong, A. M., Adatte, T., Ngos III, S., Keller, G., Karabeyoğlu, A. U., & Spangenberg, J. E. (2023). The Paleocene-Eocene transition in the Gulf of Guinea: Evidence of the PETM in the Douala basin, Cameroon. *Marine and Petroleum Geology*, *157*, 106504.

Bolle, M. P., Tantawy, A. A., Pardo, A., Adatte Therry., Burns, S., & Kassab, A. (2000). Climatic and environmental changes documented in the upper Paleocene to lower Eocene of Egypt. *Eclogae Geologicae Helvetiae*, *93*(1), 33-52.

Bou-Rabee, F., & Burke, C. D. (1987). Lithostratigraphy and environment of deposition of the top of the Wafra member, Radhuma formation (Wafra field, Kuwait). Palaeogeography, palaeoclimatology, palaeoecology, 59, 269-277.

Bowen, G. J., Maibauer, B. J., Kraus, M. J., Röhl, U., Westerhold, T., Steimke, A., Gingerich, P.D., Wing, S.L., & Clyde, W. C. (2015). Two massive, rapid releases of carbon during the onset of the Paleocene–Eocene thermal maximum. *Nature Geoscience*, *8*(1), 44-47.

Bralower, T. J., Kump, L. R., Self-Trail, J. M., Robinson, M. M., Lyons, S., Babila, T., Ogg, J. G., & Zachos, J. C. (2018). Evidence for shelf acidification during the onset of the Paleocene-Eocene thermal maximum. Paleoceanography and Paleoclimatology, 33(12), 1408-1426.

Cao, W., Xi, D., Melinte-Dobrinescu, M. C., Jiang, T., Wise Jr, S. W., & Wan, X. (2018). Calcareous nannofossil changes linked to climate deterioration during the Paleocene–Eocene thermal maximum in Tarim Basin, NW China. Geoscience Frontiers, 9(5), 1465-1478.

Charles, A. J., Condon, D. J., Harding, I. C., Pälike, H., Marshall, J. E., Cui, Y., Kump, L. R., & Croudace, I. W. (2011). Constraints on the numerical age of the Paleocene-Eocene boundary. Geochemistry, Geophysics, Geosystems, 12(6), Q0AA17.

Chen, C., Guerit, L., Foreman, B.Z., Hassenruck-Gudipati, H.J., Adatte, T., Honegger, L., Perret, M., Sluijs, A., Castelltort, S., 2018. Estimating regional flood discharge during Paleocene-Eocene global warming. Sci. Rep. 8, 1–8. https://doi.org/10.1038/ s41598-018-31076-3.

Coletti, G., Mariani, L., Garzanti, E., Consani, S., Bosio, G., Vezzoli, G., Hu, X., & Basso, D. (2021). Skeletal assemblages and terrigenous input in the Eocene carbonate systems of the Nummulitic Limestone (NW Europe). *Sedimentary Geology*, *425*, 106005.

Coletti, G., Commissioner, L., Mariani, L., Bosio, G., Desbiolles, F., Soldi, M., & Bialik, OM (2022). Paleocene to Miocene southern Tethyan carbonate factories: A meta-analysis of

the successions of South-western and Western Central Asia. *The Depositional Record* , *8* (3), 1031-1054.

Dong, Y., Gachetti, A., Wu, Q., De Palma, M., Hu, X., Brachfeld, S., Passaglia, G., Jiang, L., Zhao, Y., & Cui, Y. (2024). Paleoenvironment reconstruction of the eastern Tethys during the pre-onset excursion preceding the PETM. Palaeogeography, Palaeoclimatology, Palaeoecology, 647, 112234.

El Hassi, A. M. (1995). Facies and sequence stratigraphy of the tamet formation (middle eocene), eastern sirte basin, Libya (Doctoral dissertation, Durham University).

Fantasia, A., Adatte, T., Spangenberg, J. E., Font, E., Duarte, L. V., & Föllmi, K. B. (2019). Global versus local processes during the Pliensbachian–Toarcian transition at the Peniche GSSP, Portugal: a multi-proxy record. *Earth-Science Reviews*, *198*, 102932.

Farouk, S., Khalifa, M. A., El-Hassan, M. M. A., Papazzoni, C. A., Frontalini, F., Coccioni, R., & Zaky, A. S. (2019). Upper Paleocene to lower Eocene microfacies, biostratigraphy, and paleoenvironmental reconstruction in the northern Farafra Oasis, Western Desert (Egypt). Micropaleontology, 65(5), 381-406.

Flügel, E., & Munnecke, A. (2010). *Microfacies of carbonate rocks: analysis, interpretation and application* (Vol. 976, p. 2004). Berlin: springer.

Garzanti, E. (2019). The Himalayan Foreland Basin from collision onset to the present: A sedimentary–petrology perspective. *Geological Society, London, Special Publications*, *483*(1), 65-122.

Geel, T. (2000). Recognition of stratigraphic sequences in carbonate platform and slope deposits: empirical models based on microfacies analysis of Palaeogene deposits in southeastern Spain. *Palaeogeography, palaeoclimatology, palaeoecology*, *155*(3-4), 211-238.

Gibson, T. G., Bybell, L. M., Thomas, E., & Zachos, J. C. (2000). Kaolinite distribution in Paleocene/Eocene boundary strata of northeastern United States and Pakistan–climatic and stratigraphic implications. *GFF* , *122* (1), 56-56.

Görmüş, M., Yildiz, M., Bozkurt, A., & Hakyemez, A. (2024). Paleocene-Eocene foraminifera from the Tuz Gölü Basin (Salt Lake Basin, Central Türkiye) and their paleoenvironmental interpretations. Bulletin of the Mineral Research and Exploration, (early view), 1-1.

Hallock, P., & Glenn, E. C. (1986). Larger foraminifera: a tool for paleoenvironmental analysis of Cenozoic carbonate depositional facies. Palaios, 55-64.

Hama Salih, H. M., Baziany, M. M., Hama Salih, T. M., & Surdashy, A. M. (2022). Synorogenic carbonate sedimentation in the Zagros Peripheral Foreland Basin: the Sinjar Formation in Sulaimani area, Iraqi Kurdistan region as a case study. Arabian Journal of Geosciences, 15(23), 1716.

Handley, L., O'Happelloran, A., Pearson, P. N., Hawkins, E., Nicholas, C. J., Schouten, S., McMillan, I.K., & Pancost, R. D. (2012). Changes in the hydrological cycle in tropical East Africa during the Paleocene–Eocene Thermal Maximum. *Palaeogeography, Palaeoclimatology, Palaeoecology* , *329* , 10-21.

Hasson, P. F. (1985). New observations on the biostratigraphy of the Saudi Arabian Umm er Radhuma Formation (Paleogene) and its correlation with neighboring regions. Micropaleontology, 335-364.

Hewaidy, A., & Al-Hitmi, H. H. (1993). Cretaceous-early eocene foraminifera from dukhan oil field, west qatar, arabian gulf. Suborders Textulariina, Involutinina and Miliolina. Al-Azhar Bulletin of Science, 4(2), 469-494.

Hewaidy, A. G. (1994). Biostratigraphy of the Umm er Radhuma Formation in southeast Qatar, Arabian Gulf. Neues Jahrbuch für Geologie und Paläontologie, Abhandlungen, 193, 145-164.

Höntzsch, S., Scheibner, C., Kuss, J., Marzouk, A. M., & Rasser, M. W. (2011a). Tectonically driven carbonate ramp evolution at the southern Tethyan shelf: the Lower Eocene succession of the Galala Mountains, Egypt. Facies, 57, 51-72.

Höntzsch, S., Scheibner, C., Guasti, E., Kuss, J., Marzouk, A. M., & Rasser, M. W. (2011b). Increasing restriction of the Egyptian shelf during the Early Eocene?—New insights from a southern Tethyan carbonate platform. Palaeogeography, Palaeoclimatology, Palaeoecology, 302(3-4), 349-366.

Hottinger, L. (2009). The Paleocene and earliest Eocene foraminiferal Family Miscellaneidae: neither nummulitids nor rotaliids. *Carnets de Géologie/Notebooks on Geology, Brest, Article*, *6*.

Hottinger, L., & Bassi, D. (2014). *Paleogene larger rotaliid foraminifera from the western and central Neotethys* (pp. 3-191). Berlin: Springer.

Hu, X., Garzanti, E., Wang, J., Huang, W., An, W., & Webb, A. (2016). The timing of India-Asia collision onset–Facts, theories, controversies. *Earth-Science Reviews*, *160*, 264-299.

Hussain, H. S., Abbott, A., Löhr, S. C., Hanif, M., Murray, S. T., Mohibullah, M., & Ghani, M. (2024). Expression of the Paleocene-Eocene Thermal Maximum in shallow-water carbonates of central eastern Tethys (Lower Indus Basin, Pakistan). Authorea Preprints.

Jiang, J., Hu, X., Li, J., BouDagher-Fadel, M., & Garzanti, E. (2021). Discovery of the Paleocene-Eocene Thermal Maximum in shallow-marine sediments of the Xigaze forearc basin, Tibet: A record of enhanced extreme precipitation and siliciclastic sediment flux. Palaeogeography, Palaeoclimatology, Palaeoecology, 562, 110095.

Jiang, J., Hu, X., Li, J., Garzanti, E., Jiang, S., Cui, Y., & Wang, Y. (2023). Eustatic change across the Paleocene-Eocene Thermal Maximum in the epicontinental Tarim seaway. Global and Planetary Change, 229, 104241.

Jones, M. T., Stokke, E. W., Rooney, A. D., Frieling, J., Pogge von Strandmann, P. A. E., Wilson, D. J., Selnes, H., Mather, T. A., Schreck, S., Schwark, L., & Schultz, B. P. (2023). Tracing North Atlantic volcanism and seaway connectivity across the Paleocene–Eocene thermal maximum (PETM). Climate of the Past, 19(8), 1623-1652. https://doi.org/10.5194/cp-19-1623-2023

Kahsnitz, M. M., Willems, H., Luo, H., & Zhou, Z. C. (2018). Paleocene and Lower Eocene shallow-water limestones of Tibet: Microfacies analysis and correlation of the eastern Neo-Tethyan Ocean. Palaeoworld, 27(2), 226-246.

Kahsnitz, M. M., Zhang, Q., & Willems, H. (2016). Stratigraphic distribution of the larger benthic foraminifera Lockhartia in south Tibet (China). The Journal of Foraminiferal Research, 46(1), 34-47.

Kahsnitz, M. M., & Willems, H. (2019). Genesis of Paleocene and Lower Eocene shallow-water nodular limestone of South Tibet (China). Carbonates and Evaporites, 34, 199-218.

Kakemem, U., Cotton, L. J., Hadavand-Khani, N., Fallah-Bagtash, R., Thibault, N., & Anderskouv, K. (2023). Litho-and biostratigraphy of the early Eocenelarger benthic foraminifera-dominated carbonates of the central Tethys domain, Zagros Foreland Basin, SW Iran. Sedimentary Geology, 455, 106477.

Kamran, M., Frontalini, F., Xi, D., Papazzoni, C. A., Jafarian, A., Latif, K., Jiang, T., Mirza, K., Song, H., & Wan, X. (2021). Larger benthic foraminiferal response to the PETM in the Potwar Basin (Eastern Neotethys, Pakistan). *Palaeogeography, Palaeoclimatology, Palaeoecology* , *575* , 110450.

Kazmi, A.H. & Rana, R.A. (1982). Tectonic map of Pakistan at a scale of 1:200,000. Geological Survey of Pakistan, Quetta.

Kender, S., Bogus, K., Pedersen, G. K., Dybkjær, K., Mather, T. A., Mariani, E., Ridgwell, A., Riding, J.B., Wagner, T., Hesselbo, S.P. & Leng, M. J. (2021). Paleocene/Eocene carbon feedbacks triggered by volcanic activity. *Nature communications*, *12*(1), 5186.

Kennett, J. P., & Stott, L. D. (1991). Abrupt deep-sea warming, palaeoceanographic changes and benthic extinctions at the end of the Paleocene. Nature, 353(6341), 225–229

Kemp, S. J., Ellis, M. A., Mounteney, I., & Kender, S. (2016). Palaeoclimatic implications of high-resolution clay mineral assemblages preceding and across the onset of the Paleocene–Eocene Thermal Maximum, North Sea Basin. *Clay Minerals* , *51* (5), 793-813.

Khanolkar, S., & Saraswati, P. K. (2019). Eocene foraminiferal biofacies in Kutch Basin (India) in context of palaeoclimate and palaeoecology. Journal of Palaeogeography, 8(1), 21.

Khanolkar, S., Choudhury, T. R., Saraswati, P. K., & Banerjee, S. (2021). Late Paleocene-early Eocene foraminiferal assemblage and carbon isotope excursion indicating hyperthermal events in paleotropical succession of northwestern India. Journal of Foraminiferal Research, 51(1), 4-13.

Khozyem, H., Adatte, T., Spangenberg, J. E., Keller, G., Tantawy, A. A., & Ulianov, A. (2015). New geochemical constraints on the Paleocene–Eocene thermal maximum: Dababiya GSSP, Egypt. Palaeogeography, Palaeoclimatology, Palaeoecology, 429, 117-135.

Khozyem, H., Adatte, T., & Keller, G. (2023). Climatic and Environmental Changes During Paleocene-Eocene Thermal Maximum in Egypt: An Overview. *The Phanerozoic Geology and Natural Resources of Egypt*, 305-338.

Kiessling, W., Flügel, E., & Golonka, J. (1999). Paleoreef maps: evaluation of a comprehensive database on Phanerozoic reefs. AAPG bulletin, 83(10), 1552-1587.

Klug, H. P., & Alexander, L. E. (1974). *X-ray diffraction procedures: for polycrystalline and amorphous materials* (p. 992).

Knauth, L.P., Kennedy, M.J., 2009. The late Precambrian greening of the Earth. Nature, 460 (7256), 728–732.

Knoll, A. H., Hayes, J. M., Kaufman, A. J., Swett, K., & Lambert, I. B. (1986). Secular variation in carbon isotope ratios from Upper Proterozoic successions of Svalbard and East Greenland. Nature, 321(6073), 832-838.

Komar, N., & Zeebe, R. E. (2017). Redox-controlled carbon and phosphorus burial: A mechanism for enhanced organic carbon sequestration during the PETM. Earth and Planetary Science Letters, 479, 71-82.

Kumar, R., Hameed, A., & Srivastava, P. (2023). Clay mineralogical evidence of near-equatorial Paleocene–Eocene Thermal Maximum in Barmer Basin, India. *Clay Minerals*, *58*(2), 121-142.

Li, J., Hu, X., Zachos, J. C., Garzanti, E., & BouDagher-Fadel, M. (2020). Sea level, biotic and carbon-isotope response to the Paleocene–Eocene thermal maximum in Tibetan Himalayan platform carbonates. *Global and Planetary Change*, *194*, 103316.

Li, J., Hu, X., Garzanti, E., & BouDagher-Fadel, M. (2021). Climate-driven hydrological change and carbonate platform demise induced by the Paleocene–Eocene Thermal Maximum (southern Pyrenees). Palaeogeography, Palaeoclimatology, Palaeoecology, 567, 110250.

Li, J., Hu, X., Garzanti, E., & BouDagher-Fadel, M. (2022). Spatial heterogeneity in carbonate-platform environments and carbon isotope values across the Paleocene–Eocene thermal maximum (Tethys Himalaya, South Tibet). Global and Planetary Change, 214, 103853.

Lohmann, K. C. (1988). Geochemical patterns of meteoric diagenetic systems and their application to studies of paleokarst. In paleokarst (pp. 58-80). New York, NY: Springer New York.

Martini, E., 1971. Standard Tertiary and Quaternary calcareous nannoplankton zonation. In: Farinacci, A. (Ed.), Proceedings 2nd International Conference Planktonic Microfossils. Tecnosci, Rome, pp. 739–785.

Mathur, N. S., Juyal, K. P., & Kumar, K. (2009). Larger foraminiferal biostratigraphy of lower Paleogene successions of Zanskar Tethyan and Indus-Tsangpo Suture Zones, Ladakh, India in the light of additional data. Himalayan Geology, 30(1), 45-68.

Mattern, F., & Bernecker, M. (2019). A shallow marine clinoform system in limestones (Paleocene/Eocene Jafnayn Formation, Oman): geometry, microfacies, environment and processes. Carbonates and Evaporites, 34, 101-113.

McInerney, F. A., & Wing, S. L. (2011). The Paleocene-Eocene Thermal Maximum: A perturbation of carbon cycle, climate, and biosphere with implications for the future. *Annual Review of Earth and Planetary Sciences*, *39*, 489-516.

McDougall, J. W., & Hussain, A. (1991). Fold and thrust propagation in the western Himalaya based on a balanced cross section of the Surghar Range and Kohat Plateau, Pakistan. *AAPG bulletin*, *75*(3), 463-478.

Menini, A., Mattioli, E., Vinçon-Laugier, A., & Suan, G. (2022). Calcareous nannofossil biostratigraphy across the Paleocene-Eocene Thermal Maximum. Newsletters on Stratigraphy, 55(1), 69-97.

Midwood, A. J., & Boutton, T. W. (1998). Soil carbonate decomposition by acid has little effect on δ13C of organic matter. Soil biology and biochemistry, 30(10-11), 1301-1307.

Mousa, A. K., Mohammed, I. Q., Al-Dulaimi, S. I., & Lawa, F. A. (2023). Stratigraphic Analysis and Depositional Environment of the Newly Recorded Umm Er Rhadhuma Formation (Paleocene) from the Borehole K. H12/7, South Anah City, Western Iraq. The Iraqi Geological Journal, 94-109.

Nicora, A., Garzanti, E., & Fois, E. (1987). Evolution of the Tethys Himalaya continental shelf during Maastrichtian to Paleocene (Zanskar, India). Rivista Italiana di Paleontologia e Stratigrafia, 92(4), 399-434

Özcan, E., Scheibner, C., & Boukhalfa, K. (2014). Orthophragminids (foraminifera) across the Paleocene–Eocene transition from North Africa: taxonomy, biostratigraphy, and paleobiogeographic implications. The Journal of Foraminiferal Research, 44(3), 203-229.

Özcan, E., Pignatti, J., Pereira, C., Yücel, A. O., Drobne, K., Barattolo, F., & Saraswati, P. K. (2018). Paleocene orthophragminids from the Lakadong Limestone, Mawmluh Quarry section, Meghalaya (Shillong, NE India): implications for the regional geology and paleobiogeography. Journal of Micropalaeontology, 37(1), 357-381.

Özgen-Erdem, N., İnan, N., Akyazı, M., & Tunoğlu, C. (2005). Benthonic foraminiferal assemblages and microfacies analysis of Paleocene–Eocene carbonate rocks in the Kastamonu region, Northern Turkey. *Journal of Asian Earth Sciences*, *25*(3), 403-417.

Papazzoni, C. A., Fornaciari, B., Giusberti, L., Simonato, M., & Fornaciari, E. (2023). A new definition of the Paleocene Shallow Benthic Zones (SBP) by means of larger foraminiferal biohorizons, and their calibration with calcareous nannofossil biostratigraphy. Micropaleontology, 69(4-5), 363-400

Pereira, C. D., Khanolkar, S., Banerjee, S., Özcan, E., & Saraswati, P. K. (2022). Larger benthic foraminifera and microfacies of late Paleocene-early Eocene sections in Meghalaya, Northeast India. Journal of Foraminiferal Research, 52(1), 40-56.

Pomar, L., Baceta, J. I., Hallock, P., Mateu-Vicens, G., & Basso, D. (2017). Reef building and carbonate production modes in the west-central Tethys during the Cenozoic. Marine and Petroleum Geology, 83, 261-304.

Pujalte, V., Orue-Etxebarria, X., Schmitz, B., Tosquella, J., Baceta, J. I., Payros, A., Bernaola, G., Caballero, F., & Apellaniz, E. (2003). Basal Ilerdian (earliest Eocene) turnover of larger foraminifera: Age constraints based on calcareous plankton and 13C isotopic profiles from new southern Pyrenean sections (Spain). *Causes and consequences of globally warm climates in the early Paleogene: Geological Society of America Special Paper*, (369), 205-221.

Révész, K. M., & Landwehr, J. M. (2002). δ13C and δ18O isotopic composition of CaCO3 measured by continuous flow isotope ratio mass spectrometry: statistical evaluation and verification by application to Devils Hole core DH-11 calcite. *Rapid Communications in Mass Spectrometry*, *16*(22), 2102-2114.

Robert, C., & Kennett, J. P. (1992). Paleocene and Eocene kaolinite distribution in the South Atlantic and Southern Ocean: Antarctic climatic and paleoceanographic implications. *Marine Geology*, *103*(1-3), 99-110.

Röhl, U., Westerhold, T., Bralower, T. J., & Zachos, J. C. (2007). On the duration of the Paleocene-Eocene thermal maximum (PETM). *Geochemistry, Geophysics, Geosystems* , *8* (12).

Sanei, H., Grasby, S. E., & Beauchamp, B. (2012). Latest Permian mercury anomalies. *Geology* , *40* (1), 63-66.

Salih, H. D. (2012). Larger benthic foraminiferal assemblages from sinjar formation, sw Sulaimaniyah city Kurdistan Region, Iraq. Iraqi Bulletin of Geology and Mining, 8(1), 1-17.

Sarkar, S. (2015). Thanetian–Ilerdian coralline algae and benthic foraminifera from northeast India: microfacies analysis and new insights into the Tethyan perspective. Lethaia, 48(1), 13-28.

Sarkar, S. (2018). The enigmatic Paleocene-Eocene coralline Distichoplax: Approaching the structural complexities, ecological affinities and extinction hypotheses. Marine Micropaleontology, 139, 72-83.

Sarkar, S., Cotton, L. J., Valdes, P. J., & Schmidt, D. N. (2022). Shallow water records of the PETM: Novel insights from NE India (eastern Tethys). *Paleoceanography and Paleoclimatology* , *37* (7), e2021PA004257.

Scheibner, C., & Speijer, R. P. (2008). Late Paleocene–early Eocene Tethyan carbonate platform evolution—a response to long-and short-term paleoclimatic change. *Earth-science reviews*, *90*(3-4), 71-102.

Schulte, P., Scheibner, C., & Speijer, R. P. (2011). Fluvial discharge and sea-level changes controlling black shale deposition during the Paleocene–Eocene Thermal Maximum in the Dababiya Quarry section, Egypt. *Chemical Geology* , *285* (1-4), 167-183.

Serra-Kiel, J., Vicedo, V., Baceta, J. I., Bernaola, G., & Robador, A. (2020). Paleocene larger foraminifera from the Pyrenean Basin with a recalibration of the Paleocene shallow benthic zones. *Geologica Acta, 18.8, 1-69, I-III.*

Serra-Kiel, J., Hottinger, L., Caus, E., Drobne, K., Ferrandez, C., Jauhri, A. K., Less, G., Pavlovec, R., Pignatti, J., Samso, J. M., Schaub, H., Sirel, E., Strougo, A., Tambareau, Y., Tosquella, J., & Zakrevskaya, E. (1998). Larger foraminiferal biostratigraphy of the Tethyan Paleocene and Eocene. Bulletin de la Société géologique de France, 169(2), 281-299.

Shah, S. M. I. (2009). Stratigraphy of Pakistan. Geological Survey Pakistan Membership, 22, 1-381.

Sluijs, A., Bowen, G. J., Brinkhuis, H., Lourens, L. J., & Thomas, E. (2007). The Paleocene–Eocene Thermal Maximum super greenhouse: biotic and geochemical signatures, age models and mechanisms of global change.

Sluijs, A., Bijl, P.K., Schouten, S., Rohl, U., Reichart, G.J., Brinkhuis, H., 2011. Southern ocean warming, sea level and hydrological change during the Paleocene-Eocene thermal maximum. Clim. Past 7, 47–61. https://doi.org/10.5194/cp-7-47-2011.

Spangenberg, J. E., Jacomet, S., & Schibler, J. (2006). Chemical analyses of organic residues in archaeological pottery from Arbon Bleiche 3, Switzerland–evidence for dairying in the late Neolithic. *Journal of archaeological science*, *33*(1), 1-13.

Speijer, R. P., Scheibner, C., Stassen, P., & Morsi, A. M. M. (2012). Response of marine ecosystems to deep-time global warming: a synthesis of biotic patterns across the Paleocene-Eocene thermal maximum (PETM). Austrian Journal of Earth Sciences, 105(1).

Spötl, C., & Vennemann, T. W. (2003). Continuous-flow isotope ratio mass spectrometric analysis of carbonate minerals. Rapid communications in mass spectrometry , 17 (9), 1004-1006.

Sreenivasan, S. P., Samanta, A., BouDagher-Fadel, M., Mukherjee, S., Vadlamani, R., & Bera, M. K. (2022). Increasing primary productivity in the oligotrophic Tethyan coastal ocean during the Paleocene-Eocene warming episode. Global and Planetary Change, 216, 103898.

Swart, P. K. (2015). The geochemistry of carbonate diagenesis: The past, present and future. Sedimentology, 62(5), 1233-1304.

Tamar-Agha, M. Y., Salih, A. L., & Al-Zaidy, A. A. (2015). Depositional setting and basin development of the Paleocene—Lower Eocene Sinjar and Khurmala formations, Northern Iraq. Arabian Journal of Geosciences, 8, 9441-9467.

Thiry, M. (2000). Palaeoclimatic interpretation of clay minerals in marine deposits: an outlook from the continental origin. *Earth-Science Reviews*, *49*(1-4), 201-221.

Thomas, E., & Shackleton, N.J. (1996). The Paleocene-Eocene benthic foraminiferal extinction and stable isotope anomalies. Geological Society, London, Special Publications , 101 (1), 401-441.

Tomassetti, L., & Benedetti, A. (2020). To be allochthonous or autochthonous? The late Paleocene–late Eocene slope sedimentary succession of the Latium–Abruzzi carbonate platform (Central Apennines, Italy). Facies, 66(1),

Tremblin, M., Khozyem, H., Adatte, T., Spangenberg, J. E., Fillon, C., Grauls, A., Hunger, T., Nowak, A., Läuchli, C., Lasseur, E., Roig , J. Y., Serrano, O., Calassou, S., Guillocheau, F., & Castelltort, S. (2022). Mercury enrichments of the Pyrenean foreland basins sediments support enhanced volcanism during the Paleocene-Eocene thermal maximum (PETM). *Global and Planetary Change*, *212*, 103794.

Vršič, A., Gawlick, H. J., Schlagintweit, F., Machaniec, E., & Gharsalla, M. (2021a). Age, microfacies and depositional environment of the Middle to Late Paleocene shallow-marine carbonates in the Sirt Basin of Libya (Upper Sabil Formation):“Are Intisar domal structures pinnacle reefs?”. Facies, 67(4), 27.

Vršič, A., Machaniec, E., & Gawlick, H. J. (2021b). Middle to Late Paleocene larger benthic foraminifera from the Sirt Basin (Libya). Revue de Micropaléontologie, 71, 100481.

Walsh, S. L. (2004). Solutions in chronostratigraphy: the Paleocene/Eocene boundary debate, and Aubry vs. Hedberg on chronostratigraphic principles. Earth-Science Reviews, 64(1-2), 119-155.

Westerhold, T., Marwan, N., Drury, A. J., Liebrand, D., Agnini, C., Anagnostou, E., Barnet, J. S. K., Bohaty, S. M., De Vleeschouwer, D., Florindo, F., Frederichs, T., Hodell, D. A., Holbourn, A. E., Kroon, D., Lauretano, V., Littler, K., Lourens, L. J., Lyle, M., Pälike, H., Röhl, U., Tian, J., Wilkens, R. H., Wilson, P. A., & Zachos, J. C. (2020). An astronomically dated record of Earth’s climate and its predictability over the last 66 million years. Science, 369(6509), 1383-1387.

Yans, J., Amaghzaz, M., Bouya, B., Cappetta, H., Iacumin, P., Kocsis, L., Mouflih, M., Selloum, O., Sen, S., Storme1, J.-Y. & Gheerbrant, E. (2014): First carbon isotope chemostratigraphy of the Ouled Abdoun phosphate Basin, Morocco; implications for dating and evolution of earliest African placental mammals. – Gondwana Research, 25, 257–269

Yeats, R. S., & Lawrence, R. D. (1982, November). Tectonics of the Himalayan thrust belt in northern Pakistan. In *US-Pakistan Workshop on Marine Sciences in Pakistan*.

Young, J.R., Bown P.R., Lees J.A. (2023) Nannotax3 website. International Nannoplankton Association. Accessed April 2023. URL: www.mikrotax.org/Nannotax3

Zachos, J. C., Wara, M. W., Bohaty, S., Delaney, M. L., Petrizzo, M. R., Brill, A., Bralower, T. J., & Premoli-Silva, I. (2003). A transient rise in tropical sea surface temperature during the Paleocene-Eocene Thermal Maximum. Science, 302(5650), 1551–1554.

Zachos, J. C., Röhl, U., Schellenberg, S. A., Sluijs, A., Hodell, D. A., Kelly, D. C., & Kroon, D. (2005). Rapid acidification of the ocean during the Paleocene-Eocene thermal maximum. *Science*, *308*(5728), 1611-1615.

Zamagni, J., Mutti, M., & Košir, A. (2008). Evolution of shallow benthic communities during the Late Paleocene–earliest Eocene transition in the Northern Tethys (SW Slovenia). Facies, 54, 25-43.

Zamagni, J., Mutti, M., Ballato, P., & Košir, A. (2012a). The Paleocene–Eocene thermal maximum (PETM) in shallow-marine successions of the Adriatic carbonate platform (SW Slovenia). *Bulletin*, *124*(7-8), 1071-1086.

Zamagni, J., Mutti, M., & Košir, A. (2012b). The evolution of mid Paleocene-early Eocene coral communities: How to survive during rapid global warming. *Palaeogeography, palaeoclimatology, palaeoecology*, *317*, 48-65.

Zintwana, M. P., Cawthorn, R. G., Ashwal, L. D., Roelofse, F., & Cronwright, H. (2012). Mercury in the Bushveld complex, South Africa, and the Skaergaard intrusion, Greenland. *Chemical Geology*, *320*, 147-155.

Zhang, Q., Willems, H., & Ding, L. (2013). Evolution of the Paleocene-Early Eocene larger benthic foraminifera in the Tethyan Himalaya of Tibet, China. International Journal of Earth Sciences, 102, 1427-1445.

Zhang, Q., Willems, H., Ding, L., & Xu, X. (2019). Response of larger benthic foraminifera to the Paleocene-Eocene thermal maximum and the position of the Paleocene/Eocene boundary in the Tethyan shallow benthic zones: Evidence from south Tibet. GSA Bulletin, 131(1-2), 84-98.

Zhang, Q., Ding, L., Kitajima, K., Valley, J. W., Zhang, B., Xu, X., ... & Klügel, A. (2020). Constraining the magnitude of the carbon isotope excursion during the Paleocene-Eocene thermal maximum using larger benthic foraminifera. Global and Planetary Change, 184, 103049.

Zhang, Q., Ding, L., Chen, X., Brennecka, G. A., Sun, Y., Ma, X., ... & Willems, H. (2023). The large decline in carbonate δ238U from a PETM section at Tingri (South Tibet) was driven by local sea-level changes, not global oceanic anoxia. Earth and Planetary Science Letters, 612, 118164.

Chapter 5 – Evolution of carbonate factories across Tethys during Late Paleocene warming events

This chapter correlates the various sections investigated in northern Pakistan (upper Indus Basin) using the Baroch Nala section as a key reference point. Northern Pakistan is then correlated with other sections in the Himalayan region and then with the remainder of Tethys to understand the global evolution of carbonate factories and shallow-water environments during the Late Paleocene.

5.1. Abstract

Using a multiproxy approach that includes paleontological, sedimentological, mineralogical, and geochemical analysis, we investigate three Paleocene-Eocene shallow water marine successions from the upper Indus Basin, North Pakistan.

Based on that, five sub-stages of the Paleocene Eocene interval are established including 1) pre-PETM, 2) pre-onset excursion (POE), 3) PETM onset, 4) PETM body and Recovery, and 5) post-PETM Phase. The Baroch Nala, one of the detailed studied sections displays a complete and continuous tracking of paleoenvironmental changes across POE and PETM and shows how these hyperthermal events have strong effects on biological, mineralogical, and geochemical signals. Providing a complete picture of the event the Baroch Nala becomes a linchpin to correlate together the other investigated sections and other sections in the Himalayan region.

Taking the Baroch Nala as a reference point, we first correlate the close by Nammal Gorge section. The two sections from the Salt and Surghar ranges are then correlated along with the Ghumanwan section (Hazara Basin). This correlation provides a detailed overview of basin-wide environmental changes associated with POE and PETM.

Then, in light of the data from the upper Indus Basin, other sections from the Himalayan area are partially re-interpreted.

Finally, in order to move from the regional to the global scale, biotic assemblages from sections ranging from the Selandian to the Ypresian, from all over Tethys, are quantitatively analyzed.

Furthermore, the studied geochemical records from the upper Indus Basins are correlated with other multi-proxy records from various parts of the world. This indicates that the biotic changes are well synchronized with environmental changes during the PETM and the POE.

These findings show that moving from pre-PETM to post-PETM the abundance of reef corals and red calcareous algae decreases while the abundance of LBF increases. At the same time, a major turnover in LBF assemblage is recorded with the demise of most Paleocene genera at or close to the Paleocene – Eocene boundary. The nummulitids, the group that flourished during the POE and the onset of the PETM probably resulted in victorious from the competition with other carbonate producers during the stressful conditions caused by the hyperthermals, and from the Lower Eocene to the middle Oligocene, they became one of the most distinctive elements of the carbonate platforms of Tethys. Furthermore, the overall pattern resulting from the global comparison clearly highlights the existence of the POE as a separate event from the PETM, reconciling the shallow-water record with the deep-water record.

5.2. Introduction

Anthropogenic activities like the combustion of fossil fuels and mass deforestation lead to modern-day levels of greenhouse gases and the current phase of intense global warming (Rajak, 2021). This makes modern ecosystems vulnerable, causing rapid and unpredictable changes in environmental conditions (Hulme, 2005). These changes disrupt the stability of ecosystems that have evolved over long periods within specific temperature ranges and climatic patterns (Traill et al., 2010). For a better understanding of modern-day climatic effects and to predict future scenarios, the study of the past will be considered “as a key to the imminent future”.

Since the emergence of life on the Earth, several warning episodes severely struck the Earth's biosphere. These episodes include early Paleozoic warming, Mesozoic hot-house phase, and early Cenozoic hyperthermal events like the Pre-Onset Excursion and the well-known Paleocene-Eocene Thermal Maximum (PETM) (See Chapter 1 for further details). During past geological warm phases, CO_2 levels in the atmosphere and hydrosphere were high and this made Earth inhospitable for several types of organisms. Similarly, high CO_2 levels caused the demise of several marine benthic and sessile flora and fauna (See Chapter 1 for further details). Similar processes can be observed in modern oceans as carbonate factories across the tropics (Maldives and Great

Barrier Reef) have been under stressful conditions due to rising temperatures, resulting in the bleaching of colonial corals (See Chapter 1 for further details).

In the past, specifically, during the early Cenozoic, carbonate producers like Corals recovered fast after the K-Pg mass extension event and dominated the shallow water carbonate factories across the Tethys until the early Thanetian (see Chapter 2 for further details). Afterward, the Late Paleocene warming trend started and affected the corals and their symbiotic algae, resulting in reef corals becoming less important during the late Thanetian (see Chapter 3 for further details). Interestingly LBF became progressively more abundant as the climate became warmer, but the warming resulted in the collapse of Paleocene assemblages and in the rise of Eocene assemblages (see Chapter 4 for further details). These changes in skeletal assemblage and the associated Larger benthic turnover (LFT) have been observed in the Tethyan realm by several authors, but most of the studies were conducted in the western Tethys (Scheibner& Speijer, 2008, Zamagni et al., 2012). Conversely, in the eastern Tethys, the biotic turnovers and complete tracking of Late Paleocene to Early Eocene environmental changes are much less studied (Afzal et al., 2011, Kamran et al., 2021, Zhang et al., 2013, 2019, Sarkar et al., 2022). Several factors might have resulted in the lower amount of analysis in eastern Tethys, including the local geodynamics and the Himalayan orogenic event. Additionally, ancient shallow marine sediment once exposed to the surface, very often has their original geochemical signal altered by diagenesis and secondary processes (Swart, 2015). These processes usually do not cause both $\delta^{13}C_{carb}$ and $\delta^{13}C_{org}$ to shift in the same direction at the same rate, resulting in major consistent changes in both isotopic indices, throughout the geological record, being generally considered indicators of global changes in the carbon cycle (Knoll et al., 1986; Swart, 2015). Nonetheless, in shallow marine depositional systems, increased organic carbon deposition triggered complex diagenetic processes, resulting in localized dolomite precipitation, which also affects $\delta^{13}C_{carb}$ (Komar and Zeebe, 2017; Swart, 2015) and, in sub-aerial environments, simultaneous shifts in both $\delta^{13}C_{carb}$ and $\delta^{13}C_{org}$ in the same direction can occur (Swart, 2015).

Based on the multiproxy analysis, the biological, geochemical, and mineralogical changes were deeply discussed along a well-preserved section, i.e. the Baroch Nala section in the Surghar Range (see Chapter 4 for further details). Two major warming events, the POE and PETM were recorded, associated with related changes in skeletal assemblages where POE shows minimal changes in skeletal assemblages and the PETM exhibits a major change in skeletal assemblages. Unlike most

shallow-marine successions, which include the break in the sedimentation, the Baroch Nala section displays no evidence of hiatus or of exposure surfaces providing a complete picture of paleoenvironmental change across the Paleocene - Eocene boundary (see Chapter 4 for further details). This allows us to use the Baroch Nala section as a reference point for POE and PETM in eastern Tethys and correlate to other sections from northern Pakistan and from eastern Tethys. Thanks to this, we provide in this study a complete basin-wide correlation of three Paleocene - Eocene successions from the upper Indus Basin. First, we correlate the well-preserved Baroch Nala section with the close by Nammal Gorge section and then by using biotic assemblages, we correlate the more northernly located Ghumanwan section. Then we correlate the studied sections from the upper Indus Basin with other sections from Pakistan and the Himalayan area at large. Finally, the assembled record of the Himalayan area is compared with the remainder of Tethys and with other well-known Late Paleocene to Early Eocene sections worldwide to enhance our understanding of climatic events and biotic turnovers during this fundamental interval of Earth's History.

5.3. Geological Setting

During the Paleocene-Eocene interval the main study area, i.e. Northern Pakistan, was involved in the convergence of India and Eurasia. The latter event leads to the collision of the two continental plates (60 Ma; Hu et al., 2016; Rehman et al., 2011), the closure of the eastern Tethys (Early to Middle Eocene, ~50 Ma; Garzanti et al., 1987; Najman et al., 2017) and to the Himalayan orogenic event.

The three investigated sections in northern Pakistan i) Ghumanwan (Hazara basin: 34°10′09.16″ N, 73°16′39.73″ E), ii) Nammal Gorge (Salt range: 32°40′09.49″ N, 71°47′44.42″ E), and iii) Baroch Nala (Surghar range: 32°56′25.74″ N, 71°08′57.88″ E) are situated within the western extremity of the Himalayan Fold and Thrust Belt (HFTB) (Figure 5.1)

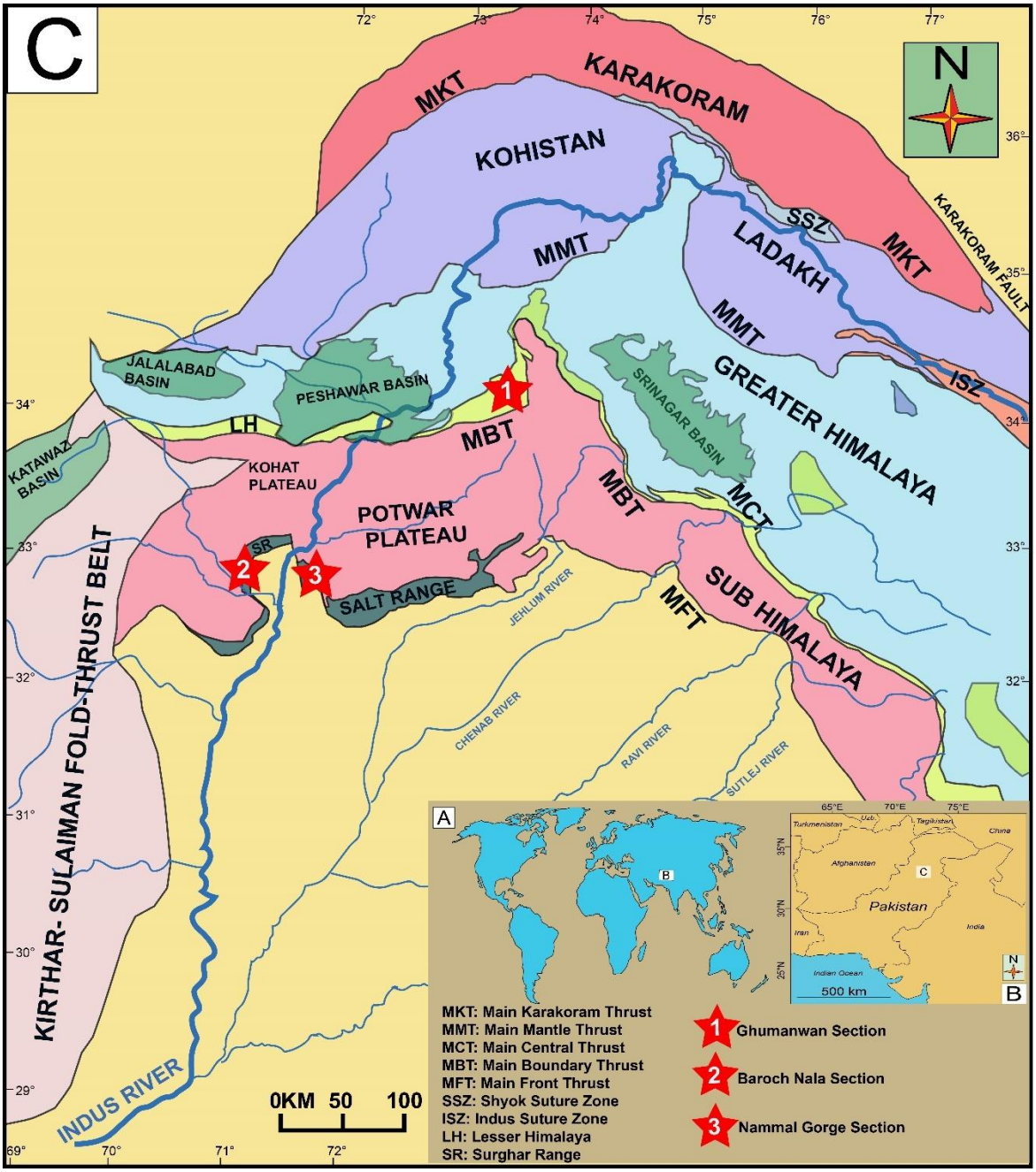

Figure 5.1, Shows the geological map of Pakistan and the western Himalayas. This map also shows the geographical position of three studied sections, 1) the Ghumanwan section (Hazara Basin), 2) the Baroch Nala section (Surghar Range), and 3) the Nammal Gorge section (Salt Range, Pakistan). (Modified after Garzanti et al., 2020

The HFTB formed as a consequence of the convergence between the Indian and Asian plates. In the western Himalayas, the HFTB is associated with intra-oceanic subduction and the subsequent obduction of the Kohistan Island Arc (KIA) (Jadoon et al., 2021).

This convergence of Indian and Asian plates also resulted in the formation of the Himalayan Foreland Basin (Najman & Garzanti, 2000), a vast sedimentary basin that extends southward from the foothills of the Himalayas and spans across several countries, including India, Pakistan, and Nepal (Pivnik & Well, 1996). The studied sections fall in the westernmost extremity of the Himalayan Foreland Basin which is regionally called the Indus Basin.

The closure of the eastern Tethys, both north and south of the KIA, created two regional sutures called the Main Karakoram Thrust and the Main Mantle Thrust (Rehman et al., 2011). The Indian-KIA collision pushed the deformation front southward, resulting in the development of two regional thrusts: the Main Boundary Thrust (MBT) and the Salt Range Thrust (SRT; Yeats and Lawrence, 1982; Acharyya, 2007; Najman et al., 2010). The MBT emplaced Mesozoic strata over Miocene continental strata, while the SRT emplaced Precambrian evaporites over Neogene Siwaliks (Abbasi and McElroy, 1991). The SRT is the youngest frontal thrust of the HFTB (4 Ma; Ghani et al., 2020; 4.5 Ma; Baker et al., 1988) and is an echelon offshoot of the Chaman Transform Fault (Butler et al., 1987; McDougall and Khan, 1990; Treloar et al., 1992). The SRT led to the development of two mountain ranges: the Salt Range to the East of the River Indus and the Trans Indus Surghar Range to the west (Figure 5.1).

All the studied sections belong to the Indus Basin. The Nammal Gorge section lies within the vicinity of the western Salt Range (upper Indus basin). The Baroch Nala section is located in the Trans Indus Surghar Range (upper Indus Basin). The Ghumanwan section is located in the Hazara Basin, a northern sub-basin of the upper Indus Basin.

5.3.1. Stratigraphic of Ghumanwan section:

The studied Ghumanwan section is located in the vicinity of Abbottabad city, in the Hazara Basin, geographically located in the northernmost part of the Indus Basin. The lithostratigraphic units of the Hazara Basin span from the Neoproterozoic to the Early Eocene (Umar et al., 2015). The Neoproterozoic-Cambrian Hazara Formation consists of deep marine shales, low-grade metamorphosed slates, and phyllites (Butt, 1972) and is overlain by Early Jurassic fluvio-marine sediments of the Datta Formation, indicating an unconformable contact. From the Jurassic to Eocene, shallow water carbonates dominate the sedimentary records of the Hazara basin. During the Early Jurassic, the depositional environment of the Hazara basin changes from fluvial-deltaic to shallow marine. Datta Formation consists of variegated lithology and comprises sandstone-

limestone lithology with coal seams (Abbasi et al., 2012). This formation is overlain by inner to outer ramp limestones of the Early Jurassic Samana Suk Formation (Ahsan and Chaudhry, 2008; Shah et al., 2020). The Samana Suk Formation has an unconformable contact with the following Early Cretaceous Chichali Formation (Shah, 2009; Ahsan and Choudhary, 2008). The Chichali Formation consists of glauconitic shales and subordinated sandstones, deposited in restricted anoxic conditions (Umar 2015; Shah, 2009). Glauconitic shales are often characterized by belemnite-rich beds. The Early Cretaceous Chichali Formation has a conformable upper contact with the Late Cretaceous Lumshiwal Formation. This unit consists of deltaic sandstones, limestones, and dolomites. The following Late Cretaceous carbonates of the Kawgarh Formation capped the Lumshiwal Formation. The Kawagarh Formation is further overlain by the Early Paleocene Hangu Formation (Umar et al., 2015; Saboor et al., 2021). The bauxite and laterite beds mark the Cretaceous-Paleogene boundary (K-Pg). The poorly deposited Hangu Formation in the Hazara Basin is comprised of various lithologies, that include red laterite, coal, calcareous shale, and sandstone (Ahsan and Chaudhry, 2008). The overlain Middle to Late Paleocene Lockhart Limestone is dominated by shallow water carbonates and the skeletal assemblages consist of large benthic foraminifera (LBF), corals, and calcareous algae (Ali et al., 2024). The Lockhart Limestone is overlain by Late Paleocene to Early Eocene Patala Formation. Which is dominated by calcareous shales and marls with interbedded fossiliferous limestones. A clear turnover in large benthic foraminiferal assemblages is recorded at the Paleocene-Eocene boundary, and typically Paleogene LBFs, like *Miscellanea* and *Ranikotalia*, are replaced by nummulitids and alveolinids (Scheibner et al., 2005). At the top, the Early Eocene Margalla Hill Limestone sealed the underlain Patala formation. The Margalla Hill Limestone is characterized by LBF taxa, including nummulitiids and alveolinds. The Early Eocene LBF-rich carbonates of the Chorgali Formation overlain the Margalla Hill Limestone and are composed of inner to middle ramp carbonates.

5.3.2. **Stratigraphy of Nammal Gorge section**

The Nammal Gorge section is located in the western Salt Range (upper Indus basin) and on the eastern side of the river Indus. The litho-stratigraphic units outcropping along the Nammal Gorge section ranging from the Late Permian to the Early Eocene. The Late Permian mixed siliciclastic carbonates of the Amb Formation (Mertmann, 2003) are exposed at the entrance to the Nammal

Gorge, forming an upper conformable contact with the massive carbonates of the Late Permian Wargal Formation. These carbonates are overlain by the Late Permian mixed siliciclastic carbonates of the Chiddru Formation. A white calcareous sandstone bed marks the Permian Triassic boundary and separates the Chiddru Formation from the overlying early Triassic Mianwali Formation. The carbonates, shale, and deltaic sandstone of the Mianwali Formation display a conformable contact with the overlying deltaic sandstone-bearing Tredian Formation (Iqbal et al., 2014), which are further overlain by the shallow marine carbonates of the Late Triassic Kingriali Formation. The Kingrali Formation is further overlain by the Early Jurassic fluvial-deltaic sandstones interbedded with limestones and shales of the Datta Formation which are in turn overlain by the early Jurassic carbonates of the Samana-Suk Formation. The Samana Suk Formation is unconformably overlain by Early Paleocene laterites and sandstones of the Hangu Formation which are followed by the Late Paleocene shallow marine limestones of the Lockhart Limestone. The latter displays an upper conformable contact with the Late Paleocene to Early Eocene shales with interbedded limestones of the Patala Formation. Further upwards, the Early Eocene chert-bearing carbonates and shales of Nammal Formation, form a conformable contact with the Patala Formation. The Nammal Formation is further overlain by the Early Eocene nodular limestones of the Sakessar Limestone.

5.3.3. **Stratigraphy of Baroch Nala section**

The Baroch Nala section is situated in the Trans-Indus Surghar range (upper Indus basin) and lies approximately 40 km west of the Nammal Gorge section and of the Indus River itself.

The Baroch Nala section displays rocks ranging in age from the Early Jurassic to Late Neogene. The mouth of the gorge is formed by highly folded, Early Jurassic fluvial-deltaic sedimentary rocks of the Datta Formation. These are overlain by the Early to Middle Jurassic deep marine shales interbedded and shallow water carbonates of the Shinawari Formation (Ali et al., 2019). The overlying, Late Jurassic Samana Suk Formation includes massive shallow marine limestones and is overlain by the Early Cretaceous, belemnites-bearing, green glauconitic shales, and sandstones of the Chichali Formation. The Chichali Formation is followed by the Early Cretaceous Lumshiwal Formation, which comprises shallow marine sandy carbonates and deltaic sandstones. The

Lumshiwal Formation displays an upper unconformable contact with the Early Paleocene sandstones interbedded with the limestones of the Hangu Formation. The Hangu Formation is in turn overlain by the Late Paleocene shallow-water nodular limestones of the Lockhart Limestone. The Lockhart Limestone is conformably overlain by the Late Paleocene to Early Eocene pelagic to hemipelagic shales interbedded with limestones of the Patala Formation, which include the Paleocene-Eocene boundary. Further above the section is characterized by the Early Eocene chert-bearing carbonates and shales of the Nammal Formation and by the Early Eocene nodular limestone of the Sakessar Limestone. The Latter, Sakessar Limestone is unconformably overlain by thick Neogene Siwaliks.

5.4. Methods and Materials

Two field trips to the Ghumanwan section were arranged during the first and second years of the doctoral program (2022 and 2023) to better understand the geological context of the study area. Additionally, a field trip to the Nammal Gorge (Salt Range) and Baroch Nala (Surghar Range) was arranged during the second year (2023), with a focus on high-resolution systematic sampling of the Paleocene-Eocene interval. The investigated sections were measured with a measuring tape and the macroscopic petrographic lithological variations were noted. Representative samples were collected along the section following the observed lithological variation, collecting more samples in intervals with remarkable variations in petrographic characteristics and paleontological content. A total of 230 samples were collected from the Lockhart Limestone and the Patala Formation at the Ghumawan 34°10′09.16″ N, 73°16′39.73″ E), Baroch Nala (32°56′25.74″ N, 71°08′57.88″ E), and Nammal Gorge (32°40′09.49″ N, 71°47′44.42″ E) sections. Due to the deep weathering profiles of the poorly lithified marls and black shales of the Patala Formation, approximately 1 meter of digging was done for every poorly compacted sample, in order to collect only fresh and (possibly) unweathered material. All the samples were initially processed at the Department of Earth and Environmental Science (DISAT) of the University of Milano Bicocca (UNIMIB) Italy, for sedimentological and paleontological analysis.

A total of 181 thin sections of limestone and shales from Ghumanwan, Baroch nala, and Nammal gorge sections were prepared at the thin section laboratory of the DISAT-UNIMIB by Mubashir

Ali, Giovanni Coletti., and Luca Mariani. Thin sections were prepared following the approach detailed in Chapter 2 and based on repeated embedding in epoxy resin for consolidating poorly lithified and porous. Thin sections were studied through a Leica Leitz Laborlux S transmitted light optical microscope, investigating microfacies and rock texture. The skeletal assemblages were examined and quantified using the point counting technique (Flügel, 2010) in 119 thin sections. For this analysis, a 200 μm grid was used and more than 800 points were identified in each analyzed section (nearly 100000 counted points).

Thin sections were also used for Large Benthic Foraminifera (LBF) biostratigraphy. Identification was performed following mainly Hottinger (2014) for rotaliids, and mainly Leppig, 1988, Hottinger, 2009, Leppig and Langer, 2015, and subordinately other studies (e.g., Di Carlo et al., 2010, Sirel, 2018) for miscellaneids. The taxonomic analysis of LBF was generally based on a typological approach; whereas and whenever possible, lockhartiids, miscellaneids, and nummulitids were identified at the species level by biometric measurements (e.g., Benedetti et al., 2018). The LBF assemblages allowed us to provide biostratigraphic constraints following the biozonal scheme (Shallow Benthic Zones, SBZ) of Serra-Kiel et al., 1998, recently recalibrated for the Paleocene by Serra-Kiel et al., 2020 and Papazzoni et al., 2023.

A total of 76 samples from the Baroch Nala section, 64 from Nammal Gorge, and 36 from Ghumanwan were prepared as standard smear slides using a 22 × 40 mm coverslip and Norland mounting medium for calcareous nannofossil biostratigraphic analyses. Each sample was scanned through an Olympux BX50 polarized light microscope at 1000x with immersion oil. Due to the scarcity of nannofossils, 4-6 transects were observed for most slides in order to find useful markers. The presence and relative abundance of calcareous nannofossils per field of view (FOV) was assessed for each sample and tabulated as: A = abundant; >10/FOV; C = common; 1–10 /FOV; F = few; 1/10 FOVs; R= rare; ≥ 3 /transect; VR = 1 /transect. Taxonomic identification follows Young et al. (2023) and the biostratigraphic schemes of Martini (1971) and Agnini et al. (2014) were used.

Representative rock samples from the three sections (92-Baroch Nala section; 64-Nammal Gorge section; 58-Ghumanwan section) were also used for geochemical analyses. The samples were initially oven-dried at 45°C and then gently crushed or milled (when required) using an agate mill at the Department of Earth and Environmental Sciences, University of Geneva, Switzerland. The subsequent mineralogical and geochemical analyses were conducted at the Institute of Earth

Science (ISTE) and Institute of Earth Surface Dynamics (IDYST) University of Lausanne (UNIL), Switzerland.

The organic matter (OM) characterization was determined at ISTE -UNIL Switzerland. Rock-Eval 6 calibrated with the IFP16000 standard, was used for the OM characterization total of 201 (Baroch Nala section – 92; Nammal Gorge section – 64 & Ghumanwan section- 45) bulk powdered samples and following the procedures described by (Behar et al., 2001). The samples first pyrolyzed at 300°C and heated up to 650°C in the presence of nitrogen, followed by combustion up to 850°C in the oxidation chamber. Rock-Eval 6 data sets include Total organic carbon (TOC; wt.%), Oxygen (OI; mg CO2/g TOC), Hydrogen index, (HI; mg HC/g TOC), and Tmax (°C; thermal maturity indicator). The HI and OI values were utilized for the interpretation of OM type and source and only samples containing TOC value ≥0.25 wt.% were considered for the interpretation. (Espitalie et al., 1985).

The organic matter $\delta^{13}C$ stable isotope ratios were determined at IDYST-UNIL on 10% HCl-treated, decarbonated 190 (92-Baroch Nala section; 64-Nammal Gorge section, 34-Lower part of Ghumanwan section) samples by using Elemental analysis/isotope ratio mass spectrometry (EA/IRMS) (Spangenberg et al., 2006, 2014). Depending on the TOC wt %, different aliquots were weighed and capsuled by using microbalance. The sample aliquots were combusted by using Carlo Erba 1108 elemental analyzer (Milan, Italy) coupled with Thermo Fisher Scientific Delta V Plus (Bremen, Germany) isotope ratio mass spectrometer. All the results were reported in the δ notation relative to the Vienna Pee Dee Belemnite (VPDB) international standard. 04 Reference materials including international and UNIL-based local standards (Spangenberg et al., 2006) were used for the calibration and normalization of the measured isotopic values. The accuracy and precision for $\delta^{13}C$ org EA/IRMS analyses were better than 0.1‰.

Bulk carbonate $\delta^{13}C$ and $\delta^{18}O$ stable isotope values were determined for 72 (40-Baroch Nala section; 32-Nammal Gorge section) powdered samples ($CaCO_3$ >10 wt %) following the method described by (Revesz & Landwehr., 2002). Sample aliquots were weighed and analyzed by using Thermo Fisher Scientific Gas Bench II coupled with a Delta Plus XL isotope ratio mass spectrometer (Thermo Fisher Scientific GmbH, Bremen, Germany). All the results were reported in the δ notation relative to the Vienna Pee Dee Belemnite (VPDB) international standard. Standard reference gases of the International Atomic Energy Agency and UNIL local gases were used to normalize and calibrate isotope values. The analytical uncertainty (1σ) did not exceed ±0.05% for

$\delta^{13}C$ and ± 0.1% for $\delta^{18}O$, which can be assessed through 45 samples base-seven replicated analyses of the international calcite standard NBS-19 and Carrara marble standard of the laboratory.

The Hg concentrations were measured in 203 (91-Baroch Nala section; 64-Nammal Gorge section & 48-Ghumanwan section) bulk powdered samples at ISTE-UNIL, Switzerland, by using a high-frequency Zeeman R-915F atomic absorption spectrometer, tuned at Mode 1. Hg contents were determined by the direct thermal evaporation of Hg from the bulk sample at 700C. The accuracy of the machine was confirmed by the treatment of external standard, certified GSD-11 reference material (Chinese alluvium: 72.0 ± 3.6 ppb; Zintwana et al., 2012), for better results, every sample was processed twice.

The X-ray diffraction-based bulk rock and clay mineralogical analysis was carried out at ISTE-UNIL, Switzerland by using a Thermo Scientific ARL X-TRA diffractometer, following the methods described in Klug and Alexander (1974). The bulk rock mineralogy was performed on 209 (92-Baroch Nala section; 62-Nammal Gorge section & 55-Ghumanwan section) powdered samples, and measurements were obtained from the peak intensities of the distinguished minerals. Phyllosilicates contain an error margin between 5 to 10% because of their sheet-like appearance, while for the other minerals, the error margin is < 5%.

For clay mineralogy, 155 (91-Baroch Nala section; 64-Nammal Gorge section) samples (consisting of chip-sized elements) were analyzed. Before the analysis, a multi-step, sample preparation methodology was adopted including decarbonization with 10 % HCl, ultrasonic disaggregation (3 minutes), and treatment with ethylene glycol. Clay fractions <2 μm grain size were considered for XRD analysis. Peak intensities can be interpreted as kaolinite, chlorite, smectite, palygorskite, illite, and illite-smectite mixed layers.

Diagenetic and secondary processes usually do not cause both $\delta^{13}C_{carb}$ and $\delta^{13}C_{org}$ to shift in the same direction at the same rate, resulting in major consistent changes in both geochemical indices, throughout the geological record, being generally considered indicators of global changes in the carbon cycle (Knoll et al., 1986; Swart, 2015). Therefore, we consistently used both $\delta^{13}C_{carb}$ and $\delta^{13}C_{org}$ in our analysis. However, the PETM record is often characterized by carbonate-free intervals. Ocean acidification, particularly in deep-water sediments, led to the occurrence of intervals devoid of carbonates (McInerney and Wing, 2011; Khozyem et al., 2015). In shallower contexts, increased organic carbon deposition triggered complex diagenetic processes, resulting in

localized dolomite precipitation, which also affects $\delta^{13}C_{carb}$ (Komar and Zeebe, 2017; Swart, 2015). Locally, higher rates of terrigenous supply make the PETM interval poor in carbonates, rendering $\delta^{13}C_{carb}$ less reliable. Conversely, organic matter is relatively common during the PETM and has been widely used as the main, and often the only, $\delta^{13}C$ proxy Consequently, we decided to focus primarily on organic carbon, as it could provide a continuous record of environmental fluctuations, even in carbonate-free layers.

Since, albeit generally rare, there are processes that can shift both $\delta^{13}C_{carb}$ and $\delta^{13}C_{org}$ simultaneously in the same direction (Swart, 2015), particularly in sub-aerial environments, we considered it safer to use a combination of proxies to define our intervals. In particular a combination of $\delta^{13}C_{org}$, $\delta^{13}C_{carb}$, bulk rock XRD, clay assemblages, and notable variations in skeletal assemblages recorded via point-counting were used to define our intervals. Only clear variations of all these primary proxies were considered significant environmental oscillations, as a single proxy might be faulty, but a combination of several is statistically less likely to fail.

To better understand the global significance of the paleoenvironmental changes observed in the main study area, the results of our analyses of the three sections from northern Pakistan have been correlated with results from other sections from various parts of the Tethys. A detailed literature-based study was conducted on 34 exposed Paleocene-Eocene sections across the Tethys. The collected literature focuses on skeletal assemblages, specifically large benthic foraminifera (LBF) species, reported during the Late Paleocene to Early Eocene interval. A comprehensive dataset was generated to track the abundance of the main genera of LBF from SBZ3 to SBZ5/6. As the boundary between SBZ5-6 is unclear due to certain genera occurring commonly in both biozones, it is difficult to determine where the SBZ5–6 borders are. Since species-level identifications are a major factor in separating these two biozones and the latter can mainly be determined by using orientated thin sections or CT scans, the boundary between these two biozones is sometimes blurred or unreliable. Because of this, during the literature analysis, the two zones have been considered as one. All the referenced research articles are available online and can be accessed through Google Scholar and ResearchGate. Using a presence/absence quantitative approach, several LBF genera such as *Lockhartia*, *Miscellanea*, *Daviesina*, *Ranikothalia*, *Nummulites*, *Assilina*, *Alveolina*, *Glomalveolina*, *Kathina*, *Lakadongia*, *Orbitiosiphon*, *Orbitolites*, orthophragminids, *Coskinon*, and *Operculina* were analyzed. Species abundance in the various LBF groups was evaluated as well as presence absence trends. Furthermore, the presence/absence

of other main groups of benthic carbonate producers such as symbiont-bearing colonial corals, red calcareous algae, and green calcareous algae was also evaluated.

5.5 Results

5.5.1. **Microfacies description**

Based on point counting analysis and quantitative data, seven microfacies have been recognized in the analyzed sections of northern Pakistan: Baroch Nala, Nammal Gorge, and Ghumawan sections. Five of these microfacies have been recognized in more than one section and thus have been considered to be standard biofacies, useful for local correlations. These can be observed in the Baroch Nala and Nammal Gorge sections and in the lower part of the Ghumawan section and are described in the following paragraphs (Table 5.1).

Biofacies: *Lockhartia* and hyaline SBF with orbitoidiform hyaline LBF (BF1)

This facies, is found at the base of all successions. It generally consists of mudstone to wackestone with a variable siliciclastic fraction mostly consisting of phyllosilicates. The scarce skeletal assemblage is dominated by hyaline LBF (mainly trocospiral forms like *Lockhartia* and orbitoidiforms like *Lakadongia* and *Orbitosiphon*) and SBF, with scarce ostracods, rare green calcareous algae (Dasycladales), corals, echinoderms and mollusks, and very rare Characeae. More coarse-grained layers (generally consisting of packstones) can occur. The latter displays a richer skeletal assemblage including, locally, common *Miscellanea* (Table 5.1).

Biofacies: *Lockhartia, Daviesina, Miscellanea* and hyaline SBF (BF2)

This facies, characterizes the lower to lower/middle part of both Baroch Nala and Nammal sections. It generally consists of locally dolomitized, mudstone/wackstone with a variable siliciclastic fraction consisting of phyllosilicates and locally abundant sand-sized quartz grains. The skeletal assemblage is dominated by hyaline LBF (mainly trocospiral forms like *Lockhartia* but also large miscellanids) with common SBF, scarce green calcareous algae (Dasycladales), ostracods and echinoderms, and very rare corals and mollusks(Table 5.1).

Biofacies: *Lockhartia*, *Daviesina*, *Miscellanea*, and hyaline SBF, with *Ranikothalia* (BF3)

This facies, characterizes the middle part of both Baroch Nala and Nammal sections. It usually consists of packstone, floatstone, and rudstone with associated relevant siliciclastic fractions mainly consisting of abundant phyllosilicates. The skeletal assemblage is dominated by hyaline LBF, mostly miscellanids but also nummulitids (*Ranikothalia* and subordinate *Assilina*) with common SBF, rare corals and green calcareous algae (Dasycladales), very rare echinoderms, mollusks, agglutinated LBF, and ostracods(Table 5.1).

Biofacies: Nummulitids and orthophragminids with GCA (BF4)

This biofacies, characterizes the upper part of both the Baroch Nala and Nammal Gorge sections. It usually consists of floatstone and rudstone with a relevant siliciclastic fraction. The latter mainly consists of phyllosilicates, and locally can include abundant sand-sized quartz grains. The skeletal assemblage is dominated by hyaline LBF, mainly nummulitids (*Assilina* and *Operculina* with subordinate *Nummulites* and *Ranikothalia*) but also orthophragminids and miscellaneids, with common green calcareous algae (mainly Dasycladales but also Bryopsidales), scarce alveolinids, rare SBF, mollusks and corals, and very rare echinoderms, red calcareous algae and ostracods(Table 5.1).

Biofacies: Nummulitids and orthophragminids (BF5)

This biofacies, characterize the uppermost part of both Baroch Nala and Nammal Gorge sections. It usually consists of packstone to rudstone with a variable siliciclastic fraction mainly consisting of phyllosilicates. The skeletal assemblage is dominated by hyaline LBF, mainly nummulitids (*Nummulites, Assilina* and *Operculina*) and orthophragminids, with common alveolinids, scarce SBF, rare green calcareous algae (mainly Dasycladales), and very rare corals, mollusks and ostracods(Table 5.1).

Site	**Baroch**	**Baroch**	**Baroch**	**Baroch**	**Baroch**	**Nammal**	**Nammal**	**Nammal**	**Nammal**	**Nammal**
Biofaices	BF1 Pre-PETM	BF2 POE	BF3 PETM onset	BF4 PETM body Recovery	BF5 Post-PETM	BF1 Pre-PETM	BF2 POE	BF3 PETM onset	BF4 PETM body + Recovery	BF5 Post-PETM
Planispiral rotaliids (*Miscellanea* and *Daviesina*)	16.6	21.9	37.8	1.76	0.0	8.3	16.7	20.7	18.9	0.0
Trocospiral rotaliids (Lockhartiids; *Rotorbinella; Katina*)	25.3	30.2	26.5	1.86	6.8	33.8	39.4	5.5	0.1	1.4
Orbitoidiform (*Orbitosiphon; Lakadonghia*)	13.1	0.6	0.0	0.00	0.0	8.7	1.2	0.0	0.0	0.0
Ranikothalia	0.0	1.0	13.1	10.02	0.0	0.0	0.0	14.1	16.7	0.0
Nummulitids (*Operculina;Assilina*)	0.0	0.0	0.1	16.05	21.4	0.0	0.0	15.3	24.9	10.7
Nummulites	0.0	0.0	0.0	10.3	36.8	0.0	0.0	0.0	2.7	42.9
Orthophragminids	0.0	0.0	0.0	20.6	21.0	0.0	0.0	0.0	0.3	25.4
Other hyaline LBF	2.1	5.6	1.6	7.8	1.6	14.5	2.8	16.4	6.3	0.0
Porcelanaceous foraminifera (mainly *Alveolina*)	0.0	0.0	0.0	4.5	4.6	0.0	0.0	0.0	4.8	12.1
Agglutinated foraminifera (mainly *Coskinon rajikae*)	0.0	0.0	1.2	0.0	0.0	0.0	0.0	0.8	0.0	0.0
EBF	0.0	0.0	0.0	0.0	0.0	0.0	0.0	0.0	0.0	0.0
SBF	24.0	23.9	18.0	4.6	1.1	11.7	21.2	12.6	3.7	6.7
GCA	3.7	3.1	0.0	13.4	3.8	4.7	7.3	6.7	14.9	0.3
Characeae	0.4	0.0	0.0	0.0	0.0	0.0	0.0	0.0	0.0	0.0
RCA	0.0	0.0	0.0	0.5	0.0	0.0	0.0	0.0	0.1	0.0
Corals	2.1	1.7	0.0	0.4	2.1	5.4	0.0	3.7	5.3	0.3
Echinoderms	4.8	4.0	0.6	0.3	0.0	2.2	6.1	2.2	0.3	0.0
Mollusks	1.1	0.4	0.2	7.4	0.1	5.8	0.6	1.5	0.0	0.0
Ostracods	6.4	7.2	0.5	0.1	0.3	4.5	4.2	0.1	0.2	0.0
Others	0.0	0.0	0.0	0.0	0.0	0.05	0.0	0.0	0.0	0.0
Recrystallization (%)										
Recrystallized	2.5	1.3	5.93	1.1	9.3	6.7	4.8	16.7	10.9	11.4
Non recrystallized	97.4	98.6	94.07	98.8	90.6	93.2	95.1	83.2	89.1	88.5
Matrix (%)										
Micrite	54.9	57.6	45.52	7.2	37.6	71.5	38.7	16.8	2.0	0.0
63-250	22.1	10.6	9.50	19.5	7.1	6.9	42.6	26.5	42.9	24.4
250-500	0.0	0.0	0.0	5.01	0.0	0.7	0.0	2.1	1.9	0.0
500-2000	9.0	15.2	13.4	22.1	9.4	6.9	8.4	17.7	14.3	10.1
>2000	13.8	16.4	31.4	46.1	45.8	13.8	10.1	36.7	38.7	65.4

Table 5.1: Details of the skeletal assemblages of the Baroch and Nammal Gorge.

In addition to the aforementioned standard biofacies, the other two facies can be observed only in the Ghumanwan section. The carbonate system of the Hazara Basin was indeed different from that of those of the investigated areas of the Salt Range (Nammal Gorge) and Surghar Range (Baroch Nala). The Hazara Basin was characterized by small patch reefs resulting in a remarkable contribution from symbiont-bearing colonial corals. This results in the presence of two main lithofacies, one related to the patch reefs and the presence of a bioconstructed framework and one characterizing the bioclastic sediment surrounding the patch-reefs. The one related to the patch-reefs (Lithofacies: Coral framestone; LF1) consists of almost purely bioclastic carbonates dominated by fragments of thin branching colonial corals associated with lesser amounts of SBF and LBF and rare red calcareous algae. The second lithofacies characterizing the sediment surrounding and covering the patches (Lithofacies LBF packstone; LF2) also consists of pure carbonates and is dominated by LBF and SBF associated with common green calcareous algae, and rare red calcareous algae, echinoderms, mollusks and colonial corals.

5.6. Section descriptions

5.6.1. **Baroch Nala section**

The Baroch Nala section is located on the western side of the River Indus in the Trans-Indus Surghar Ranges (upper Indus Basin), at the political border of the provinces of Punjab and Khyber Pakhtunkhwa regions.

The 60 meters long studied interval comprises the thick nodular limestone of Lockhart Limestone at the base of the section. Upwards is dominated by the poorly consolidated calcareous marls interbedded with limestone layers which characterize the lithological composition of the Patala Formation.

Based on micropaleontological, sedimentological, and geochemical evidence, five stratigraphic intervals can be identified in the Baroch Section. The first interval partially belongs to the Lockhart Limestone and the other four are included in the Patala Formation. These intervals correspond to different moments in the environmental and ecological transition that characterizes the Late Paleocene: 1) pre-PETM, base of the section up to 15.6 m above the base of the section (*abs* from

here onwards; 2) pre-onset excursion (POE) (15.6 - 23.4 m *abs*); 3) PETM onset (23.4 - 27.5 m *abs*); 4) PETM body and early recovery (27.5 - 47.5 m *abs*); 5) post-PETM (47.5 – 59.5 m *abs*) (see Chapter 4 for more details) Detailed data sheets available in Appendix Supplementary Tables BS1, BS2, and BS3.

Pre-PETM interval

The lowermost 6 meters of the interval are characterized by light-grey, nodular limestones, with a mudstone to wackestone texture (Lockhart Limestone). The upper part of the interval (6 - 15.6 m *abs*) consists of dark grey, poorly lithified calcareous marls with a wackestone-to-packstone texture (Patala Formation). Nodular phosphate and pyrite, along with other authigenic minerals like glauconite also occur.

In the lower part of the interval, $\delta^{13}C_{org}$ values range from -19.3‰ to -20.4‰. The TOC is low and ranges from 0.1 to 0.2 wt % (HI: 209 - 288 mg HC/g TOC; OI: 49 - 107 mg CO2/g TOC; T-max: 420 – 444 °C). Very low Hg concentrations are recorded between 0.6 and 1.0 ppb. The terrigenous fraction is characterized, in decreasing order of abundance, by phyllosilicates, quartz, feldspar, and plagioclase, whereas the clay assemblage is characterized by smectite, palygorskite, kaolinite, chlorite, and illite (Figure 5.4).

In the upper part, $\delta^{13}C_{org}$ ranges from -18.5‰ and -22.0‰., whereas $\delta^{13}C_{carb}$ ranges from 1.7‰ to 2.5‰ and displays a pattern similar to that of $\delta^{13}C_{org}$. $\delta^{18}O_{carb}$ values are comprised between -4.7‰ and - 6.0‰, whereas TOC ranges between 0.1 to 1.0 wt% (HI: 76 - 240mg HC/g TOC; OI: 56 - 235 mg CO2/g TOC; T-max: 424 – 438 °C). Hg values are low, ranging from 0.7 to 9.6 ppb and peaking close to the boundary with the overlying interval. The terrigenous fraction is characterized by phyllosilicates associated with lesser amounts of fine-sand-sized quartz, feldspar, and plagioclase, whereas the clay fraction is characterized by smectite, associated with kaolinite and palygorskite, and minor illite, illite-smectite mixed layers, and chlorite.

The skeletal assemblage of this interval displays all the characteristics of BF1. The overall foraminiferal assemblage is dominated by hyaline LBF typical of the Paleocene (mainly trocospiral forms like *Lockhartia* and orbitoidiforms like *Lakdongia* and *Orbitosiphon*). Diagnostic LBF taxa indicate a placement within SBZ3 for the base of the interval (upper Selandian to lower Thanetian; Papazzoni et al., 2023) and within SBZ4 for the top of the interval

(upper Thanetian; Papazzoni et al., 2023)(Figure 5.3 and Chapter 4, Figure 4.6). . Calcareous nannofossils indicate a placement within NP4 and NP5 (upper Danian to Selandian)(Figure 5.2). This is consistent with $\delta^{13}C$ (both bulk carbonates and organic matter) which, with its limited oscillations, supports a placement within the pre-PETM phase.

Pre-onset excursion (POE) interval

The interval consists of grey-colored, impure nodular limestone with a wackestone to packstone texture; dark grey, poorly-lithified, calcareous marls with a wackestone to packstone texture; a poorly-lithified dark-colored shale layer at 16.8 m *abs*; a dolomite-rich layer at 19.8 m *abs*. Between 15.6 and 16.8 m *abs*, $\delta^{13}C_{org}$ shifts from -19.4‰ to -23.0‰, $\delta^{13}C_{carb}$ from 1.8‰ to 1.0‰, and $\delta^{18}O_{carb}$ from - 4.8‰ to -6.6‰. Upwards, $\delta^{13}C_{org}$ and $\delta^{13}C_{carb}$ recover back to less negative and more positive values respectively, whereas $\delta^{18}O_{carb}$ moves towards less negative values. TOC values fluctuate irregularly between 0.1 to 1.0 wt% (HI: 43 - 182 mg HC/g TOC; OI: 64 - 212 mg CO2/g TOC; T-max: 417 – 438 °C). Hg content ranges from 0.4 ppb to 7.7 ppb, with a clear peak at 16.8 m *abs*. The overall terrigenous fraction mainly consists of phyllosilicates, associated with quartz, very rare feldspar, and plagioclase. The overall clay assemblage is characterized by smectite associated with kaolinite and minor palygorskite, illite, and chlorite, whereas the dark-colored shale layer at 16.8 m *abs* displays an assemblage dominated by kaolinite.

The interval is characterised by BF2 and is dominated by hyaline LBF typical of the Paleocene (mainly trocospiral forms like *Lockhartia* but also large miscellaneids) associated with SBF, green calcareous algae (Dasycladales), ostracods and echinoderms, very rare corals and mollusks. Differently from the underlying interval orbitoidiforms are less common. The occurrence of abundant large miscellaneids suggest that this interval should be entirely placed within SBZ4 (upper Thanetian; Serra-Kiel et al., 2020; Papazzoni et al., 2023)(Figure 5.3 and Chapter 4, Figure 4.6). This is in agreement with the calcareous nannofossil assemblage that, notwithstanding the scarcity and poor preservation of the specimens, indicates a placement between NP6 and NP8 (Thanetian).(Figure 5.2)

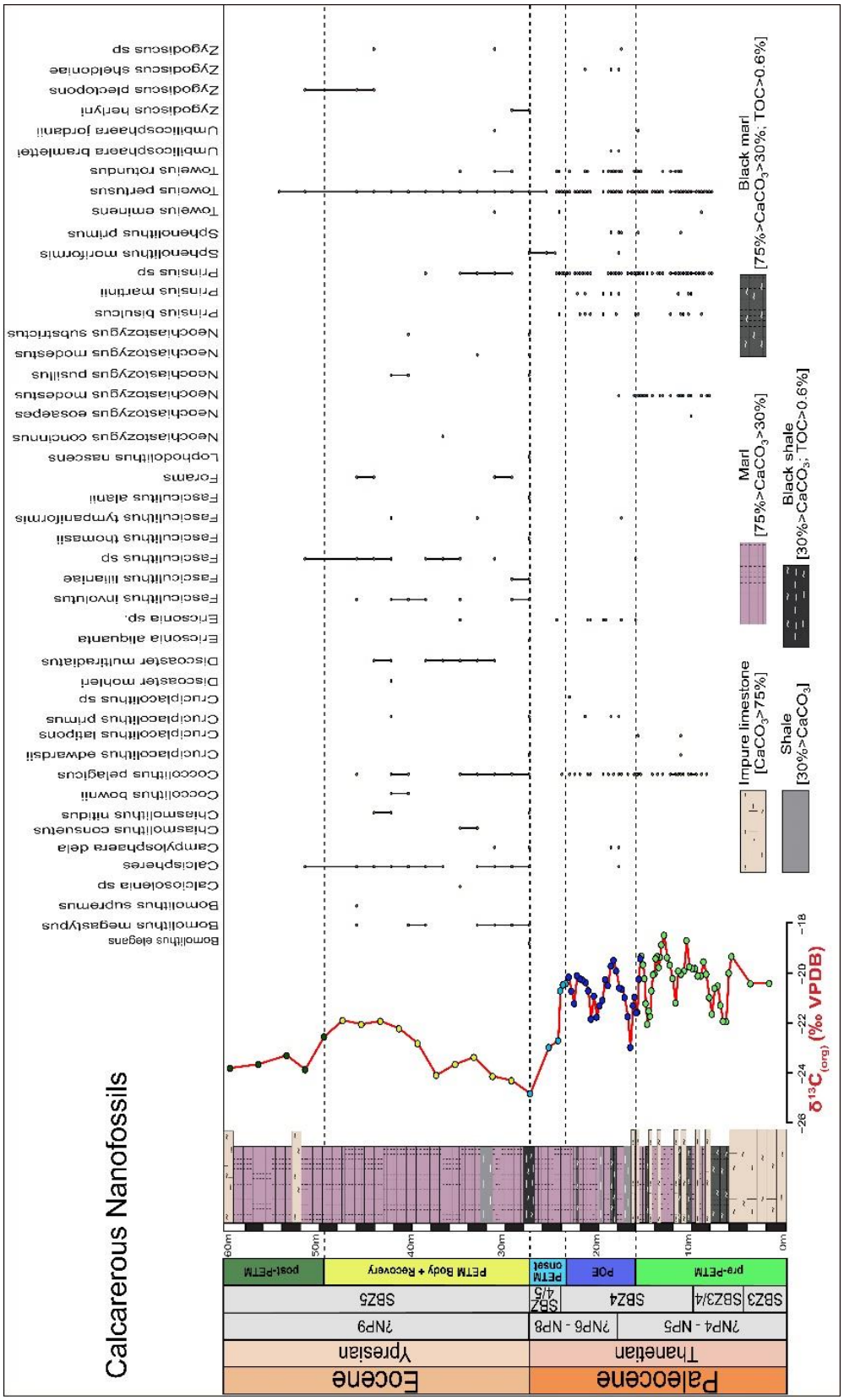

Figure 5.2 Baroch Nala section (Surghar Range, Pakistan) shows the response of Late Palaeocene to Early Eocene calcareous nannofossils (NP) assemblages along the carbon (organic matter) stable isotope records. The section is subdivided into 05 phases including pre-PETM (Palaeocene-Eocene Thermal Maximum), Pre-Onset Excursion (POE), PETM onset, PETM body and recovery, and post-PETM.

Biostratigraphy is consistent with $\delta^{13}C$. The latter parameter displays a first relevant negative shift (16.8 m *abs*) that could correspond to one of the late Thanetian hyperthermal (Barnet et al., 2019; Tremblin et al., 2022), i.e., a Pre-Onset Excursion (POE). This excursion is also associated with a significant decrease in the calcite content and with a remarkable variation in the assemblage of clay minerals. Based on the observed pattern of $\delta^{13}C_{org}$ is also possible to recognize the event, its onset (15.6 – 16.8 m *abs*), and the following recovery phase (16.8 to 23.4m *abs*.).

PETM onset interval

The lower part of the interval consists of dark grey, unconsolidated, calcareous marls with a mudstone to packstone texture, followed by a layer of TOC-rich black shale at 27.5 m *abs*. $\delta^{13}C_{org}$ and $\delta^{13}C_{carb}$ display similar trends, ranging from -20.4‰ to -24.8‰ and 1.7‰ to 1.1‰, respectively, and both displaying a sharp negative shift (-4.4 ‰ $\delta^{13}C_{org}$) at about 27.5 m *abs*. $\delta^{18}O_{carb}$ values range between -4.4‰ and -5.3‰. TOC ranges from 0.1 to 0.8 wt% peaking at 27.5 m *abs* (HI: 38 - 163 mg HC/g TOC; OI: 70 - 209 mg CO2/g TOC; T-max: 415 – 435 °C). Hg concentrations range between 2.3 and 8.5 ppb, with a sharp spike at 27.5 m *abs*. The terrigenous fraction is characterized by phyllosilicates associated with rare quartz, plagioclase, and feldspar. Dolomitic grains and authigenic minerals like glauconite and pyrite are also present. A clear increase in the abundance of phyllosilicates and quartz can be observed at the top of the interval (27.5 m *abs*). In the lower part of the interval, clays are mainly represented by smectite associated with kaolinite and rare chlorite, illite, and palygorskite, whereas in the black shale layer at 27.5 m *abs* kaolinite becomes the dominant phase and is associated with smectite and rare illite and chlorite (Figure 5.4).

The interval is characterized by BF3 and dominated by large miscellaneids LBF associated with nummulitids (mainly *Ranikothalia* but also *Assilina*) and SBF. Rare corals, green calcareous algae (Dasycladales), and echinoderms also occur. Age diagnostic taxa of LBF places most of this interval at the transition between SBZ4 and SBZ5 and thus at the very end of the Thanetian (Serra-Kiel et al., 2020; Papazzoni et al., 2023)(Figure 5.3 and Chapter 4, Figure 4.6). This is also supported by calcareous nannofossils which are representative of NP9 and thus of the upper Thanetian (Menini et al., 2021). This is consistent with the negative shift in δ13C. The magnitude

of the excursion identifies this CIE with the PETM, whose negative peak marks the Paleocene-Eocene boundary (Walsh, 2004).

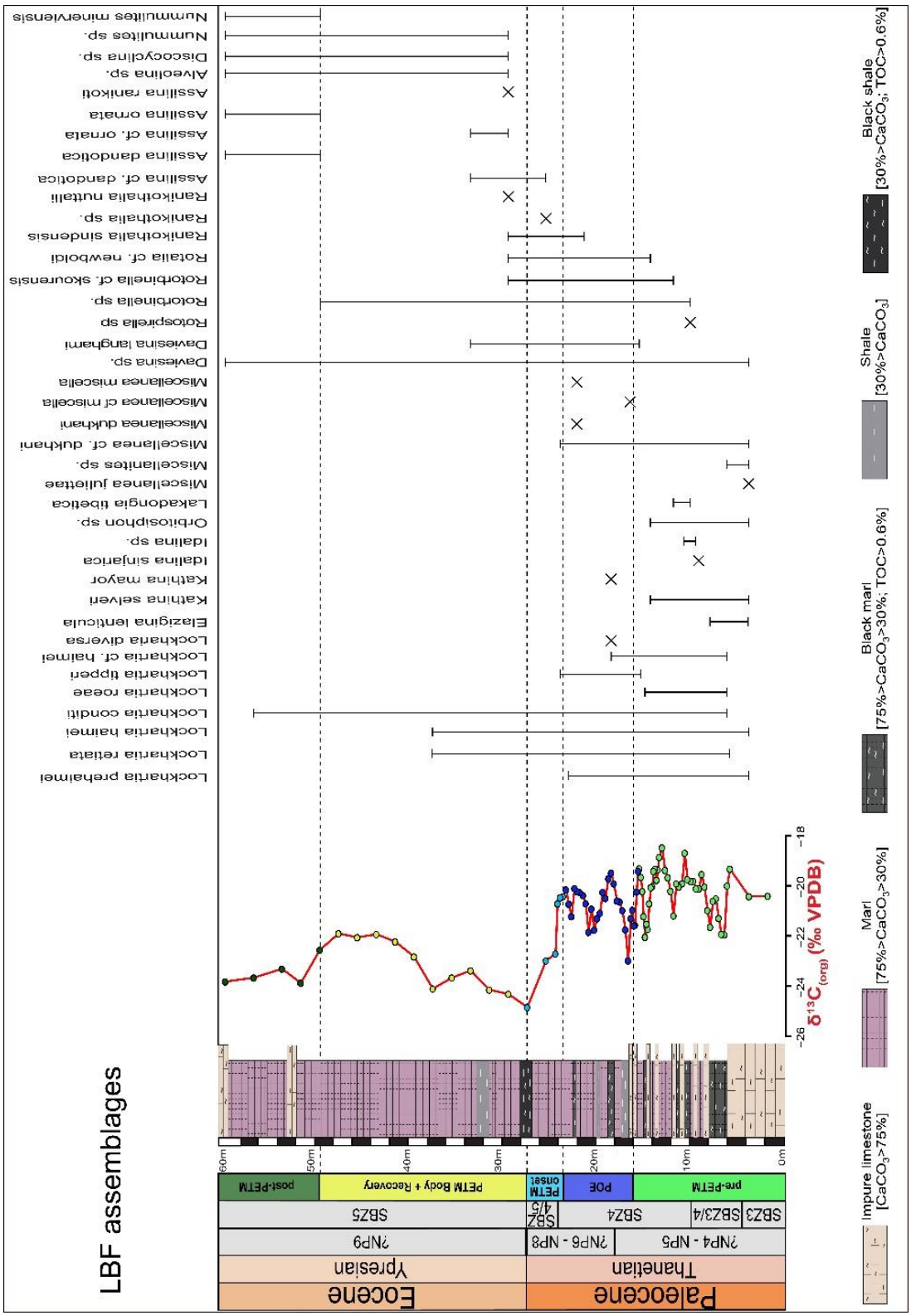

Figure 5.3: Baroch Nala section (Surghar Range, Pakistan) shows the response of Late Palaeocene to Early Eocene large benthic foraminifera (LBF) assemblages along the carbon (organic matter) stable isotope records. The section is subdivided into 05 phases including pre-PETM (Palaeocene-Eocene Thermal Maximum), Pre-Onset Excursion (POE), PETM onset, PETM body and recovery, and post-PETM.

The bulk mineralogical composition also supports the placement of the boundary at the top of this interval. Indeed, similarly to the Paleocene - Eocene boundary GSSP (Dababiya quarry in Egypt) (Khozyem et al., 2023), the negative peak of the CIE corresponds to a remarkable decrease in calcite and an increase in phyllosilicates.

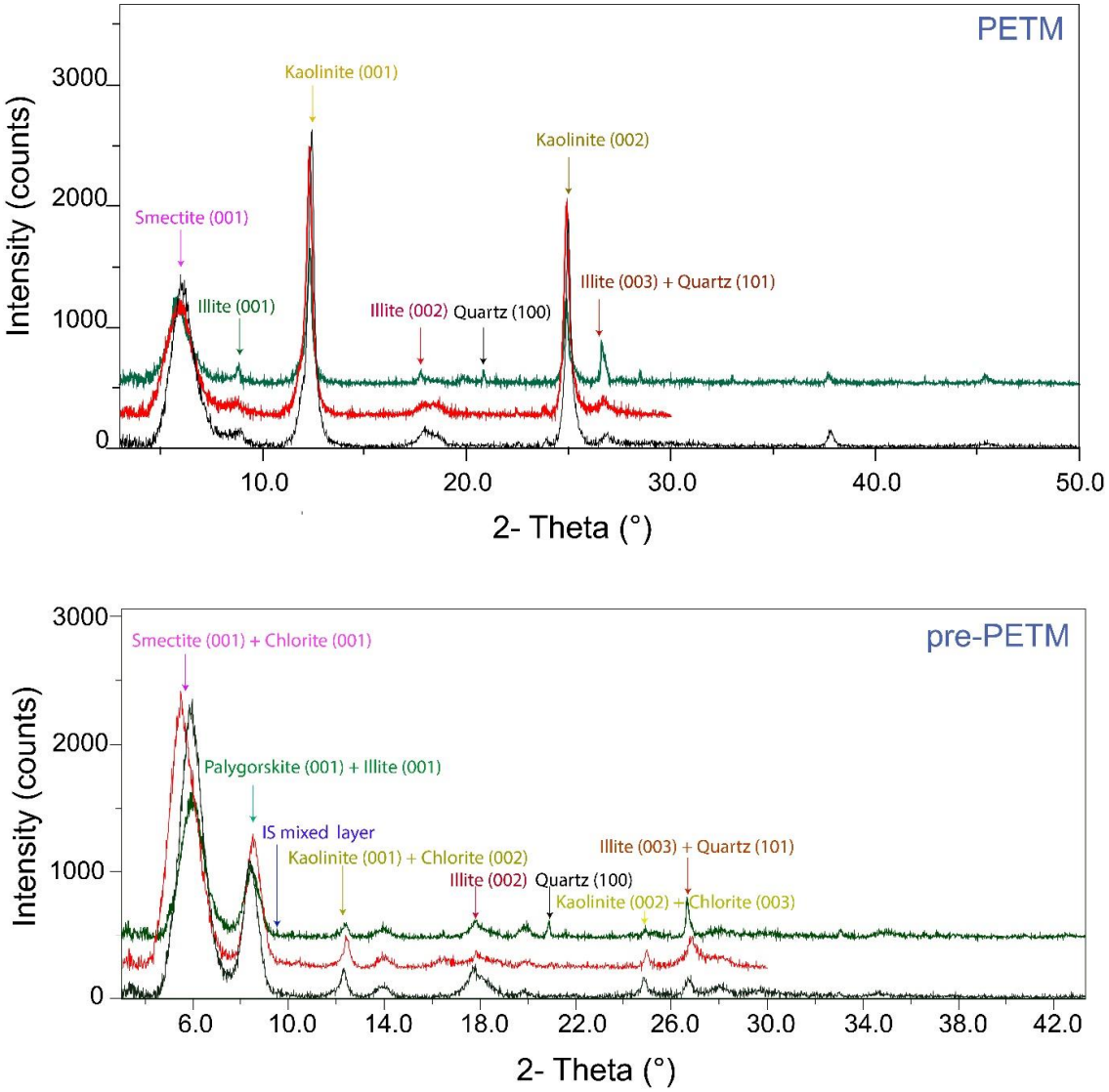

Figure 5.4: XRD spectra of clay mineralogical composition of PETM onset show the abundance of Kaolinite and smectite which marks the warm and humid climate conditions during PETM. On the other hand, the pre-PETM clay mineralogical composition indicates the abundance of palygorskite due to the arid conditions

PETM body and recovery interval

This interval (27.5-47.5 m *abs*) consists of poorly lithified, dark-grey, highly fossiliferous calcareous marls with a rudstone texture. Between 27.5 and 37.5 m *abs*, $\delta^{13}C_{org}$ values fluctuated between -23.4‰ to -24.3‰, $\delta^{13}C_{carb}$ ranging from 1.3‰ to 1.9‰, and $\delta^{18}O_{carb}$ from – 5.2‰ to -6.52‰. TOC values fluctuate between 0.1 and 0.2 wt% (HI: 25 - 68 mg HC/g TOC; OI: 203 - 226 mg CO2/g TOC; T-max: 402 – 428 °C) and Hg content from 2.1 ppb to 6.3 ppb. Based on $\delta^{13}C$, this lower part of the interval should correspond to the "body" phase of the CIE. Upwards, between 37.5 to 47.5 m *abs*, $\delta^{13}C_{org}$ ranges from 21.9 ‰ - 22.8 ‰, $\delta^{13}C_{carb}$ from 2.3‰ to 2.7‰, and $\delta^{18}O_{carb}$ from - 4.7‰ to -7.0‰. TOC values fluctuate irregularly between 0.1 to 0.2 wt% (HI: 48 - 86 mg HC/g TOC; OI: 178 - 332 mg CO2/g TOC; T-max: 408 – 434 °C), whereas Hg content ranges from 2.9 ppb to 3.8ppb. Since δ13C values move back towards pre-CIE levels, this upper part of the interval should correspond to the recovery phase of the CIE. The terrigenous fraction is dominated by phyllosilicates with minimal amounts of quartz, feldspar, and plagioclase. Clays are mainly represented by kaolinite, which dominates the lower part of the interval (27.5 – 37.5 m *abs*) corresponding to the body phase, and by smectite which dominates the upper part (37.5 – 47.5 m *abs*), corresponding to the recovery phase.

The interval is characterised by BF4 and is dominated by hyaline LBF typical of the Eocene (*Assilina* and *Operculina, Discocyclina,* and rare *Nummulites)*. Although Eocene taxa largely dominate, specimens of taxa mainly occurring during the Paleocene (e.g., *Ranikothalia* and *Lockhartia*) still occur. Hyaline LBF are associated with common green calcareous algae (mainly Dasycladales, but also Bryopsidales), and less common alveolinids, SBF, mollusks, corals, echinoderms, red calcareous algae, and ostracods. Consistently with carbon stable isotope stratigraphy, the LBF assemblage indicates SBZ5 and thus an early Ypresian age (Serra-Kiel et al. 2020; Papazzoni et al., 2023)(Figure 5.3 and Chapter 4, Figure 4.6). . A placement very close to the boundary between Paleocene and Eocene is also supported by the calcareous nannofossil assemblage (Menini et al., 2021) (Figure 5.2).

Post-PETM interval

This interval (47.5–59.5 m *abs*), consists of calcareous marls and brown-colored, bioclastic, impure limestones with a grainstone texture in the lower part. Upwards it is characterized by dark gray marls and impure limestones displaying a rudstone texture. $\delta^{13}C_{org}$ ranges from -22.6‰ to -23.9‰, $\delta^{13}C_{carb}$ from 2.0‰ to 2.4‰, $\delta^{18}O_{carb}$ from -4.5‰ and -5.0‰, and TOC from 0.03 to 0.1 wt% (HI: 59 - 105 mg HC/g TOC; OI: 236 - 376 mg CO2/g TOC; T-max: 405 – 435 °C). Hg concentrations fluctuate between 0.3 and 2.21 ppb, with no major spikes. The limited terrigenous fraction mainly consists of phyllosilicates associated with rare quartz and other detrital minerals. The clay fraction is dominated by smectite associated with kaolinite, rare illite, palygorskite, and chlorite. The interval is characterized by BF5 and entirely dominated by taxa of hyaline LBF that typically occur during the Eocene: *Nummulites, Assilina, Operculina,* and *Discocyclin*a. These are associated with common alveolinids, and lesser amounts of SBF, green calcareous algae (mainly Dasycladales), corals, mollusks and ostracods. LBF taxa indicates a placement in SBZ5 (lower Ypresian), consistently with $\delta^{13}C$, which recovers close to pre-excursion values and no longer shows prominent negative shifts. Therefore, this interval should be representative of the beginning of the post-PETM phase.

.

5.6.2. **Nammal Gorge section**

The Nammal Gorge section is located in the extremity of Nammal Lake, on the eastern side of the Indus River, in the western Salt Range (upper Indus Basin), approximately 40 km on the east of the Baroch Nala section.

The investigated 38 m thick Paleocene-Eocene Patala Formation consists of calcareous marls interbedded with thin limestone layers in the lower part. In the middle portion of the section, it comprises thick calcareous marls with the local occurrence of dolomite layers. The upper part of the Patala Formation is dominated by carbonate layers associated with the presence of minor dark marl layers. Following the same approach used for the Baroch Nala section and based on multiproxy-integrated analysis, the Patala Formation at the Nammal Gorge section has been subdivided into five stratigraphic levels. Based on the results of the geochemical and paleontological analysis and the comparison with the well-preserved record of the Baroch Nala section these five intervals have been identified as: 1) pre-PETM, up to 22.7 m *abs*; 2) pre-onset excursion (POE; 22.7-27.1 m *abs*); 3) PETM onset (27.1 29.8 m *abs*); 4) PETM body and early recovery (29.8-36.6 m *abs*); 5) post-PETM (36.6–38 m

abs)(Figure 5.5). Detailed data sheets available in Appendix Supplementary Tables NS1, NS2, and NS3

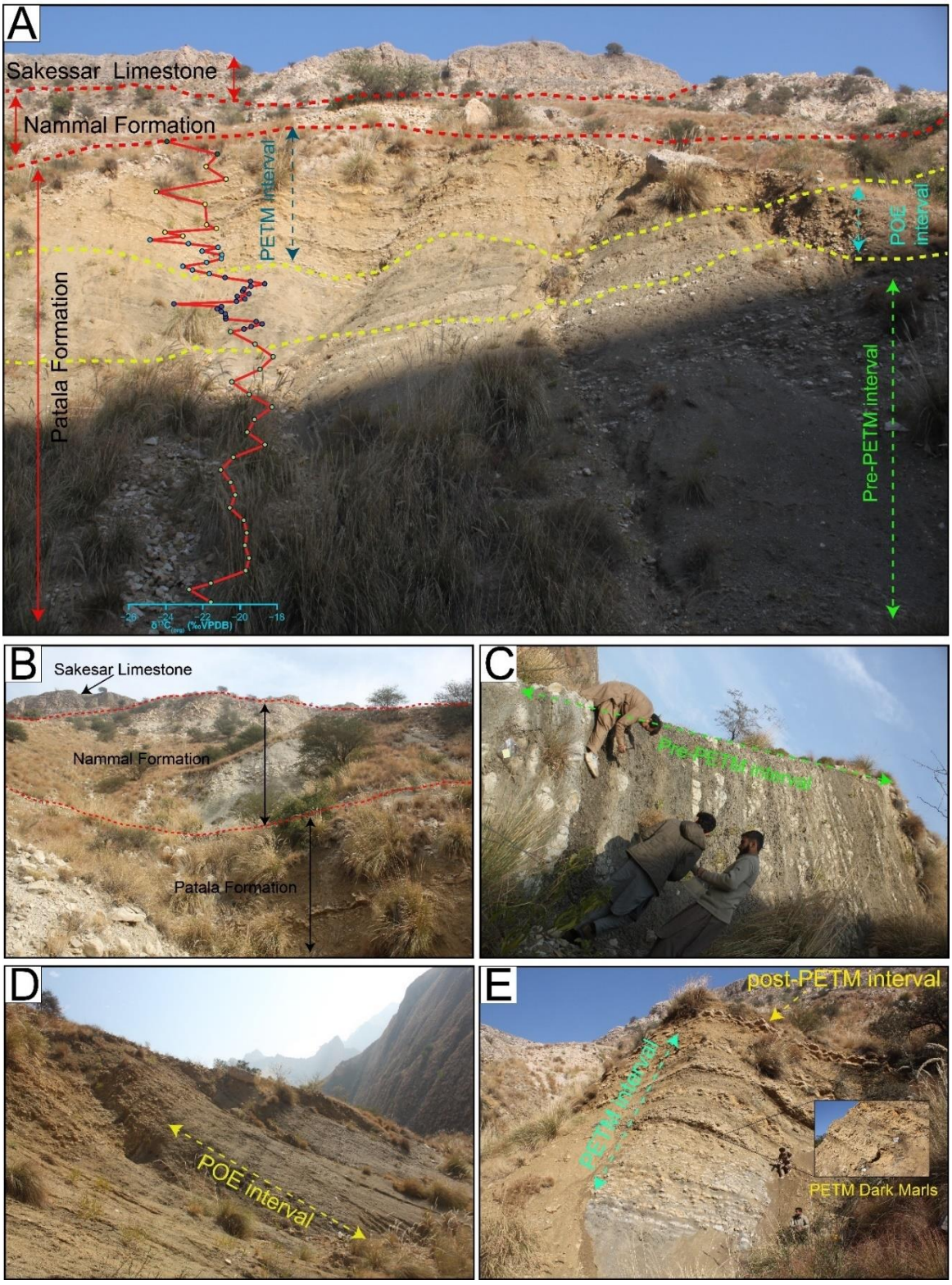

Figure 5.5 shows paleontologically, geochemically, and mineralogically identified five intervals of the Paleocene-Eocene transition in the Patala Formation in the Nammal Gorge section. These consist of pre-PETM, POE, PETM, and post-PETM stages.

Pre-PETM stage

The lowermost 22.7 m thick interval is characterized by poorly lithified mudstone, interbedded with thin nodular packstone-wackestone and dark shale layers (Figure 5.5). . In the lower part of the interval, $\delta^{13}C_{org}$ ranges from -18.2‰ to -22.7‰ and $\delta^{13}C_{carb}$ from 2.3‰ to 1.3‰. $\delta^{18}O_{carb}$ varies between -4.5‰ and -6.4‰. TOC ranges from 0.07 to 1.1 wt%, (HI 70-196 mg HC/g TOC; OI 42-249 mg CO2/g TOC; T_{max} 420–449°C)(Figure 5.8). Mercury (Hg) concentrations are low, ranging from 0.1 to 11.5 ppb, while Hg/TOC ranges from 7 to 18 ppb/wt%. The terrigenous fraction (~ 35% of the whole interval) consists of phyllosilicates and fine quartz (Figure 5.10). The clay assemblage is dominated by smectite, palygorskite, illite, rare kaolinite, and mixed-layer illite-smectite also occur (Figure 5.11, 5.14). Authigenic nodules occur in the marly lithology.

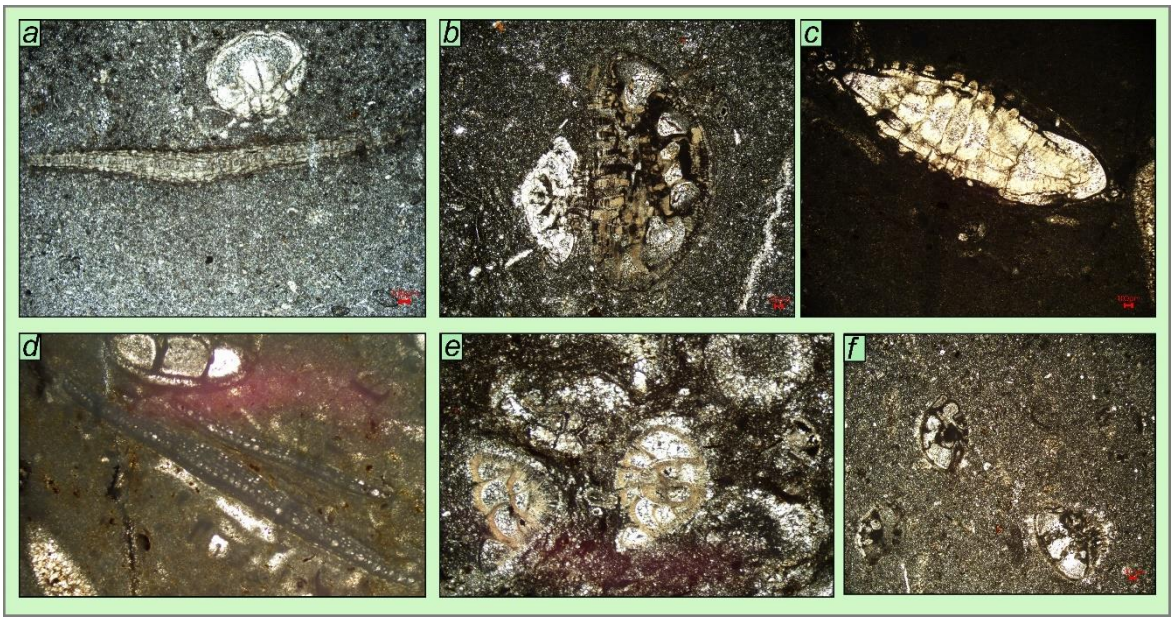

Figure 5.6 shows the Nammal Gorge section pre-PETM LBF assemblages a) *Orbitosiphon cf. punjabensis* and *Lockhartia* sp. b) Two different species of *Lockhartia sp.* c) *Daviesina sp* d) *Lakadongia sp.* e, f) Conical hyaline LBF

BF1 characterizes the interval with dominant hyaline LBF (mainly trocospiral forms like *Lockhartia* ass ociated with scarce large planispiral rotaliids *Daviesina* and orbitoidiforms like *Lakadongia* and *Orbitosiphon)* and common SBF. Rare ostracods, Dsycladales, colonial corals, echinoderms, and mollusks, also occur (Figure 5.6 & 5.12). The occurrence of *Daviesina praegarumnensis* with *Lockhartia haimei* indicates SBZ3 (upper Selandian - lower Thanetian; Papazzoni et al., 2023) for the lowermost part of the interval (4.5 m *abs*). The presence *Lakadongia tibetica* associated with *Daviesina cf. intermedia, D. langhami, Kathina aquitanica, Orbitosiphon cf. punjabensis,*and *Elazigina lenticula* indicates SBZ4

(upper Thanetian; Papazzoni et al., 2023) for the upper part of the interval (15.5-22.7m *abs*). This is consistent with both $\delta^{13}C_{org}$ and $\delta^{13}C_{carb}$ that are consistent with pre-PETM conditions

Pre-onset excursion (POE)

This interval (22.7-27.1. m *abs*) consists of poorly lithified dark grey mudstones interbedded with a dolomite and shale layer at 23.5m and 24.7m *abs* respectively (Figure 5.5). The interval is capped with a cream-colored packstone layer at 27.1 m *abs*. At 23.5, a thin dolomite layer also occurs. The overall, terrigenous fraction is dominated by phyllosilicate with rare fine-grain quartz (Figure 5.10).

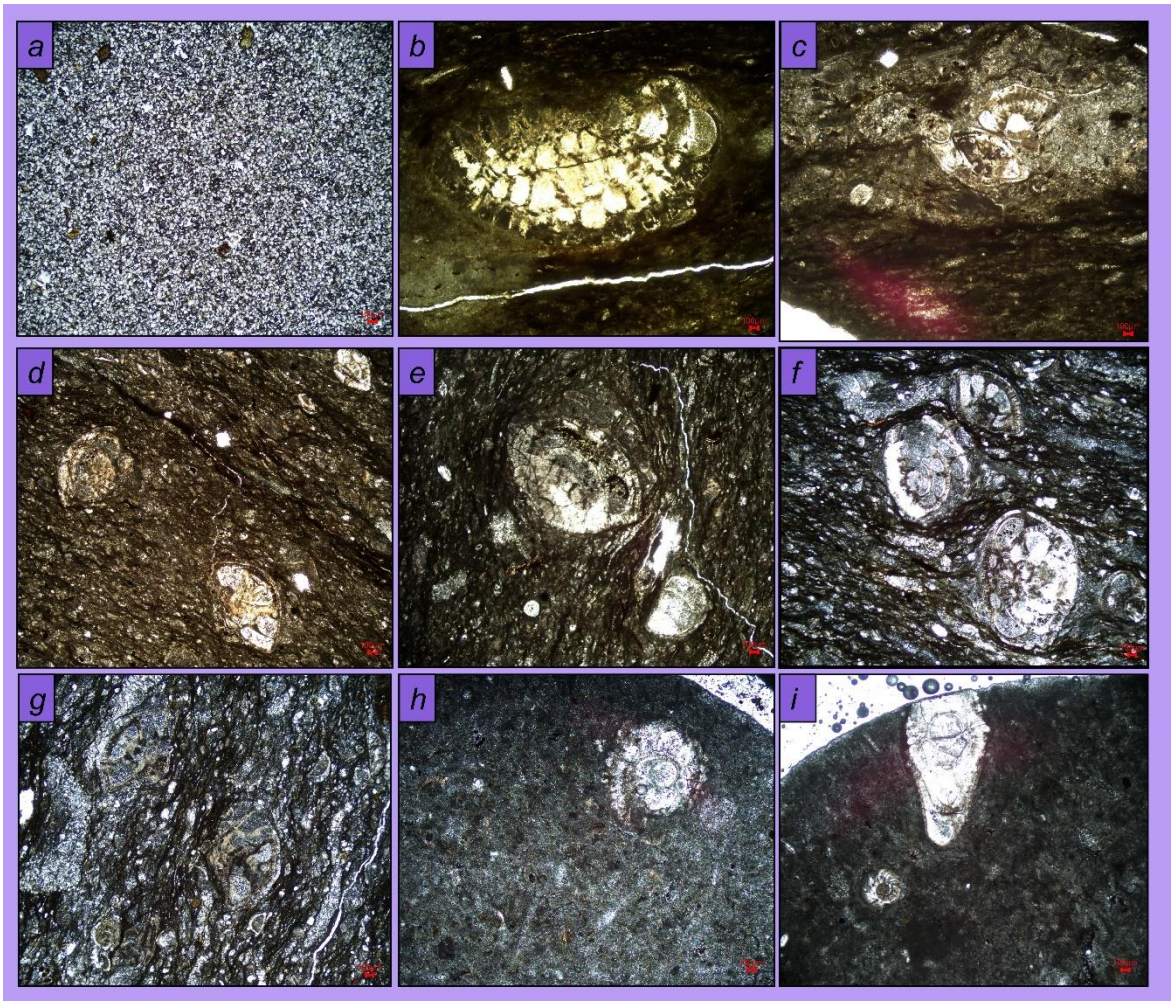

Figure 5.7 shows the Nammal Gorge section POE LBF assemblages a) Dolomite. b,c,d) Conical hyaline LBF e) *Lockhartia sp.* f, g) Conical hyaline LBF. h) *Miscellanea miscella* equatorial section displaying the large protoconch. i) *Miscellanea miscella* axial section displaying the large protoconch.

The clay fraction is dominated by smectite (45%) and kaolinite (26%), with common illite and rare mixed-layer illite -smectite (Figure 5.11, 5.14). From 22.7 – 24.7m *abs,* $\delta^{13}C_{org}$ ranges from -18.8‰ to -23.6‰ and displays a prominent shift (-4.8 ‰) toward more

negative values. $\delta^{13}C_{carb}$ ranges between 2.4‰ and 0.7‰, and $\delta^{18}O_{carb}$ ranges between -2.9‰ and -7.0‰. Up section $\delta^{13}C_{org}$, $\delta^{13}C_{carb}$, and $\delta^{18}O_{carb}$ recover back to less negative from 24.7 - 27.1 m *abs*. TOC fluctuates between 0.07 and 1.3 wt%; (HI 23-229 mg HC/g TOC; OI 56-259 mg CO2/g TOC; T_{max} 423–448°C). Hg ranges between 0.5 and 15 ppb with Hg/TOC varying between 5 and 36 ppb/wt%. (Figure 5.8).

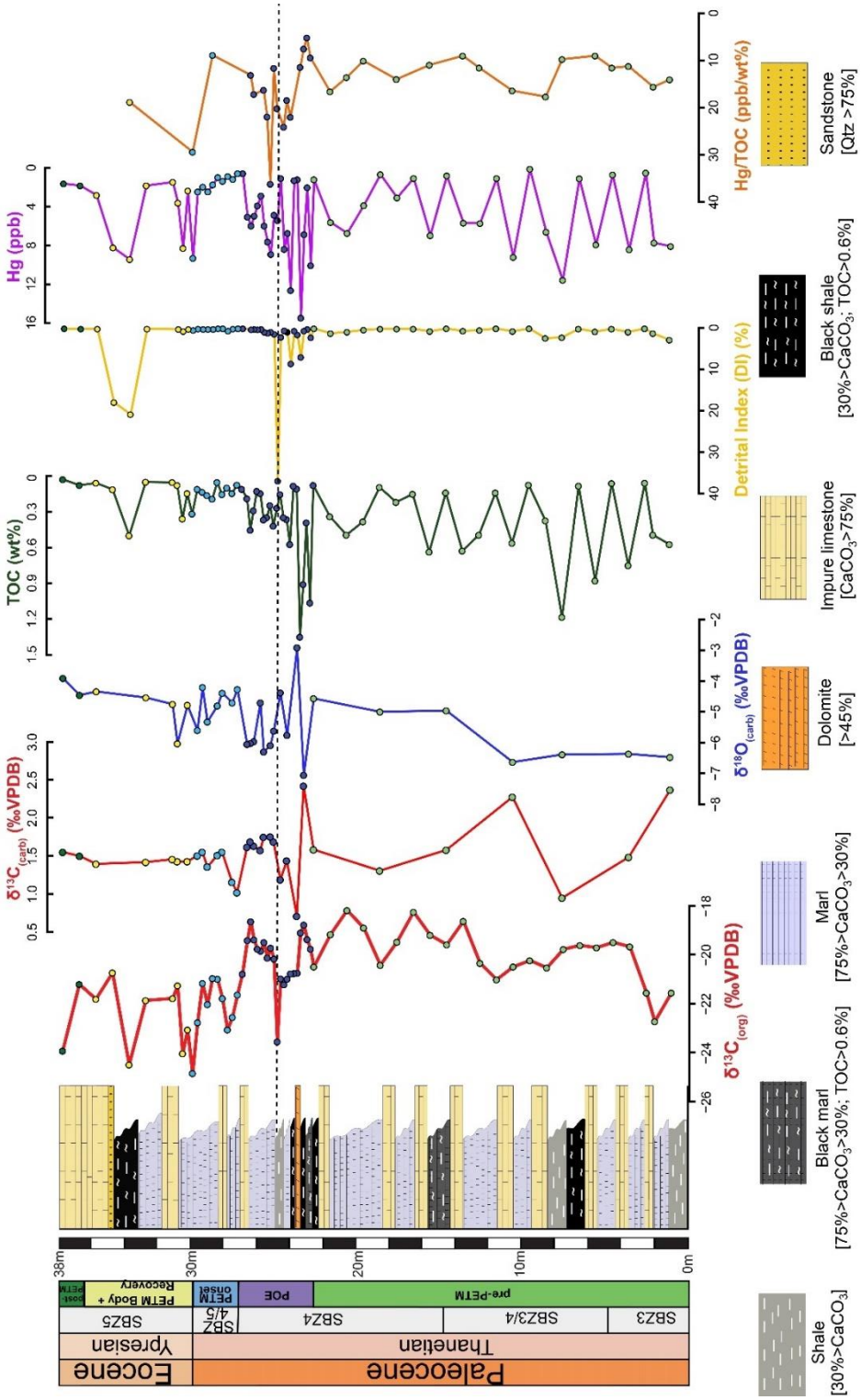

Figure 5.8: Complete carbon and oxygen stable-isotope record [$\delta^{13}C_{org}$, $\delta^{13}C_{carb}$, $\delta^{18}O_{carb}$] through Nammal Gorge section, coupled with TOC, detrital index, Hg concentration and Hg/TOC ratio, testify to major environmental perturbations at Late Paleocene to Early Eocene times.

At 24.7m *abs*, the terrigenous fraction abruptly increases and is dominated by phyllosilicate (68%) and quartz (19%)(Figure 5.10). The clay fraction becomes dominated by kaolinite (39%) whereas smectite and palygorskite decrease(Figure 5.11, 5.14).

The interval is dominated by BF2 and with hyaline LBF (mainly trocospiral forms like *Lockhartia,* and large flattened planispiral rotaliids like miscellaneids) dominating the assemblage together with abundant SBF. Scarce dasycladales, ostracods, and echinoderms also occur. The abundance of large miscellaneids such as *Miscellanea miscella, M. dukhani,* and the presence of *Lockhartia haimei*, *L. conditi, Elazigina lenticula, Dictyoconoides cf. flemingi, Kathina mayor* and *Rotalia* cf. *newboldi*, suggests a placement within SBZ4 (upper Thanetian; Papazzoni et al., 2023)(Figure 5.7 & 5.12). The shale layer at 24.7 records a first relevant negative $\delta^{13}C$ shift that may correspond to the Pre-Onset Excursion POE (Tremblin et al., 2022). The observed $\delta^{13}C_{org}$ pattern identifies the onset phase of the excursion between 22.7 and 24.1 m *abs* and the recovery phase between 24.1 and 27.1 m *abs*.(Figure 5.8).

PETM onset

This interval (27.1-29.8 m *abs*) is characterized by poorly lithified grey mudstone interbedded with dark mudstone and LBF-rich wackstone-packstone layers (Figure 5.5). . $\delta^{13}C_{org}$, $\delta^{13}C_{carb,}$ and $\delta^{18}O_{carb}$ shift from -21.0‰ to – 24.8‰, 1.7‰ to 1.0‰, and -4.2‰ to -5.5‰ respectively, and display a coherent trend characterized by a sharp negative shift (-3.8 ‰ $\delta^{13}C_{org}$), peaking at 29.8m *abs*. TOC remains low at 0.15 wt%, (HI 22-293 mg HC/g TOC; OI 102-245 mg CO2/g TOC; T_{max} 427–443°C). Hg concentrations range from 0.8 to 9.3 ppb, with Hg/TOC comprised between 8 and 29 ppb/wt%. The terrigenous fraction is dominated by phyllosilicates (19%)(Figure 5.10), and the clay assemblages mainly consists of smectite and kaolinite which increase from the underlying interval (Figure 5.11, 5.14).

BF3 characterizes the interval. The assemblage is dominated by large flattened planispiral rotaliids (mainly *Miscellanea miscella*) associated with common nummulitids (*Ranikothalia* and *Assilina*), SBF, scarce Dasycladales, rare colonial corals, and echinoderms. The occurrence of *Miscellanea miscella, Ranikothalia sindensis*, *Assilina ranikoti*, and rotaliids (*Lockharta tipperi*, *L. haimei*, *L. retiata*, *Daviesina langhami*) indicates a placement in the uppermost Thanetian, i.e. at the transition between SBZ4 and SBZ5 (Figure 5.9 & 5.12). Consistently with biostratigraphy, the large negative shift in $\delta^{13}C$ is identified at the PETM onset. (Figure 5.8).

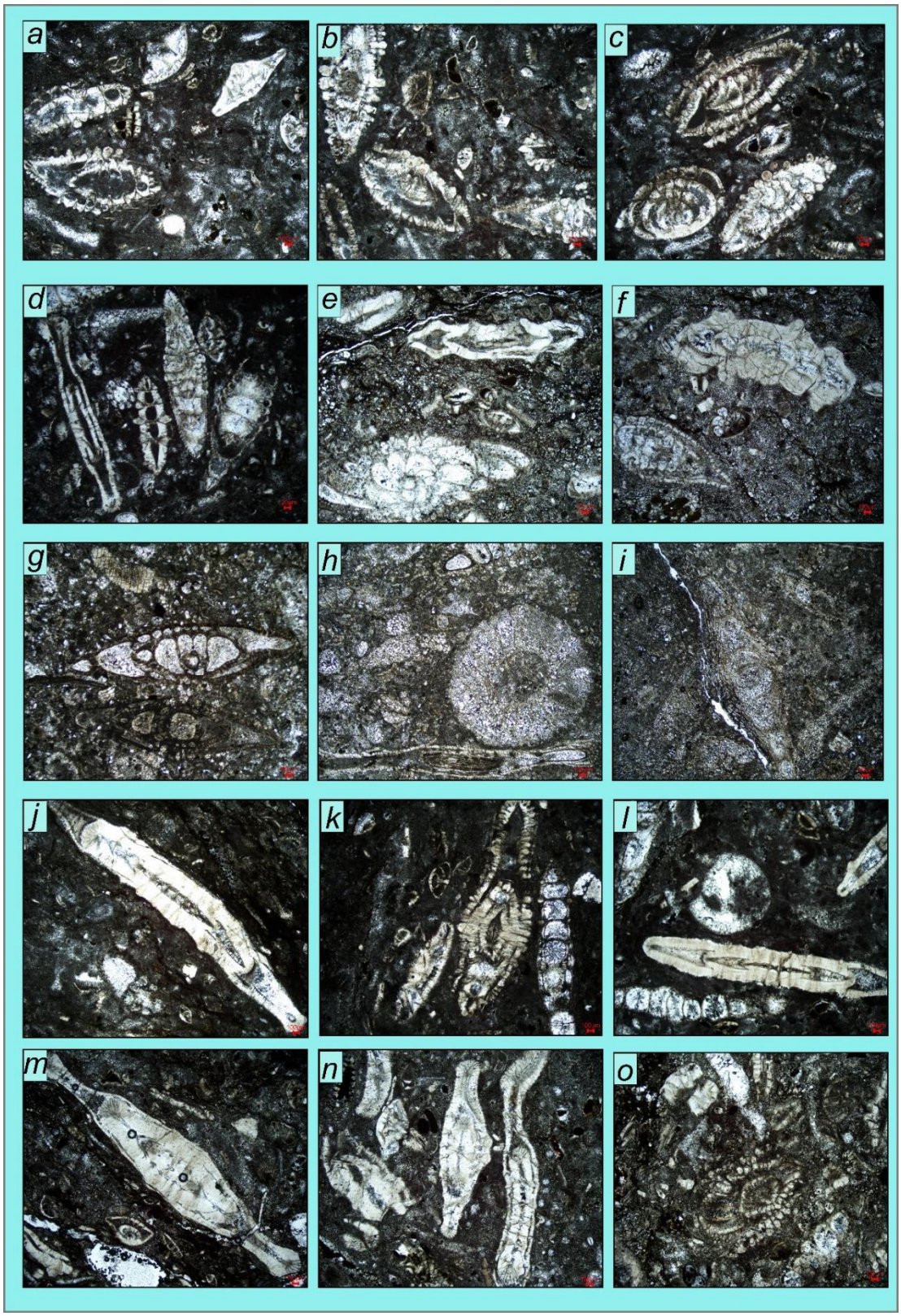

Figure 5.9 shows the Nammal Gorge section PETM onset LBF assemblages a, b) *Miscellanea dukhani*. c) *Miscellanea dukhani* and *Lockhartia*. d) *Miscellanea dukhani* and *Ranikothalia sindensis* e) *Miscellanea miscella* and *Assilina ranikoti*. f*) Assilina ranikoti*. g) *Miscellanea miscella.* h) *Ranikothalia sindensis* and Dasycladales green calcareous algae. i) *Miscellanea miscella*. j) Assilina ranikoti. k) *Daviesina*. l) *Assilina ranikoti.* M, n) *Ranikothalia sindensis* o) *Miscellanea miscella.*

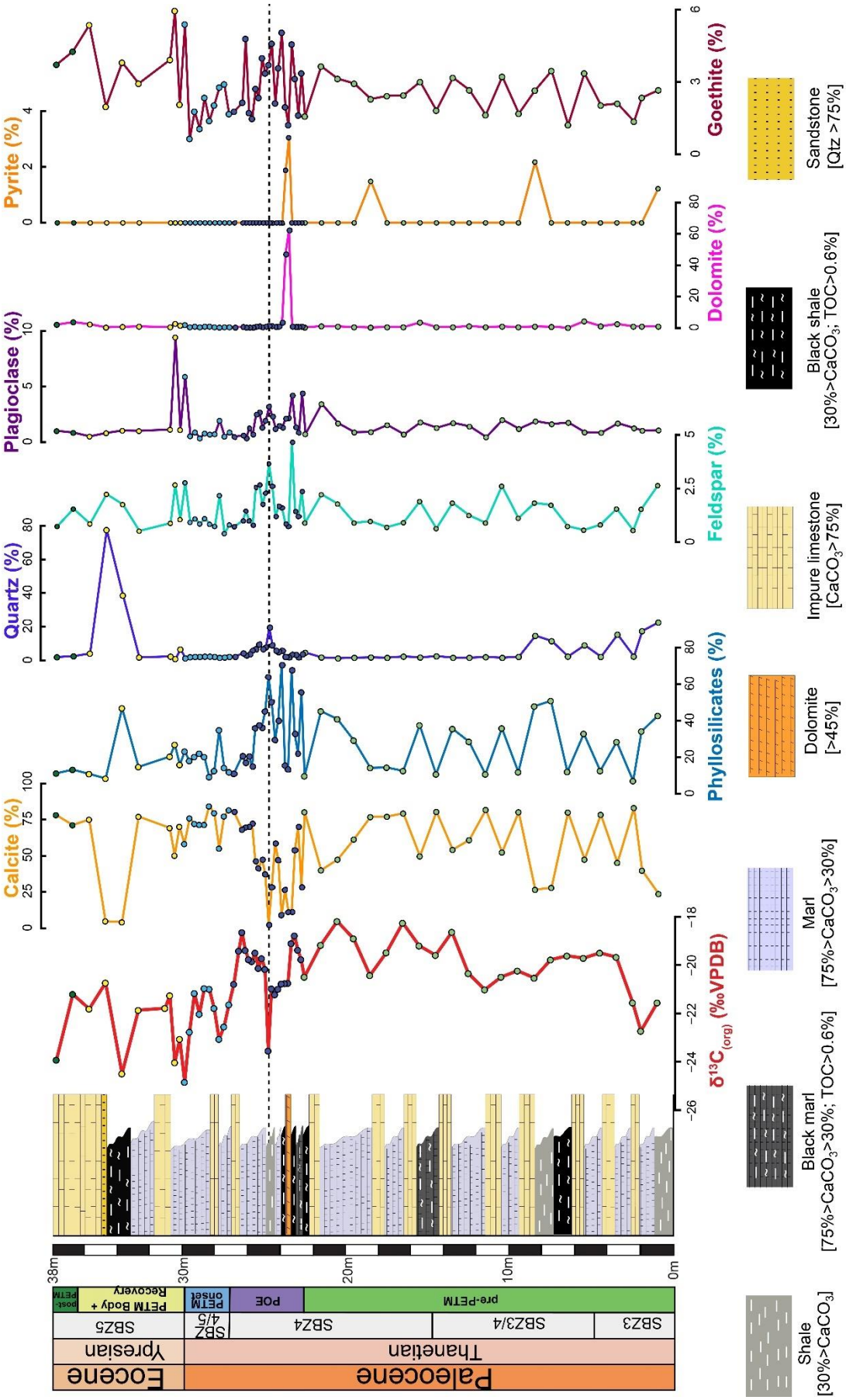

Figure 5.10: Complete record of bulk-rock mineralogical composition through Upper Paleocene to Lower Eocene strata at Nammal Gorge section. Note sharp calcite drop and phyllosilicate increase in POE and PETM intervals

PETM body and recovery

This interval (29.8-36.6 m *abs*) consists of LBF-rich packstone, interbedded with poorly lithified, dark grey, highly fossiliferous marly mudstone. A sandstone layer also occur at 34.6m *abs* (Figure 5.5).

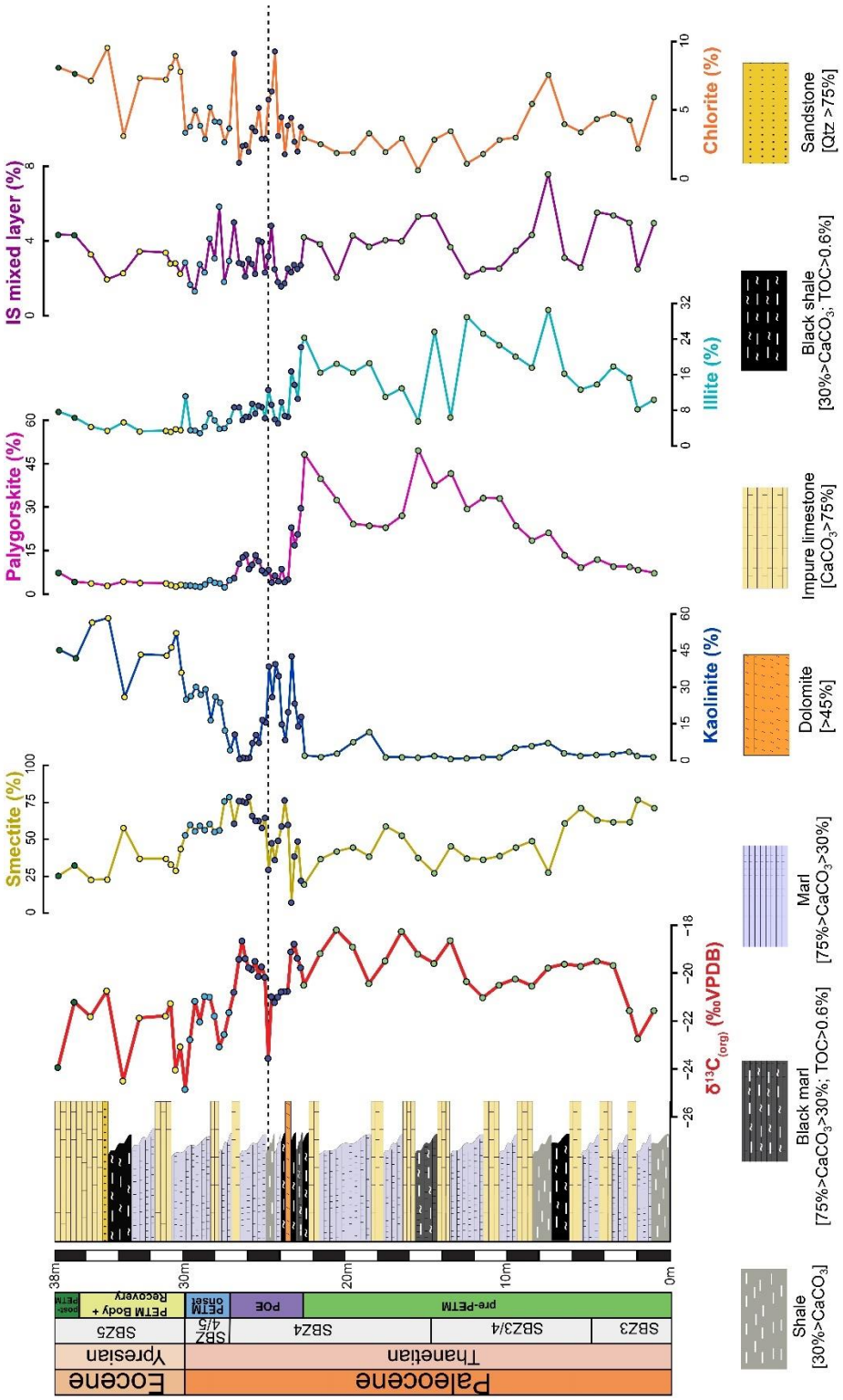

Figure 5.11: Clay mineralogy through Upper Paleocene to Lower Eocene strata at Nammal Gorge section. Note the increase in kaolinite at the expense of smectite and palygorskite during POE and PETM intervals.

$\delta^{13}C_{org}$ ranges from -20.7‰ to -24.0‰, while $\delta^{13}C_{carb}$ remains stable at around 1.4‰. $\delta^{18}O_{carb}$ fluctuates between -4.3‰ and -6.0‰. TOC is low (0.05 to 0.5 wt%) (HI 18-81 mg HC/g TOC; OI 131-482 mg CO2/g TOC; T_{max} 424–456°C). (Figure 5.8).

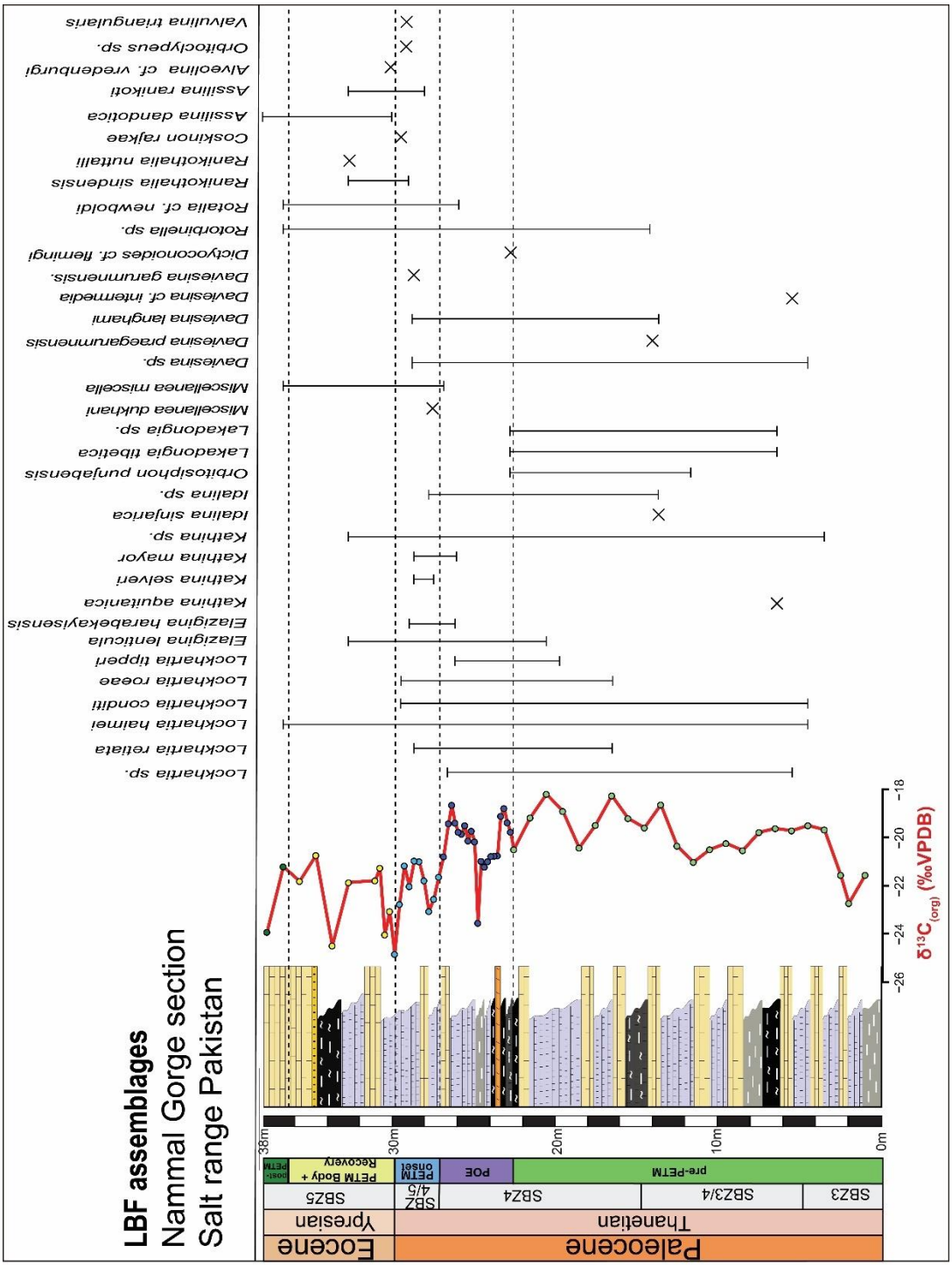

Fig 5.12 Nammal Gorge section (Salt Range, Pakistan) shows the response of Late Palaeocene to Early Eocene large benthic foraminifera (LBF) assemblages along the carbon (organic matter) stable isotope records. The section is subdivided into 05 phases including pre-PETM (Palaeocene-Eocene Thermal Maximum), Pre-Onset Excursion (POE), PETM body and recovery, and post-PETM.

Hg concentrations range from 1.4 to 9.4 ppb, with Hg/TOC fluctuating between 16 and 73 ppb/wt%. The terrigenous fraction is dominated by phyllosilicates associated with minor quartz. Quartz becomes more abundant in the sandstone layer(Figure 5.10). Kaolinite and smectite dominate the clay-minerals fraction (Figure 5.11, 5.14).

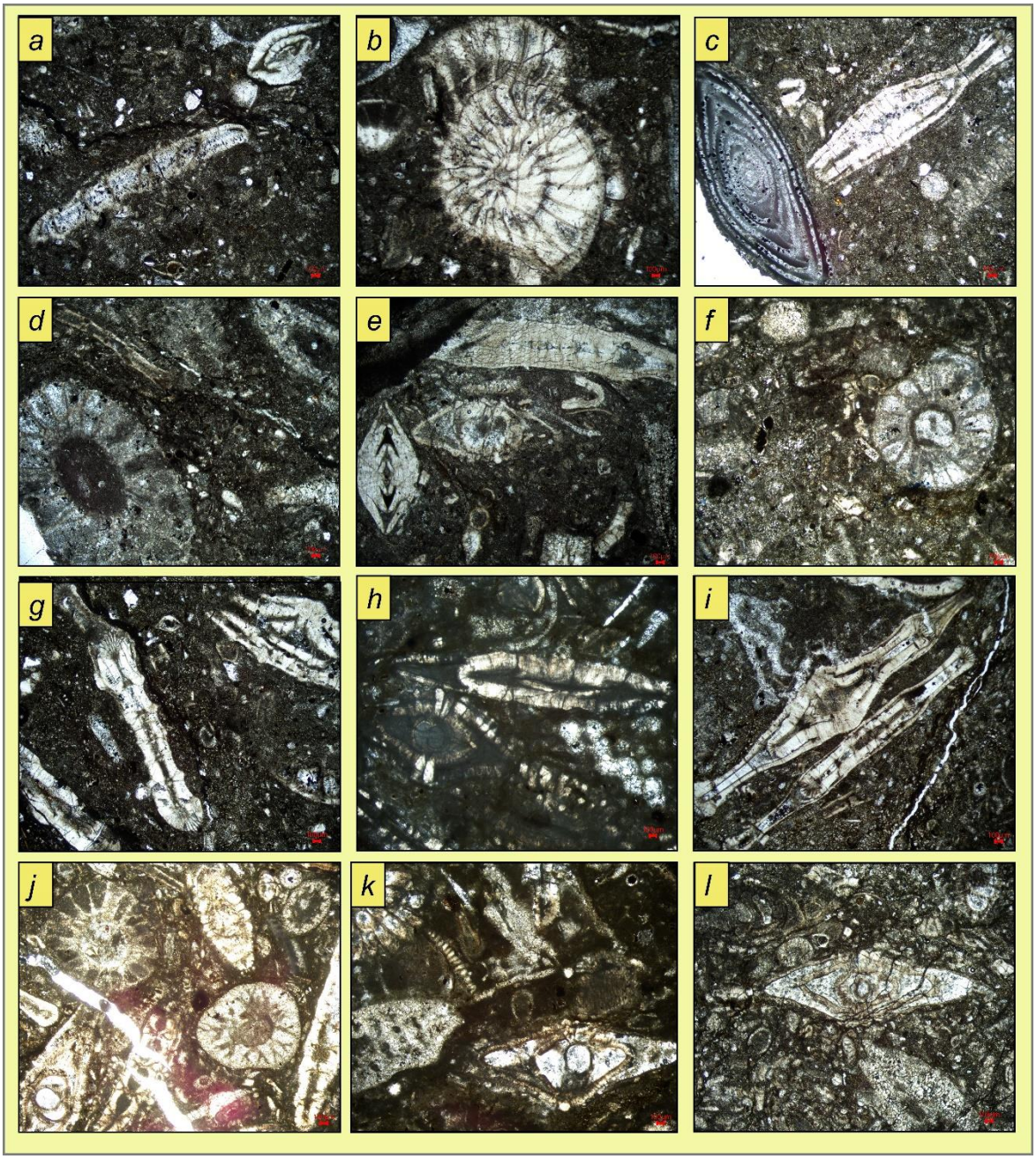

Figure 5.13 shows the Nammal Gorge section PETM body and recovery phase LBF assemblages a,e) *Assilina ranikoti* and *Assilina dandotica*. b) Nummulitid equatorial section. c) *Ranikothalia* with *Alveolina cf. vredenburgi*. D,f) Dasycladales. g) *Ranikothalia sindensis* . h) *Miscellanea miscella* and nummulitid. i) *Ranikothalia nuttali*. j) Dasycladales and hyaline LBF. K,l) *Miscellanea miscella*

Ranikothalia sindensis e) *Miscellanea miscella* and *Assilina ranikoti*. f*) Assilina ranikoti*. g) *Miscellanea miscella.* h) *Ranikothalia sindensis* and Dasycladales green calcareous algae. i) *Miscellanea miscella*. j) Assilina ranikoti. k) *Daviesina*. l) *Assilina ranikoti.* M, n) *Ranikothalia sindensis* o) *Miscellanea miscella*

BF4 characterizes the interval. The skeletal assemblage is dominated by hyaline LBF (mainly Nummulitids like *Ranikothalia Assilina*, and *Operculina,* associated with large miscellaneids), associated with common Dasycladales, and rare alveolinids, SBF, mollusks, corals, echinoderms, and red calcareous algae. The presence of *Alveolina cf. vredenburgi, Assilina dandotica, M. miscella, A. ranikoti, R. cf. newboldi, Ranikothalia nuttalli* with the *Lockhartia conditi, L. haimei, E. lenticula, Rotalia cf. newboldi* − indicates SBZ5 (lower most Ypresian), consistently with a body+recovery phase of the PETM. (Figure 5.13 & 5.12)

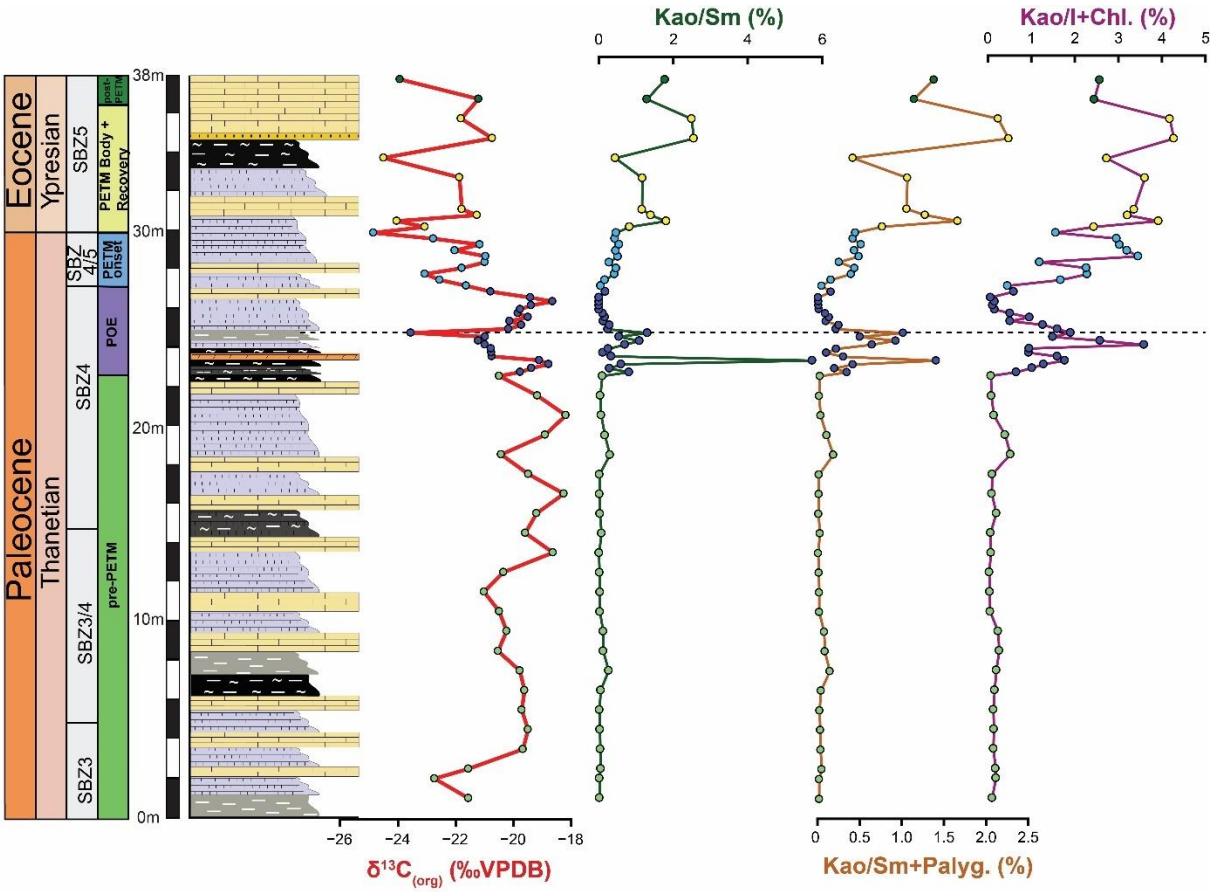

Figure 5.14: Increasing kaolinite indicates a transition to more humid and warm conditions at the base of POE and PETM body.

Post-PETM stage

This topmost interval (36.6-38 m *abs*) consists of brown colored LBF-rich packstones (Figure 5.5). The isotopic $\delta^{13}C_{org}$ value is -23.9‰; $\delta^{13}C_{carb}$ 1.5‰ and and $\delta^{18}O_{carb}$ is -3.9‰ showing stable conditions. TOC remains vwery low (0.03 wt%; HI 73 mg HC/g TOC; OI

536 mg CO2/g TOC; T_{max} 445°C). Hg concentrations are low (1.6 ppb) and Hg/TOC is around 57.3 ppb/wt% (Figure 5.8). The geochemical signals of $\delta^{13}C$ indicates a return to pre-excursion values (post-PETM phase). The terrigenous fraction (~11% of whole rock) consists of phyllosilicates with rare quartz(Figure 5.10). The clay fraction is dominated by kaolinite and smectite associated with minor illite, and palygorskite(Figure 5.11, 5.14).

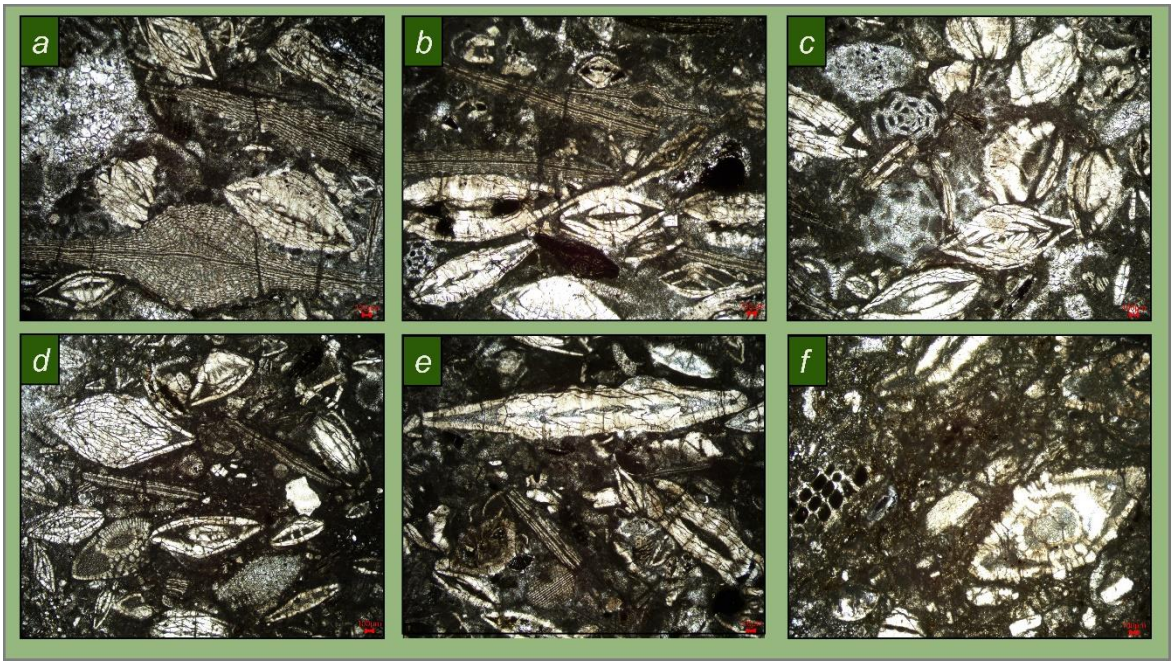

Figure 5.15 shows the Nammal Gorge section post-PETM phase LBF assemblages a) *Nummulites* and orthophragminids. b*) Nummulites, Assilina dandotica* and orthophragminids. c) Nummulitids and partially dissolved porcelanaceous foraminifera. d) Nummulitids, orthophragminids and *Lockhartia*. e) *Assilina dandotica*. f) *Miscellanea sp.*

BF5 characterizes the interval. The skeletal assemblage is dominated by hyaline LBF (nummulitids like *Assilina, Operculina*, and orthophragminids like *Discocyclina*), associated with common porcelanaceous LBF (mainly *Alveolina*), scares SBF and very rare lockhartiids. The Ypresian zone SBZ5 is indicated by the occurrence of *Assilina dandotica*. The increasing frequency of *Alveolina* and orthophragminids is also distinctive of the Eocene. Both biostratigraphy and isotopic values indicate a post-PETM phase for the interval.(Figure 5.15 & 5.12)

5.6.3. **Ghumanwan section**

The Ghumanwan section (Hazara Basin) is located in the proximity of the city of Abbottabad. The studied section lies above the Main Boundary Thrust, due to this tectonic feature the studied area falls in a complex and tectonically disturbed setting.

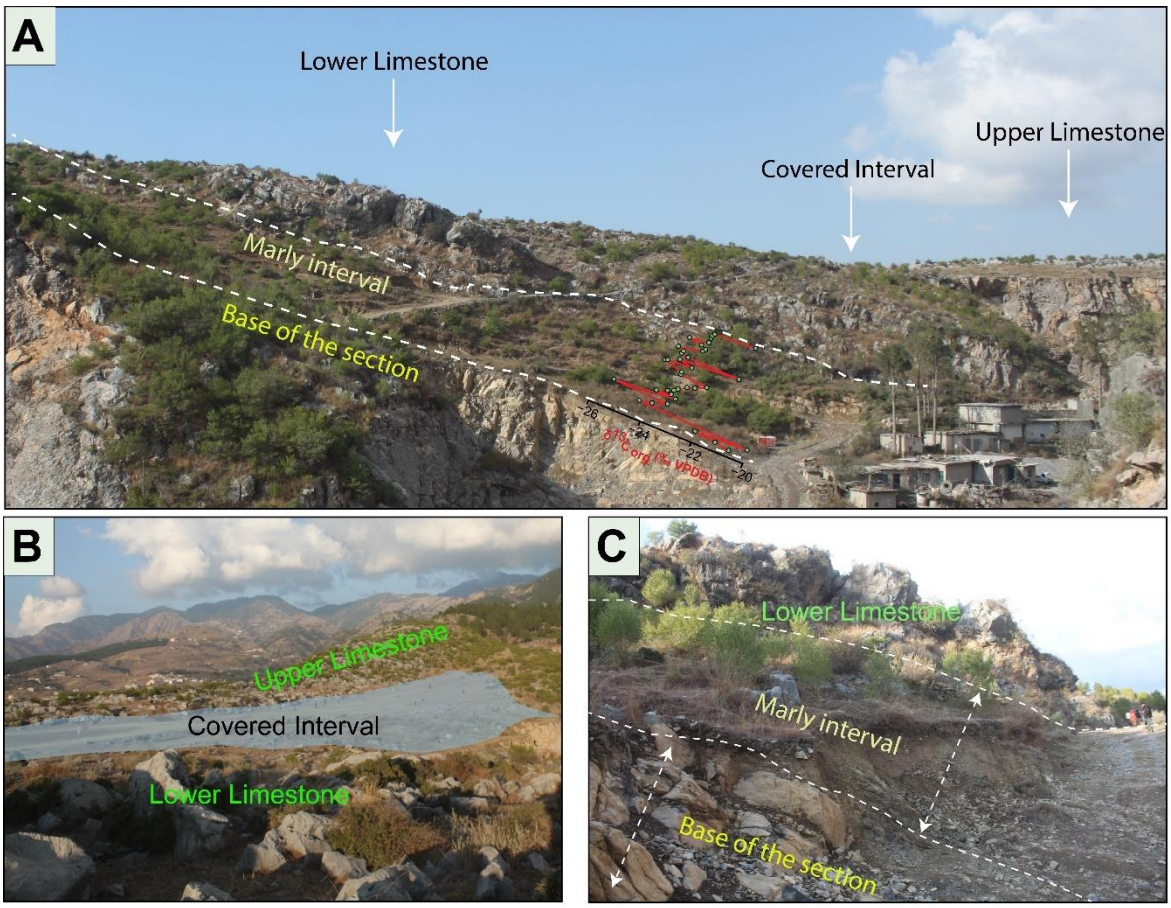

Figure 5.16 shows paleontologically, geochemically, and mineralogically identified pre-PETM interval in Ghumanwan section. The pre-PETM contains different outcrop stages. Like Base of the section (BS) 0-4m *abs*, Marly Interval (04-26m *abs*), Lower Limestone (26-70 m *abs*), Covered interval 70-90m *abs* and Upper Limestone (90-107m *abs*)

The first 4 m of the measured 107 m thick section are confidently placed within the Lockhart Limestone formation which, in the investigated area, consists of greyish, hard, compacted, fossiliferous, nodular limestones. Up section, the following part of the section (up to 26 m *abs*) are partially covered by soil and colluvial material interval. They mainly consist of layered carbonates interbedded with unconsolidated calcareous marls. Due to the disturbed nature of the study area and the poor exposure, it is impossible to exclude that a duplication of the succession due to thrusting occurs in this interval. Further above (26 to 70 m *abs*) the rocks are better exposed. They consist of limestone characterized by small, coral-dominated, patch reefs and the associated bioclastic sediments (See Chapter 3 for further details).

Further above, the 70 - 90m *abs* interval is covered by soil. Limestone crops out once again between 90 m abs and the top of the section. Similarly to the underlying limestone interval they consist of small, coral-dominated, patch reefs and the associated bioclastic sediments (See Chapter 3 for further details)(Figure 5.16) Detailed data sheets available in Appendix Supplementary Tables GS1, and GS2,

Base of the section (0 to 4 m abs)

The lowermost part of the section consists of greyish thick-bedded, compact, nodular (especially on weathered surfaces), limestones of the Lockhart Limestone. They consist of mudstone to wackestone with a scarce skeletal assemblage comparable to BF1 and dominated by hyaline SBF and ostracods associated with common hyaline LBF and rare calcareous green algae. The LBF assemblage mainly consisting trocospiral forms like *Lockhartia* associated with *Daviesina* and poorly preserved orbitoidiform specimens. The latter suggests a placement in either SBZ3 or SBZ4 and therefore from the upper Selandian to the upper Thanetian (Papazzoni et al., 2023)(Figure 5.16).

Marly Interval (Limestones interbedded with unconsolidated calcareous marls 4 to 26 m abs)

This interval consists of nodular, thin- to thick-bedded limestones interbedded with poorly lithified calcareous marls. The terrigenous fraction (40% on average) is dominated by phyllosilicates and quartz. $\delta^{13}C_{org}$ values range from -20.3‰ to -25.7‰, with a -5.4‰ negative carbon isotope excursion (CIE) observed between 5.5 and 16 m abs. Although this negative shift is pretty remarkable, it does not correspond to an equally clear and persistent variation in the detrital fraction (phyllosilicates + quartz = 37%)(Figure 5.16). TOC ranges from 0.04 to 0.2 wt% (HI 6-96; OI 203-1280; Tmax 340–608°C). Mercury (Hg) concentrations range from 0.8 to 41.3 ppb, with Hg/TOC values between 90.4 and 190 ppb/wt% (Hg/TOC values are calculated for only three samples with TOC higher than 0.2 wt%)(Figure 5.17). The overall lack of microfossils and the poor preservation of the material does not allow us to assign this interval to any of the commonly observed biofacies (BF1 – BF5). Based on the presence of *Orbitoshiphon sp* and *Ranikothalia* sp, this interval could be included in intervals spanning from SBZ3 to SBZ4 (upper Selandian - upper Thanetian; Papazzoni et al., 2023)(Figure 5.16).

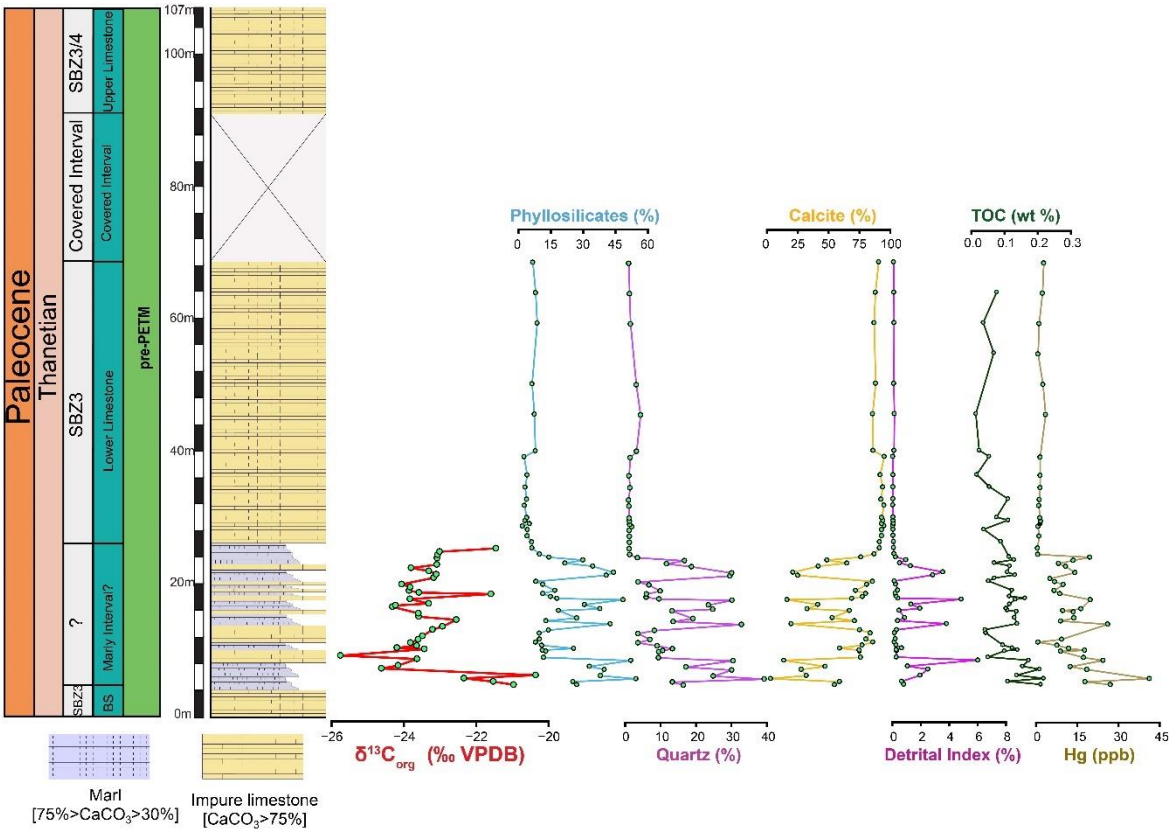

Figure 5.17: Shows the Ghumanwan section pre-PETM interval that contains different sub-stages. like Base of the section (BS) 0-4m *abs*, Marly Interval (04-26m *abs*), Lower Limestone (26-70 m *abs*), Covered interval 70-90m *abs* and Upper Limestone (90-107m *abs*). Marly interval geochemical data based on carbon stable isotope [$\delta^{13}C_{org}$] coupled with XRD whole rock mineralogy, mercury, and Rock eval TOC.

Lower limestone interval (26 – 70 m abs)

Greyish, thick bedded to massive limestones with a negligible terrigenous fraction (average calcite content is 91%). TOC content is also minimal and ranges from 0.01 to 0.1 wt% (HI 26 to 332; OI 258 to 1185; Tmax 346 to 489°C). Mercury content is also minimal and ranges from 0.6 to 3.5 ppb. The skeletal assemblage is characterized by the coral framestone and by the LBF packstone lithofacies (see Chapter 3 for further details). The LBF assemblage includes *Coskinon rajkae, Elazigina lenticula, Lakadongia primitiva, Lockhartia haimei, L. roeae, Miscellanea yvettae, M. juliettae, and Ranikothalia sp*. The presence of *Lakadongia primitiva, Miscellanea yvettae*, and *M. juliettae* indicating a placement within SBZ3 (upper Selandian – lower Thanetian; Papazzoni et al., 2023)(Figure 5.16).

Lower limestone interval (92 – 107 m abs)

Greyish, thick bedded to massive limestones with a negligible terrigenous fraction. Similarly to the lower interval the upper interval is characterized by the LBF packstone and coral framestone lithofacies. However, in the upper limestone reef corals and green calcareous algae are less abundant whereas LBF and red calcareous algae are more abundant (see Chapter 3 for further details). The LBF assemblage includes *Coskinon sp., Daviesina sp., Idalina sp., Lakadongia sp., Lockhartia conditi, L. haimei, L. roeae, L. tipperi, Miscellanea yvettae, M. juliettae, M. cf. miscella, Orbitosiphon sp., Operculina sp., Ranikothalia sahnii,* and possibly *Assilina*. The presence of *Miscellanea yvettae, M. juliettae*, along with *M. cf. miscella* suggesting a placement at the transition between SBZ3 and SBZ4 (i.e. at the base of the upper Thanetian)(Figure 5.16).

5.7. Discussion

5.7.1. **Correlations within the Upper Indus Basin**

The LBF and calcareous nannofossils assemblages, combined and supported by quantitative paleontological analysis and geochemical data provide strong stratigraphic constraints for correlating the Baroch Nala and Nammal Gorge sections.

The lowermost intervals of Baroch Nala (0-15.6 m *abs)* and Nammal Gorge (0-22.7 m *abs*) are both characterized by BF1 and LBF assemblages dominated by *Lockhartia* and orbitoidiform LBF. The latter suggests a placement ranging from SBZ3 to the lower part of SBZ4 thus corresponding to an interval that goes from the upper Selandian to the base of the upper Thanetian. In both sections $\delta^{13}C_{org}$ and $\delta^{13}C_{carb}$ are suggestive of pre-PETM conditions and in both cases, the limited terrigenous fraction and the clay assemblages, dominated by smectite and palygorskite, indicate an arid to semi-arid climate.

Upwards, the Baroch Nala (15.6 – 23.4 m *abs)* and Nammal Gorge (22.7- 27.1 m *abs*) are still closely correlated, as they are both characterized by BF2 (Figure 5.18). LBF assemblages are dominated by *Lockhartia, Daviesina,* and *Miscellanea,* while the importance of orbitoidiform LBF decreases. Biostratigraphically significant taxa indicate that both intervals can be fully placed within SBZ4 (upper Thanetian). The decrease in orbitoidiform represents the first noticeable variation in the skeletal assemblages.

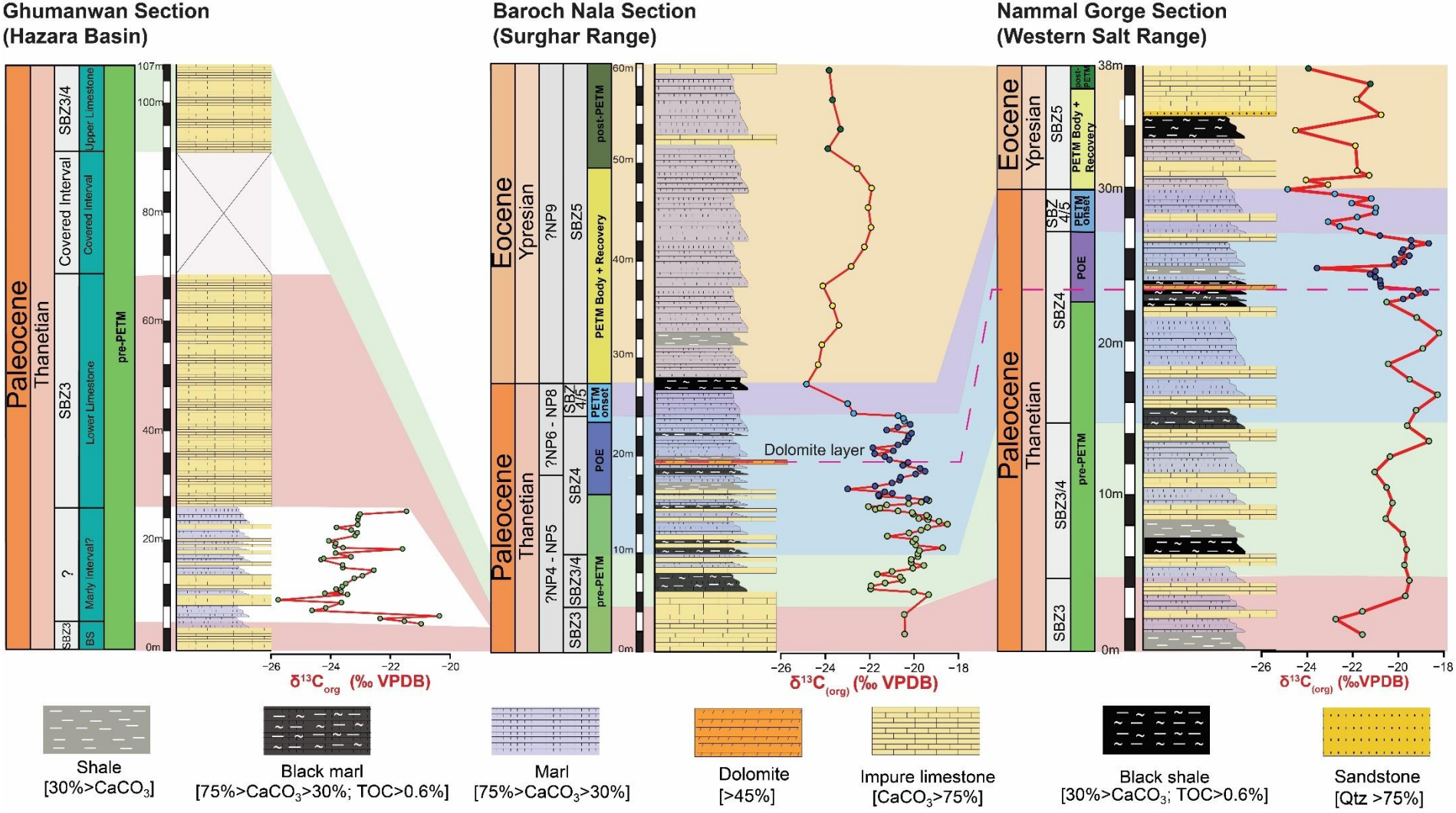

Figure:5.18 shows a detailed correlation between three studied Ghumanwan section (Hazara Basin), Baroch Nala section and Nammal Gorge section.

In both sections $\delta^{13}C_{org}$ and $\delta^{13}C_{carb}$ display a relevant, sharp, and sudden negative shift followed soon after by a recovery phase. This shift in stable isotopes is also associated with a sudden increase in kaolinite and a drop in palygorskite, suggesting a transition from arid conditions towards humid conditions. This shift is short lived, and the climate turns back to arid in the recovery phase of the event. The presence of a consistent and coherent shift in geochemical and mineralogical proxies, followed by a recovery to pre-CIE conditions, clearly indicates that this late Thanetian event represents an excursion separated by the PETM, a POE similar and probably corresponding to the one recorded by Tremblin et al. (2022) in Spain. During the POE, both in the Baroch Nala (at 16.8m *abs*) and Nammal Gorge (at 23.3 m *abs*) sections, a prominent peak in Hg and Hg/TOC is suggestive that this event was probably associated with volcanic activity. The presence of a dolomite-rich layer in both sections (19.8m *abs* in the Baroch Nala; 23.5 m *abs* in the Nammal Gorge) is also quite remarkable. This layer might have resulted from clay minerals-related diagenesis, certain clay minerals can indeed play a catalytic role during dolomitization by providing magnesium ions to the system (Kahle, 1965)(Figure 5.18). Another possibility is that this dolomite might result from the deposition of organic matter. Humid conditions have resulted in increased run-off from the continent and thus to increases in nutrient supply that might increase the sedimentation rate of organic matter. The abundant presence of organic matter may in turn foster the formation of dolomite during early diagenesis (Swart, 2015).

Further above the sections are characterized by BF3, which displays a remarkable increase in both the diversity and abundance of LBF. In both cases, LBF assemblages are suggestive of the latest Thanetian to early Ypresian age (transition between SBZ4 and SBZ5)(Figure 5.18). At 27.5 m a*bs* in Baroch Nala and at 29.8 m *abs* in Baroch, the $\delta^{13}C_{org}$ and $\delta^{13}C_{carb}$ values drop significantly. This prominent negative shift corresponds to the onset of the PETM. The event is marked in the Baroch Nala by a dark shale layer with low calcite content (5%), while in the Nammal Gorge is marked by a dark calcareous marl layer with 58% of calcite. In both cases, the onset is associated with an abrupt increase in kaolinite and a drop in palygorskite indicating a shift towards a humid climate. In the Baroch Nala section, the PETM onset is well preserved in the $\delta^{13}C_{org}$ record due to the relatively deep depositional environment that prevented erosion and sub-aerial exposure of the succession. On the other hand, the geochemical signals are disturbed in the Nammal Gorge section especially $\delta^{13}C_{org}$, most likely due to the shallower depositional environment. Overall, during the PETM onset

phase, the best correlation between the two sections is provided by the changes in both biotic and clay assemblages.

The following interval records, in both sections, the body phase and the early recovery from the PETM. In both Baroch Nala (27.5 – 49.5 m *abs)* and Nammal Gorge (29.8 – 36.6 m *abs*) sections it is characterized by BF4, a biofacies dominated by nummulitids and orthophragminids associated with abundant GCA and a wide variety of other LBF. The biostratigraphic analysis suggests an early Ypresian age (SBZ5)(Figure 5.18). The stable isotope record of carbon displays a progressive recovery from the initially very low value toward more positive values. In both sections, the clay assemblages indicate humid and wet conditions during the body phase. In the Baroch Nala Section from 37.5 m – 49.5m *abs*, the increase in smectite and the decrease in kaolinite shows the recovery phase of the PETM with a progressive return to semi-arid conditions. The same occurs from 33.6 m *abs* onwards in the Nammal Gorge section.

The uppermost intervals of the Baroch Nala (49.5 – 60 m *abs)* and Nammal Gorge (36.6 – 38 m *abs*) are characterized by BF5. The skeletal assemblages are entirely dominated by nummulitids and orthophragminids, associated with other typically Eocene genera while Paleocene genera become extremely rare. The LBF biostratigraphic analysis suggests a placement within SBZ5 (lower Ypresian). All geochemical and mineralogical indices in both sections indicate an overall recovery to values similar to those of pre-PETM conditions.

While the similarities between the carbonate systems of the Nammal Gorge and Baroch Nala sections facilitate the correlation between the two sections, the coral-rich carbonate systems of the Ghumanwan section make things significantly more complex. The correlation is also hindered by the poor exposure, and the poor preservation of the Ghumanwan section, which is further reduced by the local tectonic activity. Nonetheless, the presence of BF1 in the basal interval of the Ghumanwan section allows us to correlate the latter to the pre-PETM phase. The placement of the following interval (limestones interbedded with unconsolidated calcareous marls; 4 - 26 m *abs*), is more complex as it lacks well-preserved skeletal assemblages and LBF. The observed negative shift in $\delta^{13}C$ does not correlate to clear changes in either skeletal assemblages and mineralogical proxies. Consistently, it did not correlate to any event. On the other hand, the decrease in reef corals and increase in LBF that can be observed moving from the lower limestone interval to the upper limestone interval might be related to the POE as it occurs close to the lower portion of SBZ4 like in the other two sections.

Given the similarities between the three sections it is thus possible to draft a paleoenvironment reconstruction of the study area during an interval spanning from the end of the time period characterized by SBZ3, i.e. the early Thanetian (Papazzoni et al., 2023), to the beginning of the "age" of *Nummulites*, i.e. the earliest Ypresian.

The early Thanetian was characterized by relatively stable conditions, that, in the study area, have been mainly recorded by mudstone and wackestones characterized by BF1. The latter probably developed at an intermediate water depth characterized by limited hydrodynamic energy, as suggested by the dominance of hyaline LBF, the relevant presence of green calcareous algae, the lack of planktic foraminifera and the abundance of micrite (Flugel 2010; Bialik et al., 2023; Mariani et al., 2024). Locally small patch reefs were also present, like in the Ghumanwan section area of the Hazara Basin. These relatively stable conditions were interrupted by an initial environmental variation related to a perturbation in the global carbon cycle. This pre-onset excursion, i.e. the POE, happened around the boundary between SBZ3 and SBZ4, i.e. between the middle and late Thanetian (Papazzoni et al., 2023). The oscillation most likely represents one of the Thanetian hyperthermal events well recorded in the deep-water record (Barnet et al., 2019). Timewise, the closest match is represented by the C1/C2 event, which occurred around 57 Ma and displays a relevant shift in the $\delta^{13}C$ that corresponds to an increase in the global temperature recorded by the $\delta^{18}O$ record (Barnet et al., 2019). On the other hand, the D1/D2 event, which occurred slightly later (around 56.5 Ma), could be a better match due to its larger negative shift in $\delta^{13}C$ (Barnet et al., 2019). However, the latter event is associated with a much smaller temperature increase recorded by the $\delta^{18}O$ (Barnet et al. 2019). Current data do not allow us to provide a definitive answer to which match is the best. Regardless of this, the SBZ3/SBZ4 boundary event displays the same major characteristics of the PETM. It displays a drop in both $\delta^{13}C_{org}$ and $\delta^{13}C_{carb}$, an increase in detrital material, and a shift from an arid to a humid climate. Mercury (Hg) and its normalization over organic matter (Hg/TOC) is considered as useful proxy for volcanic activity (Grasby et al., 2019). In Baroch Nala and Nammal Gorge Sections, the overall mercury concentrations are low. However, a peak in Hg and its ratio with respect to organic matter (Hg/TOC) at the beginning of POE suggests volcanic activity during the Thanetian (Tremblin et al., 2022). The possible reason for the provenance of the mercury and its low concentration could be associated with the distal positioning of the studied sections from the North Atlantic Igneous province – NAIP (Paleocene-Eocene volcanic activity) (Kender et al., 2021; Jones et al., 2019, 2023). The POE also corresponds

to a minor biotic change, marking the shift from BF1 to BF2. This is also recorded along the Ghumanwan of the Hazara Basin as an increase in LBF abundance and diversity moving from the lower limestones corresponding to SBZ3 to the upper limestones corresponding to SBZ3/SBZ4. In the Hazara Basin, this event also effected colonial corals, with the patch reef (LF1_Coral framestone lithofacies) in the upper limestones being characterized by less corals.

Shortly after the recovery from the POE a new and stronger climate change impacted the benthic communities of the upper Indus Basin: the onset of the PETM. This is recorded as a marked and progressive shift toward a humid climate, an increase in the detrital fluxes from the continent, and a drop in $\delta^{13}C$. This major variation is testified in both Nammal Gorge and Baroch Nala section by a new biofacies change (from BF2 to BF3) characterized by an increase in LBF driven in particular by the increase of nummulitids (in particular *Assilina* and *Ranikothalia*).

After the onset of the PETM, the event reaches its body phase, followed up by a progressive recovery. The negative peak in $\delta^{13}C$ is recorded at the beginning of the interval together with a peak in detrital fluxes and proxies of humid conditions. Afterwards, all paleoenvironment parameters move back towards values comparable to those of the phase preceding the excursion (i.e. pre-PETM conditions). This phase is marked by the coexistence of both typical Paleocene taxa such as *Lockhartia*, *Miscellanea,* and *Ranikothalia,* and Eocene taxa such as *Nummulites* and *Alveolina,* and by a shift from BF3 to BF4. In both sections recording this interval it is possible to observe also an increase in both green calcareous algae and porcelaneous benthic foraminifera, suggesting an overall decrease in water depth (Bialik et al., 2023; Mariani et al., 2024).

Following the body and early recovery phases of the PETM the environmental parameters reached values comparable to those preceding the beginning of the oscillations (i.e. early Thanetian, SBZ3). This new stable phase is characterized by the appearance of BF5, which displays all the characteristics of the typical Eocene shallow-water facies, i.e. an overwhelming dominance from LBF, and the dominance of *Nummulites* and *Alveolina* (Coletti et al., 2022). Paleocene taxa, like *Lockhartia*, still occur but they are exceedingly rare.

This overall pattern is consistent with the recently published results of the analysis of the Duleram section in the Potwar Basin (sub-basin of the upper Indus Basin), located halfway between the locations of Nammal Gorge and Baroch Nala sections and the location of the

Ghumanwan section. Similarly to our analysis, the author constrains the main biotic shift, represented by the demise of Paleocene LBF assemblages and the rise of Eocene LBF assemblages, during the $\delta^{13}C$ excursion of the PETM (Kamran et al., 2021). Similar results have also been achieved by Afzal and Butt (2023) which, based on a review of foraminiferal assemblages from northern Pakistan place the major LBF biotic turnover at the Paleocene-Eocene boundary (i.e. the PETM).

5.7.2 **Regional correlation**

Based on these results it is possible to correlate other sections of the Hymalian area to the investigated sector of the upper Indus Basin and to the overall northern Pakistan.

A close correlation between the Baroch Nala and Nammal Gorge sections and the shallow marine calcareous marl-dominated Kuzigongsu section of the Tarim Basin (eastern Tethys, China) can be drafted based on geochemical and mineralogical data (Dong et al., 2024). The $\delta^{13}C_{org}$ and $\delta^{13}C_{carb}$, of Baroch Nala and Nammal Nala shows a very similar negative shift both in magnitude and timing (within NP9) before the onset of the PETM. This CIE identified as the POE and is characterized by a rapid onset and a rapid recovery (Dong et al., 2024), can be easily correlated with the investigated part of the upper Indus Basin. In addition to the similarities in $\delta^{13}C_{org}$ and $\delta^{13}C_{carb}$, the Kuzigongsu section also displays a resemblance in terms of mercury content and of its normalization over total organic matter (Hg/TOC) at the beginning of the POE. In both the Tarim Basin and Upper Indus Basin, the peaks of Hg and Hg/TOC show a connection between POE and volcanism. Similarly, the enhanced weathering and fast continental runoff during the POE make a strong connection between the Kuzigongsu section and the studied Baroch Nala and Nammal Gorge sections. These similarities between the two areas during the POE strongly support the validity of the POE as a regionally recognized hyperthermal event before PETM.

A pattern strikingly similar to the one observed in northern Pakistan can be seen in the Düela section, located in the Yadong area of southern Tibet (Li et al., 2022). The data provided for the section indeed allows to recognize the same intervals identified in the Baroch Nala, Nammal Gorge, and Ghumanwan sections. The base of the section consists of *nodular limestones* characterized by micrite-rich packstones dominated by hyaline LBF and green calcareous algae, similar to the layers characterized by BF1 within the investigated sections. The LBF assemblage largely consists of typical Paleocene genera like *Lockhartia*,

Miscellanea, *Daviesina.* Following these elements, this *nodular limestone interval* of the Düela section can be correlated to the pre-PETM phase. This is also supported by the presence of colonial coral fragments. The latter do not occur upsection and, based on the data from the Ghumanwan section, they are estimated to decrease after the pre-PETM phase. The first negative shift in $\delta^{13}C$ along the Düela section is recorded at the boundary between the *nodular limestone* and the overlying interval of *thin-bedded limestone*. If the *nodular limestone* represents pre-PETM conditions, this first CIE might represent the POE. This initial oscillation, similar to the Baroch Nala and Nammal Gorge sections, corresponds only to a minor biotic change and, similarly to the Ghumanwan section, corresponds to a decrease in the abundance of corals (Li et al., 2022). Furthermore, as in the Baroch Nala and Nammal Gorge sections, the POE interval of the Düela section is characterized by the presence of dolomite-rich layers (Li et al. 2022).

Following this new interpretation of the Düela section, the PETM body and recovery phases should take place in the *calcareous marl interval* which overlies the *thin-bedded limestone interval*. The *calcareous marl interval*, similar to the PETM interval of the Baroch Nala and Nammal Gorge sections, is characterized by an increase in the terrigenous fraction (Li et al., 2022). This new interpretation of the Düela section is more consistent with the overall LBF stratigraphy of Tethys as it places the PETM at the boundary between assemblages dominated by Paleocene taxa (which dominate in the *nodular limestone* and in the *thin bedded limestone* intervals of the Düela section) and assemblages dominated by Eocene taxa (which dominate in the uppermost part of the section, i.e. the *massive limestone interval*) (Li et al., 2022). Furthermore, similarly to the Baroch Nala and Nammal Gorge sections, the PETM interval is correlated to a relative sea-level drop. The presence of a general regressive phase during the PETM interval is well supported, on a regional scale by the Gamba area in Tibet and by the Mawmluh area in India, both displaying conglomerates and continental deposits at the PETM (Ozcan et al., 2018, Pereira et al.,2022),

A similar re-interpretation could also be proposed for the Shenkezha section of the Tigri area of southern Tibet (Li et al., 2020). Based on microfacies and stable isotopes correlations, the initial negative shift, originally interpreted as the onset of the PETM, could instead represent the POE, and the body phase of the PETM could represent the proper peak of the PETM.

This re-interpretation of these two Himalayan sections is more consistent with the overall timing of the event as the CIE of the PETM is associated with a rapid onset, likely in the orders of millennia, followed by around 100000 yr of stable values representing the body

and then by around 50000 to 100000 yr of recovery phase (Frieling et al., 2016). Given that, on the 10^5 to 10^8 yr time-scale, neritic carbonates accumulate with a rate of around 0.05 – 0.1 mm/yr - and this rates still represent the high-end as they are calculated referring to fast-growing corals- (Schlager, 1999) – the upper limit of neritic carbonates accumulated between the onset and the end of the body of the PETM should be something around 5 to 10 m at most. Sediment compaction over the millions of years would probably further reduce this amount. On the other hand, the sediment thickness deposited between the presumed onset of the PETM, and the end of the event is nearly 35 m in the Düela section and around 12 m in the Shenkezha section, so above the uppermost possible limit.

Following this new interpretation, the local trends observed in the upper Indus Basin are consistent on a regional scale and offer a reasonable and plausible explanation for the observed biotic, lithological, and geochemical trends observed in the Upper Paleocene strata of the remainder of the Himalayan region.

5.7.3. **Global correlations:**

To better evaluate the early Selandian to early Ypresian (SBZ3 to SBZ5/6) record of biotic changes in the Baroch Nala section, Nammal Gorge and Ghumanwan section, a close connection has been built between the studied sections and a literature-based, quantitatively analyzed, database of thirty-four other sections of neritic carbonates from Tethys (See Chapter 4, Figure 4.9). These were investigated considering LBF species diversity (and focusing on the most relevant genera) and based on the presence/absence of the main genera of LBF and the main types of shallow-water carbonate producers (Detailed data sheet of LBF assemblages is available in Appendix Supplementary Table **"Tethys".**

Within SBZ3 (pre-PETM phase) in Baroch Nala, Nammal Gorge, and Ghumanwan section, the overall species diversity of LBF is relatively limited, including the diversity of several typical Paleocene taxa (i.e *Lockhartia, Kathina, Miscellanea, Daviesina, Ranikothalia, Glomalveolina*) is relatively limited. This low diversity of LBF is in agreement with the picture drafted by all the other 34 sections scattered across Tethys (Figure 5.19). Upward, within SBZ4 the overall diversity of LBF increased. This is related to an increase in the diversity of typical Paleocene genera like *Lockhartia, Kathina, Miscellanea, Daviesina, Ranikothalia, Glomalveolina* and by the first appearance of typical Eocene genera such as

Nummulites, Assilina, and *Alveolina*. Only the diversity of the agglutinated genera *Coskinon* and *Coskinolina* decreased moving from SBZ3 to SBZ4. Along the studied sections from northern Pakistan, moving from SBZ3 to SBZ4 is possible to observe an increase in the relevance of LBF as carbonate producers (except *Orbitosiphon* and *Lakadongia* which instead decrease), in particular in the Ghumanwan section. An increase in species diversity of certain genera such as *Lockhartia* can also be observed. Within the investigated sections, this initial biotic change corresponds to the POE hyperthermal event.

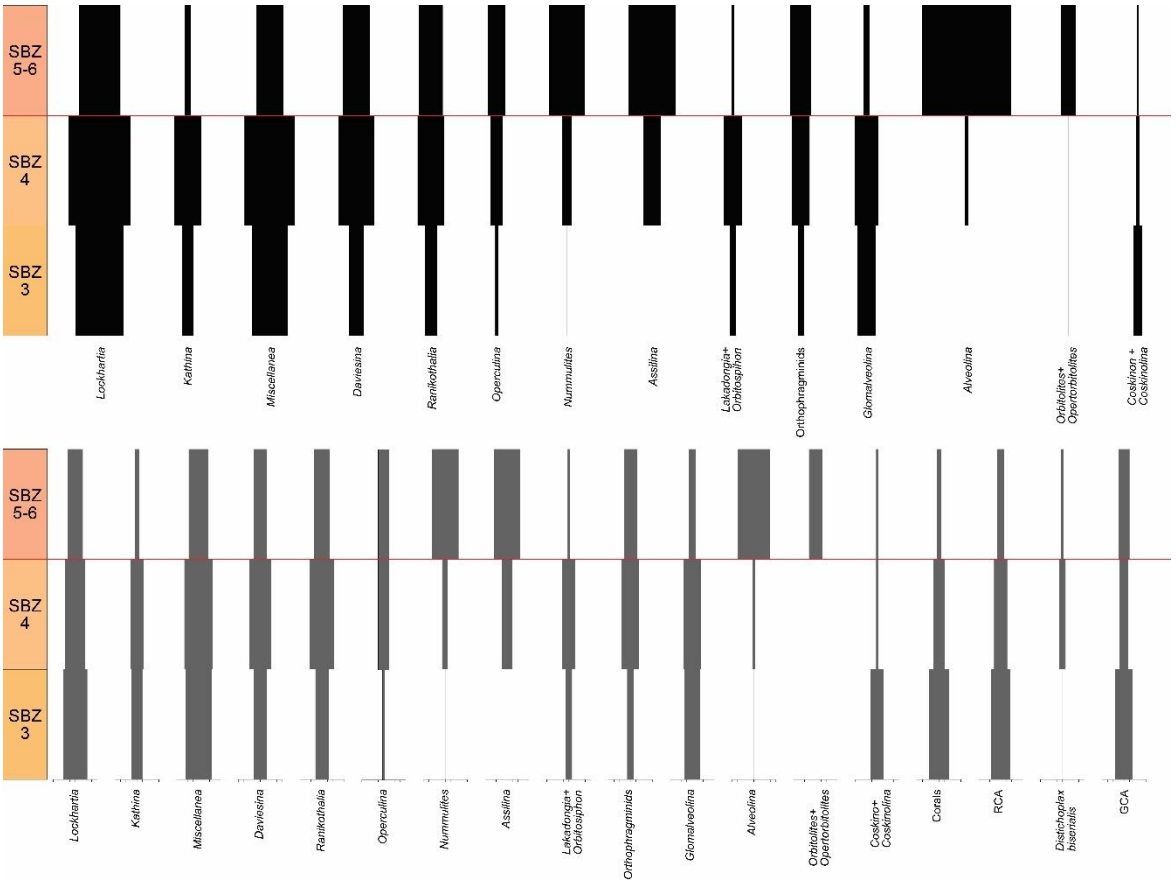

Figure 5.19 shows the LBF species diversity (most relevant genera) and based on the presence/absence of the main genera of LBF and the main types of shallow-water carbonate producers. These two LBF diversity and presence/absence models were developed by taking 34 shallow water sections into account and exposed across the Tethys. (See Chapter 4, Figure 4.9)

Tethys-wide, moving from SBZ4 to the interval characterized by SBZ5 and SBZ6, i.e. from the uppermost Thanetian to the lower Ypresian and thus across the PETM, a major biotic change can be observed. Based on the presence/absence model LBF becomes, overall, more frequent whereas red calcareous algae and corals become less frequent. This increase in LBF relevance as carbonate producers is mainly driven by Eocene taxa and is sufficiently large

to offset the decrease of the typical Paleocene groups which become much less frequent. This is matched by trends in diversity with Paleocene taxa greatly decreasing in terms of diversity and Eocene taxa significantly expanding. This trend is well reflected in the Nammal Gorge and Baroch Nala sections, where LBF becomes overwhelmingly dominant in the post-PETM skeletal assemblages. Within these two sections, it is also possible to observe that while in the PETM body and recovery phase, both Paleocene and Eocene genera are present, in the post-PETM the former group is very rare and represented by few species.

This Tethys wide analysis spanning from middle Paleocene strata characterized by SBZ3 to lowermost Eocene strata characterized by SBZ5/6, displays trends that are consistent with those of the study area. During SBZ4, an interval already characterized by notable hyperthermal events such as the POE, the diversity of Late Paleocene taxa like *Lockhartia* and large benthic foraminifera (LBF) showed a notable increase, with rotaliids diversifying more significantly than nummulitids (Kahsnitz et al., 2016; Benedetti and Papazzoni, 2022). As the Paleocene transitioned into the Early Eocene, LBF diversity continued to rise, particularly with the expansion of genera such as *Nummulites* and *Alveolina*. At the same time, the diversity of typical Paleocene genera and rotaliids declined (Benedetti and Papazzoni, 2022; Benedetti et al., 2024). This shift in diversity had a considerable impact on global carbonate production, with LBF contributing significantly more to the Early Eocene compared to reef corals and calcareous algae (both red and green) (Kiessling et al., 1999; Zamagni et al., 2012; Pomar et al., 2017; Aguilera et al., 2020; Coletti et al., 2022; Benedetti and Papazzoni, 2022; Benedetti et al., 2024; Baceta et al., 2005). This pattern, observed globally, has been attributed to rising temperatures and fluctuations in the nutrient cycle (Zamagni et al., 2012; Coletti et al., 2022), as biotic records from certain areas correlate with geochemical records from others. In the Baroch Nala section, however, the increase in LBF abundance and the transition between Late Paleocene and Early Eocene assemblages can be directly linked to geochemical evidence of environmental changes, further highlighting the relationship between climate shifts and ecosystem transformations. The overall pattern of decrease in corals and increase in LBF following the increase in temperature during the SBZ3 to SBZ5/6 interval is actually part of a longer trend that starts with the Danian and is characterized by a decrease in the relevance of reef corals and a simultaneous increase in LBF moving from the relatively cool early Paleocene to the warm

Late Paleocene and Early Eocene (Scheibner & Speijer, 2008, Zamagni 2012, Baceta 2005; see Chapter 2 for further details).

To explore the triggers of the climate change observed during the Late Paleocene and in particular during the PETM, isotopic curves, clay assemblages, and mercury concentrations from the Baroch Nala and Nammal sections, which display a relatively well-preserved and complete record of various proxies, are compared with other well-studied sections from other part of the world. These include the Dababiya section in Egypt (Khozayem et al., 2023), the North Sea records (Kender et al., 2021, Kemp et al., 2016), and the Dibamba in Cameroon (Bitchong et al., 2023). All these sections are characterized by having a complete record of both $\delta^{13}C_{org}$ and $\delta^{13}C_{carb}$, analysis of mercury concentrations, TOC, and clay mineral assemblages, similar to the two investigate sections from Northern Pakistan.

The negative $\delta^{13}C_{org}$ shift in Baroch Nala is slightly larger than in Dibamba and similar to those of Egypt and from the North Sea, aligning with the global marine record. Unlike these sections, the Baroch Nala and Nammal Gorge sections also clearly record the earlier hyperthermal event, the pre-onset excursion (POE). Across all sections, the PETM is linked to increased kaolinite, indicating heightened weathering and warm-humid conditions. Global warming likely enhanced the hydrological cycle, increasing terrigenous input, and leading to ocean acidification, explaining the widespread calcite reduction by both increase in the terrigenous fraction and calcite dissolution. Globally, in shallow-marine and terrestrial settings, the POE is overall poorly documented with limited examples of sections recording the event (Tremblin et al., 2022, Dong et al., 2024; Babila et al., 2022; Doubrawa et al., 2022; Bowen et al., 2015). Due to the limited rise in temperature (around 2 °C) and its short duration, the POE is also poorly recorded in the slowly accumulating deep marine successions (Kemp et al., 2016; Jones et al., 2019, 2023; Kender et al., 2021) and can be resolved only in super-high-resolution analyses (Barnet et al., 2019). Based on the latter and assuming that the POE corresponds to the C1/C2 (or D1/D2) event, it should have occurred within the NP9 zone (corresponding to CP8a, the lower part of C24r, and a time span comprised between 56 and 57 Ma) (Barnet et al., 2019). Some of the limited available knowledge on POE comes from the South Dover Bridge section (Maryland, USA; Babila et al., 2022; Doubrawa et al., 2022), Bighorn Basin (Wyoming, USA, Bowen et al., 2015) Kuzigongsu section (Tarim Basin, China; Dong et al., 2024); Esplugafreda, Lussagnet and Serraduy sections (Pyrenean Basin, Spain; Tremblin et al., 2022). The investigated sections from northern Pakistan record the event comparatively well, clearly highlighting an

onset+body phase and a recovery phase. The magnitude of $\delta^{13}C$ recorded in the Baroch Nala and Nammal Gorge section is similar to the one recorded in South Dover Bridge and so is the decrease in the calcite content (Babila et al., 2022; Doubrawa et al., 2022). The latter was probably related to enhanced weathering and hydrological cycles (Doubrawa et al., 2022). In South Dover Bridge, similarly to northern Pakistan, the changes in the biotic assemblage are also small, especially compared to those occurring during the PETM (Doubrawa et al., 2022). The Esplugafreda, Lussagnet section in the Pyrenees, and Kuzigongsu section, Tarim Basin show a significant peak in Hg during the POE suggesting a possible connection with a volcanic activity, possibly in the North Atlantic Igneous Province (Tremblin et al., 2022).

While the POE represented a minor event, the PETM was characterized by a large increase in temperature rises and a more severe biotic turnover than the other hyperthermals. Increased temperature and greatly enhanced hydrological cycle resulted in significantly stressful conditions triggering the major biotic turnover (Doubrawa et al., 2022). Indeed, while most Paleocene hyperthermals were linked to orbital eccentricity, the PETM's exceptional scale suggests an additional volcanic trigger, likely from the North Atlantic Igneous Province. This is supported by the presence of peaks in the Hg/TOC that can be seen in most sections, including those from the upper Indus Basin. This volcanic activity likely pushed global conditions past a tipping point, disrupting carbonate-producing ecosystems.

Apart from volcanism as a source of carbon pumping during the POE and PETM, there are several other carbon sources under debate like methane hydrate dissociation, as ocean temperatures rose, likely contributed further, releasing methane, a potent greenhouse gas, into the atmosphere (McInerney & Wing, 2011). Thawing permafrost and increased microbial activity in soils may have also released carbon stored in frozen organic matter, while ocean warming reduced the solubility of CO_2, leading to its release from the oceans. Shifts in vegetation, including increased decomposition of organic matter, and the reduction in the oceanic biological pump may have amplified the carbon cycle feedbacks, further warming the planet. Additionally, forest fires, facilitated by drier conditions, likely contributed to atmospheric CO_2. Isotopic evidence, including negative carbon isotope excursions, supports these sources of carbon release, showing that these warming events were driven by a combination of geological, biological, and climatic processes that released vast amounts of carbon into the atmosphere (McInerney & Wing, 2011).

5.8. Conclusions

The PETM is one of the major hyperthermal events of the Cenozoic. It is characterized by a sharp release of carbon in the atmosphere and an associated increase in temperatures. The effects of this climate shift were recorded in the geological record on a global scale. Some of the most striking differences can be observed in the tropical shallow-water record of Tethys. The pre-PETM neritic assemblages are characterized by a remarkable variety of carbonate producers including abundant reef-corals. On the other hand, the post-PETM assemblages are overwhelmingly dominated by LBF and almost devoid of relevant coral reefs.

Due to the striking similarities between this pattern and what is occurring today due to anthropogenic climate change, the PETM has been investigated in detail. Our analysis focuses on a poorly investigated study area, the upper Indus Basin of northern Pakistan, a remnant of the eastern Tethys. These sections of shallow marine carbonates record the variations that occurred during this crucial interval both in terms of biotic assemblages and of geochemical proxies that can track the environmental changes causing the biotic changes. The two investigated sections in the southern portion of the upper Indus Basin (Surghar and Salt Ranges), the Baroch Nala and Nammal Gorge sections provide a perfect record of both elements.

The two sections display a complete succession of fossil assemblages that track the changes from pre-PETM conditions to post-PETM conditions, matched with geochemical proxies. The Baroch Nala section, in particular, is characterized by a well-preserved record of both $\delta^{13}C_{org}$ and $\delta^{13}C_{carb}$, clay minerals, and mercury. In both sections pre-PETM conditions (corresponding to middle Paleocene to lower upper Paleocene) are recorded by deposits related to intermediate water depth, limited hydrodynamic energy, and common (but not overwhelmingly dominant) LBF. $\delta^{13}C_{org}$ and $\delta^{13}C_{carb}$ do not indicate major variations in the carbon cycle and clay minerals suggest an arid to semi-arid climate.

Later on, in the upper Paleocene, the first excursion is recorded. This is associated with a minor biotic change and a first and brief shift towards humid conditions. The excursion is short-lived and environmental conditions turn back to arid relatively fast. This pre-PETM excursion (POE), most likely corresponds to one of the hyperthermal events that happened in the late Thanetian (between 57 and 56 Ma) and that are recorded in extremely high-resolution deep water record and poorly recorded in the shallow water record of Tethys and

North America. This event is also associated with a minor release of mercury suggesting a contribution from volcanic activity.

In the uppermost Paleocene, the PETM starts, and it is associated with a major biotic turnover consisting of an increase in the abundance of LBF as carbonate producers, and in the emergence of many taxa typical of the Eocene (which still occur together with taxa typical of the Paleocene). The event is associated with a marked and prolonged shift towards humid conditions and an increase in detrital material due to enhanced weathering. Due to the increase in continental run-off and in weathering rates the delivery of nutrients to the shallow sea most likely increased as well. Both temperatures increase and nitrification results in changes in the biotic components. Within the study, the event was also associated with a decrease in relative water depth, possibly due to a regional phase of uplift.

At the end of the PETM, the climate became once again arid, however, neritic carbonate factories were dramatically changed by the event. The recorded post-PETM assemblages are overwhelmingly dominated by LBF and most of Paleocene taxa are either extinct or significantly diminished.

The more northerly located Ghumanwan section (Hazara Basin) does not record the entirety of the Late Paleocene climate change due to the tectonic complexity of the area. Nonetheless, it is possible to observe pre-PETM settings, similar to those of the other two sections and the effects of the POE. This latter event, in the Hazara Basin, is associated with an increase in both the abundance of LBF as carbonate producers and in their diversity.

Overall, the sections from the upper Indus basin can be correlated with other sections from northern Pakistan and from northern India, both in terms of environmental changes (relative sea level drop during the PETM) and in terms of changes in LBF assemblages (major LBF turnover during the PETM). This provides a strong framework to re-interpret several key sections in Tibet, with the new interpretation resolving previous inconsistency in terms of both LBF stratigraphy and timing of carbon stable isotope excursions. These sections from Tibet, together with a section from Tarim Basin (China) further support the existence of the POE as a hyperthermal event clearly separated from the PETM and occurring slightly before.

By comparing the overall picture from eastern Tethys to a set of other shallow water sections scattered across the Tethys, it is possible to observe the same general trends regarding the abundance of major carbonate producers and of LBF, albeit with a lower resolution. The Tethys-wide consistency of the observed pattern supports the nature of these biotic changes

as the result of changes in the global climate. The affinity of these changes with the PETM clearly shows that carbonate production can be severely affected by hyperthermal events.
Finally, the comparison between the well-preserved, multi-proxy, record from Surghar and Salt ranges is compared to other detailed multiproxy geochemical records from all over the world. This comparison highlights notable similarities between the study area, the Tethys and the global picture, further supporting the consistency of the various datasets. This comparison also provides further evidence for interpreting the POE as one of the late Thanetian hyperthermal reconciling shallow-water and deep-water records of Late Paleocene climate change. This makes it clear that the PETM is only one of several hyperthermal events that occur during this time period, even if it is the strongest. Unlike previous events which were characterized by a short recovery, Paleocene carbonate factories never recovered from the PETM. New carbonate factories that were overwhelmingly dominated by LBF and, in particular, by nummulitids replaced the factories that had dominated carbonate platforms throughout the majority of the Thanetian. These new factories became one of the most distinctive elements of the shallow-water tropical carbonate system for the 20 million years that followed the PETM.
Our analysis clearly ties these changes to rising temperatures and to the increase in weathering rates (and thus in the delivery rate of nutrients to the sea) highlighting that short changes might have long-lasting consequences on marine ecosystems.

5.9. References

Abbasi, I. A., & McElroy, R. (1991). Thrust kinematics in the Kohat plateau, trans Indus range, Pakistan. Journal of structural geology, 13(3), 319-327.

Abbasi, I.A., Haneef, M., Obaid, S., Daud, F., Qureshi, A.W., 2012. The Mesozoic deltaic system along the western margin of the Indian plate: lithofacies and depositional setting of Datta Formation, North Pakistan. Arabian Journal of Geosciences 5(3), 471-480.

Acharyya, S. K. (2007). Evolution of the Himalayan Paleogene foreland basin, influence of its litho-packet on the formation of thrust-related domes and windows in the Eastern Himalayas–A review. Journal of Asian Earth Sciences, 31(1), 1-17.

Agnini, C., Fornaciari, E., Raffi, I., Catanzariti, R., Palike, H., Backman, J., Rio, D., 2014. Biozonation and biochronology of Paleogene calcareous nannofossils from low and middle latitudes. Newsl. Stratigr. 47, 131–181.

Aguilera, O., Bencomo, K., de Araújo, O.M.O., Dias, B.B., Coletti, G., Lima, D., Silane, A.F., Polk, M., Alves-¬Martin, M.V., Jaramillo, C., Kutter, V.T. & Lopes, R.T. (2020) Miocene

Ahsan, N., Chaudhry, M.N., 2008. Geology of Hettangian to middle Eocene rocks of Hazara and Kashmir basins, Northwest lesser Himalayas, Pakistan. Geological Bulletin of the Punjab University 43, 131-152.

Ali, F., Qiang, J., Ahmad, S., Khan, S., Hanif, M., & Jan, I. U. (2019). Seditiological and geochemical analysis of the middle Jurassic Shinawari Formation, upper Indus basin, Pakistan: implications for palaeoenvironmental and hydrocarbon assessment. Arabian Journal for Science and Engineering , 44 , 6465-6487.

Ali, M., Coletti, G., Mariani, L., Benedetti, A., Munawar, M. J., Rehman, S. U., ... & Garzanti, E. (2024). Shallow-water carbonate facies herald the onset of the Paleocene-Eocene Thermal Maximum (Hazara basin, Northern Pakistan). Journal of Asian Earth Sciences: X, 11, 100169.

Ali, M., Coletti, G., Garzanti, E., Adatte, T., Castelltort, S., Sternai, P., ... & Usman, M. (2025). The Baroch Nala section (NE Pakistan): A new PETM standard for the eastern Tethys. *Marine and Petroleum Geology*, *171*, 107183.

Afzal, J., Williams, M., Leng, M. J., & Aldridge, R. J. (2011). Dynamic response of the shallow marine benthic ecosystem to regional and pan-Tethyan environmental change at the Paleocene–Eocene boundary. Palaeogeography, Palaeoclimatology, Palaeoecology, 309(3-4), 141-160.

Afzal, J., & Butt, A. A. (2023). Late Paleocene to Early Eocene integrated biostratigraphic framework, chronostratigraphy and Paleocene/Eocene boundary in the Salt Range, Pakistan. In Stratigraphy & Timescales (Vol. 8, pp. 265-330). Academic Press.

Baceta, J. I., Pujalte, V., & Bernaola, G. (2005). Paleocene coralgal reefs of the western Pyrenean basin, northern Spain: New evidence supporting an earliest Paleogene recovery of reefal ecosystems. Palaeogeography, Palaeoclimatology, Palaeoecology, 224(1-3), 117-143.

Babila, T. L., Penman, D. E., Standish, C. D., Doubrawa, M., Bralower, T. J., Robinson, M. M., ... & Zachos, J. C. (2022). Surface ocean warming and acidification driven by rapid carbon release precedes Paleocene-Eocene Thermal Maximum. Science Advances , 8 (11), eabg1025.

Baker, D. M., Lillie, R. J., Yeats, R. S., Johnson, G. D., Yousuf, M., & Zamin, A. S. H. (1988). Development of the Himalayan frontal thrust zone: Salt Range, Pakistan. Geology , 16 (1), 3-7.

Bialik, O. M., Coletti, G., Mariani, L., Commissario, L., Desbiolles, F., & Meroni, A. N. (2023). Availability and type of energy regulate the global distribution of neritic carbonates. Scientific Reports, 13(1), 19687.

Barnet J. S., Littler K., Westerhold T., Kroon D., Leng M. J., Bailey I., Rohl U. & Zachos J. C. (2019) - A high-Fidelity benthic stable isotope record of late Cretaceous–early Eocene

climate change and carbon-cycling. Paleoceanography and Paleoclimatology, 34(4): 672-691.

Benedetti, A., Marino, M., Pichezzi, R.M., 2018. Paleocene to Lower Eocene larger foraminiferal assemblages from Central Italy: new remarks on biostratigraphy. Rivista Italiana di Paleontologia e Stratigrafia 124, 73–90.

Benedetti, A., & Papazzoni, C. A. (2022). Rise and fall of rotaliid foraminifera across the Paleocene and Eocene times. Micropaleontology, 68(2).

Benedetti, A., Papazzoni, C. A., & Bosellini, F. R. (2024). Unparallel resilience of shallow-water tropical calcifiers (foraminifera and scleractinian reef corals) during the early Paleogene global warming intervals. Palaeogeography, Palaeoclimatology, Palaeoecology, 651, 112393.

Behar, F., Beaumont, V. D. E. B., & Penteado, H. D. B. (2001). Rock-Eval 6 technology: performances and developments. Oil & Gas Science and Technology, 56(2), 111-134.

Bitchong, A. M., Adatte, T., Ngos III, S., Keller, G., Karabeyoğlu, A. U., & Spangenberg, J. E. (2023). The Paleocene-Eocene transition in the Gulf of Guinea: Evidence of the PETM in the Douala basin, Cameroon. Marine and Petroleum Geology, 157, 106504.

Bowen, G. J., Maibauer, B. J., Kraus, M. J., Röhl, U., Westerhold, T., Steimke, A., ... & Clyde, W. C. (2015). Two massive, rapid releases of carbon during the onset of the Paleocene–Eocene thermal maximum. Nature Geoscience , 8 (1), 44-47.

Butler, R. W. (2020). Syn-kinematic strata influence the structural evolution of emergent fold–thrust belts. Geological Society, London, Special Publications, 490(1), 57-78.

Butt, A.A., 1972. Problems of stratigraphic nomenclature in the Hazara District, NWFP, Pakistan. Geological Bulletin of the Punjab University 9, 65-69.

Coletti G., Commissario L., Mariani L., Bosio G., Desbiolles F., Soldi M. & Bialik O. M. (2022) - Paleocene to Miocene southern Tethyan carbonate factories: A meta-analysis of the successions of South-western and Western Central Asia. The Depositional Record, 8(3): 1031-1054.

Di Carlo, M., Accordi, G., Carbone, F., Pignatti, J., 2010. Biostratigraphic analysis of Paleogene lowstand wedge conglomerates of a tectonically active platform margin (Zakynthos Islands, Greece). Journal of Mediterranean Earth Sciences 2, 31-92.

Dong, Y., Gachetti, A., Wu, Q., De Palma, M., Hu, X., Brachfeld, S., ... & Cui, Y. (2024). Paleoenvironment reconstruction of the eastern Tethys during the pre-onset excursion preceding the PETM. Palaeogeography, Palaeoclimatology, Palaeoecology , 647 , 112234.

Doubrawa, M., Stassen, P., Robinson, M. M., Babila, T. L., Zachos, J. C., & Speijer, R. P. (2022). Shelf Ecosystems Along the US Atlantic Coastal Plain Prior to and During the Paleocene-Eocene Thermal Maximum: Insights Into the Stratigraphic Architecture. Paleoceanography and Paleoclimatology , 37 (10), e2022PA004475.

Espitalié, J., Deroo, G., & Marquis, F. (1985). La pyrolyse Rock-Eval et ses applications. Second party. Revue de l'Institut français du Pétrole , 40 (6), 755-784.

Flügel, E., & Munnecke, A. (2010). Microfacies of carbonate rocks: analysis, interpretation and application (Vol. 976, p. 2004). Berlin: springer.

Frieling, J., Svensen, H. H., Planke, S., Cramwinckel, M. J., Selnes, H., & Sluijs, A. (2016). Thermogenic methane release as a cause for the long duration of the PETM. Proceedings of the National Academy of Sciences , 113 (43), 12059-12064.

Garzanti, E., Baud, A., & Mascle, G. (1987). Sedimentary record of the northward flight of India and its collision with Eurasia (Ladakh Himalaya, India). Geodinamica Acta , 1 (4-5), 297-312.

Garzanti, E., Liang, W., Andò, S., Clift, P. D., Resentini, A., Vermeesch, P., & Vezzoli, G. (2020). Provenance of Thal Desert sand: Focused erosion in the western Himalayan syntaxis and foreland-basin deposition driven by latest Quaternary climate change. Earth-science reviews , 207 , 103220.

Ghani, H., Sobel, E. R., Zeilinger, G., Glodny, J., Zapata, S., & Irum, I. (2021). Palaeozoic and Pliocene tectonic evolution of the Salt Range constrained by low-temperature thermochronology. Terra Nova , 33 (3), 293-305.

Grasby, S. E., Them II, T. R., Chen, Z., Yin, R., & Ardakani, O. H. (2019). Mercury as a proxy for volcanic emissions in the geological record. Earth-Science Reviews , 196 , 102880.

Hanif, M., Sabba, M., Ali, N., Rahman, M. U., Ali, F., & Swati, M. A. F. (2021). A multi-proxy based high-resolution stratigraphical analysis of the possible Paleocene–Eocene boundary interval, Salt Range, Pakistan. Geological Journal , 56 (1), 434-456.

Hu, X., Garzanti, E., Wang, J., Huang, W., An, W., & Webb, A. (2016). The timing of India-Asia collision onset–Facts, theories, controversies. Earth-Science Reviews, 160, 264-299.

Hulme, P. E. (2005). Adapting to climate change: is there scope for ecological management in the face of a global threat?. Journal of Applied ecology , 42 (5), 784-794.

Hottinger, L. (2009). The Paleocene and earliest Eocene foraminiferal Family Miscellaneidae: neither nummulitids nor rotaliids. Carnets de Géologie/Notebooks on Geology, Brest, Article, 6.

Hottinger, L., & Bassi, D. (2014). Paleogene larger rotaliid foraminifera from the western and central Neotethys (pp. 3-191). Berlin: Springer.

Iqbal, S., Jan, I. U., & Hanif, M. (2014). The Mianwali and Tredian formations: An example of the Triassic Progradational deltaic system in the low-latitude western Salt Range, Pakistan. Arabian Journal for Science and Engineering , 39 , 5489-5507.

Jadoon, U. F., Huang, B., Zhao, Q., Shah, S. A., & Rahim, Y. (2021). Remagnetization of Jutal dykes in Gilgit area of the Kohistan Island Arc: Perspectives from the India–Asia collision. Geophysical Journal International, 226(1), 33-46.

Jones, M. T., Percival, L. M., Stokke, E. W., Frieling, J., Mather, T. A., Riber, L., ... & Svensen, H. H. (2019). Mercury anomalies across the Paleocene–Eocene thermal maximum. Climate of the Past, 15(1), 217-236.

Jones, M. T., Stokke, E. W., Rooney, A. D., Frieling, J., Pogge von Strandmann, P. A. E., Wilson, D. J., Selnes, H., Mather, T. A., Schreck, S., Schwark, L., & Schultz, B. P. (2023). Tracing North Atlantic volcanism and seaway connectivity across the Paleocene–Eocene thermal maximum (PETM). Climate of the Past, 19(8), 1623-1652. https://doi.org/10.5194/cp-19-1623-2023

Kadri, I.B., (1995), Petroleum geology of Pakistan. Pakistan Petroleum Limited, Karachi.

Kahsnitz, M. M., Zhang, Q., & Willems, H. (2016). Stratigraphic distribution of the larger benthic foraminifera Lockhartia in south Tibet (China). The Journal of Foraminiferal Research, 46(1), 34-47.

Kamran, M., Frontalini, F., Xi, D., Papazzoni, C. A., Jafarian, A., Latif, K., ... & Wan, X. (2021). Larger benthic foraminiferal response to the PETM in the Potwar Basin (Eastern Neotethys, Pakistan). Palaeogeography, Palaeoclimatology, Palaeoecology, 575, 110450.

Kahle, C. F. (1965). Possible roles of clay minerals in the formation of dolomite. Journal of Sedimentary Research , 35 (2).

Kender, S., Bogus, K., Pedersen, G. K., Dybkjær, K., Mather, T. A., Mariani, E., Ridgwell, A., Riding, J.B., Wagner, T., Hesselbo, S.P. & Leng, M. J. (2021). Paleocene/Eocene carbon feedbacks triggered by volcanic activity. Nature communications, 12(1), 5186.

Kemp, S. J., Ellis, M. A., Mounteney, I., & Kender, S. (2016). Palaeoclimatic implications of high-resolution clay mineral assemblages preceding and across the onset of the Paleocene–Eocene Thermal Maximum, North Sea Basin. Clay Minerals , 51 (5), 793-813.

Khozyem, H., Adatte, T., Spangenberg, J. E., Keller, G., Tantawy, A. A., & Ulianov, A. (2015). New geochemical constraints on the Paleocene–Eocene thermal maximum: Dababiya GSSP, Egypt. Palaeogeography, Palaeoclimatology, Palaeoecology, 429, 117-135.

Khozyem, H., Adatte, T., & Keller, G. (2023). Climatic and Environmental Changes During Paleocene-Eocene Thermal Maximum in Egypt: An Overview. The Phanerozoic Geology and Natural Resources of Egypt, 305-338.

Kiessling, W., Flügel, E., & Golonka, J. (1999). Paleoreef maps: evaluation of a comprehensive database on Phanerozoic reefs. AAPG bulletin , 83 (10), 1552-1587.

Klug, H. P., & Alexander, L. E. (1974). X-ray diffraction procedures: for polycrystalline and amorphous materials (p. 992).

Knoll, A. H., Hayes, J. M., Kaufman, A. J., Swett, K., & Lambert, I. B. (1986). Secular variation in carbon isotope ratios from Upper Proterozoic successions of Svalbard and East Greenland. Nature, 321(6073), 832-838.

Komar, N., & Zeebe, R. E. (2017). Redox-controlled carbon and phosphorus burial: A mechanism for enhanced organic carbon sequestration during the PETM. Earth and Planetary Science Letters, 479, 71-82.

Leppig, U., 1988. Structural analysis and taxonomic revision of Miscellanea, Paleocene larger Foraminifera.- Eclogae Geologicae Helvetiae, Basel 81(3), 689-721.

Leppig, U., Langer M.R., 2015. Emendation and taxonomic revision of Miscellanea juliettae pfenderae and M. juliettae villattea with designation of the respective holotype. Micropaleontology 61, 227-230.

Li, J., Hu, X., Zachos, J. C., Garzanti, E., & BouDagher-Fadel, M. (2020). Sea level, biotic and carbon-isotope response to the Paleocene–Eocene thermal maximum in Tibetan Himalayan platform carbonates. Global and Planetary Change, 194, 103316.

Li, J., Hu, X., Garzanti, E., & BouDagher-Fadel, M. (2022). Spatial heterogeneity in carbonate-platform environments and carbon isotope values across the Paleocene–Eocene thermal maximum (Tethys Himalaya, South Tibet). Global and Planetary Change, 214, 103853.

Mariani, L., Coletti, G., Bosio, G., Vicens, G. M., Ali, M., Cavallo, A., ... & Mal winter, E. (2024). Tectonically-controlled biofacies distribution in the Eocene Foraminiferal Limestone (Pag, Croatia): A quantitative-based palaeontological analysis. Sedimentary Geology , 472 , 106743.

Martini, E., 1971. Standard Tertiary and Quaternary calcareous nannoplankton zonation. In: Farinacci, A. (Ed.), Proceedings 2nd International Conference Planktonic Microfossils. Tecnosci, Rome, pp. 739–785.

Menini, A., Mattioli, E., Vinçon-Laugier, A., & Suan, G. (2022). Calcareous nannofossil biostratigraphy across the Paleocene-Eocene Thermal Maximum. Newsletters on Stratigraphy, 55(1), 69-97.

McDougall, J. W., & Khan, S. H. (1990). Strike-slip faulting in a foreland fold-thrust belt: The Kalabagh Fault and Western Salt Range, Pakistan. Tectonics, 9(5), 1061-1075.

McInerney, F. A., & Wing, S. L. (2011). The Paleocene-Eocene Thermal Maximum: A perturbation of carbon cycle, climate, and biosphere with implications for the future. Annual Review of Earth and Planetary Sciences, 39, 489-516.

Mertmann, D. (2003). Evolution of the marine Permian carbonate platform in the Salt Range (Pakistan). Palaeogeography, Palaeoclimatology, Palaeoecology, 191(3-4), 373-384.

Najman, Y., Jenks, D., Godin, L., Boudagher-Fadel, M., Millar, I., Garzanti, E., ... & Bracciali, L. (2017). The Tethyan Himalayan detrital record shows that India–Asia terminal

collision occurred by 54 Ma in the Western Himalaya. Earth and Planetary Science Letters, 459, 301-310

Najman, Y., Appel, E., Boudagher-Fadel, M., Bown, P., Carter, A., Garzanti, E., ... & Vezzoli, G. (2010). Timing of India-Asia collision: Geological, biostratigraphic, and palaeomagnetic constraints. Journal of Geophysical Research: Solid Earth, 115(B12).

Najman, Y., & Garzanti, E. (2000). Reconstructing early Himalayan tectonic evolution and paleogeography from Tertiary foreland basin sedimentary rocks, northern India. Geological Society of America Bulletin, 112(3), 435-449.

Özcan, E., Pignatti, J., Pereira, C., Yücel, A. O., Drobne, K., Barattolo, F., & Saraswati, P. K. (2018). Paleocene orthophragminids from the Lakadong Limestone, Mawmluh Quarry section, Meghalaya (Shillong, NE India): implications for the regional geology and paleobiogeography. Journal of Micropalaeontology, 37(1), 357-381.

Papazzoni, C.A., Fornaciari, B., Giusberti, L., Simonato, M., & Fornaciari, E. (2023) - A new definition of the Paleocene Shallow Benthic Zones (SBP) by means of larger foraminiferal biohorizons, and their calibration with calcareous nannofossil biostratigrapy. Micropaleontology, 69(4): 363-399.

Pereira, C. D., Khanolkar, S., Banerjee, S., Özcan, E., & Saraswati, P. K. (2022). Larger benthic foraminifera and microfacies of late Paleocene-early Eocene sections in Meghalaya, Northeast India. Journal of Foraminiferal Research, 52(1), 40-56.

Pivnik, D. A., & Wells, N. A. (1996). The transition from Tethys to the Himalaya as recorded in northwest Pakistan. Geological Society of America Bulletin, 108(10), 1295-1313.

Pomar, L., Baceta, J. I., Hallock, P., Mateu-Vicens, G., & Basso, D. (2017). Reef building and carbonate production modes in the west-central Tethys during the Cenozoic. Marine and Petroleum Geology, 83, 261-304.

Rajak, J. (2021). A preliminary review on impact of climate change and our environment with reference to global warming. Int. J. Environ. Sci , 10 , 11-14.

Rehman, H. U., Seno, T., Yamamoto, H., & Khan, T. (2011). Timing of collision of the Kohistan–Ladakh Arc with India and Asia: debate. Island Arc, 20(3), 308-328.

Révész, K. M., & Landwehr, J. M. (2002). δ13C and δ18O isotopic composition of CaCO3 measured by continuous flow isotope ratio mass spectrometry: statistical evaluation and verification by application to Devils Hole core DH-11 calcite. Rapid Communications in Mass Spectrometry, 16(22), 2102-2114.

Sarkar, S., Cotton, L. J., Valdes, P. J., & Schmidt, D. N. (2022). Shallow water records of the PETM: Novel insights from NE India (eastern Tethys). Paleoceanography and Paleoclimatology , 37 (7), e2021PA004257.

Saboor, A., Ahmad, J., Khan, S., Latif, K., Khan, A., Haider, A.T., 2021. Foraminiferal biostratigraphy, facies, and sequence stratigraphy analysis across the K-Pg Boundary in Hazara, Lesser Himalayas (Dhudial Section). Geodiversitas 43(18), 663-682.

Scheibner, C., Speijer, R.P., Marzouk, A.M., 2005. Turnover of larger foraminifera during the Paleocene-Eocene Thermal Maximum and paleoclimatic control on the evolution of platform ecosystems. Geology 33(6), 493-496.

Scheibner, C., & Speijer, R. P. (2008). Late Paleocene–early Eocene Tethyan carbonate platform evolution—a response to long-and short-term paleoclimatic change. Earth-science reviews, 90(3-4), 71-102.

Schlager, W. (1999). Scaling of sedimentation rates and drowning of reefs and carbonate platforms. Geology , 27 (2), 183-186.

Serra-Kiel, J., Hottinger, L., Caus, E., Drobne, K., Ferrandez, C., Jauhri, A.K., Less, G., Pavlovec, R., Pignatti, J., Samso, J.M., Schaub, H., Sirel, E., Strougo, A., Tambareau, Y., Tosquella, J., Zakrevskaya, E., 1998. Larger foraminiferal biostratigraphy of the Tethyan. Bulletin de la Société géologique de France 169, 281-299.

Serra-Kiel, J., Vicedo, V., Baceta, J.I., Bernaola, G., Robador, A., 2020. Paleocene Larger Foraminifera from the Pyrenean Basin with a recalibration of the Paleocene Shallow Benthic Zones. Geologica acta 18, 1-69, I-III.

Shah, S. M. I. (2009). Stratigraphy of Pakistan. Geological Survey Pakistan Membership, 22, 1-381.

Shah, M.M., Rahim, H.U., Hassan, A., Mustafa, M.R., Ahmad, I., 2020. Facies control on selective dolomitization and its impact on reservoir heterogeneities in the Samana Suk Formation (Middle Jurassic), Southern Hazara Basin (NW Himalaya, Pakistan): an outcrop analogue. Geosciences Journal 24(3), 295-314.

Sirel, E., 2018. Revision of the Paleocene and partly early Eocene larger benthic foraminifera of Turkey. Department of Geological Engineering, Ankara University: Ankara Üniversitesi Yayýnevi Yayin 27, 260 pp.

Spangenberg, J. E., Jacomet, S., & Schibler, J. (2006). Chemical analyses of organic residues in archaeological pottery from Arbon Bleiche 3, Switzerland–evidence for dairying in the late Neolithic. Journal of archaeological science, 33(1), 1-13.

Swart, P. K. (2015). The geochemistry of carbonate diagenesis: The past, present and future. Sedimentology, 62(5), 1233-1304.

Swati, M. A. F., Hanif, M., Haneef, M., & Saboor, A. (2021). Late Paleocene to Early Eocene biostratigraphic framework from Upper Indus Basin, Pakistan, Eastern Tethys. Geological Journal , 56 (7), 3541-3556.

Traill, L. W., Lim, M. L., Sodhi, N. S., & Bradshaw, C. J. (2010). Mechanisms driving change: altered species interactions and ecosystem function through global warming. Journal of Animal
Ecology , 79 (5), 937-947.

Treloar, P. J., Coward, M. P., Chambers, A. F., Izatt, C. N., & Jackson, K. C. (1992). Thrust geometries, interferences and rotations in the Northwest Himalaya. Thrust tectonics, 325-342.

Tremblin, M., Khozyem, H., Adatte, T., Spangenberg, J.E., Fillon, C., Grauls, A., Hunger, T., Nowak, A., Läuchli, C., Lasseur, E., Roig, J.Y., Serrano, O., Calassou, S., Guillocheau, F., Castelltort, S., 2022. Mercury enrichments of the Pyrenean foreland basins sediments support enhanced volcanism during the Paleocene-Eocene thermal maximum (PETM). Global and Planetary Change 212, 103794.

Umar, M., Sabir, M.A., Farooq, M., Khan, M.M.S.S., Faridullah, F., Jadoon, U.K., Khan, A.S., 2015. Stratigraphic and sedimentological attributes in Hazara Basin Lesser Himalaya, North Pakistan: their role in deciphering minerals potential. Arabian Journal of Geosciences 8(3), 1653-1667.

Walsh, S. L. (2004). Solutions in chronostratigraphy: the Paleocene/Eocene boundary debate, and Aubry vs. Hedberg on chronostratigraphic principles. Earth-Science Reviews, 64(1-2), 119-155.

Wadood, B., Khan, S., & Li, H. (2022). Middle Permian Mixed Siliciclastic-Carbonate System on the Northwestern Margin of the Indian Plate, Pakistan: Implications for Paleoclimate and Carbonate Platform Evolution. Acta Geologica Sinica-English Edition, 96(1), 321-336

Yeats, R. S., & Lawrence, R. D. (1982, November). Tectonics of the Himalayan thrust belt in northern Pakistan. In US-Pakistan Workshop on Marine Sciences in Pakistan.

Young, J.R., Bown P.R., Lees J.A. (2023) Nannotax3 website. International Nannoplankton Association. Accessed April 2023. URL: www.mikrotax.org/Nannotax3

Zamagni, J., Mutti, M., Ballato, P., Kosir, A., 2012. The Paleocene-Eocene thermal maximum (PETM) in shallow-marine successions of the Adriatic carbonate platform (SW Slovenia). Geol. Soc. Am. Bull. 124, 1071–1086. https://doi.org/10.1130/ B30553.1.

Zhang, Q., Willems, H., & Ding, L. (2013). Evolution of the Paleocene-Early Eocene larger benthic foraminifera in the Tethyan Himalaya of Tibet, China. International Journal of Earth Sciences, 102, 1427-1445.

Zhang, Q., Willems, H., Ding, L., & Xu, X. (2019). Response of larger benthic foraminifera to the Paleocene-Eocene thermal maximum and the position of the Paleocene/Eocene boundary in the Tethyan shallow benthic zones: Evidence from south Tibet. GSA Bulletin, 131(1-2), 84-98.

Zintwana, M. P., Cawthorn, R. G., Ashwal, L. D., Roelofse, F., & Cronwright, H. (2012). Mercury in the Bushveld complex, South Africa, and the Skaergaard intrusion, Greenland. Chemical Geology, 320, 1

Conclusions

During the geological history of the Earth several well-known greenhouse phases effected the production of carbonates and also on carbonate producing organisms. Many of these notable events affected the biosphere of the Cenozoic and can be used as proxies to understand what is going to occur in the near future on our planet.

At the beginning of the Cenozoic, after the K-Pg mass extension, reef corals, the most distinctive carbonate producers of modern tropical oceans, recovered very fast. During the Late Cretaceous they were less abundant than reef-building mollusks (the rudists). During the Early Paleocene, they had become dominant. This can be seen very well in the succession of central Italy from Maiella. Here rocks from the lower Paleocene (SBZ1 – SBZ2) sit on the top of Upper Cretaceous reefs and clearly display this event. The same pattern can be seen in other areas of Tethys.

During the Late Paleocene global temperatures began to rise. This most likely occurred not in a linear way but through a series of sharp events. One of these events is well recorded in the lower part of the rocks characterized by large benthic foraminiferal assemblage typical of SBZ4 (at the boundary with the rocks characterized by assemblages typical of SBZ3) from the Hazara Basin (northern upper Indus Basin, Northern Pakistan). Here it is possible to observe a progressive decrease in the abundance of reef corals matched by an increase in large benthic foraminifera.

The remainder of the Late Paleocene climate change can be observed in the rocks from the Surghar and Salt ranges (upper Indus Basin, Northern Pakistan). In the study area, these successions span from SBZ3 (Selandian to lower Thanetian) to SBZ5 (lowermost Ypresian). Among the successions studied from this area, the Baroch Nala section displays a particularly well-preserved record, with no evidence of erosional surfaces, major interruptions in sedimentation, or major alteration from diagenesis. This section provides a wonderful framework to constrain the skeletal assemblages, connect them with geochemical variation and use both elements to correlate other sections, in particular with the close by Nammal Gorge section. The overall record shows a first departure from the arid climate of the early Thanetian in the lower part of SBZ4, allowing for a correlation with the Hazara Basin. This first oscillation, recognized on a regional scale, can be also traced on a global scale and represents a late Thanetian hyperthermal events that precede the PETM. Further

above the PETM event begins. This is marked by major changes in skeletal assemblages with an increase in the abundance of nummulitids at the expense of genera of LBF typical of the Paleocene like *Lockhartia* and *Miscellanea*. This change might have been related to the stressful conditions caused by the increase in temperatures and the increase in nutrient supply related to the enhanced weathering of continents. Later, When the global climate recovered from PETM, carbonate platform assemblage was drastically changed, reef corals had become much more rare and large benthic foraminifera much more common. Among them, most of the Paleocene taxa had disappeared and nummulitids had become dominant. This latter group will end up becoming one of the most distinctive elements of the carbonate platforms of Tethys for the 20 million years following the PETM.

The diversification of LBF was closely linked to the Increase in nutrient (phosphorous and silica) supply during the PETM, which significantly increases the productivity of their symbiotic algae within shallow marine environments. The enriched nutrient conditions not only supported the metabolic demands of LBF but also facilitated the calcification processes. These favorable conditions, alongside the warm tropical climate, created ecological opportunities for the evolutionary radiation of LBF, allowing them to adapt to diverse niches and flourish despite the global environmental changes of PETM.

The presence of Hg/TOC peaking trends during the POE and PETM intervals suggests a possible link between volcanic activity connected with North Atlantic Igneous Province (NAIP). This connection implies that volcanism may have played a significant role as a potential forcing mechanism. However, the relatively low Hg/TOC values also indicate that the studied section was a considerable distance from the NAIP, reflecting its distal positioning. Along with volcanism, other forcing factors contributed to the climatic and environmental changes during the late Paleocene to the early Eocene interval. These factors include orbital forcing, which influenced Earth's climate system through changes in solar insolation; methane hydrate destabilization, releasing substantial quantities of methane, and widespread wildfires, which would have added further carbon to the atmosphere. Together, these processes drive the significant global warming and associated environmental changes characteristic of this period.

Taking the Baroch Nala section as a reference point for the POE and PETM in the eastern Tethys and world-wide, various sections can be correlated. This shows similarities in the biological, mineralogical, and geochemical signals in response to POE and PETM,

further cementing the paleoenvironmental interpretation based on the study of northern Pakistan

Acknowledgments

I am profoundly thankful to Allah Almighty, the ultimate source of wisdom and strength, and to the Holy Prophet Muhammad (PBUH), whose exemplary life continues to guide and inspire me. Their blessings have given me the courage and perseverance needed to undertake and complete this PhD journey.

I am deeply grateful to the University of Milano-Bicocca (Unimib), Italy, for the fully funded PhD scholarship that allowed me to pursue my research aspirations. I extend my sincere appreciation to my tutor and supervisor, **Professor Eduardo Garzanti**, and my supervisors, **Professor Pietro Sternai** and **Dr. Giovanni Coletti**, for their unwavering support, insightful guidance, and mentorship throughout my academic journey.

I would also like to express my gratitude to **Professor Sébastien Castelltort** from the University of Geneva, Switzerland, and **Professor Thierry Adatte** from the University of Lausanne, Switzerland for their vital contributions. Their support in facilitating laboratory analyses, offering financial assistance during my mobility period, and providing feedback greatly enhanced my research, ultimately leading to the publication of my work in international journals.

A special note of thanks is owed to **Dr. Giovanni Coletti**, not only for his significant contributions to my research but also for his moral support and mentorship, which have been invaluable throughout my doctoral studies.

I am also thankful to **Prof. Suliman Khan, Dr. Andrea Benedetti, Prof. Elisa Malinverno, Prof. Daniela Basso, Prof. Elias Samankassou Prof. Sergio Andò (Unimib**), Prof. **Muhammad Jawad Munawar,** and Prof. **Saif ur Rehman** for their key contributions to my project, and to Dr. **Luca Mariani, Dr. Muhammad Usman, Dr. Muhammad Awais** and **Mr. Siraj Mehboob** for their constructive feedback during various stages of my research. My gratitude extends to **Miss Marta Barbarano** for her invaluable assistance in refining my laboratory skills.

I am also very thankful to **Dr. Kasia Sliwinska** (Geological Survey of Denmark and Greenland-GEUS) and Dr. David Naafs (University of Bristol) for TEX^{86} analysis. I am grateful to **Dr. Jorge E. Spangenberg** and **Dr. László Kocsis** for the stable C-O isotopes, and **Dr. Brahimsamba Bomou** and **Ms. Tiffany Monnier** for XRD, Mercury and Rock eval analysis.

I am grateful to the Cushman Foundation and IGCP739 for their financial support, which enabled me to present my work at AGU 2024 in Washington, DC.

To my family, I owe endless thanks: to my parents**, Mr. Gohar Ali** and **Mrs. Mussarat Begum**, for their constant encouragement and prayers; to my wife, **Ms. Masira Rabia**, for her love and patience; to my son, **Muhammad Wamiq Ali**, whose presence brings joy to my life; and to my siblings for their steadfast support. Their belief in me has been a constant source of strength, despite the miles that have separated us during this journey.

Finally, I would like to thank my dear friends from Unimib and Switzerland. Their friendship and kindness have made my time abroad both fulfilling and memorable. I will always cherish the moments of laughter and companionship we shared, which helped me feel at home in unfamiliar places.

Mubashir Ali
Registration Number: 886085

Appendix

Table BS1 Baroch Nala section Five interval information based on average geochemical and biological data.

Tables BS2 Summary of Baroch Nala section geochemical proxies from the base of the section including $\delta^{13}C_{org}$, $\delta^{13}C_{carb,}$ and $\delta^{18}O_{carb}$, Rock eval and Mercury data with biology According to different successive stages of the Paleocene-Eocene transition.

Tables BS3 Summary of Baroch Nala section Bulk rock mineralogy and clay mineralogy and assemblages and its ratio.

Table NS1 Nammal Gorge section interval-wise information based on average geochemical and biological data.

Tables NS2 Summary of Nammal Gorge section geochemical proxies from the base of the section including $\delta^{13}C_{org}$, $\delta^{13}C_{carb,}$ and $\delta^{18}O_{carb}$, Rock eval and Mercury data with biology According to different successive stages of the Paleocene-Eocene transition.

Tables NS3 Summary of Nammal Gorge section Bulk rock mineralogy and clay mineralogy and assemblages and its ratio.

Table GS1 Ghumawan section interval-wise information based on average geochemical and biological data.

Tables GS2 Summary of Ghumanwan section geochemical data with bulk rock mineralogy and Mercury concentrations.

.

Table "Tethys" LBF-based information from 34 shallow section across the Tethys spanning from SBZ3 to SBZ5/6

Table BS1 Baroch Nala section Five interval information based on average geochemical and biological data.

Events		Formation	Thickness (mbs)	Lithology	Biofacies	LBF species	Calcareous nannofossils	Bulk Mineralogy Avg % (min-max)				Clay Mineralogy Avg % (min-max)					$^{13}C_{org}$ (max-min)	$^{13}C_{carb}$ (max-min)	$^{18}O_{Carb}$ (max-min)	Rock-Eval Avg % (min-max)				Volcanic Proxy Avg % (min-max)	
								Phy %	Qtz %	Cal %	Dol %	Sm %	Kao %	Palyg %.	Illite %	I/S mixed %	(‰ VPDB)	(‰ VPDB)	(‰ VPDB)	TOC (wt%)	HI (mg $HC/g TOC$)	OI (mg $CO_2/g TOC$)	Tmax (°C)	Hg (ppb)	Hg/TOC (ppb/wt%)
pre-PETM		Lockhart Limeston e	0-6	Nodular Limestone	BF1: Lockhartia and hyaline SBF with orbitoidiform hyaline LBF	*Miscellanea juliettae, Miscellanites sp., Lockhartia prehaimei, Lockhartia retiata, Elazigina lenticula, Kathina selveri, Orbitosiphon sp.*	-	10 (8-11)	3 (2-5)	84 (83-84)	0	70 (56-79)	3 (1-6)	14 (6-39)	9 (4-14)	3 (2-3)	-19.3 to -20.4	1.70	-5.0	0.18 (0.1-0.2)	257 (209-288)	78 (49-107)	430 (420-444)	0.7 (0.6-1.0)	4.7 (3.6-5.8)
		Patala Formation	6-15.6	Calcareous marls , Limestone		*Miscellanites sp., Miscellanea cf. dukhani, Daviesina sp., L.haimei, L.conditi, L.roeae, Lockhartia tipperi, Kathina silver, Elazigina lenticula, Rotospirella sp., Rotalia cf. newboldi, Rotorbinella sp., Orbitosiphon sp., Lakadongia tibetica.*	Very rare to Few *Toweius pertusus*, *Prinsius* spp. (small), *Coccolithus pelagicus*, very rare to rare *Neochiastozygus modestus*, *Prinsius bisulcus*, *P. martini*, *Cruciplacolithus edwardsii*	25 (10-42)	4 (2-17)	64 (35-85)	1 (0-10)	48 (30-73)	22 (4-45)	13 (5-37)	9 (2-19)	3 (1-5)	-18.5 to -22.0	1.65 to2.51	-4.7 to -6.0	0.47 (0.1-1.0)	129 (76-240)	111 (56-235)	431 (424-438)	3.3 (0.7-9.5)	7.8 (4.2-14.4)
Pre Onset Excursion	Onset		15.6-16.8	Nodular limestone, Black shale	BF2:Lockhartia, Daviesina, Miscellanea and hyaline SBF	*L.haimei, L.conditi, Rotalia cf. newboldi, Miscellanea cf miscella.*	Very rare to Few *Toweius pertusus*, *Prinsius* spp. (small), *Coccolithus pelagicus*, Very Rare *T. rotundus*	23 (10-63)	4 (2-15)	67 (8-86)	1 (0-8)	38 (29-53	34 (25-53)	11 (4-22)	9 (4-17)	3 (2-6)	-19.4 to -23.0	1.06	-4.5	0.20 (0.1-0.3)	97 (47-139)	159 (124-212)	433 (428-437)	2.1 (0.4-7.6)	9 (6.4-20)
	Recovery		16.8-23.4	Calcareous marls		*L.prehaimei, L. cf. haimei, L.conditi, L.diversa, L.retiata, Kathina mayor, Miscellanea miscella, Miscellanea dukhani Ranikothalia sindensis*	Very rare to Few *Toweius pertusus*, *Prinsius* spp. (small), *Coccolithus* pelagicus; Very rare to Rare *Prinsius bisulcus*, *P. martini*, *T. rotundus*, Very rare *Sphenolithus primus*, *Zygodiscus sheldoniae*, *Campylosphaera dela*, *Umbilicosphaera bramlettei*	28 (15.56)	5 (2-20)	52 (17-70)	6 (0-44)	56 (37-78)	23 (4-42)	7 (2-15)	7 (5-10)	2 (1-4)	-19.5 to 21.8	1.77 to 2.07	-4.8 to -6.5	0.53 (0.3-0.9)	91 (43-182)	90 (67-163)	429 (417-437)	4.2 (2-5.7)	8.5 (4.7-12)
PETM Onset			23.4-27.5	Calcareous marls , Black shale	BF3:Lockhartia, Daviesina, Miscellanea and hyaline SBF with Ranikothalia	*L.tipperi, L.haimei, L.retiata, Miscellanea cf. dukhani, Daviesina langhami, Ranikothalia spp., Assilina cf. dandotica*	Very rare to Few *Toweius pertusus*, *Coccolithus* pelagicus; Very rare to Rare *Prinsius* spp. (small), *T. rotundus*, *Fasciculitus alanii*, *F. involutus*, *F. lilianiae*, *F. thomasii*, *Bomolithus elegans*, *B. megastypus*, *Cruciplacolithus edwardsii*	28 (16-70)	3 (2-8)	56 (5-78)	5 (0-14)	61 (28-77)	23 (6-53)	4 (3-4)	3 (3-6)	3 (2-3)	-20.4 to -24.8	1.1 to 1.7	-4.47 to -5.3	0.36 (0.1 -0.8)	97 (38-163)	122 (70-209)	430 (415-435)	4 (2.3-8.5)	12.7 (8.5-23)
	PETM Body		27.5-37.5	Calcareous marls	BF4:Nummulitids and orthophragminids with Green calcareous algae (GCA)	*L.conditi, L.haimei, Rotalia cf. newboldi, Daviesina langhami, Ranikothalia nuttalli, Assilina ranikoti, Assilina cf. ornata, Assilina cf. dandotica, Nummulites sp., Discocyclina sp., Alveolina sp.*	Rare to Few *Toweius pertusus*, *Coccolithus pelagicus*, Very rare to Rare *Prinsius* spp. (small), *Bomolithus megastypus*, *Discoaster multiradiatus*, *Fasciculithus involutus*, very rare *Fasciculithus tympaniformis*, *Neochiastozygus pusillus*, *Toweius eminens*, *Zygodiscus herlyni*,	34 (27-53)	5 (2-11)	50 (21-61)	2 (0-8)	24 (19-32)	59 (53 – 68)	3 (3-4)	4 (3-5)	2 (1-3)	-23.4 to -24.3	1.3 to1.9	-5.2 to -6.2	0.16 (0.1-0.2)	48 (25-68)	213 (203-226)	410 (402-428)	4.2 (2.1 - 6.3)	27.2 (15.5-31.6)
	PETM Recovery		37.5-49.5					33 (25-39)	3 (2-4)	55 (50-62)	1 (1-2)	60 (41-75)	23 (14-35)	5 (3-7)	4 (2-7)	3 (2-7)	-21.9 to 22.8	2.3 to 2.7	-4.7 to -7.0	0.20 (0.1-0.2)	60 (48-86)	246 (178-332)	422 (408-434)	3.4 (2.9-3.8)	18.3 (14.4-27)
post-PETM			49.5-59.5	Calcareous marls	BF5: Nummulitids and orthophragminids	*L.conditi, Daviesina sp., Assilina ornata, Assilina dandotica, Nummulites minerviensis, Discocyclina sp., Alveolina sp.*	Very rare to Rare *Toweius pertusus*; Very rare *Zygodiscus plectopons*, *Fasciculithus* sp.	12 (8-17)	2	79 (74-84)	3 (2-4)	68 (61-80)	17 (11-27)	4 (2-7)	3 (2-5)	3 (2-6)	-22.6 to -23.9	2.0 to 2.4	-4.4 to 5.0	0.07 (0.03-0.1)	87 (59-105)	279 (236-376)	423 (405-435)	1.3 (0.3 – 2.1)	12.48 (8.6-19.3)

Tables BS2 Summary of Baroch Nala section geochemical proxies from the base of the section including $\delta^{13}C_{org}$, $\delta^{13}C_{carb,}$ and $\delta^{18}O_{carb}$, Rock eval and Mercury data with biology According to different successive stages of the Paleocene-Eocene transition

Sample No	Thickness	Biofacies	$^{13}C_{(org)}$	$^{13}C_{(Bulk)}$	$^{18}O_{(Bulk)}$	TOC	Hydrogen Index (HI)	Oxygen Index (OI)	Tmax	Mercury Hg(ppb)	Hg/TOC	Hg/Phy
BP-01	2	Pre PETM	-20.4	1.70	-5.03	0.11	209	107	426	0.65	5.81	**0.059153**
BP-02	4		-20.4	-	-	0.13	276	78	444	0.6	4.66	**0.071892**
BP-03	6		-19.3	-	-	0.29	288	49	420	1.05	3.67	**0.096972**
BP-04	6.3		-20.0	-	-	0.62	240	68	424	4.45	7.21	**0.18071**
BP-05	6.6		-21.9	2.16	-5.48	0.62	166	73	438	3.8	6.16	**0.157053**
BP-06	6.9		-21.9	-	-	0.64	169	81	431	4.4	6.86	**0.17197**
BP-07	7.2		-21.3	-	-	0.27	109	138	429	3.85	14.24	**0.185274**
BP-08	7.5		-20.5	-	-	0.63	167	87	432	5.2	8.29	**0.17283**
BP-09	7.8		-20.6	2.17	-5.47	0.67	198	73	432	4.05	6.02	**0.170475**
BP-10	8.1		-21.6	-	-	0.17	103	187	428	2.5	14.95	**0.142944**
BP-11	8.4		-21.0	-	-	0.25	166	115	431	1.8	7.18	**0.13338**
BP-12	8.7		-20.0	-	-	0.42	115	105	428	3.95	9.49	**0.139867**
BP-13	9		-19.5	-	-	0.63	167	75	435	3.5	5.58	**0.118213**
BP-14	9.3		-20.1	2.51	-4.70	0.14	105	141	428	0.95	7.03	**0.054137**
BP-15	9.6		-20.1	-	-	0.35	96	112	432	2.7	7.72	**0.088041**
BP-16	9.9		-19.8	-	-	0.52	106	92	431	4.2	8.01	**0.121212**
BP-17	10.2		-19.8	-	-	0.25	116	111	427	1.65	6.72	**0.063643**
BP-18	10.5		-19.7	2.48	-4.68	0.34	136	106	427	2.2	6.40	**0.087511**
BP-19	10.8		-18.7	-	-	0.10	139	148	426	0.7	6.84	**0.073048**
BP-20	11.1		-19.9	-	-	0.60	125	85	427	3.75	6.26	**0.121678**
BP-21	11.4		-20.0	-	-	0.42	147	85	430	2.4	5.71	**0.126869**
BP-22	11.7		-19.9	-	-	0.32	141	91	428	1.4	4.33	**0.085957**
BP-23	12		-21.2	2.41	-5.09	0.20	88	103	427	2.85	14.47	**0.121071**
BP-24	12.3		-20.2	-	-	1.01	185	56	430	4.15	4.11	**0.154966**
BP-25	12.6		-19.7	-	-	0.84	138	71	434	4.85	5.79	**0.168869**
BP-26	12.9		-19.4	-	-	0.34	106	118	434	2.4	7.04	**0.130186**
BP-27	13.2		-18.5	2.44	-6.03	0.75	168	89	430	3.85	5.11	**0.163894**
BP-28	13.5		-18.9	-	-	0.88	178	76	430	3.7	4.20	**0.100887**
BP-29	13.65		-19.4	-	-	0.68	120	115	436	5.45	8.05	**0.140609**
BP-30	13.8		-19.8	2.20	-5.58	0.57	111	90	434	3.9	6.78	**0.111751**
BP-31	13.95		-19.3	-	-	0.15	115	137	433	1.1	7.58	**0.10107**
BP-32	14.1		-19.4	-	-	0.43	138	121	435	3.75	8.63	**0.132739**
BP-33	14.25		-20.0	-	-	0.34	76	117	432	2.2	6.53	**0.097768**
BP-34	14.4		-20.1	2.16	-4.71	0.11	101	235	437	1.1	10.32	**0.085086**
BP-35	14.55		-20.7	-	-	0.21	93	144	436	1.4	6.62	**0.074201**
BP-36	14.7		-21.7	-	-	0.10	86	220	431	1.7	16.52	**0.110821**
BP-37	14.85		-21.5	2.01	-5.75	0.46	77	149	427	5.75	12.43	**0.139145**
BP-38	15		-22.0	-	-	0.89	102	95	434	9.5	10.68	**0.225707**
BP-39	15.15		-21.2	-	-	0.48	89	103	430	3.5	7.37	**0.115946**
BP-40	15.3		-20.2	1.87	-6.54	0.98	93	100	434	6.7	6.82	**0.166392**
BP-41	15.45		-19.7	-	-	0.70	148	84	433	3.3	4.74	**0.166746**
BP-42	15.6		-19.3	1.65	-4.47	0.33	109	129	436	2.75	8.39	**0.110932**
BP-43	15.75	POE	-19.4	-	-	0.11	139	212	434	0.4	3.51	**0.02872**
BP-44	15.9		-20.2	-	-	0.11	86	182	437	0.9	7.83	**0.047974**
BP-45	16.05		-21.6	-	-	0.34	94	124	434	3	8.93	**0.139862**
BP-46	16.2		-21.6	1.06	-4.55	0.14	88	161	432	1.6	11.84	**0.093659**

BP-47	16.35		-21.0	-	-	0.17	110	151	437	1.1	6.42	**0.076623**
BP-48	16.5		-21.3	-	-	0.12	117	130	428	0.45	3.77	**0.04531**
BP-49	16.8		-23.0	-	-	0.38	47	155	429	7.65	20.22	**0.122283**
BP-50	17.1		-21.7	2.06	-5.93	0.46	67	117	425	5.55	12.00	**0.099498**
BP-51	17.4		-21.0	-	-	0.44	59	92	428	3.8	8.62	**0.107517**
BP-52	17.7		-20.6	-	-	0.31	118	113	428	2.35	7.50	**0.081419**
BP-53	18		-20.6	-	-	0.70	145	74	435	3.95	5.67	**0.123863**
BP-54	18.3		-19.9	1.77	-5.85	0.80	182	71	429	3.85	4.78	**0.186379**
BP-55	18.6		-19.5	-	-	0.79	151	70	431	4.35	5.51	**0.163954**
BP-56	18.9		-19.7	-	-	0.42	65	104	427	3.25	7.66	**0.164975**
BP-57	19.2		-20.5	-	-	0.70	102	64	430	3.45	4.93	**0.10186**
BP-58	19.5		-20.3	1.80	-5.75	0.98	95	65	432	4.65	4.77	**0.15642**
BP-59	19.8		-21.1	-	-	0.43	46	83	425	2.05	4.72	**0.09901**
BP-60	20.1		-21.3	-	-	0.30	46	101	417	4.1	13.50	**0.158362**
BP-61	20.4		-21.8	-	-	0.51	43	82	424	4.75	9.34	**0.172351**
BP-62	20.7		-20.9	1.90	-6.59	0.42	70	106	430	5.45	13.11	**0.157193**
BP-63	21		-21.8	-	-	0.35	57	163	428	5.4	15.47	**0.177248**
BP-64	21.3		-20.7	-	-	0.57	85	96	429	5.3	9.22	**0.189439**
BP-65	21.6		-20.4	2.07	-6.17	0.51	77	112	429	5	9.82	**0.183012**
BP-66	21.9		-20.3	-	-	0.57	102	85	437	4.95	8.63	**0.191287**
BP-67	22.2		-20.2	-	-	0.64	114	70	432	4.85	7.60	**0.162801**
BP-68	22.5		-20.1	1.95	-4.89	0.38	126	80	433	2.75	7.16	**0.182375**
BP-69	22.8		-21.2	-	-	0.52	70	83	434	5.75	11.12	**0.194491**
BP-70	23.1		-20.7	1.94	-4.80	0.37	70	85	426	3.1	8.48	**0.140747**
BP-71	23.4		-20.2	1.82	-5.05	0.45	108	67	432	3.95	8.87	**0.179879**
BP-72	23.7	PETM Onset	-20.4	1.65	-4.64	0.38	137	88	435	3.25	8.53	**0.166265**
BP-73	24		-20.5	1.73	-4.47	0.40	128	70	432	2.5	6.25	**0.156418**
BP-74	24.3		-20.7	1.54	-4.59	0.21	163	130	430	2.35	11.27	**0.113914**
BP-75	24.5		-22.7	1.32	-4.60	0.14	72	149	431	2.55	17.77	**0.150531**
BP-76	25.5		-23.0	1.16	-5.36	0.20	47	209	415	4.5	22.92	**0.172731**
BP-77	27.5		-24.8	-	-	0.86	38	83	435	8.55	9.96	**0.121934**
BP-78	29.5	PETM Body and Recovery	-24.3	1.52	-5.21	0.13	53	226	406	4.2	31.24	**0.155039**
BP-79	31.5		-24.1	1.89	-5.72	0.25	25	212	410	6.3	25.17	**0.117836**
BP-80	33.5		-23.4	1.38	-6.26	0.14	68	203	406	2.1	15.49	**0.078096**
BP-81	35.5		-23.7	1.71	-5.93	0.16	56	210	402	5.2	31.64	**0.167796**
BP-82	37.5		-24.1	1.63	-5.99	0.11	38	212	428	3.5	32.70	**0.111814**
BP-83	39.5		-22.8	2.31	-6.29	0.11	48	332	408	2.9	27.02	**0.074397**
BP-84	41.5		-22.2	2.71	-7.08	0.23	57	178	424	3.2	13.68	**0.08884**
BP-85	43.5		-21.9	2.65	-5.37	0.22	64	240	413	4.3	19.19	**0.121913**
BP-86	45.5		-22.1	2.43	-4.75	0.21	73	240	434	3.05	14.43	**0.12093**
BP-87	47.5		-21.9	2.67	-5.08	0.22	61	238	432	3.85	17.64	**0.133255**
BP-88	49.5	Post PETM	-22.6	2.41	-4.45	0.06	86	287	434	1.15	19.39	**0.118026**
BP-89	51.5		-23.9	2.04	-4.66	0.03	105	376	405		0.00	**0**
BP-90	53.5		-23.3	2.32	-5.02	0.10	59	250	435	1.9	18.20	**0.135557**
BP-91	56.5		-23.7	-	-	0.13	85	236	414	2.15	16.24	**0.127294**
BP-92	59.5		-23.8	2.28	-4.49	0.04	100	248	428	0.35	8.60	**0.025739**

Table BS3 Summary of Baroch Nala section Bulk rock mineralogy and clay mineralogy and assemblages and its ratio.

Sample No	Thickness (m)	Biofacies	Quartz	Feldspath-K	Plagioclase-Na	Calcite	Dolomite	Pyrite	Goethite	Smectite	%IS	% Kaolinite	% Chlorite	Kaolinite/smectite	Kaolinite /Smecite+ palyg.	Kaolinite/(Illite+ Chlorit
BP-01	2		2.18	0.62	0.96	84.34	0.00	0.00	0.00	73.55	3.40	1.41	1.36	0.02	0.02	0.09
BP-02	4		4.93	0.75	1.11	82.89	0.00	0.00	0.00	79.25	2.36	1.46	1.16	0.02	0.02	0.13
BP-03	6		2.33	0.48	0.53	83.78	0.00	0.00	0.00	55.60	2.84	5.55	2.53	0.10	0.07	0.80
BP-04	6.3		2.34	0.58	0.90	67.34	0.00	0.00	3.37	50.42	4.22	4.33	1.69	0.09	0.06	0.26
BP-05	6.6		8.05	1.41	0.62	54.78	5.38	0.00	2.61	60.10	4.33	13.42	2.83	0.22	0.19	1.05
BP-06	6.9		2.00	1.86	0.38	62.21	1.16	1.46	3.86	64.19	2.63	10.94	4.11	0.17	0.15	0.88
BP-07	7.2		3.82	0.78	0.76	66.89	1.30	0.00	3.01	61.38	2.82	16.57	4.17	0.27	0.24	1.33
BP-08	7.5		2.14	1.35	0.39	61.78	0.00	0.00	3.72	70.3	2.25	10.81	2.53	0.15	0.14	1.16
BP-09	7.8		2.99	1.27	1.08	63.61	1.44	0.00	5.06	73.3	1.51	10.94	1.14	0.15	0.14	1.49
BP-10	8.1		6.20	0.82	0.68	63.90	2.42	0.00	5.58	60.7	3.41	21.31	1.23	0.35	0.32	2.31
BP-11	8.4		3.04	0.50	0.83	79.85	0.00	0.00	0.00	60.6	4.13	17.93	3.59	0.30	0.27	1.56
BP-12	8.7		4.19	2.06	1.53	56.23	1.80	0.00	3.35	44	2.97	32.16	6.55	0.74	0.63	2.28
BP-13	9		1.78	0.81	1.48	60.66	2.46	1.55	0.00	54	2.38	24.94	5.16	0.46	0.41	2.19
BP-14	9.3		1.75	0.45	0.55	77.09	0.00	0.00	0.00	43	2.57	23.50	14.00	0.55	0.46	1.05
BP-15	9.6		2.57	0.95	0.90	58.87	3.29	1.22	0.00	42	2.84	34.46	2.93	0.81	0.67	3.04
BP-16	9.9		2.05	1.73	1.39	47.23	9.30	1.56	0.00	47	3.55	30.77	6.81	0.65	0.56	2.79
BP-17	10.2		1.69	0.90	0.64	69.69	0.00	0.00	0.00	41	3.08	38.14	1.17	0.92	0.71	7.22
BP-18	10.5		3.63	1.31	0.81	59.89	4.20	1.29	2.00	32	1.34	45.01	4.24	1.39	1.10	3.52
BP-19	10.8		1.79	0.66	0.79	85.00	0.00	0.00	0.00	39	2.70	30.21	9.82	0.78	0.56	2.35
BP-20	11.1		10.08	0.97	0.98	49.89	1.74	2.05	1.88	30	2.60	45.30	3.70	1.53	1.20	3.15
BP-21	11.4		3.43	0.67	0.52	76.03	0.00	0.00	0.00	46.01	3.61	25.37	9.35	0.55	0.47	1.52
BP-22	11.7		4.18	0.67	0.62	77.76	0.00	0.00	0.00	47	2.35	30.05	4.55	0.64	0.54	2.43
BP-23	12	Pre PETM	14.70	0.98	0.66	58.75	0.00	0.00	0.00	44	1.06	39.72	2.73	0.91	0.81	3.82
BP-24	12.3		17.13	1.04	0.95	51.64	0.00	1.98	0.00	56	2.58	24.80	7.54	0.44	0.41	2.06
BP-25	12.6		6.72	1.02	0.79	59.05	0.95	1.81	0.00	63	2.59	19.50	3.84	0.31	0.29	2.05
BP-26	12.9		8.23	1.05	1.25	70.45	0.00	0.00	0.00	54	2.81	27.53	4.00	0.51	0.47	2.61
BP-27	13.2		1.85	0.86	0.76	70.79	0.00	2.02	0.00	48	2.41	24.64	3.83	0.51	0.41	1.86
BP-28	13.5		1.71	1.38	1.13	55.87	0.00	2.50	0.00	43	3.94	17.44	9.04	0.41	0.30	0.84
BP-29	13.65		3.44	2.11	2.48	46.76	1.02	0.00	3.80	36	3.10	13.06	2.51	0.37	0.19	0.94
BP-30	13.8		2.11	1.43	1.38	59.34	0.00	0.00	0.00	30	3.68	9.78	4.85	0.33	0.15	0.49
BP-31	13.95		1.98	0.82	0.74	85.05	0.00	0.00	0.00	31	4.71	4.50	2.33	0.14	0.07	0.20
BP-32	14.1		2.18	1.90	1.66	62.86	1.67	0.00	0.00	47	1.83	4.70	2.21	0.10	0.06	0.32
BP-33	14.25		2.26	1.05	0.87	71.40	0.00	0.00	0.00		-	-	-	-	-	-
BP-34	14.4		2.09	0.88	0.87	80.83	1.53	0.00	0.00	40	3.25	9.32	3.04	0.23	0.14	0.47
BP-35	14.55		2.16	1.58	1.06	75.09	0.00	0.00	0.00	58	2.60	3.65	4.21	0.06	0.05	0.22
BP-36	14.7		3.14	0.86	1.69	77.33	0.00	0.00	0.00	47	2.73	20.62	5.08	0.44	0.31	2.28
BP-37	14.85		9.11	1.82	3.88	34.72	1.21	1.89	3.92	56	2.63	22.76	2.24	0.41	0.35	2.43
BP-38	15		3.82	3.78	1.38	40.76	1.14	3.08	3.04	35	2.82	26.61	5.68	0.75	0.52	1.35
BP-39	15.15		2.19	1.15	1.47	62.14	0.00	1.63	0.00	47	2.15	28.63	3.40	0.60	0.48	3.06
BP-40	15.3		1.60	3.33	1.32	47.73	0.00	2.46	2.81	33	2.84	25.80	17.87	0.79	0.59	0.93
BP-41	15.45		2.06	0.77	0.92	74.10	0.00	0.00	0.00	56	1.74	26.23	5.06	0.46	0.40	3.72
BP-42	15.6		2.14	1.35	1.21	57.89	10.09	1.17	0.00	51	1.91	28.17	6.27	0.55	0.47	2.67
BP-43	15.75		2.15	1.25	0.85	80.34	0.00	0.00	0.00	53	2.35	26.66	6.98	0.50	0.46	2.12
BP-44	15.9		1.73	0.70	1.42	74.70	0.00	0.00	0.00	33	3.84	32.98	5.24	1.00	0.70	2.03
BP-45	16.05		2.09	0.83	0.80	72.67	0.00	0.00	0.00	40	2.99	33.72	3.97	0.84	0.67	2.65
BP-46	16.2	POE	1.98	0.59	0.30	70.76	8.25	0.00	0.00	35	2.16	38.94	5.37	1.09	0.88	2.68
BP-47	16.35		1.79	1.13	0.82	80.12	0.00	0.00	0.00	44	3.10	27.88	5.07	0.64	0.50	2.14
BP-48	16.5		1.90	0.57	0.44	86.09	0.00	0.00	0.00	29	4.11	24.52	3.62	0.84	0.48	1.20
BP-49	16.8		15.21	2.30	1.47	7.67	0.86	3.19	4.93	29	5.68	53.13	4.23	1.81	1.60	6.65

BP-50	17.1		12.89	2.23	1.42	17.56	1.27	2.95	3.99	40	1.06	41.70	6.06	1.03	0.92	3.47
BP-51	17.4		2.50	1.80	1.52	48.64	7.05	0.00	2.74	48	1.14	30.71	8.30	0.63	0.59	1.91
BP-52	17.7		2.17	1.28	0.58	64.09	2.56	0.00	0.00	37	2.01	35.16	7.11	0.94	0.76	2.09
BP-53	18		2.14	2.11	1.40	51.75	3.82	2.36	2.64	42	4.12	33.44	7.41	0.80	0.68	2.49
BP-54	18.3		1.85	1.14	0.99	69.34	0.00	3.22	0.00	46	2.36	33.30	5.72	0.73	0.63	2.86
BP-55	18.6		2.58	0.85	1.27	60.18	1.05	2.85	2.50	60	2.25	18.28	12.59	0.40	0.32	0.83
BP-56	18.9		4.54	1.86	0.66	70.09	0.00	1.78	0.00	51	2.82	24.34	4.72	0.41	0.39	2.47
BP-57	19.2		2.98	0.90	0.69	56.22	0.00	1.81	2.61	49	1.99	36.63	3.25	0.72	0.69	4.61
BP-58	19.5		2.54	0.84	0.93	62.36	0.00	3.24	0.00	42	3.11	37.33	2.28	0.76	0.72	4.97
BP-59	19.8		8.28	4.17	2.56	17.11	43.76	2.07	0.00	48	2.32	34.86	9.05	0.83	0.74	2.23
BP-60	20.1		2.59	1.26	1.14	53.39	10.30	1.08	2.16	50	2.20	33.49	5.78	0.69	0.64	2.82
BP-61	20.4		9.89	1.38	2.90	46.94	5.35	1.59	2.30	56	2.12	31.87	5.65	0.64	0.58	2.88
BP-62	20.7		12.67	2.23	3.75	35.98	2.45	3.10	3.51	58	3.54	14.63	4.94	0.26	0.22	0.99
BP-63	21		20.14	2.71	1.93	38.09	2.03	1.90	2.09	48	2.29	19.47	4.46	0.34	0.29	1.64
BP-64	21.3		3.99	1.96	1.73	53.76	3.78	3.03	3.40	62	3.43	27.72	4.86	0.58	0.49	2.18
BP-65	21.6		5.66	3.79	1.43	50.78	2.41	2.25	3.62	72.75	2.03	10.62	2.40	0.17	0.14	0.99
BP-66	21.9		2.68	1.26	0.79	60.65	0.00	2.92	4.43	75	2.11	7.89	3.46	0.11	0.10	0.76
BP-67	22.2		4.03	2.96	1.62	41.94	12.67	2.58	2.96	79	2.26	5.95	2.75	0.08	0.07	0.63
BP-68	22.5		5.22	0.66	0.64	63.74	11.63	1.13	0.00	79	2.13	5.08	2.95	0.06	0.06	0.60
BP-69	22.8		4.55	3.96	1.64	55.09	1.63	2.71	0.00	70	2.18	4.23	3.24	0.05	0.05	0.46
BP-70	23.1		2.70	0.56	0.72	54.01	17.45	1.42	0.00	71	2.07	11.20	4.42	0.16	0.15	1.08
BP-71	23.4		3.05	2.02	1.31	67.92	1.18	1.37	0.00	73	2.94	9.02	4.12	0.13	0.12	0.80
BP-72	23.7	PETM Onset	2.46	2.22	0.86	71.98	1.46	0.00	0.00	77	2.86	10.33	3.71	0.14	0.13	1.09
BP-73	24		2.07	1.58	1.22	61.55	14.00	1.33	0.00	69	3.09	6.42	3.82	0.08	0.08	0.65
BP-74	24.3		2.01	2.00	1.29	60.84	12.92	0.00	0.00	72	3.24	13.96	4.48	0.20	0.19	1.45
BP-75	24.5		2.46	1.10	1.17	77.63	0.00	0.00	0.00	44	1.62	17.15	2.50	0.24	0.23	2.96
BP-76	25.5		3.01	1.74	1.43	61.07	0.00	0.00	5.80	33	3.15	37.60	8.68	0.85	0.80	3.07
BP-77	27.5		7.49	2.80	1.45	5.21	0.00	2.98	7.26	28	1.99	53.45	9.97	1.93	1.73	3.91
BP-78	29.5	PETM Body and Recovery	4.67	1.32	0.74	52.02	8.01	1.55	2.56	19	2.21	67.68	5.73	3.60	3.11	8.09
BP-79	31.5		11.23	3.63	1.84	20.59	1.00	2.18	4.09	21	2.58	59.60	8.23	2.84	2.38	4.67
BP-80	33.5		2.49	1.18	1.68	60.67	1.39	0.00	3.77	22	2.37	60.02	9.36	2.71	2.35	4.98
BP-81	35.5		3.93	2.35	1.50	58.65	1.10	0.00	0.00	26	2.07	56.32	7.74	2.13	1.89	4.78
BP-82	37.5		4.34	1.80	1.05	60.34	0.00	0.00	0.00	32	1.36	52.65	7.15	1.64	1.49	4.98
BP-83	39.5		4.02	1.98	2.33	49.78	1.30	0.00	0.00	46	2.93	35.20	3.97	0.76	0.68	3.61
BP-84	41.5		2.48	1.44	1.02	49.87	1.84	2.00	3.87	41	7.07	30.12	7.89	0.73	0.63	2.05
BP-85	43.5		2.50	1.45	2.57	54.65	0.99	2.40	0.00	66	2.12	20.56	3.98	0.31	0.29	2.81
BP-86	45.5		2.07	1.12	4.10	61.72	1.44	0.00	2.72	75	2.03	13.71	3.83	0.18	0.18	2.17
BP-87	47.5		2.81	0.91	0.92	59.67	1.11	1.61	2.87	71	2.74	17.04	3.01	0.24	0.23	2.75
BP-88	49.5	Post PETM	2.27	1.44	1.98	82.00	1.68	0.00	0.00	74	3.22	11.21	3.15	0.15	0.14	1.56
BP-89	51.5		2.08	0.80	1.25	84.32	2.88	0.00	0.00	65	5.63	11.09	5.96	0.17	0.15	0.97
BP-90	53.5		2.33	1.35	1.05	76.09	4.23	0.00	0.00	62	2.69	24.94	4.83	0.40	0.38	3.31
BP-91	56.5		2.18	1.22	0.94	73.93	4.36	0.00	0.00	61	1.56	26.81	5.52	0.44	0.42	3.30
BP-92	59.5		2.12	1.07	1.95	76.56	2.99	0.00	0.00	80	1.63	11.82	2.85	0.15	0.15	2.32

Table NS1 Nammal Gorge section interval-wise information based on average geochemical and biological data.

Events		Formation	Thickness (mbs)	Lithology	Biofacies	LBF species	Bulk Mineralogy Avg % (min-max)				Clay Mineralogy Avg % (min-max)					$^{13}C_{org}$ (max-min)	$^{13}C_{carb}$ (max-min)	$^{18}O_{Carb}$ (max-min)	Rock-Eval Avg % (min-max)				Volcanic Proxy Avg % (min-max)	
							Phy %	Qtz %	Cal %	Dol %	Sm %	Kao %	Palyg %.	Illite %	I/S mixed %	(‰ VPDB)	(‰ VPDB)	(‰ VPDB)	TOC (wt%)	HI (mg HC/gTOC	OI (mg CO_2/gTOC	Tmax (°C)	Hg (ppb)	Hg/TOC (ppb/wt%)
pre-PETM		Patala Formation	0 - 22.7	Calcareous marls , Limestone interbedded with shales	*BF1*	*Daviesina praegarumnensis, Daviesina cf. intermedia, Kathina aquitanica, Orbitosiphon cf. punjabensis, Daviesina langhami Idalina sinjarica, Lockhartia haimei, Lockhartia cf. roeae, Lockhatia retiata, Rotalia implumis, Lockhartia conditi, Elazigina lenticula Dictyoconoides cf. flemingi, Lakadongia tibetica*	28 (7-56)	6 (1-22)	59 (24-83)	1.1 (0.3-4.4)	47 (20-77)	4 (0.6 – 18)	25 (7 – 50)	17 (6 – 31)	4 (2 – 8)	-20.0 (- 18.2 to -22.7)	1.65 (2.3 to 1.3)	-5.7 (-4.5 to -6.4)	0.4 (0.07 – 1.1)	126 (70 – 196)	123 (42-249)	434 (420 – 449)	4.7 (0.1 to 11.5)	11 (7 to 18)
Pre Onset Excursion	Onset		22.7 – 24.7	Dark shales interbedded with dolomite and marl layers	*BF2*	*L.conditi,*	41 (14 – 68)	6 (2 – 20)	32 (2 – 70)	12 (0.7 - 62)	45 (7 – 76)	26 (9 – 43)	10 (4 – 23)	10 (5 – 17)	2.5 (1.5 - 4.8)	-20.6 (-18.8 to -23.6)	1.4 (2.4 to 0.7)	-5.0 (-2.9 to -7.0)	0.4 (0.1 to 1.3)	90 (23 – 229)	138 (56 – 196)	439 (423 – 448)	6 (2 - 15)	14 (5 – 20)
	Recovery		24.7 – 27.1	Calcareous marls		*Elazigina harabekayisensis, E. lenticula, Lockhartia sp. Kathina mayor, L. haimei, Rotalia cf. newboldi, L. conditi, Miscellanea miscella*	25 (11 – 45)	5 (2 – 10)	62 (38 – 82)	0.7 (0.3 – 1.2)	69 (58 – 79)	7 (0.7 – 16.6)	10 (5 – 14)	7.5 (5.6 - 9.5)	3 (2 – 5)	-19.9 (-19.4 to -21.6)	1.5 (1.7 to 1.0)	-5.6 (-4.2 to -6.2)	0.2 (0.07 to 0.4)	87 (75 – 139)	186 (119 – 259)	440 (426 – 446)	4.6 (0.5 – 8.9)	19 (5 – 36)
PETM Onset			27.1 – 29.8	Calcareous marls , Black shale	*BF3*	*Kathina selveri, E. lenticula, L. conditi, L. haimei, Miscellanea dukhani, Ranikothalia sindensis, R. cf. newboldi. Idalina sp. Assilina ranikoti, M. miscella, K. mayor, Pachycolumella acuta Daviesina garumnensis, L. retiata, D. langhami, E. harabekayisensis ,Lockhartia roae, Orbitoclypeus sp. Valvulina triangularis, Coskinon rajkae*	19 (9 – 38)	2.1 (1.3 – 2.4)	72 (55 – 80)	0.8 (0.3 – 1.9)	59 (53 – 76)	24 (12 – 30)	3.3 (2.4 – 4.8)	5 (3 – 11)	2.8 (1.3 – 5.8)	-22.2 (-21.0 to – 24.8)	1.44 (1.5 – 1.1)	-4.8 (-4.2 to -5.5)	0.15 (0.05 to 0.3)	102 (22 – 293)	144 (102 – 245)	430 (427 – 443)	2.4 (0.8 – 9.3)	15 (8 – 29)
PETM Body + Recovery			29.8 - 36.6	Calcareous marls and Limestone interbedded with sandy layer and dark shale	*BF4*	*Alveolina cf. vredenburgi, Assilina dandotica M. miscella, L.haimei A. ranikotiR. cf. newboldi E. lenticulaRanikothalia nuttalli*	20 (8 –47)	17 (1 – 78)	53 (5 – 77)	1.6 (0.4 – 3.7)	35 (23 – 58)	45 (26 – 59)	3.5 (2.6 – 4.2)	4 (3.2 – 6.3)	2.9 (2.3 - 4.3)	-22.3 (-20.7 to 24.0)	1.4 (1.5 – 1.4)	-4.8 (-4.3 to -6.0)	0.16 (0.05 – 0.5)	49 (18 – 81)	315 (131 – 482)	444 (424 – 456)	4.4 (1.4 – 9.4)	35 (16 – 73)
post-PETM			36.6-38	Limestone	*BF5*	*Assilina dandotica*	11	2	78	2.1	25	45	7	7	4.34	-23.9	1.5	-3.9	0.03	73	536	445	1.6	*57.3*

Table NS2 Summary of Nammal Gorge section geochemical proxies from the base of the section including $\delta^{13}C_{org}$, $\delta^{13}C_{carb,}$ and $\delta^{18}O_{carb}$, Rock eval and Mercury data with biofacies According to different successive stages of the Paleocene-Eocene transition.

Sample No	Thickness	Biofacies	$^{13}C_{(org)}$	$^{13}C_{(Bulk)}$	$^{18}O_{(Bulk)}$	TOC	(HI)	(OI)	Tmax	Hg(ppb)	Hg/TOC
NP-01	1		-21.6	2.37	-6.47	0.57	70	90	427	8.05	14.03
NP-02	2		-22.7			0.49	79	87	427	7.7	15.62
NP-03	2.5		-21.6			0.06	87	170	420	0.5	8.68
NP-04	3.5		-19.7	1.49	-6.36	0.75	143	59	432	8.4	11.22
NP-05	4.5		-19.5			0.06	166	146	426	0.7	11.57
NP-06	5.5		-19.7			0.88	195	43	429	7.9	8.99
NP-07	6.5		-19.6			0.08	196	120	432	1.1	13.43
NP-08	7.5		-19.8	0.95	-6.38	1.18	184	42	426	11.55	9.77
NP-09	8.5		-20.5			0.37	81	95	422	6.6	17.68
NP-10	9.5		-20.2			0.07	83	163	427	0.1	1.38
NP-11	10.5		-20.5	2.28	-6.64	0.56	93	128	442	9.2	16.39
NP-12	11.5		-21.0			0.14	144	84	431	1.05	7.50
NP-13	12.5		-20.3			0.49	110	124	442	5.7	11.54
NP-14	13.5		-18.6			0.63	114	104	442	5.65	9.01
NP-15	14.5		-19.6	1.58	-4.96	0.14	160	121	428	0.8	5.77
NP-16	15.5		-19.2			0.64	131	106	443	6.95	10.93
NP-17	16.5		-18.3			0.15	183	139	434	1.05	7.05
NP-18	17.5		-19.5			0.22	130	146	443	3.05	14.01
NP-19	18.5		-20.4	1.30	-5.00	0.09	120	214	438	0.65	7.03
NP-20	19.5		-18.9			0.38	117	128	446	3.85	10.12
NP-21	20.5		-18.2			0.49	96	143	449	6.7	13.58
NP-22	21.5		-19.2			0.34	93	165	443	5.6	16.59
NP-23	22.5		-20.5	1.58	-4.56	0.08	133	249	442	1.2	15.80
NP-24	22.7	Pre-PETM	-19.8			1.06	107	88	439	10.05	9.44
NP-25	22.9		-19.4			0.39	229	56	423	2	5.15
NP-26	23.1		-18.8	2.42	-7.06	0.91	114	89	440	6.85	7.54
NP-27	23.3		-19.1			1.35	106	103	441	15.45	11.43
NP-28	23.5		-20.8	0.71	-2.91	0.11	57	195	448	1.2	11.17
NP-29	23.7		-20.8			0.08	112	196	442	1.3	15.93
NP-30	23.9		-20.8			0.57	65	136	437	12.6	21.99
NP-31	24.1		-21.0	1.44	-5.75	0.36	58	166	444	6.7	18.42
NP-32	24.3		-21.2			0.35	52	191	444	8.35	24.09
NP-33	24.5		-21.0	1.19	-4.38	0.15	86	104	428	1.05	6.90
NP-34	24.7		-23.6			0.27	23	141	440	5.4	20.20
NP-35	24.9		-20.2	1.69	-5.61	0.42	75	138	438	4.85	11.62
NP-36	25.1		-19.7	1.75	-6.08	0.25	62	259	444	8.9	36.14
NP-37	25.3		-20.1			0.35	64	181	443	7.6	21.92
NP-38	25.5		-19.5	1.75	-6.29	0.37	61	170	445	5.95	16.28
NP-39	25.7		-19.9	1.58	-4.70	0.15	84	214	437	2.85	19.65
NP-40	25.9		-19.8			0.12	90	258	441	3.9	31.33
NP-41	26.1		-19.4	1.63	-5.97	0.29	91	160	446	4.95	17.12
NP-42	26.3		-18.6	1.69	-6.02	0.45	90	122	444	5.95	13.11
NP-43	26.5		-19.4	1.61	-6.05	0.19	103	236	444	5.05	26.92
NP-44	26.8		-20.8			0.11	139	119	426	0.55	4.99
NP-45	27.1	POE	-21.6	1.02	-4.26	0.07	97	193	430	0.55	7.50

NP-46	27.4	PETM onset	-22.6	1.15	-4.70	0.15	91	135	429	1.15	7.93
NP-47	27.7		-23.1			0.10	94	161	432	0.85	8.75
NP-48	28		-21.8	1.55	-4.38	0.15	86	121	430	1.35	8.80
NP-49	28.3		-21.0	1.51	-4.80	0.05	293	245	430	0.95	18.28
NP-50	28.6		-21.0			0.19	90	102	427	1.7	8.84
NP-51	28.9		-22.0	1.36	-5.32	0.16	88	115	427	2.45	15.13
NP-52	29.2		-21.2	1.55	-4.20	0.13	83	118	428	1.95	14.57
NP-53	29.5		-22.8	1.50	-5.59	0.11	74	144	428	2.45	22.35
NP-54	29.8		-24.8			0.32	22	152	443	9.3	29.36
NP-55	30.1	PETM body and Recovery	-23.1	1.43	-4.77	0.14	49	137	424	2.35	16.30
NP-56	30.4		-24.0			0.36	23	166	438	8.25	23.11
NP-57	30.7		-21.3	1.43	-6.02	0.08	67	353	449	3.6	47.60
NP-58A	31		-21.8	1.46	-4.75	0.05	59	306	437	1.45	28.04
NP-59	32.6		-21.9	1.42	-4.53	0.05	81	477	455	1.8	36.06
NP-60	33.6		-24.5			0.50	18	131	441	9.4	18.86
NP-61	34.6		-20.7			0.11	36	461	456	8.2	73.08
NP-62	35.6		-21.8	1.39	-4.34	0.06	53	482	448	2.8	48.42
NP-63	36.6		-21.2	1.50	-4.45	0.08	53	324	447	1.8	23.39
NP-64	37.6	Post PETM	-23.9	1.55	-3.90	0.03	73	536	445	1.6	57.37

Table NS3 Summary of Nammal Gorge section Bulk rock mineralogy and clay mineralogy and assemblages and its ratio.

Sample No	Thickness (m)	Biofacies	Phyllosilicates	Quartz	Feldspath-K	Plagioclase-Na	Calcite	Dolomite	Pyrite	Goethite	DI (Detrital Index)	% Smectite	% palygorskite	% Illite	%IS	% Kaolinite	% Chlorite	Kao/sm	Kao /Sm+ palyg.	Kaol/I+Chl
NP-01	1	Pre-PETM	42.7	22.7	2.6	1.1	23.9	0.9	1.2	2.7	2.9	71.2	7.3	10.4	5.0	1.6	6.0	0.0	0.0	0.1
NP-02	2		34.2	17.7	1.5	1.1	40.0	1.1	0.0	2.3	1.4	76.8	8.4	8.3	2.5	2.0	2.2	0.0	0.0	0.2
NP-03	2.5		7.1	2.4	0.5	1.3	83.1	0.9	0.0	1.4	0.1	61.8	9.4	15.3	5.0	3.6	4.3	0.1	0.1	0.2
NP-04	3.5		28.3	15.4	1.5	1.7	45.3	2.6	0.0	2.1	1.0	61.8	9.6	17.9	5.4	2.7	4.8	0.0	0.0	0.1
NP-05	4.5		12.6	2.3	0.8	0.9	78.5	1.3	0.0	2.0	0.2	63.1	12.0	13.9	5.5	2.4	4.4	0.0	0.0	0.1
NP-06	5.5		32.9	9.2	0.6	0.9	47.5	4.5	0.0	3.4	0.9	71.2	9.2	12.7	2.6	1.9	3.4	0.0	0.0	0.1
NP-07	6.5		12.0	2.4	0.7	1.8	80.1	0.3	0.0	1.2	0.2	61.0	13.5	16.3	3.1	3.1	4.0	0.1	0.0	0.2
NP-08	7.5		50.8	11.7	1.7	1.6	28.0	0.8	0.0	3.5	2.4	27.6	21.2	30.6	7.6	7.3	7.6	0.3	0.1	0.2
NP-09	8.5		47.9	14.8	1.8	1.9	26.7	1.0	2.2	2.7	2.5	48.9	18.5	17.6	4.3	6.0	5.5	0.1	0.1	0.3
NP-10	9.5		11.9	2.3	1.1	1.2	80.3	0.6	0.0	1.7	0.2	44.6	23.6	20.1	3.5	5.4	3.0	0.1	0.1	0.2
NP-11	10.5		35.8	1.8	2.6	2.0	52.6	0.9	0.0	3.2	0.8	38.9	33.1	22.7	2.6	1.4	2.9	0.0	0.0	0.1
NP-12	11.5		10.7	2.1	0.9	0.5	81.9	0.5	0.0	1.6	0.2	36.3	33.2	25.2	2.5	1.3	1.8	0.0	0.0	0.1
NP-13	12.5		28.6	1.8	1.2	1.4	61.1	1.2	0.0	2.7	0.5	37.1	29.5	29.0	2.1	1.0	1.1	0.0	0.0	0.0
NP-14	13.5		35.5	1.8	1.8	1.7	54.3	0.7	0.0	3.2	0.8	45.4	41.7	6.5	3.7	0.6	3.5	0.0	0.0	0.1
NP-15	14.5		10.7	2.6	0.6	1.3	80.6	0.5	0.0	1.8	0.2	27.2	37.6	25.7	5.4	2.0	2.9	0.1	0.0	0.1
NP-16	15.5		37.6	1.9	1.9	1.8	49.7	3.5	0.0	3.0	0.9	37.5	49.6	5.5	5.3	1.2	0.6	0.0	0.0	0.2
NP-17	16.5		12.5	2.5	0.9	0.7	79.5	0.6	0.0	2.4	0.2	52.8	27.2	13.0	4.0	1.4	3.0	0.0	0.0	0.1
NP-18	17.5		14.3	1.8	0.7	1.6	77.1	0.6	0.0	2.4	0.2	58.8	23.0	11.1	4.1	1.4	2.0	0.0	0.0	0.1
NP-19	18.5		14.1	2.0	1.0	0.9	76.9	0.5	1.5	2.3	0.2	38.4	23.7	18.6	3.7	11.7	3.3	0.3	0.2	0.5
NP-20	19.5		29.1	1.8	0.9	0.9	61.5	0.6	0.0	2.9	0.5	44.7	24.2	16.5	4.3	7.6	1.9	0.2	0.1	0.4
NP-21	20.5		40.8	1.4	1.8	1.7	47.5	1.1	0.0	3.1	1.0	41.9	32.5	18.5	2.1	2.9	1.9	0.1	0.0	0.1

NP-22	21.5		45.1	2.0	2.2	3.5	40.2	1.2	0.0	3.6	1.3	36.8	39.8	16.5	3.8	1.6	2.5	0.0	0.0	0.1
NP-23	22.5		9.7	4.7	0.9	0.7	80.3	0.4	0.0	1.6	0.2	19.6	48.2	24.3	4.2	2.1	3.0	0.1	0.0	0.1
NP-24	22.7		55.6	3.8	2.4	4.4	28.6	0.9	0.0	3.4	2.3	22.0	29.8	22.2	2.7	18.0	3.8	0.8	0.3	0.7
NP-25	22.9		22.0	2.0	1.2	0.9	70.2	0.8	0.0	1.6	0.4	48.7	20.7	10.7	2.5	14.2	2.0	0.3	0.2	1.0
NP-26	23.1		32.9	3.6	1.4	1.4	54.0	0.7	0.0	3.1	0.7	38.7	17.0	13.8	2.7	23.4	2.7	0.6	0.4	1.3
NP-27	23.3		67.6	3.7	4.7	4.2	11.3	1.0	0.0	4.6	7.1	7.5	23.0	16.8	2.3	42.9	4.5	5.7	1.4	1.8
NP-28	23.5		13.6	2.1	0.7	2.2	11.5	62.5	3.1	1.2	1.6	60.0	5.1	6.6	2.5	19.9	3.9	0.3	0.3	1.6
NP-29	23.7		15.6	2.3	0.9	2.1	26.8	47.2	1.9	2.0	0.8	76.5	4.2	6.8	1.7	8.5	1.8	0.1	0.1	0.9
NP-30	23.9		70.5	6.0	1.6	1.3	9.2	3.6	0.0	5.1	8.6	59.0	8.8	9.9	1.6	15.0	4.5	0.3	0.2	1.0
NP-31	24.1		40.0	5.1	1.7	1.5	47.2	0.9	0.0	3.6	1.0	49.2	4.5	5.1	1.8	34.8	3.1	0.7	0.6	3.6
NP-32	24.3		29.6	6.0	1.2	1.2	58.7	0.7	0.0	2.1	0.6	36.2	6.4	6.0	2.5	39.6	9.3	1.1	0.9	2.6
NP-33	24.5		50.2	9.2	2.6	2.3	28.4	1.4	0.0	4.6	2.3	47.5	4.1	9.4	4.8	26.1	6.4	0.5	0.5	1.5
NP-34	24.7		63.9	19.8	3.7	3.2	2.5	1.4	0.0	3.7	37.0	29.6	8.4	12.6	3.2	38.6	5.8	1.3	1.0	1.9
NP-35	24.9		45.1	7.9	2.3	2.0	37.5	1.1	0.0	3.4	1.5	64.8	7.3	6.3	2.3	15.8	2.9	0.2	0.2	1.6
NP-36	25.1		36.2	6.9	1.8	1.3	47.5	0.6	0.0	4.0	1.0	57.9	8.3	8.8	4.0	16.7	2.9	0.3	0.3	1.3
NP-37	25.3		37.6	9.7	2.7	2.7	41.5	1.2	0.0	2.3	1.3	62.7	11.4	9.1	4.1	7.5	5.2	0.1	0.1	0.5
NP-38	25.5		35.8	6.9	2.6	2.5	46.3	1.0	0.0	2.7	1.0	62.6	13.5	7.4	2.3	10.6	3.5	0.2	0.1	1.0
NP-39	25.7		15.0	6.2	0.8	0.7	72.5	0.4	0.0	1.5	0.3	65.8	10.2	9.5	2.8	7.2	3.8	0.1	0.1	0.5
NP-40	25.9		20.6	3.8	1.0	1.3	70.1	0.5	0.0	1.7	0.4	79.0	8.7	6.6	3.0	1.3	2.0	0.0	0.0	0.2
NP-41	26.1		17.0	3.3	1.5	0.4	69.8	0.5	0.0	4.8	0.3	75.0	13.6	6.6	2.1	0.9	2.5	0.0	0.0	0.1
NP-42	26.3		20.7	4.4	1.0	0.6	68.2	0.8	0.0	2.1	0.4	75.9	12.8	5.9	2.8	1.2	2.4	0.0	0.0	0.2
NP-43	26.5											76.1	10.5	8.7	2.8	0.7	1.2	0.0	0.0	0.1
NP-44	26.8	POE	10.9	2.2	0.7	0.5	80.5	0.5	0.0	1.8	0.2	60.7	5.6	8.7	5.0	10.7	9.2	0.2	0.2	0.6
NP-45	27.1		11.8	2.3	0.8	0.9	81.7	0.5	0.0	1.7	0.2	78.6	4.8	5.7	2.9	4.3	3.7	0.1	0.1	0.5
NP-46	27.4		14.1	2.0	0.4	0.5	77.4	0.7	0.0	2.9	0.2	75.8	2.4	4.0	1.8	12.5	2.7	0.2	0.2	1.7
NP-47	27.7		34.8	1.8	2.2	2.0	55.1	0.4	0.0	2.8	0.7	56.1	3.8	3.9	5.9	23.9	4.2	0.4	0.4	2.3
NP-48	28		12.6	2.2	0.7	0.7	79.6	0.7	0.0	2.0	0.2	55.3	4.0	5.8	3.1	26.2	4.2	0.5	0.4	2.3
NP-49	28.3		9.1	2.4	0.8	0.7	84.3	0.9	0.0	1.4	0.2	60.4	4.9	7.4	4.1	16.6	5.2	0.3	0.3	1.2
NP-50	28.6		20.1	2.4	1.1	0.8	71.5	1.0	0.0	2.3	0.3	56.4	3.4	4.4	2.3	29.4	2.9	0.5	0.5	3.5
NP-51	28.9		21.9	2.4	0.9	0.4	71.6	0.6	0.0	1.1	0.4	59.3	2.5	2.9	2.8	27.0	3.9	0.5	0.4	3.2
NP-52	29.2		20.1	2.2	1.1	0.9	72.1	1.0	0.0	1.8	0.3	55.6	2.8	3.6	1.3	30.2	5.0	0.5	0.5	3.0
NP-53	29.5		18.1	2.2	0.9	0.6	76.0	0.6	0.0	0.7	0.3	59.9	3.0	3.6	1.7	26.5	3.8	0.4	0.4	3.0
NP-54	29.8	PETM onset	23.1	1.3	2.8	5.9	58.2	1.9	0.0	5.4	0.6	53.0	3.0	11.2	2.9	25.1	3.4	0.5	0.4	1.6
NP-55	30.1																			
	15.9		1.1	1.1	70.1	1.5	0.0	2.1	0.4	43.6	3.3	3.6	2.3	36.1	7.8	0.8	0.8	2.4		
NP-56	30.4		26.8	1.0	2.7	9.5	50.1	2.8	0.0	6.0	0.8	28.9	2.6	3.8	2.8	52.3	9.0	1.8	1.7	3.9
NP-57	30.7		20.4	2.5	0.9	1.2	69.3	0.5	0.0	3.9	0.4	33.2	3.2	3.3	2.8	46.4	8.1	1.4	1.3	3.2
NP-58A	31											37.0	3.7	3.4	3.4	43.1	7.2	1.2	1.1	3.4
NP-59	32.6		14.7	2.0	0.5	1.0	77.1	1.1	0.0	2.9	0.2	36.9	3.9	3.3	3.5	43.6	7.4	1.2	1.1	3.6
NP-60	33.6		46.9	38.7	1.8	1.0	4.2	0.7	0.0	3.8	20.9	57.8	4.3	5.3	2.3	26.1	3.1	0.5	0.4	2.7
NP-61	34.6		8.3	77.5	2.2	0.8	5.0	0.5	0.0	2.0	17.9	22.9	2.9	3.4	2.0	58.5	9.6	2.6	2.3	4.3
NP-62	35.6	PETM body and Recovery	10.9	4.3	0.9	0.5	75.2	2.4	0.0	5.4	0.2	22.7	3.7	4.3	3.3	56.7	7.1	2.5	2.1	4.2
NP-63	36.6		13.2	2.6	1.6	0.9	71.2	3.7	0.0	4.3	0.3	32.4	4.2	6.4	4.3	41.9	7.7	1.3	1.1	2.4
NP-64	37.6	Post PETM	11.2	2.0	0.7	1.0	78.2	2.2	0.0	3.7	0.2	25.4	7.4	7.7	4.3	45.3	8.1	1.8	1.4	2.6

Table GS1 Ghumawan section interval-wise information based on average geochemical and biological data.

Events	Formation	Intervals	Thickness (mbs)	Lithology	Shallow benthic Zoness	LBF species	Avg % (min-max)				(max-min)	Avg % (min-max)				Proxy Avg % (min-max)	
							Phy %	Qtz %	Cal %	Dol %	(‰ VPDB)	TOC (wt%)	HI (mg HC/gTOC	OI (mg CO_2/gTOC	Tmax (°C)	Hg (ppb)	Hg/TOC (ppb/wt%)
Pre PETM	Lockhart	Base of the	0-4	Limestone	SBZ3	*Miscellanea juliettae, Miscellanites sp., Lockhartia prehaimei, Lockhartia retiata, Elazigina lenticula, Kathina selveri, .*	-	-	-	-	-	-	-	-	-	-	-
?	Patala Formation or Lockhart Limestone?	Marly Interval	04 - 26	Calcareous marls and Limestone	?	*Ranikothalia sp? Orbitosiphon sp.?*	24.7 (8 to 54.5)	16 (3.5 to 39.2)	56 (2.5 to 86)	0.06 (0 to 1)	-23.3 (-20.3to -25.7)	0.1 (0.04 to 0.22)	31 (6 to 96)	480 (203 to 1208)	421 (340 to 608)	14.2 (0.8 to 41.3)	136.7 (90.4 to 190)
pre-PETM	Lockhart	Lower Limestone	26-70	Limestone	SBZ3	*Coskinon rajkae, Elazigina lenticula, Lakadongia primitiva, Lockhartia haimei, L. roeae, Miscellanea yvettae, M. juliettae, and Ranikothalia sp.*	5.2 (1.8 to 8.6)	1.6 (0.9 to 4.3)	91.5 (85 to 95)	0.07 (0 to 1.3)	-	0.5 (0.01 to 0.1)	123 (26 to 332)	540 (258 to 1185)	424 (346 to 489)	1.5 (0.6 to 3.5)	-
	From 70 to 90 m (Covered interval)																
pre-PETM	Lockhart	Upper Limestone	90 – 107m	Limestone	SBZ3/4	*Coskinon sp., Daviesina sp., Idalina sp., Lakadongia sp., Lockhartia conditi, L. haimei, L. roeae, L. tipperi, Miscellanea yvettae, M. juliettae, M. cf. miscella, Orbitosiphon sp., Operculina sp., Ranikothalia sahnii, and possibly Assilina*	-	-	-	-	-	-	-	-	-	-	-

Sample No	Thickness (m)	Phase	$^{13}C_{(org)}$	TOC	(HI)	(OI)	Tmax	Hg	Hg/TOC	Phyllosilicates	Quartz	Calcite	Dolomite	Goethite	DI (Detrital Index)
Sp-01	0.5	Pre-PETM	-21.0	0.21	10	231	587	27.1	129.6	27.12	16.50	54.90	0.00	0.00	0.79
Sp-02	1.0		-21.5	0.11	9	203	493	17.9	163.1	25.31	13.41	58.98	0.00	0.00	0.66
Sp-03	1.5		-22.3	0.22	9	222	512	41.3	190.1	54.56	39.28	0.00	0.89	3.38	
Sp-04	2.0		-20.3	0.14	15	464	469			38.05	24.89	32.12	0.00	3.23	1.96
Sp-05	3.0		-24.6	0.21	15	285	608	18.6	90.4	39.85	30.09	27.94	0.00	1.85	2.50
Sp-06	3.5		-24.2	0.15	6	259	494	12.5	80.9	32.92	17.24	47.34	0.00	0.00	1.06
Sp-07	4.5		-23.6	0.17	17	324	340	24.4	141.6	52.11	30.45	13.70	0.00	2.67	6.03
Sp-08	5.0		-25.7	0.05	60	1208	399	17.3	345.8	11.68	9.44	76.23	0.00	0.00	0.28
Sp-09	6.0		-23.4	0.10	40	533	345	9.0	90.6	12.78	9.54	75.04	0.00	0.00	0.30
Sp-10	6.2		-24.2	0.14	21	388	367	17.7	127.5	11.09	10.67	74.94	0.00	0.00	0.29
Sp-11	6.5		-23.6	0.12	32	431	368	11.9	96.8	25.62	13.43	59.04	0.00	0.00	0.66
Sp-12	7.0		-23.8	0.09	52	539	362	7.7	81.2	10.88	9.09	77.34	0.00	0.00	0.26
Sp-13	7.5		-	-	-	-	-	0.8	-	7.95	3.67	86.04	0.00	0.00	0.14
Sp-14	8.0		-23.49	-	-			9.4	-	9.78	7.03	80.49	0.00	0.00	0.21
Sp-15	9.0		-23.21	0.04	69	909	350		-	9.67	3.67	83.89	0.00	0.00	0.16
Sp-16	9.5		-22.93	0.04	96	945	374	-	-	14.01	8.34	75.34	0.00	0.00	0.30
Sp-17	10.5		-22.55	0.14	22	439	483	26.1	189.4	42.62	32.89	19.78	0.00	1.90	3.82
Sp-18	11.0		-23.59	-	-	-	-	9	-	12.74	13.59	71.23	0.00	0.00	0.37
Sp-19	11.5		-23.59	0.13	38	373	494	13.8	106.5	27.09	19.19	53.01	0.00	0.00	0.87
Sp-20	12.5		-24.31	0.14	29	363	377	13.6	100.3	-	-				
Sp-21	12.7		-24.23	0.11	37	343	382	9.8	90.4	18.65	13.31	67.02	0.00	0.00	0.48
Sp-22	13.0		-23.31	0.10	38	420	366	16.4	157.8	37.87	24.78	32.78	0.00	0.00	1.95
Sp-23	13.7		-23.83	0.11	17	251	494	-	-	30.67	23.57	41.44	0.00	2.38	1.31
Sp-24	14.5		-21.59	0.13	22	477	408	19.8	149.3	48.54	30.22	16.45	0.64	0.00	4.85
Sp-25	14.7		-23.58	0.16	18	271	481	-	-	17.90	9.56	68.98	0.00	0.00	0.40
Sp-26	15.0		-23.85	0.11	35	350	479	-	-	14.87	6.02	77.56	0.00	0.00	0.27
Sp-27	15.5		-23.82					8.7	-	11.30	6.04	80.23	0.00	0.00	0.22
Sp-28	16.0		-24.05	0.12	49	320	360	6.6	54.0	16.90	9.92	71.98	0.00	0.00	0.37
Sp-29	17.0		-23.17					9.9		11.34	6.76	81.09	0.00	0.00	0.22
Sp-30	17.5		-23.11	0.05	19	688	374	6.8	132.4	8.16	3.73	85.76	0.00	0.00	0.14
Sp-31	18.0		-23.30	0.07	29	887	364	5.1	73.76	-	-	-	-	-	-
Sp-32	18.5		-23.80	0.13	23	283	379	-	-	40.79	29.65	25.12	0.65	0.00	2.84
Sp-33	19.0		-23.09	0.11	27	524	385	14.2	131.1	44.12	30.12	21.25	0.00	0.00	3.55
Sp-34	20.0		-	0.12	26	370	361	10.8	93.4	34.43	18.73	41.70	0.00	2.12	1.27
Sp-35	20.5		-	0.07	58	759	355	8.2	119.5	21.54	11.68	65.10	0.00	0.00	0.51
Sp-36	21.0		-23.01	0.13	38	506	360	13.5	104.9	29.99	16.82	48.75	0.00	3.00	0.96
Sp-37	21.5		-21.46	0.11	26	779	493	19.6	173.0	14.15	3.55	76.29	0.00	3.71	0.23
Sp-38	22.0		-	-	-	-		0.7	-	9.82	1.34	87.10	0.00	0.00	0.13
Sp-39	23.0		-	-	-	-	-	0.6	-	6.34	1.19	91.45	0.00	0.00	0.08
Sp-40	24.0		-	0.09	179	411	425		-	6.23	1.28	91.32	0.00	0.00	0.08
Sp-41	25.0		-		-			1.1	-	4.09	1.25	93.14	0.00	0.00	0.06
Sp-42	26.0		-	0.04	132	674	380		-	4.12	1.19	93.23	0.00	0.00	0.06
Sp-43	26.6		-	-	-	-	-	0.8	-	1.89	1.89	95.09	0.00	0.00	0.04
Sp-44	27.0		-	-	-	-	-	1.5	-	5.12	1.32	93.12	0.00	0.00	0.07
Sp-45	27.5		-	0.11	80	318	476	1.7	15.3	3.13	1.26	94.17	0.00	0.00	0.05
Sp-46	28.0		-	0.08	26	258	487	1.4	18.4	3.89	1.21	93.12	0.00	0.00	0.05
Sp-49	30.0		-	-	-		-	1.0	-	2.78	1.14	95.07	0.00	0.00	0.04
Sp-50	31.0		-	0.11	45	252	481	1.2	10.8	3.76	0.96	92.67	0.00	0.00	0.05
Sp-51	33.0		-	0.05	37	343	365	1.5	27.7	3.08	1.39	94.10	0.00	0.00	0.05
Sp-52	35.0		-	0.02	240	1185	482	1.5	91.0	4.06	1.16	91.97	0.00	0.00	0.06
Sp-53	38.0		-	0.05	55	330	346	1.5	28	2.67	1.46	95.34	0.00	0.00	0.04
Sp-54	39.0		-	0.02	332	1017	466		-	7.90	3.24	86.13	0.00	0.00	0.13
Sp-55	45.0		-	0.01	216	1078	386	3.5	253.7	7.34	4.34	85.78	0.00	0.00	0.14
Sp-56	50.0		-	-	-	-	-	2.6	-	6.31	3.19	88.19	1.34	0.00	0.11
Sp-57	55.0		-	0.07	59	316	350	0.8	11.8	-	-	-	-	-	-
Sp-58	60.0		-	0.04	111	469	374	1.1	30.8	8.67	1.54	87.10	0.00	0.00	0.12
Sp-59	65.0		-	0.08	91	366	489	2.4	31.5	7.97	1.29	88.09	0.00	0.00	0.11
Sp-60	70.0		-	-	-	-	-	2.8	-	6.73	1.08	90.79	0.00	0.00	0.09

Table GS2 Summary of Ghumanwan section geochemical data with bulk rock mineralogy and Mercury concentrations.

Table "Tethys" LBF-based information from 34 shallow section across the Tethys spanning from SBZ3 to SBZ5/6

Country	Location	Formation	SBZ 3	SBZ 4	SBZ 5/6	References
India	Ladakh (North Zanskar Tethyan)	Marpo and Dibling Foramation	*Daviesina danieli, Rotalia trochidiformis, R. bermudezi Kathiana bermudezi, L. haimei*, and **RCA**.	*Ranikothalia nuttalli,Miscellanea miscella, Daviesina garumnensis, L. haimei, Rotalia trochidiformis, Daviesina langhami*, and **RCA**.	*Nummulites minervensis, Assilina sp., A. pustulosa, Glomalveolina lepidula, Daviesina langhami, Rotalia trochidiformis, D. khatiyahi, Assilina leymeriei, Alveolina sp., A. ilerdensis, Miscellanea miscella*, glomalveolinids, and **GCA**.	Mathur et al.,2009, Nicora et al.,1987
	Ladakh (South Zanskar Tethyan)	Lingshet Formation	No information	*Daviesina garumnensis, Glomalveolina levis, Broeckinella arabica, Rotorbinella, Lockhartia, Kathina,* and **GCA.**	*Daviesina tenuis, Nummulites minervensis,Glomalveolina lepidula, Miscellanea miscella, Ranikothalia nuttalli, Daviesina langhami, D. khatiyahi, Alveolina sp., Lakadongia*	Mathur et al.,2009, Kahsnitz et al.,2018
	Ladakh (Indus–Tsangpo suture zones)	Indus Foramtion	No information	*Broeckinella arabica, Actinosiphon tibetica, Discocyclina spp.*, and **RCA**	*Alveolina ellipsoidalis , Nummulites minervensis, Alveolina Vredenburgi, Assilina pustulosa*	Mathur et al.,2009
	Katuch Basin	Naredi Limestone	No information	No information	*Nummulites sp.*,	Khanolkar & Saraswati, 2019
	Jaisalmer Basin	Khuiala Formation	clastic sediments	Clastic sediments	*Nummulites* cf. *gamardensis* and *Assilina dandotica*	Khanolkar et al., 2021
	Meghalaya	Lakadong Limestone	*Miscellanea juliettae, Glomalveolina primaeva, Lockhartia sp,, Lakadongia tibetica,* **GCA** and **RCA**.	*Glomalveolina levis, Miscellanea miscella , orthophragminids, Lakadongia Tibetica , Ranikothalia cf. nuttali*, and **RCA *(Distichoplax biserialis)***	*Nummulites, orthophragminids, Alveolina sp., Assilina sp., Orbitolites sp., Lakadongia Tibetica , Daviesna sp, Miscellanea miscella , Ranikothalia Nutalli*, **RCA and GCA** + clastic sediments with dinofagellate (*Apectodinium* acme*)*	Pereira et al., 2022 ; Ozcan et al., 2018 ; Sarkar, 2015, 2018, Sarkar et al., 2022 ; Sreenivasan et al.2022
Paksitan	Hazara Basin	Lockhart Limestomne and/or Patala Formation	*Lakadongia primitiva, Lockhartia sp., Miscellanea yvettae, M. juliettae, and Ranikothalia sp.,* ***GCA*** *and* **Corals**	*Daviesina sp., Lakadongia sp., Lockhartia sp.,Miscellanea yvettae, M. juliettae, M. cf. miscella,*	No information	Ali et al., 2024 a

				Orbitosiphon sp., Operculina sp., Ranikothalia sahnii, and ***RCA***		
	Salt Range	Lockhart Limestomne & Patala Formation	*Lockhartia conditi, Daviesina praegarumnensis, Lockhartia cf. haimei, Daviesina cf. intermedia,* **GCA and Corals**	*Kathina aquitanica, Orbitosiphon cf. punjabensis, Daviesina langhami Idalina sinjarica, Lockhartia haimei, Lockhartia cf. roeae, Lockhatia retiata, Rotalia implumis, Lockhartia conditi, Elazigina lenticula, Dictyoconoides cf. flemingi, Lakadongia tibetica Elazigina harabekayisensis, Lockhartia sp. Kathina mayor,, Rotalia cf. newboldi, Miscellanea miscella* **GCA**	*Alveolina cf. vredenburgi, Assilina dandotica M. miscella, L.haimei A. ranikotiR. cf. newboldi E. lenticula, Ranikothalia nuttalli* **GCA and Corals**	This study "Nammal Gorge" Ahmad et al.,2017; Afzal et al., 2023
	Surghar Range	Lockhart Limestomne & Patala Formation	*Miscellanea juliettae, Miscellanites sp., Lockhartia prehaimei, Lockhartia retiata, Elazigina lenticula, Kathina selveri, Orbitosiphon sp.* **GCA and Corals**	*Miscellanites sp., Miscellanea cf. dukhani, Daviesina sp., L.haimei, L.conditi, L.roeae, Lockhartia tipperi, Kathina silver, Elazigina lenticula, Rotospirella sp., Rotalia cf. newboldi, Rotorbinella sp., Orbitosiphon., Lakadongia tibetica. L.prehaimei, L.diversa, L.retiata, Kathina mayor, Miscellanea miscella, Ranikothalia sindensis, Daviesina langhami*	*L.conditi, L.haimei, Rotalia cf. newboldi, Lockhartia retiata Daviesina langhami, Ranikothalia nuttalli, Orbitoclypeus sp, L.hunti Assilina ranikoti, Ranikothalia sindensis, Nummulites sp., Discocyclina sp., Alveolina sp. Assilina ornata, Daviesina intermedia, Rotorbinella cf. skourensis Assilina dandotica, Nummulites minerviensis,* ***Distichoplax biserialis*** **GCA and Corals**	Ali et al., 2025 see Chapter 4); Ahmad et al.,2017; Afzal et al., 2023
	Lower Indus basin	Dungan Formation	*Coskinon rajkae, Fallotella alavensis, Vania anatolica,Miscellanea juliettae, Ranikothalia sindensis, R. sahni,*	*Glomalveolina levis, Glomalveolina telemetensis, Assilina azilensis, Kathina selveri, Dictyoconus spp, Karsella*	*Alveolina spp (A. decipiens, A. ilerdensis, A. ellipsoidlis, and A. oblonga), Ranikothalia nuttalli, Discocyclina dispansa, Assilina*	Hussian et al., 2024 (pre print) ; Afzal et al., 2010, 2011

			Lockhartia haimei, L. conditi, Kathina selveri, Lakadongia tibetica and Orbitosiphon punjabensis, **RCA**, **GCA**, and **Corals**	*hottingeri, Kathina pernavuti, Rotaliconus arachosiae, Miscellanea meandrina, Redmondina henningtoni, Azzarolina daviesi, Miscellanea miscella, Lockhartia haimei, Lockhartia conditti, Rotalia sp, Idalina sinjarica, Coskinolina sp, Glomalveolina spp,* and **RCA**	*dandotica, Discocyclina sella, Orbitolites spp, Operculina spp, Miscellanea miscella, Lockhartia haimei, Lockhartia conditti, Rotalia sp, Idalina sinjarica, Coskinolina sp, and Glomalveolina spp*	
	Potwar Basin	Patala Formation	*Glomalveolina primavea, Fallotella alavensis, Miscellanea juliettae, Lockhartia sp, Daviesina sp.*	*Aberisphaera gambanica, Daviesina langhami, G. levis, Orbitosiphon punjabensis, M. dukhani, Lakadongia Tibetica , Ranikothalia sp., Operculina sp.,*	*Alveolina vredenburgi, A. ellipsoidalis, Orbitolites biplanus , A. avellana aurignacensis, Nummulites minervensis, N. fraasi, Assilina dandotica, and A. aramaea aramaea, Orthophraminds, Operculina sp.,*	Kamran et al.,2021; Ahmad et al.,2017; Afzal et al., 2023
	Hazara Kashmir Syntaxies	Patala Formation	No Information	*Assilina subspinosa, Discocyclina ranikotensis, Operculina jiwani, Lockhartia sp., Miscellanea miscella, Nodosaria spp., and Ranikothalia bermudezi* , **RCA** and **GCA**	*Discocyclina sp, Operculin sp., Assilina spp., Discocyclina ranikotensis, Miscellanea miscella, Alveolina sp., Assilina laminosa, Heterostegina assilinoides blankenhorn, Lockhartia spp., Miscellanea spp. Miscellanea juliettae, Nummulites spp.,* and **RCA**	Bilal et al.,2024
China	Tibet (Tingri area)	Zhepure Shan Formation	*Lockhartia haimei, L. roeae, Miscellanites primitivus, Keramosphaerinopsis haydeni, Daviesina khatiyahi, and D. tenuis,* and **RCA** ,	*Rotalia cf. newboldi, Lockhartia altispira, L. aff. roeae, L. aff. conditi, Kathina nammalensis, Aberisphaera gambanica, Setia tibetica, Daviesina langhami, Ranikothaliasindensis, and Operculina cf. canalifera, and the last occurrence of*	*Lockhartia conditi, L. tipperi, L. hunti, M. minor, R.savitriae, R. thalica, Operculina patalensis, O. subsalsa, O. jiwani, and Orbitolites sp.Miscellanea miscella, Ranikothalia nuttalli, and Alveolina vredenburgi, Alveolina ellipsoidalis, A. cf. subtilis,A. agerensis,A. conradi, A. tibetica,* and **GCA**	Zhang et al.,2013, 2019, 2020 ;2023 Li et al., 2020 ; Kahsnitz et al.,2019

				Rotalia implumis (nomen nudum), Lockhartia retiata, L. roeae, Kathina cf. selveri, Miscellanites primitivus, and Keramosphaerinopsis haydeni, and **GCA**		
	Tibet (Gamba and Düela area)	Zongpu Formation	*Lockhartia haimei, L. roeae, Miscellanites primitivus, Keramosphaerinopsis haydeni, Daviesina khatiyahi, and D. tenuis.* **RCA**, **GCA** and **Corals** (Gamba Section)	*Alveolina subpyrenaica Leymerie , Lockhartia haimei , Miscellanea juliettae Leppig , and Rotospirella conica Kathina aquitanica, Daviesina khatiyahi, Daviesina garumnensis, and Lockhartia conditi, Glomalveolina primaeva, Ranikothalia sindensis, Daviesina langhami, Alveolina ilerdensis, Lockhartia tipperi, M. dukhaniRotalia cf. newboldi, Lockhartia altispira, L. aff. roeae, L. aff. conditi, Kathina nammalensis, Aberisphaera gambanica, Setia tibetica, Daviesina langhami, Ranikothalia sindensis, and Operculina cf. canalifera, and the last occurrence of Rotalia implumis (nomen nudum), Lockhartia retiata, L. roeae, Kathina cf. selveri, Miscellanites primitivus, and Keramosphaerinopsis haydeni.* and **GCA, Corals** (Gamba section)	*Lockhartia conditi, L. tipperi, L. hunti, M. minor, R.savitriae, R. thalica, Operculina patalensis, O. subsalsa, O. jiwani, and Orbitolites sp.Miscellanea miscella, Ranikothalia nuttalli, and Alveolina vredenburgi, Alveolina ellipsoidalis, A. cf. subtilis,A. agerensis,A. conradi, A. tibetica , Lockhartia sp., Glomospira sp.,Rotalia sp., (interval mostly devoid of LBF)*	Zhang et al.,2013,, 2019,

	Tarim basin (Inland China)	Qimugen Formation	Limestone (inner ramp, tidal flat to lagoon)	Calcerous marls (inner ramp, tidal flat to lagoon)	Calcaerous marls (middle to outer ramp)	Jiang et al.,2023; Dong et al.,2024, Cao et al.,2018
	Xigaze forearc basin.	Jialazi Formation	*Rotorbinella hermi, Miscellanea yvettae,* *and Ranikothalia sindensis*	*Discocyclina sella, Miscellanea yvettae, Ranikothalia sindensis, Ranikothalia nuttalli, Daviesina langhami, Nummulites globulus* ***Corals and RCA***	*Miscellanea miscella, Daviesina langhami, Assilina yvettae, Miscellanea julliettae, Discocyclina seunesi, Assilina laminosa, Assilina subspinosa , Nummulites globulus, Discocyclina sella, Assilina dandotica, Ranikothalia sindensis, and Daviesina tenuis ,Assilina granulosa, Discocyclina dispansa, Assilina leymeriei, Nummulites mamillatusn,* **RCA** (mainly *Distichoplax biserialis* in the Lower Part)	Jiang et al.,2021 ;Kahsnitz et al.,2018
Iran	Lurestan	Taleh Zang Formation	*Glomalveolina primaeva, G. telemetensis, Periloculina sp., Lockhartia diversa, Falotella alavensis, Stomatorbina binkhorsti, Vania anatolica, Coskinon rajkae, Ranikothalia sindensis, Sakesaria sp.,* **RCA** and **Corals**	*Miscellanea miscella, Miscellanea rhomboidea* and *Ranikothalia nuttalli*	*Orbitolites complanatus, Cuvillierina yarzai, Nummulites globulus, Alveolina pasticillata, A. cf. avellana, A. decipiens,* and *A. lepidula.*	Bagherpour & Vaziri, 2011, Kakemem et al., 2023, Adabi et al.,2008
Iraq	Kurdistan region	Sinjar Formation	*Fallotella alavensis, Operculina heberti, Dictyoconus baskilensis, Miscellania juliettae, Operculina subsalsa,Operculina salsa, Rotalia trochidiformis, Idalina sinjarica,* **Corals** and **RCA**	*Miscellania juliettae, Operculina subsalsa, Hottingerina lukasi,Operculina salsa, Rotalia trochidiformis, Idalina sinjarica, Miscellanea miscella,* **Corals** and **RCA**	*Alveolina globosa, Kathina pemavuti - Lockhartia hunti,Alveolina globosa, Alveolina pasticilata, Rotalia trochidiformis; Rotalia sp., Dictyoconus sp., Lokhartia sp., Textularia sp., Assilina sp., Valvulammina globularis, Lockhartia hunti, Alveolina rutimeyeri, Idalina sinjarica, Miscellanea miscella*	Al-Taee et al.,2024a, b ; Salih, 2012, Hama Salih et al., 2022, Tamar-agha et al.,2015

UAE	Western UAE (offshore)	Not published (data from oil industry report)	*D. khatiyahi, Kathina selveri, Lockhartia sp., Miscellanea rhomboidea, Mardinella daviesi, Coskinolina sp,* and **Solitary Corals**	*K. major , K. cf. delseota, Daviesina sp, Miscellanea sp., D. khatiyahi, Kathina selveri, Lockhartia sp., Miscellanea rhomboidea, Miscellanea dukhani, Discocyclina sp, Thomasella labyrinthica, Glomalveolina Dictyokathina simplex, Sakesaria sp.*	*D. intermedia, L. cf. roeae, ?Assilina spp., Ranikothalia sp.D. langhami, L. conditi, D. salsa, Nummulites spp, L. praehaimei, Ranikothalia nutalli, Rotorbinella hensoni, D. tenuis, L. haimei, Dictyokathina simplex, Sakesaria sp, M. dukhani*	Beasley et al., 2021
OMAN	Sunab Basin	Jafnayn Formation	No information	*Ranikothalia sp,* **RCA (*Distichoplax biserialis*)** and **Corals**	Alveolinids and **GCA**	Mattern et al.,2019
Saudi Arabia	Arabian Gulf	Umm Er Radhuma Formation	*Rotalia trochidiformis, Rotalia convexa, Lockhartia haimei, L. altispira, Rotalia dukhani, Lockhartia praehaimei, L. hunti, L. diversa, L. conica. Rotalia hensoni, R. dukhani, Lockhartia tipperi, Cincoriola arabica, Sakesaria ornata,* **RCA** and **GCA.**	*Lockhartia pustulosa , Nummulites* (small size) *Rotalia trochidiformis, Soriella corrugata, Nummulites cf. elegans, Discorbis vesicularis, Miscellanea miscella, Ornatanomalina inflata, Sakesaria dukhani, Sakesaria cotteri, Heterostegina sp., Kathina selveri, Redmondia henningtoni, Alabamina dubifera, Dictyokathina simplex, Daviesina Khatiyahi, Sakesaria dukhani, Daviesina langhami. Miscellanea meandrina, Lockhartia conica, L. haimei, L. diversa, Kathina major* and *Sakesaria ornata*		Hasson 1985, Mousa et al.,2023
Qatar	Arabian Gulf	Umm Er Radhuma Formation	*Rotalia trochidiformis, Rotalia convexa, Lockhartia haimei, L. altispira, Rotalia dukhani, Lockhartia praehaimei, L. hunti, L. diversa, L. conica. Rotalia hensoni, R. dukhani, Lockhartia tipperi, Cincoriola arabica, Sakesaria ornata,* **RCA** and **GCA**.	*Rotalia trochidiformis, Soriella corrugata, Nummulites cf. elegans, Discorbis vesicularis, Miscellanea miscella, Ornatanomalina inflata, Sakesaria dukhani, Sakesaria cotteri, Heterostegina sp., Kathina selveri, Redmondia henningtoni, Alabamina dubifera, Dictyokathina simplex, Daviesina Khatiyahi, Sakesaria dukhani, Daviesina langhami. Miscellanea meandrina, Lockhartia conica, L. haimei, L. diversa, Kathina major and Sakesaria ornata*		Hewaidy 1994, Hewaidy & Hatimi 1993

Kuwait	Wafra Field	Umm Er Radhuma Formation	No information	*Globigerina, Sakesaria, Lockartia, Peneroplis, Caucasina,* and **calcareous algae** (?)		Bou-rabee & Burke 1987
Egypt	Farafra Oasis,Western Desert	Tarawan Chalk and Esna Shale	Barren Interval	*Glomalveolina levis , Slovenites pembaphis, Miscellanites iranicus, Miscellanea miscella, Periloculina? sp., Glomalveolina levis* and *Idalina sinjarica*	*Alveolina cf. ellipsoidalis, Alveolina sp., Elazigina cf.lenticula, Nummulites sp., Assilina sp.* and orthophragminids	Farouk et al.,2019
	Galala Plateaus, Eastern Desert	Southern Galala Formation	*Glomalveolina primaeva*, *Elazigina lenticula*, *Discocyclina sp*., *G. dachelensis*, *Periloculina slovenica*, and *Idalina sp*.	*Glomalveolina levis*, *Elazigina lenticula*, *Miscellanea rhomboidea*, *Discocyclina sp*., *G. dachelensis*, Ranikothalia sp.,	*Alveolina vredenburgi, A. ellipsoidalis, A. minervensis, A. pasticillata, A. piper, A. rutimeyeri, A. subovata,* and *Fabularia zitteli*.	Abd-Elhameed et al., 2023; Hontzsch et al., 2011 a, b ; Ozcan et al., 2014
Libya	Sirte Basin	Upper Sabil Formation/ Harash Formation	*Kathina cf. aquitanica, Elazigina lenticula,Ranikothalia solimani, Glomalveolina primaeva, Miscellanea yvettae Leppig, Miscellanites primitivus,Rotorbinella hensoni,* **RCA** and **Corals**	*Discocyclina sp, Operculina sp, Nummulites,* **Corals** and **RCA**	Deep water shales (Kheir Formation)	Vršič et al., 2021a,b , Hassi 1995
Greece	Ionian Islands (Cephalonia and Zakynthos)	?	*Coskinon rajkae, Glomalveolina primaeva, Idalina sinjarica,, Hottingerina cf. anatolica, Dictyoconus cf. turriculus, Fallotella alavensis, Discocyclina seunesi, Rotalia cf. hensoni,* **GCA** and **Corals**.	*Assilina gr. Yvettae, Kathina suhsphaerica, and Orbitoc!ypeus sp, Coskinon rajkae, Glomalveolina primaeva, Idalina sinjarica,, Hottingerina cf. anatolica, Dictyoconus cf. turriculus, Fallotella alavensis, Discocyclina seunesi, Rotalia cf. hensoni,* **GCA** and **Corals**	*Alveolina globula, A. doliol(formis, Glomalveolina lepidula, A. ex gr. aramaea), Orbitolites sp., Nummulites spp., Assilina spp., Ranikothalia cf. sindensis, and Miscellanea sp., Assilina pasticillata, A. cf. ellipsoidalis;*	Accordi et al.,1998, 2014
Turkey	Tuz Gölü Basin	Karapınaryaylası Formation	*Idalina causae, I. sinjarica, Lockhartia conditi and L. haimei, Discocyclina sp., Rotalia trochidiformis*	*Idalina causae, I. sinjarica, Lockhartia conditi and L. haimei, Discocyclina sp., Rotalia trochidiformis*	*Rotalia trochidiformis , Alveolina sp*	GÖRMÜŞ et al.,2024

	Kastamonu region	?	*R. trochidiformis, Kathina selveri, Kathina major, Miscellanea primitiva.*	*Idalina sinjarica, Discocyclina, Assilina sp. Operculina sp., Ranikothalia sp.,* and **RCA**.	*Alveolina cf. ellipsoidalis, Glomalveolina lepidula, Idalina sinjarica, Nummulites minervensis, Discocyclina sp., Nummulites sp., Operculina sp., Assilina sp.*	Ozgen-Erdem et al.,2005
Slovenia	Adriatic Platform (Cebulovica and Kozina section)	Trstelj Formation and *Alveolina-Nummulites* Limestones	*Coskinon rajkae, Fallotella, alavensis, Cribrobulimina carniolica, Haymanella paleocenica, and Miscellanea juliettae,* **GCA**	*Assilina yvattae, Assilina azilensis, the miliolines Lacazina blumenthali, Glomalveolina dachalensis and Glomalveolina levi,* **RCA (*Distichoplax biserialis*), Corals**, and **Encrusting benthic foraminifera**.	*Aveolina. aramaea aramaea, Assilina,Nummulites orthophragminids, Alveolina globula, Alveolina ellipsoidalis,* and *Alveolina pasticillata.*	Zamangi et al., 2008, 2012
Italy	Northern Italy, Belluno Basin and Lombardian Basin	Tabiago Formation and informal units “Cugnan Formation”, “Scaglia Cinerea”, and “Marna della Vena dell’Oro” Vena d’Oro”	*Cocoarota orali*, *Coskinon* sp., *Cuvillierina sireli*, *Daviesina intermedia*, *D. praegarumennsis*, *Elazigina lenticula*, *Glomalveolina primaeva*, *Globloflarina* sp., *Kathina aquitanica, K. selveri, Miscellanea yvettae, M. juliettae, Miscellanites primitivus, Orduella sphaerica*, orthophrag- minids, *Planorbulina cretae, Ranikothalia spp., Slovenites pembaphis, Stomatorbina binkhorsti*, Thalmannita *madrugaensis*.	*Assilina sp., Assilina azilensis, A. yvettae, Cocoarota orali, Daviesina sp., Daviesina garumnensis, D. salsa, Dictyokathina simplex, Elazigina lenticula, Glomalveolina levis, Hottingerina lukasi, Miscellanea meandrina, Nummulites catari,* orthophragminids, *Ranikothalia sp.*	No information	Papazzoni et al., 2023
	Central Italy, Abruzzi Platform	Scaglia Detritica Formation	*Elazigina lenticula, Cuvillierina cf. sireli, Glomalveolina spp.,Discocyclina sp.*	*Glomalveolina spp, Miscellanea cf. miscella Ranikothalia cf. solimani, Assilina cf. dandotica, Assilina yvettae, Daviesina*	No information	Benedetti et al., 2018 ; Tomassetti & Benedetti 2020

				danieli, and Hottingerina lukasi		
Spain	Pyrenees (Urbasa-Andia plateau)	Legunbe complex	**Corals and RCA**	Ranikothalia, Discocyclina, Miscellanea **Corals and RCA**	No information	Baceta 2005
	Pyrenees (Serraduy and Campo Section)	Upper Neavarri and Lower Serraduy	*Glomalveolina primaeva, Periloculina slovenica, Vania anatolica, Coskinon rajkae, Fallotella alavensis, Cribrobulimina carniolica, Miscellanea yvettae, Miscellanea juliettae, Miscellanites primitivu,s Miscellanites minutus, Ranikothalia soldadensis*	*Glomalveolina levis and Daviesina garumnensis, Assilina yvettae, A. granulosa, and Ranikothalia thalica,Rotorbinella skourensis, and Miscellanea miscella*, **Corals** and **RCA**	*Alveolina vredenbrigi, A. aramea, Opertorbitolites gracilis, A. ellipsoidalis, Alveolina globula,Alveolina pasticillata , Alveolina globosa, Alveolina aragonensis and Operculina sp., A. dolioliformis and Opertorbitolites,* **Corals** and **RCA.**	Li et al.,2021, Serra-Kiel et al., 2020 , Aguirre et al.,2022

.